Kinematic Fractionation of the Stellar Populations in Barred Galaxies

Steven Gough-Kelly

A thesis submitted in partial fulfilment
of the requirements for the degree of
Doctor of Philosophy

Jeremiah Horrocks Institute for Mathematics, Physics and Astronomy
University of Central Lancashire

November 15, 2023

Declaration

Type of Award: Doctor of Philosophy

School: Natural Sciences

I declare that while registered as a candidate for the research degree, I have not been a registered candidate or enrolled student for another award of the University or other academic or professional institution.

I declare that no material contained in the thesis has been used in any other submission for an academic award and is solely my own work.

No proof-reading service was used in the compilation of this thesis.

Steven Gough-Kelly

November 15, 2023

"Since such a guide is lost, what other now,
Deserving to succeed, can take the reins?
Or should the stars rebel, who can restore
Them to their course, and bind with closer ties
Their wandering ways?..."

— Jeremiah Horrox

Abstract

The formation and evolution of the central regions of barred galaxies are the subject of significant ongoing study. Research has indicated that the morphology and kinematics of stellar populations are dependent on their age. Simulations suggest that this dependence occurs because populations are separated by the bar. Populations with varying radial velocity dispersions evolve differently in the presence of a growing bar, a process termed *kinematic fractionation*.

Using star-forming simulations of barred galaxies which undergo kinematic fractionation, we have reproduced the observed trends of metal-rich and metal-poor Milky Way bulge main-sequence stars observed with the *Hubble Space Telescope*. The old and young stellar populations in the models were born before and after the bar, respectively. As each population traces varying bulge structures with different bar strengths, their kinematics project onto distinct observed motions as seen from the heliocentric perspective. The predictions from these models allow us to propose follow-up observations to test the kinematics of differently-aged populations in fields away from the bulge minor axis.

To trace structures in the Milky Way using stellar ages, we explore new data from the *Gaia* satellite. We define and characterise a clean sample of Mira variables using data-motivated cuts on their relative frequency error and variability amplitude, maximising their separation from SRVs. Mira candidates were found to follow the expected trends of age in their spatial and kinematic distributions when separated by variability period. However, we determined that a larger sample of Miras is

needed to better constrain the Milky Way bar. Nevertheless, we were also able to characterise the effects of the large variability amplitude of Miras on astrometric and photometric solutions within *Gaia*, allowing us to make recommendations for future study and observation of these stars.

We have identified barred galaxies in the TNG50 cosmological simulation and defined a method based on kinematics to find those which form a box/peanut bulge. By studying the evolutionary history of bar and box/peanut strength, we can determine their formation epoch. This method is also able to distinguish between box/-peanut bulges formed through strong buckling or those which form through slower resonance heating or weak buckling. Our results show that TNG50 reproduces a similar dependence of box/peanut fraction with stellar mass but does not have as high a fraction at high mass. However, in TNG50, we find the same characteristic upturn to higher fractions of box/peanuts from low mass to high mass.

Having a large self-consistent sample of barred galaxies from TNG50, we study kinematic fractionation in a fully cosmological context. We find that the spatial distribution of kinematic quantities of populations in the bar, such as the in-plane anisotropy, can trace the bar strength as measured by the density of that population. We also find that populations within the bar of the galaxy retain the dynamical memory of the bar formation epoch. Studying box/peanut bulges in TNG50 galaxies, we find the separation of the density bimodality increases as a function of decreasing age.

Contents

List of Tables

List of Figures

"Perhaps, the future is predetermined
by the character of those who shape it."

— Davos

Acknowledgements

First and foremost, thanks must be given to Prof. Victor P. Debattista for your patience, encouragement, wisdom, and guidance for the last seven years. Working on a small project measuring the size of a BP bulge during one summer of my undergraduate, I could never have imagined making it all the way to the end of a PhD, and it would not have been possible without your support. It seems almost fitting that one of the chapters of this thesis covers that same project and serves as a reminder of how far we have progressed. Thank you is not enough for getting me through this incredible journey. I will forever be grateful for your faith and perseverance in having me as your student for so long. You have shaped me into the best scientist I could have possibly become, so know if you ever have to review one of my papers, it will be your own fault.

Second thanks go to my second supervisor Dr Mark Norris who has continuously supported me throughout my time at UCLan and kept my observational skills sharp and my paperwork (mostly) on time. I am beyond appreciative of the opportunities you gave me at Alston to develop as a science communicator.

Also, I want to acknowledge the old and new members of the Galaxy Dynamics Research Group at the Jeremiah Horrocks Institute: Stuart Anderson, Dr Tigran Khachaturyants, Dr Leandro Beraldo e Silva, Dr João Amarante, David Liddicott, Ilin Lazar, Luismi San Martin Fernandez, Karl Fiteni, Dr Chiara Buttitta, Prof.

Joseph Caruana, Maria Aquilina, Dr Virginia Cuomo, Dr Adam Clarke and Dr Sam Earp who all have been instrumental in my growth both as a researcher and a person.

Thank you to Prof. Cristina Popescu and Dr Francesca Fragkoudi for the fantastic discussion and their constructive evaluation of this thesis.

I am also grateful for my research colleagues and collaborators who have encouraged, challenged and inspired me to pursue the projects presented here in this thesis and beyond: Dr William Clarkson, Dr Oscar Gonzalez, Dr Min Du, Dr Peter Erwin, Dr Laurent Eyers, Dr Rachel Street and Dr Dimitri Veras.

Furthermore, I am grateful to everyone, both staff and students at the JHI, for their support, advice and guidance from my first open day as a prospective student all the way to this moment. Still, I would also like to name those I am particularly thankful to: Prof. Derek Ward-Thompson, Dr Megan Argo, Dr Joanne Pledger, Prof. Don Kurtz, Dr Karen Syres, Dr Tim Mercer, Dr Simon Ebo, Dr Adam Fenton, Charlotte Proverbs, Alexia Lopez, Dr Adam Hutchinson, Dr Callum Mackinnon, Joshua Stanway, Ruth Hyndman, Janik Karoly, Amelia Sharp, Amar Rambukwella-Gill, Dr Jordan Cole, Dr David Glass, Dr Daniel Johnson, Jamie Banister, Matthew Teasdale, Ethan Carter, Dr Jordan Thirlwall, Dr Daniel Gass, David Capstick, Rick Collins, Dr Dimitris Stamatellos, Dr Daniel Lee, Dr Dominic-Frederick Bowman, Dr Steve McCann, Dr Daniel Brown, Dr David Glass, Zak Meyers, William Robinson, Anne Harkness and Nuala Jones. I cannot think of a better place to have studied and worked for the last eight years.

To my wider colleagues and friends at UCLan, UCLan Students' Union, 53 Degrees, UCLan/Ri Young Scientists Centre, Preston Guild Hall and Charter Theatre: Daniel

Smith, Phillip Price, Sujata Patel, Dr Jo Brown, Joshua Pearson, James Gelson, Dave Weeks, John Wojturski, Rowan Fox, Samantha Fogg, Abbie Tutt, Jon Russ, Matt Smith, Alex Wynn, Kristie Staley, Lorri Millar, Anthony Worswick, Megan Critchley, Aaron Brown, Ian Blease, Sarah Thompson, Luke Fitzgerald, Joseph Bigland, Aaron Anderson, Phoebe Liptrot, Sophie Millar, Ste Ashurts Perryman who provided invaluable experience, fun, laughter and a wealth of opportunity to experience beyond my academic studies. There are so many memories I will cherish for the rest of my life.

I am truly honoured to have been supported throughout my PhD by the Moses Holden Studentship. The decedent of this inspirational figure, Patrick Holden, has bestowed me this opportunity to contribute new science and continue the legacy of the 'diffusion of useful knowledge' to Preston and beyond.

Dedication

This thesis is dedicated to my family, who have stuck by me on my prolonged journey through university. Your insatiable love and support provide an eternal port in stormy seas. Who would have guessed a childhood of Thomas the Tank Engine, Power Rangers, Stargate and Mythbusters could have led to a PhD in astrophysics? Yet here we are, and it would not have been possible without you all: my parents, grandparents, aunties, uncles, siblings, cousins and my extended family. Also, I cannot forget my furry therapists, Teddy, Champ and Lex.

Finally, to Xeng, you are the person I wish to wake up to every morning and sleep dreaming of every night. There is nothing I can write here that could express my gratitude for your love, compassion and support. Every day I have with you is a gift, and thankfully, we have forever and many days.

Chapter 1

Introduction

1.1 Galactic Structure

Early astronomers observed not only individual stars but also nebulae, which were thought to be clouds of gas and dust within our own Milky Way Galaxy. With the invention and development of the telescope, some such nebulae appeared to have a spiral shape. The German philosopher Immanuel Kant first used the term 'island universes' in the 18^{th} century proposing that the Milky Way Galaxy was just one of many 'island universes' scattered throughout the observable sky (Curtis 1988). However, it wasn't until the early 20^{th} century that astronomers were able to confirm the existence of other galaxies beyond our own. American astronomer Edwin Hubble made a groundbreaking discovery that significantly changed our understanding of the Universe. He observed these 'spiral nebulae' using the most powerful telescope of his time. He discovered that they were not located in the Milky Way, as previously thought, but were indeed independent galaxies located far beyond our Galaxy (Hubble 1929). Hubble's work revolutionised our understanding of the cosmos and paved the way for many more discoveries in the years to come.

Hubble began visually classifying galaxies into different morphological groups based on several key features, constructing the Hubble sequence (Hubble 1936), a

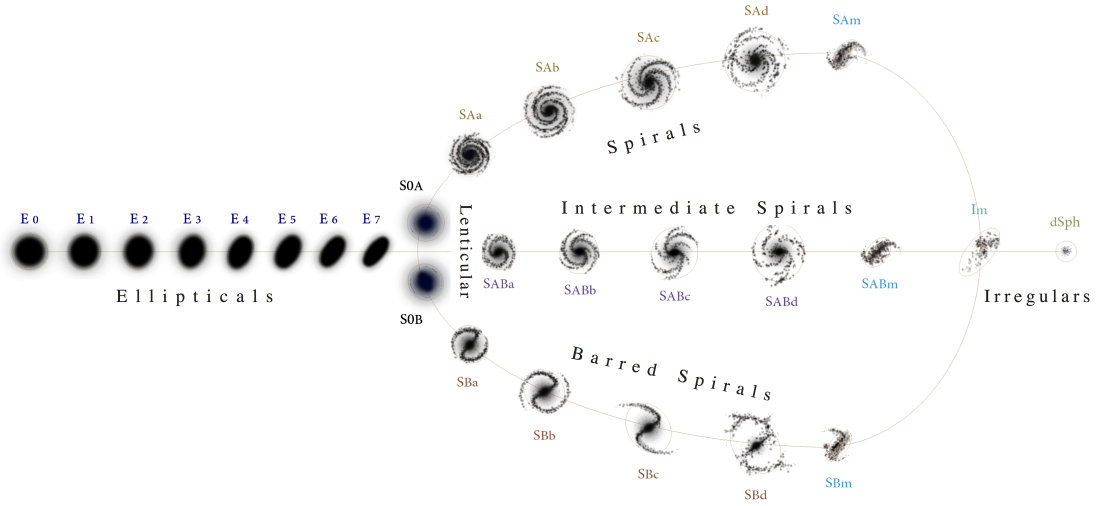

Figure 1.1: Hubble - de Vaucouleurs diagram for galaxy morphology featuring ellipticals, lenticulars, spirals, intermediate spirals, barred spirals, and irregulars. Image credit: Antonio Ciccolella and M. De Leo (2016).

system still used by astronomers today. Further classifications have expanded on the Hubble sequence, such as the work of de Vaucouleurs (1959). As telescope and computing technology developed, astronomers, citizen scientists and machine learning algorithms have defined and characterised galaxies in considerable detail (*e.g.*, Masters & Galaxy Zoo Team 2020), providing insights into their formation and evolution. The Hubble - de Vaucouleurs diagram of galaxy morphology is presented in Fig. 1.1. There are two primary types of galaxies: ellipticals and spirals.

Elliptical galaxies (left-hand side of Fig. 1.1) are rounded in shape and lack the distinct disc structure of spiral galaxies. They are made up of older stars and have a sparse interstellar medium (ISM) with small amounts of cold gas. Elliptical galaxies range in size from small dwarf galaxies to massive giants. Unlike spirals, elliptical galaxies do not have a pattern of star formation and appear redder due to the predominance of older stars. Ellipticals are further divided into subgroups based

on the ellipticity of their light distribution, from elliptical (E7) to circular (E0).

Lenticular galaxies, also known as S0 galaxies, are a type of intermediate form between spiral and elliptical galaxies. They have a central bulge like elliptical galaxies but also a disk of stars like spiral galaxies. Lenticular galaxies are characterised by their lack of spiral arms and their smooth, featureless appearance.

Spiral galaxies, on the other hand, have a cold, diffuse interstellar medium of stars, gas and dust in a disc morphology. Many have a dense central bulge region surrounded by spiral arms that extend outward (the upper track in the right-hand side of Fig. 1.1). The arms are dense regions populated by young stars, star-forming gas, and dust, while a central bulge contains older stars. Spiral galaxies often have a distinctive pattern of star formation along their spiral arms, which gives them a characteristic blue colour. The classification of spiral galaxies from 'a-d' distinguishes between how tightly wound their spirals are, with tightly wound spiral galaxies having the most prominent bulge or central spherical region (a). Loosely wound spirals have the smallest bulges (d). Spiral galaxies have three further sub-divisions: non-barred, weakly barred and strongly barred (SA, SAB and SB, respectively). These stellar bars are straight features through the galaxy centres that appear to rotate as a ridged body and commonly connect with spiral features. The same subclassifications of 'a-d' also describe the spiral windings and bulges of barred galaxies. Examples of spiral galaxies include the Milky Way (SBbc, Gerhard 2002) and the Andromeda galaxy (SAb de Vaucouleurs et al. 1991).

Irregular galaxies are unique in their shape and structure. They are typically the result of galaxy interactions or the merging of multiple galaxies (Masters & Galaxy Zoo Team 2020). They can share characteristics and features of spiral and elliptical galaxies, but they typically do not fit their distinct regular shape. Some irregular galaxies can have spiral features but have strongly distorted tails and warped discs. Many can appear as disc-like structures or chaotic collections of stars and gas, often

with clumps and pockets of intense star formation. These galaxies can come in various sizes, from small dwarfs (including compact dwarf spheroidals) to massive objects.

Many astronomers referred to elliptical galaxies as 'early-type' and spiral galaxies as 'late-type', as the assumption was that galaxies evolve from left to right or elliptical through lenticular to spirals on the Hubble sequence[1].

Subsequent work studying distant galaxies suggests that galaxy evolution does not follow this simple sequence. Due to technological constraints, studying the very early Universe with large statistical samples is challenging. Mortlock et al. (2013), who used 1 188 massive ($M_\star \geq 10^{10}\,\mathrm{M}_\odot$) galaxies at redshift $z > 2$ from the Ultra Deep Survey (UDS) region of the Cosmic Assembly Near-infrared Deep Extragalactic Legacy Survey (CANDELS) field, showed that irregular galaxies were dominant in the early Universe. They also found many spheroidal galaxies and negligible disc populations. Other studies also showed an increasing fraction of irregular and interacting galaxies for increasing redshift (Abraham et al. 1996; Conselice et al. 2000; Guo et al. 2015; Huertas-Company et al. 2016). Many early disc galaxies contain large stellar clumps (*e.g.*, Guo et al. 2015), which may lead to misclassifications if not resolved fully. Emerging results from the *James Webb Space Telescope (JWST)* including those from the Cosmic Evolution Early Release Science (CEERS) survey (Finkelstein et al. 2023) have found that very high mass galaxies ($M_\star \geq 10^{10.5}\,\mathrm{M}_\odot$) have undisturbed disk-like morphologies as early as $z \sim 5$ (Ferreira et al. 2023).

In the currently favoured picture of galaxy formation, present-day ellipticals formed due to mergers between these early galaxies. Lenticular galaxies may also be evolved spiral galaxies, whose gas has been stripped, quenching star formation. Spiral galaxies that survive to the present epoch have typically done so with fewer interactions and merger events, while those that do not survive have evolved away

[1]Although Hubble clarified that the naming conventions and the relative positions of classifications should not be interpreted as an evolutionary sequence (Hubble 1927).

from spirals forming ellipticals and lenticulars (*e.g.*, Schawinski et al. 2014).

1.1.1 Density Distribution of Galactic Discs

The surface density profiles of disc galaxies as a function of radius can typically be described with a single exponential profile, *i.e.*:

$$\Sigma(R) = \Sigma_0 e^{-R/h_R}, \tag{1.1}$$

where Σ_0 is the surface density at the galaxy centre and h_R is the disc scale length or the radius at which $\Sigma(h_R) = \Sigma_0/e$. Many disc galaxies also exhibit discs with broken exponential functions (*e.g.*, Erwin et al. 2008).

The vertical profiles of disc galaxies also follow similar exponential or double exponential functions. Photometricly galactic discs appear to have two distinct vertical components, the thin and thick discs, seen in edge-on external galaxies and first described by Burstein (1979) and Tsikoudi (1979). The origins of the two discs are still a matter of ongoing research. Within the ΛCDM framework (Section 1.2), one scenario of disc formation is the 'upside-down' mechanism. Stars form in the gas as it collapses into the protogalaxy and retain their vertical height distribution, with later star formation occurring closer in the plane.

We also observe high mass stellar clumps in high redshift galaxies, which from simulations, have been shown to strongly scatter old stars, converting in-plane motion to vertical motion, giving origin to a thick disc from an initially thin disc (Bournaud et al. 2009; Clarke et al. 2019; Beraldo e Silva et al. 2020). The formation of thick discs can also have contributions from merger events.

Typically the thin disc is younger and metal-rich. In contrast, the thick disc is older and metal-poor, allowing the discs to be defined chemically rather than geometrically (*e.g.* in the Milky Way, Hayden et al. 2017). We can define the density distributions of the thin and thick discs as first identified in the Milky Way by Yoshii

(1982) and Gilmore & Reid (1983):

$$\zeta(z|R) = \frac{1-\beta}{2h_{z,\mathrm{thin}}} e^{-|z|/h_{z,\mathrm{thin}}} + \frac{\beta}{2h_{z,\mathrm{thick}}} e^{-|z|/h_{z,\mathrm{thick}}}\,, \tag{1.2}$$

where $h_{z,\mathrm{thin}}$, $h_{z,\mathrm{thick}}$ are the thin and thick scale heights respectively. Here, β is a free parameter such that:

$$\zeta(0|R) = \frac{1-\beta}{2h_{z,\mathrm{thin}}} + \frac{\beta}{2h_{z,\mathrm{thick}}}\,, \tag{1.3}$$

where $\zeta(0|R)$ is the mid-plane density at a given radius.

At the Solar radius of the Milky Way ($R_\odot = 8.2\,\mathrm{kpc}$, Bland-Hawthorn & Gerhard 2016), the thin disc has a scale height of $h_{z,\mathrm{thin}} \approx 0.3\,\mathrm{kpc}$, whereas the thick disc has a scale height of $h_{z,\mathrm{thick}} \approx 0.9\,\mathrm{kpc}$ and both discs having a scale length of $h_R = 2.5 \pm 0.4\,\mathrm{kpc}$ (Bland-Hawthorn & Gerhard 2016). However, Bovy et al. (2012) showed that scale lengths and heights, as measured by mono-abundance populations, change as a function of age. Older populations have larger scale heights and smaller scale lengths.

1.2 Formation of Disc Galaxies in ΛCDM

Considering the formation of galaxies, we concentrate on the ΛCDM model of cosmology. Also commonly referred to as the standard model of cosmology, ΛCDM has three major components: dark energy (Λ), cold dark matter (CDM) and 'ordinary' (baryonic) matter whilst assuming that general relativity is the correct theory of gravity on cosmological scales (Faber & Gallagher 1979). Several observations suggest that our Universe is geometrically flat and dominated by dark matter and dark energy accounting for about $\sim 95\%$ of the energy density (Planck Collaboration et al. 2020). Standard model particles, baryons, make up for the remaining $\sim 5\%$ (Planck Collaboration et al. 2020). The ΛCDM framework assumes that dark matter is cold, with negligible random motions when decoupled from other matter

and is collisionless. Dark energy drives the accelerated expansion of the Universe (Lonappan et al. 2018).

Several space-based missions, such as the Cosmic Background Explorer (COBE, Smoot et al. 1990), RELIKT-1 (Klypin et al. 1992), the Wilkinson Microwave Anisotropy Probe (WMAP, Bennett et al. 2003), and the more recent *Planck* satellite (Planck Collaboration et al. 2020), have detected subtle fluctuations in the density and temperature of the cosmic microwave background. For example, although the cosmic microwave background appears nearly uniform in all directions, temperature variations of order ~ 1 in 10^5 or $RMS \approx 20\,\mu K$ was measured by *Planck*. If the cosmic microwave background were perfectly uniform, there would be no galaxies, which we do observe. On even larger scales, galaxies form in clusters and Mpc sheet-like structures, separated by voids containing few galaxies (Geller & Huchra 1989). Looking for the origin of these observed structures, we theorise that the Universe began in a hot, dense, nearly uniform state approximately ≈ 13.8 Gyr ago (Freedman 2021). The large-scale variations in the cosmic microwave background were born from tiny quantum fluctuations in the Universe's initial state, which were 'inflated'.

The Universe was dominated by radiation in its early stage (Karttunen et al. 2017). As a result, baryonic matter, which interacts with electromagnetism, could not cool; however, dark matter could begin to collapse under gravity forming the seeds of halos and filaments (the 'cosmic web') into which the baryons could later fall. The Universe was expanding rapidly and therefore cooling, allowing for the formation of protons and neutrons and primordial elements (Big Bang nucleosynthesis), which were fully ionised into nuclei and free electrons again due to the high temperature. As the Universe cooled, small quantities of deuterium, helium and lithium nuclei were created. Finally, 0.5 Gyr after the Big Bang, the Universe became cool enough for the nuclei to capture negatively charged electrons, forming

neutral atoms.

This baryonic matter then began collapsing under the gravity of its own mass and that of dark matter, which had already generated dense regions and voids which funnelled this primordial gas, creating the first generation of stars and protogalaxies. Galaxies then form in groups and clusters, creating the large structures observed today, often called hierarchical structure formation (*e.g.*, Lacey & Cole 1993).

The ΛCDM model is able to reproduce the observed large-scale distribution of galaxies, clusters, voids (Springel et al. 2006), and when fit to the cosmic microwave background (Planck Collaboration et al. 2020, and following works by the collaboration). It also consistent with the observed abundances of primordial elements across these large structures. However, considering individual galaxies, the highly nonlinear mechanisms of baryonic physics, gas heating and cooling, star formation and feedback add further complications.

For disc galaxies specifically, in the early stages of formation, gas collects under gravity at a high temperature embedded in a dark matter halo; these gas coronae begin to cool and collapse into the potential well forming a protogalaxy (Ferreras 2019). The gas experiences external torques, and the cooling process is isotropic (angular momentum is conserved when collapsing), thus rotating and flattening the protogalaxy into a disc as it contracts. Once sufficient density is reached, star formation begins in the central regions, building an early central stellar mass. Star formation then continues in the gas at larger radii and higher angular momentum, which develops into a stellar disc at later times, a process referred to as inside-out formation (Kepner 1999; Nelson et al. 2012; Patel et al. 2013). Older stars, therefore, are typically formed close to the galactic centre and the outer disc is comprised of younger stars. The accretion of gas and stars through merger events and interactions also drives disc growth through hierarchical assembly, (*e.g.* Martel & Richard 2020).

1.3 Chemical Evolution

Observationally, the ages of stars are challenging to determine. One of the most common proxies for stellar age is their chemical abundance. We describe here an overview of how different elements are generated in the Universe.

1.3.1 Big Bang Nucleosynthesis

The early Universe was hot enough for protons and neutrons to transform into each other easily, and their abundance ratio was determined only by their relative masses with one neutron to seven protons (though some neutrons decay into protons). Once the Universe cooled enough, the neutrons quickly bound with equal protons to form molecular hydrogen (^{2}H), then helium-4 (^{4}He), resulting in a Universe that is $\sim 74\%$ H and $\sim 24\%$ He by mass (Steigman 2007).

In the first twenty minutes after the Big Bang, when the temperature and density of the Universe were high enough to allow nuclear fusion to occur, the fusion of protons and neutrons formed the lightest elements, such as hydrogen, helium, and lithium. As a result, primordial nucleosynthesis is responsible for the formation of most of the Universe's helium as the isotope helium-4 (^{4}He), along with small amounts of the hydrogen isotope deuterium (^{2}H), helium-3 (^{3}He), and a minimal amount of the lithium isotope lithium-7 (^{7}Li) (Steigman 2007). Elements heavier than lithium are subsequently formed as a product of stellar evolution.

1.3.2 Elemental Abundance

We can track the chemical enrichment of stars through metallicity, defined as the logarithmic ratio of the mass fraction of iron (Fe) to hydrogen (H). We can also define the chemical abundance of any two elements (i, j) using the Sun as a reference

following Eqn. 1.4 where N_i is the number of atoms of an element i per unit volume:

$$[i/j] = \log_{10}\left(\frac{N_i}{N_j}\right)_\star - \log_{10}\left(\frac{N_i}{N_j}\right)_\odot . \tag{1.4}$$

Here $\star$ is a given star's abundance, and $\odot$ refers to the Solar abundance. For example, the Solar iron to hydrogen ratio, $\log_{10}(N_{\rm Fe}/N_{\rm H})_\odot = -2.752$ (Asplund et al. 2009) and therefore, stars with [Fe/H] > 0 have a higher abundance of iron than the Sun, and we would consider them to be 'metal-rich'. Thus 'metal-poor' stars with [Fe/H] < 0 are those with metallicity below the Solar abundance.

We can also consider the ratios of iron abundance to α-elements[2] so-called as they have isotopes that are integer multiples of the mass of a helium nucleus, the α-particle. The stable α-elements are C, O, Ne, Mg, Si and S. Commonly, the chemical space studied in galaxies is the [O/Fe]-[Fe/H] (α-Fe) plane.

1.3.3 Stellar Nucleosynthesis

The first generation of stars was born in the primordial gas without any contaminating elements heavier than lithium, referred to in the literature as population III stars (Heger & Woosley 2002)[3]. Observations of such stars have not been achieved to date but are postulated to have stellar masses hundreds of times that of the Sun (Schlaufman et al. 2018). These stars begin stellar nucleosynthesis by fusing hydrogen into helium and then into heavier elements up to iron. Many theoretical stellar models show that most high-mass stars rapidly exhaust their fuel (see Table 1.1) and explode in extremely energetic supernovae, synthesising even heavier elements. Such explosions disseminate their material into the surrounding (ISM), enriching the gas with heavier elements to be integrated into later generations of stars. This rapid destruction of population III stars suggests that none of them would be observable

[2]The α-alpha process elements: ^{16}O, ^{20}Ne, ^{24}Mg, ^{28}Si, ^{32}S, ^{36}Ar, ^{40}Ca, ^{44}Ti, ^{48}Cr, ^{52}Fe, and ^{56}Ni of which many are unstable isotopes.

[3]In discussing populations of stars, we adopt the naming conventions of Baade (1944).

by the current epoch since most are theorised to form at masses $\sim 20 - 130\,\mathrm{M}_{\odot}$ (Umeda & Nomoto 2003).

Population II are stars with a relatively low abundance of elements heavier than helium (low metallicity) and are so-called metal-poor (Caputo 1998). This generation was still formed during the early Universe and is commonly found in old structures such as the Milky Way stellar halo. The central bulge of the Milky Way also contains population II stars, though they are slightly younger and thus are less metal-poor (*e.g.*, Reggiani et al. 2020). Globular clusters are comprised entirely of population II stars (van Albada & Baker 1973; Caputo 1998). Despite the lower metallicity, they often have higher proportions of α-elements relative to iron than younger stars.

Population I stars are metal-rich with the highest metallicities and are found in regions of current active star formation, such as the spirals of disc galaxies (Karttunen et al. 2017). These population descriptions provide broad categories for generations of stars but are not necessarily discrete; therefore, their definitions overlap.

1.3.4 Stellar Evolution

The fate of a star's evolution is determined by its mass. Low-mass stars form slowly and fall onto the stable main-sequence (core hydrogen burning), where they can remain there for several Gyr (the timescales of stellar evolution for different masses are summarised in Table 1.1). Once hydrogen fuel in the core is exhausted, stars begin burning hydrogen in their outer layers and evolve into the Giant phase, where they expand their outer layers but their cores contract. Giant (post-main-sequence) stars eject the material in their outer layers as high-energy stellar winds driven by radiation pressure, releasing mass back into the ISM (Karttunen et al. 2017). Intermediate mass stars ($2.3 \leq M/\,\mathrm{M}_{\odot} \leq 8$) have a central temperature which is high enough to fuse helium. Once the central helium fuel runs out, outer layers of

helium and hydrogen can burn in shells. However, in low- and intermediate-mass stars, shell burning produces radiation pressure in the loosely bound outer layers causing them to expand, forming a planetary nebula. What remains is a carbon-oxygen white dwarf *i.e.* the stellar core.

High-mass ($> 9\,M_\odot$) stars form rapidly and only remain on the main-sequence for $\sim 10\,$Myr. High-mass stars can ignite carbon or oxygen fusion in their cores and, in some cases, destabilise the star causing a supernova. The most massive stars ($> 15\,M_\odot$) can fuse elements up to iron in shells. As fuel runs out in the core, it no longer has sufficient pressure to prevent collapse and implodes. The star's outer layers explode in a supernova, leaving behind the stellar core.

1.3.4.1 Final Stages

Stellar cores with masses lower than the Chandrasekhar mass ($M_{\rm Ch} = 1.4\,M_\odot$, Chandrasekhar 1935) will exhaust all of their fuel and become a white dwarf, no longer fusing material and thermally radiating heat away to cool and contract. This is typically the fate of low-mass stars after the outer layers create a planetary nebula. If such low-mass cores are part of a close binary system, the white dwarf can accrete material from its companion and increase its mass. If a white dwarf accretes mass, it will heat as it approaches the Chandrasekhar limit until it reaches the ignition temperature for carbon fusion. Then, the white dwarf undergoes a runaway reaction and unbinds the star in a supernova explosion, named a type Ia supernova. The spectra of such supernovae typically present strong singly ionised silicon (Si II) emission lines (Hillebrandt & Niemeyer 2000). The fact that the spectra of Type I supernovae are hydrogen poor is consistent with the fact that low-mass white dwarves have almost no hydrogen.

If a stellar core has a mass larger than the Chandrasekhar limit but lower than the Oppenheimer-Volkoff mass ($M_{\rm OV} = 2.0\,M_\odot$, Oppenheimer & Volkoff 1939),

Mass [$M_\odot$]	Spectral type	Contraction to main-sequence	Main-sequence	Main-sequence to red giant	Red giant
30	O5	0.02	4.9	0.55	0.3
15	B0	0.06	10	1.7	2
9	B2	0.2	22	0.2	5
5	B5	0.6	68	2	20
3	A0	3	240	9	80
1.5	F2	20	2×10^3	280	
1.0	G2	50	1×10^4	680	
0.5	M0	200	3×10^4		
0.1	M7	500	1×10^7		

Table 1.1: Timescales of stellar evolution from pre-main-sequence to red giant phase. All values are in units of 1 Myr. Reproduced from Karttunen et al. (2017).

its final stable state is a stellar core which is entirely degenerate, *i.e.* a neutron star. The most massive stellar cores above the Oppenheimer-Volkoff mass overcome degeneracy pressure and nuclear forces that support the neutron star and continue collapsing to form a black hole. The rapid implosion of core collapse also removes pressure support of the star's outer layers causing it to collapse and heat rapidly. The collapse is reversed by neutron degeneracy, and the energy of outwards force is sufficient to disrupt outer layers and accelerate them, forming a supernova explosion. In addition, the exceptionally high temperatures and pressures allow for a brief period of high-energy fusion, producing elements heavier than iron. Named type II supernovae, they are distinguished from other types of supernovae by the presence of hydrogen in their spectra from the outer regions of the star (Doggett & Branch 1985).

Type Ia supernovae occur in all classifications of galaxies and therefore do not occur in specific populations of stars. However, type II supernovae are not observed in elliptical galaxies and originate from high-mass stars, which rapidly evolve and therefore are coincident with population I stars in the active star-forming regions of galaxies. This distinction adds different timescales and abundances to the enrichment of chemical elements in galaxies.

1.3.5 Age Metallicity Relations

The combined effects of stellar winds and supernovae act to increase the abundance of heavier elements in each generation of stars. Young populations of stars have higher metallicities and lower α-abundance, with the opposite being true for old stars. We, therefore, expect chemical abundance to correlate with stellar ages producing an age-metallicity relation (AMR) and follow similar distributions within a galaxy.

Various methods exist for determining estimates of the ages of stars, each with its

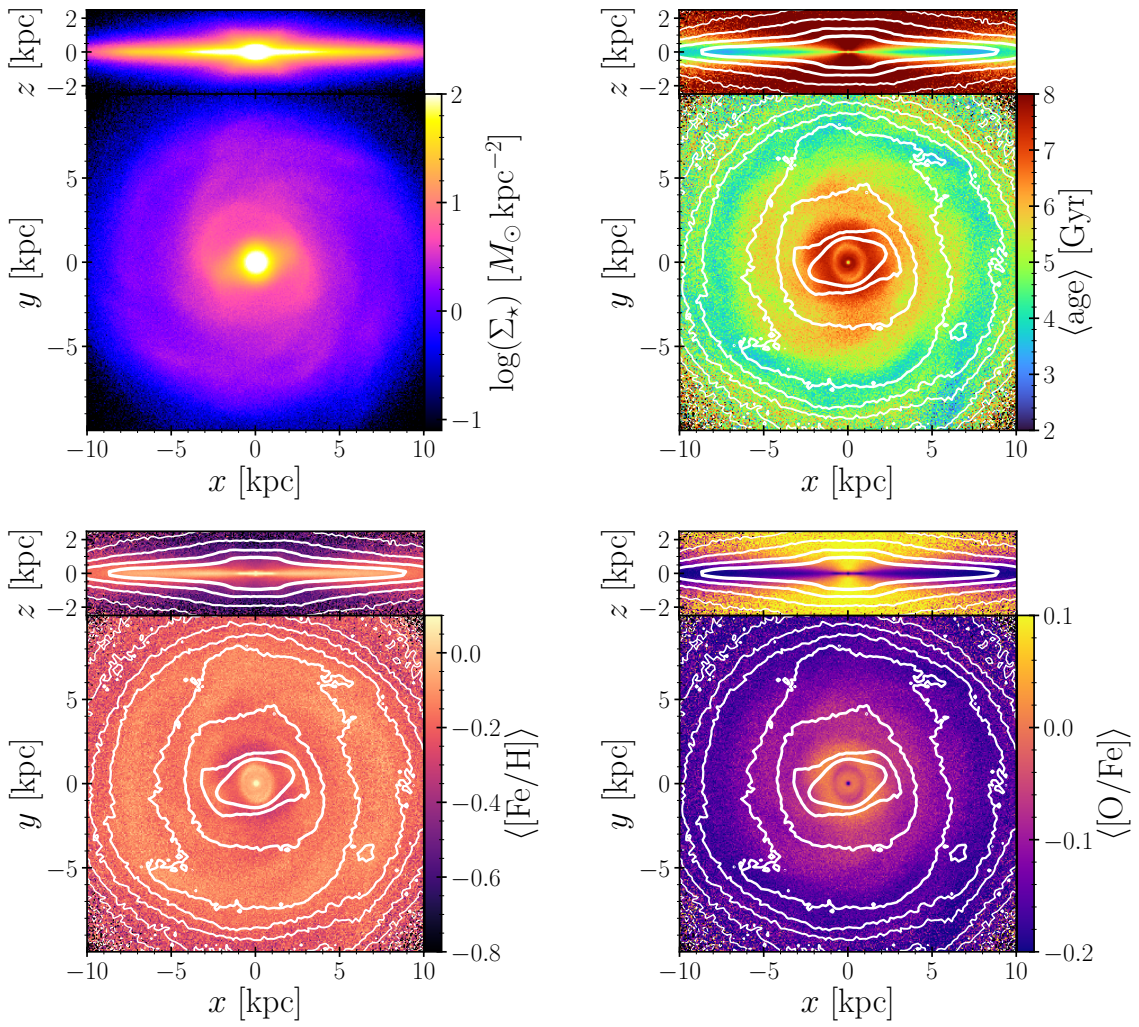

Figure 1.2: Edge-on and face-on distribution maps of the stellar surface density (top left-hand panel), average age (top right-hand panel), ⟨[Fe/H]⟩ (bottom left-hand panel) and ⟨[O/Fe]⟩ (bottom right-hand panel) of a star-forming simulation `739HF` after 10 Gyr of evolution, presented as simulation M1_c_b in Fiteni et al. (2021). The white contours follow isophotes of log density.

own advantages and shortcomings (Soderblom 2010). Estimates of stellar ages and their chemical abundance allow for the construction of age-metallicity distributions, giving insight into the formation histories of galactic structures (*e.g.*, Haywood et al. 2013; Bernard et al. 2018).

In Fig. 1.2, we present the face-on and edge-on maps of an isolated star-forming simulation which forms a disc galaxy and implements prescriptions for chemical enrichment (see Chapter 2). From the density distribution (upper left-hand panel), the central bar and bulge region is evident along with the outer disc, where we observe faint spiral features. As this is a simulation, we know the precise ages of the stellar particles (stars), and we can show their distribution in maps. Indeed, as expected, we find old stars close to the galactic centre and younger stars in the spirals of the disc. There is also a clear vertical gradient of age, with young stars occupying a thin disc while older populations are found out of the plane at greater heights. Considering the above chemical evolution theory, we expect the abundance distributions of iron and oxygen to follow those of age, which we observe in the model.

We present in Fig. 1.3, the relationships between iron and oxygen abundance with stellar age for all stars in the same model. There is a clear correlation between chemical abundance and age, with a steep gradient between the oldest and intermediate-age stars in the model. However, the gradient flattens for younger populations. Age appears to have stronger correlations with [O/Fe] than [Fe/H].

In the α-Fe plane (bottom panels of Fig. 1.3), there appears to be a dense lower track with low [O/Fe] across a range of metallicities, with further tracks at higher [O/Fe] values. Again knowing the stellar ages, we can colour this space by the average age and see that the young stars of the thin disc have low [O/Fe] with a range of [Fe/H] values. On the other hand, old stars have larger [O/Fe] and extend to lower [Fe/H]. The distinction between the lower and upper tracks of the α-Fe

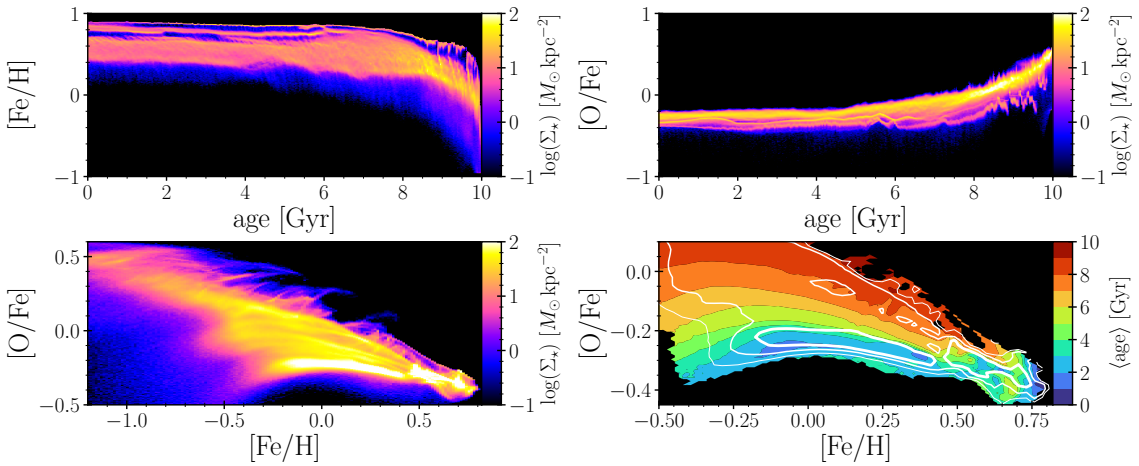

Figure 1.3: The age relation of [Fe/H] (top left-hand panel) and [O/Fe] (top right-hand panel) for all stars in the model. The α-Fe plane is presented in the bottom left-hand panel, and the same chemical space coloured by the average stellar age is shown bottom right-hand panel for the same simulation presented in Fig. 1.2. The white contours in the bottom right-hand panel follow lines of log density from the bottom left-hand panel.

plane is thought to be due to the delayed onset of Type Ia supernovae which require white dwarfs to have formed. Type II supernovae, which produce large amounts of α-elements, occur from high-mass stars which form rapidly (Table 1.1).

This view of chemical enrichment would imply that there should be a simple relationship between stellar age and chemical abundance –however, gaseous regions mix, diffusing heavy metals across the galaxy. External factors can also complicate the AMR (Ferreras 2019). The early accretion of smaller satellites is common in 'bottom-up' theories of galaxy formation. Dwarf gas-rich companions of larger galaxies with different chemical evolutionary histories are sources of infalling gas, mixing with the gas of the progenitor. Infalling cold primordial gas along cosmic filaments also contributes to the disc prompting star formation as it accretes, forming young stars with lower iron abundance. In addition to gas inflows, galactic outflows have been observed in elliptical galaxies and spirals with active galactic nuclei (AGN), which heat the gas in the disc. This heated gas could then 'evaporate' into the intergalactic medium (IGM) or fall back onto the disc.

The redistribution of gas broadens the AMR of a galaxy. Nevertheless, the general trends of such relations can still be observed in galaxies such as the Milky Way (*e.g.*, Ness et al. 2016b). Observationally, only the chemical abundances of stars are typically available to us. Therefore structures, such as the thick and thin discs, are typically defined chemically (*e.g.*, Bensby et al. 2014; Nidever et al. 2014). Stellar ages, which are challenging to measure precisely and for large samples, are still the ideal way to untangle the dynamical history of galaxies.

1.4 Dynamics of Disc Galaxies

One of the earliest questions about disc galaxies was how they rotate. The motions of planets around a star are governed by Newton's and Kepler's laws which assert a constant mass interior to the orbit where orbital velocities decrease with radial

distance from the centre. If galaxies followed similar laws, stars in the outer disc would rotate slower than those close to the centre ($V_{\rm circ}(R) = \sqrt{GM_{\rm enc}/R}$, where $M_{\rm enc}$ is the mass enclosed within the orbit).

However, observations of external disc galaxies have shown that the circular velocities increase from small radii before peaking and remaining roughly constant at large radii beyond several scale lengths of the disc (Babcock 1939; Schmidt 1957; van de Hulst et al. 1957; Volders 1959; Rubin & Ford 1970; Corbelli & Salucci 2000). Considering the fact that the stellar discs of galaxies follow exponential profiles (Eqn. 1.1), the stellar mass can not account for the fast rotation curves at a large radius. This result would suggest that more mass is present in a galaxy than is visible in the baryonic matter, and this 'dark' matter contributed more than 50% to the total galaxy mass (Rubin et al. 1980). This result was the first indirect evidence of dark matter playing a role in the dynamics of disc galaxies. Indeed in current models of disc galaxies, dark matter dominates the outer regions of the gravitational potential, whereas the stellar component dominates the inner regions.

As an example, in the left-hand panel of Fig. 1.4, we show the rotation curve of an N-body simulation of a disc galaxy with the individual contributions of the stars and dark matter components to the rotation curve of the total potential[4]. The stellar component, as expected, has a decreasing gradient beyond $\sim$2 kpc. The dark matter component of the model has a rising rotation curve which begins to dominate beyond 10 kpc, a factor of four times larger than the stellar disc scale length. The combined effect of both components is a rotation curve that is flat beyond $\sim$ 2 kpc.

[4]Calculated from the midplane gravity of interior mass using the `PYTHON` package `PYNBODY` (Pontzen et al. 2013).

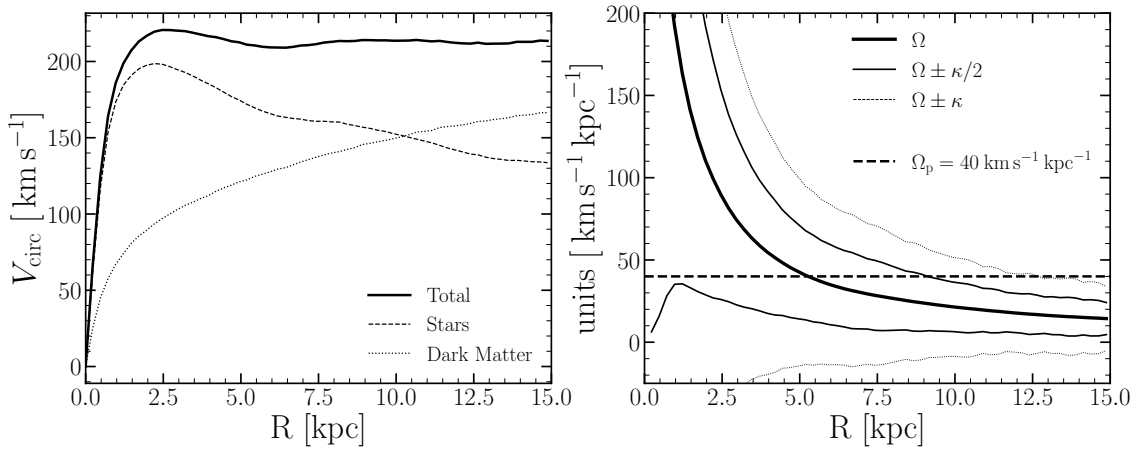

Figure 1.4: Left: the rotation curve (circular velocity) of model `741CU`, an N-body simulation of a disc galaxy after 5 Gyr of evolution presented as model CU in Debattista et al. (2017) (see Section 1.7). The thick black line is the rotation curve of the total potential which is the addition in quadrature of the stellar and dark matter components (dashed and dotted lines, respectively). Right: the lines of co-rotation and Lindblad resonances. An example pattern speed is drawn as the horizontal dashed line intersecting the rotation frequencies.

1.4.1 Orbits in Discs

When considering motions through an axisymmetric disc, stars on nearly circular orbits with small radial and vertical (perpendicular to the plane) excursions can be treated as simple harmonic oscillators. The frequency of these motions can be described as epicycles about a guiding radius (R_g) which follows a circular path at that radius within the gravity potential of the galaxy. Using the notation of Binney & Tremaine (2008), the radial and vertical epicycles are denoted as κ and ν, respectively. The rotation frequency of a star is denoted as Ω. Completing one cycle through 2π radians, the radial and azimuthal periods can be expressed as:

$$T_r = \frac{2\pi}{\kappa} \; ; \; T_\phi = \frac{2\pi}{\Omega} \, , \tag{1.5}$$

respectively.

In the vertical direction, stars act as harmonic oscillators decoupled from the in-plane motions. Assuming the density is approximately constant, close to the plane of the disc, the vertical frequency depends on the density (ρ) at the guiding radius, *i.e.*, $\nu^2(R_g) \approx 4\pi G\rho(R_g)$. As discs have exponential vertical profiles, this relationship only holds for orbits that do not stray far from the mid-plane (*e.g.*, $z_{\rm max} \leq 0.1$ kpc, Binney & Tremaine 2008).

We present a schematic of the epicycle approximation in Fig. 1.5 from the face-on and side-on view of a simple disc. While the epicycle approximation only applies to small radial and vertical excursions, it provides a good description of the majority of stellar motions in a disc.

If we place ourselves in the reference frame that rotates with an angular frequency of $\Omega_{\rm p}$, the frame changes its azimuthal angle ($\phi_{\rm p}$) with respect to the azimuthal angle of the star ($\phi_\star$) as a function of time (t) following:

$$\phi_{\rm p} = \phi_\star - \Omega_{\rm p} t \, , \tag{1.6}$$

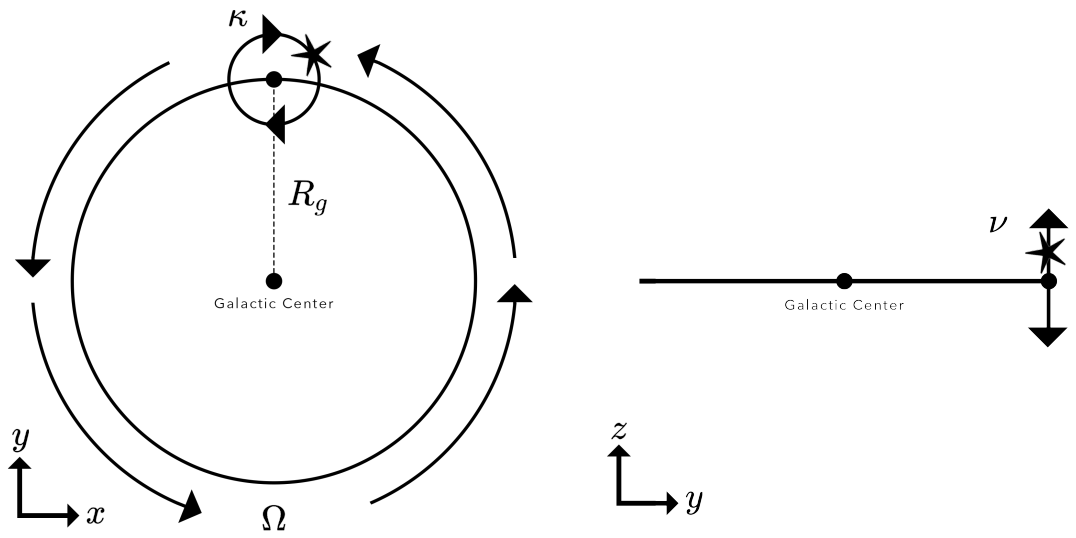

Figure 1.5: A schematic diagram of a star orbiting in a disc with small radial and vertical excursions around a guiding centre R_g, with azimuthal, radial and vertical frequencies of Ω, κ and ν, respectively. The left-hand image is from the face-on perspective, whereas the right-hand image is from the side-on perspective.

which for one radial period (Eqn. 1.5) can be expressed as the increase in the azimuthal angle of the frame and star as:

$$\Delta\phi_{\rm p} = \Delta\phi_\star - \Omega_{\rm p} T_r \,. \tag{1.7}$$

We can define a value of $\Omega_{\rm p}$, which allows the orbit of the star to form closed loops in the rotating reference frame. Orbits close such that $\Delta\phi_{\rm p} = 2\pi n/m$ where n and m are integers. Therefore closed orbits can be approximately expressed from the epicycle approximations from above, giving:

$$\Omega_{\rm p} = \Omega - \frac{n\kappa}{m} \,. \tag{1.8}$$

As Ω changes for any given star as a function of radius, no single value of $\Omega_{\rm p}$ would allow orbits at all radii to close. Indeed even at a single radius, some orbits are closed, and some with large radial oscillations are not. Closed orbits are resonant orbits in the rotating frame.

1.4.2 Disc Stability

Discs are rotationally supported, and their evolution is driven by angular momentum transport (Lynden-Bell & Kalnajs 1972; Kormendy 2013). More specifically, energy spreads outwards, causing the inner regions to contract, increasing density and expanding the outer regions, which grow more diffuse (Tremaine 1989). However, a rotating disc with no radial random motions is susceptible to axisymmetric instabilities, similar to the Jeans instability of collapsing gas clouds. Toomre (1964) derived a stability criterion (Q) for stellar discs where a disc is stable to axisymmetric perturbations when:

$$Q \equiv \frac{\sigma_R \kappa}{3.36 G \Sigma} > 1 \,, \tag{1.9}$$

where σ_R is the radial velocity dispersion, κ is the radial epicyclic frequency, G is the gravitational constant and Σ is the stellar surface density. We can use Q to

measure how kinematically 'hot' a stellar disc is. Discs with large radial velocity dispersions (large σ_R) would be considered 'hot' and therefore have large values of Q. Conversely, a 'cool' stellar disc would have low values of Q and σ_R, and completely 'cold' discs have zero values for both. Rotationally-supported discs where $Q > 1$ are typically stable to all axisymmetric perturbations.

However, thin rotationally supported discs with differential rotation are notoriously unstable to non-axisymmetric perturbations that produce density waves appearing as spirals (shown in N-body simulations by Hohl 1971; Sellwood 1981, 1985; Sellwood & Moore 1999).

Most observed spirals are trailing; however, a small number have leading arms (*e.g.*, Buta et al. 1992, 2003). An $m = 2$ (bi-symmetric) density perturbation commonly causes instabilities that grows within the disc. This perturbation will rotate about the galaxy with an angular frequency referred to as a pattern speed ($\Omega_{\rm p}$). This perturbation will interact with the stellar disc, and stars with rotational frequencies (Ω) that match that of the perturbation $\Omega = \Omega_{\rm p}$ are said to 'co-rotate' with the perturbation. The perturbation can exchange energy with closed orbits in the rotating frame (Binney & Tremaine 2008). From Eqn. 1.8, there are closed orbits also where $n/m = \pm 1/2$, which are named Lindblad resonances after Swedish astronomer Bertil Lindblad.

1.5 Stellar Bars

Toomre (1981) demonstrated that any leading spirals are unwound, becoming straight, then trailing spirals. In this process, the amplitude of the spiral is amplified in a process termed *swing amplification*. Spirals, which are commonly trailing, can propagate inwards through the centre of the disc, emerging as leading waves that propagate outwards. These new leading waves are again unwound and swing amplified (Toomre 1981). Spirals propagating outwards can experience a partial reflection at

the corotation resonance (the radius at which the spiral pattern speed intercepts the corotation curve).

So long as the pattern speed of the spiral, $\Omega_{\rm p}$, remains above that of the inner Lindblad resonance (ILR, $\Omega - \kappa/2$)[5], a feedback loop of trailing spirals propagating and emerging through the centre as leading spirals that unwind, are swing amplified and reflect off corotation, continues (Goldreich & Lynden-Bell 1965; Julian & Toomre 1966; Drury 1980; Toomre 1981; Lin & Bertin 1985; Sellwood & Wilkinson 1993). For example, in the right-hand panel of Fig. 1.4, we present the rotation frequencies of the same disc galaxy model as a function of radius, with a hypothetical spiral of a given pattern speed $\Omega_{\rm p} = 40\,{\rm km\,s^{-1}\,kpc^{-1}}$ marked as a horizontal line. As this spiral's pattern speed is above the maximum frequency of the ILR, it can propagate through to the centre; slower pattern speeds would mean the spiral reflects off or is absorbed by the ILR. As the density in the galaxy's centre increases, the circular velocity also increases, allowing a disc to build an ILR and cutting off the feedback loop of swing amplification (Sellwood & Wilkinson 1993).

Therefore the origin of bars seen in galaxies is that spirals that propagate through the centre straighten between the centre and the approximate location of the corotation resonance. This radial extent in which we expect to find bars is also measured observationally (Sellwood 1981; Combes & Sanders 1981). An example of a strongly barred galaxy, NGC 1300, is presented in Fig. 1.6. From their straight morphology, one can assume that the pattern speed along bars is constant as they do not wind. More than half of the galaxies in the local Universe host a stellar bar (Eskridge et al. 2000; Menendez-Delmestre et al. 2007; Barazza et al. 2008; Aguerri et al. 2009; Gadotti 2009) including the Milky Way, which had been hypothesised as early as the 1950s (Johnson 1957; de Vaucouleurs 1959).

[5]The Outer Lindblad resonance (OLR) is defined where $\Omega_{\rm p} = \Omega + \kappa/2$).

Figure 1.6: NGC 1300, an SB(rs)bc barred spiral galaxy. Credit: NASA, ESA, and The Hubble Heritage Team (STScI/AURA) Acknowledgment: P. Knezek (WIYN).

1.5.1 Orbits in Bars

Bars being linear structures that rotate almost like a rigid body, we can approximate their gravitational potential (Φ) as a uniformly rotating non-axisymmetric density distribution. If we put ourselves in the frame rotating with the bar, we can define an effective potential as:

$$\Phi_{\text{eff}} = \Phi - \frac{\Omega_{\text{b}}^2 R^2}{2}\,, \tag{1.10}$$

where Ω_{b} is the pattern speed of the bar (Binney & Tremaine 2008). In a rotating non-axisymmetric potential, specific energy (E) and angular momentum (J) are not conserved; however, Jacobi's integral is conserved and is typically expressed as $E_J = E - \Omega_{\text{p}} J$. Following the conventions of the effective potential, E_J can be expressed as:

$$E_J = \frac{|\mathbf{v}|^2}{2} + \Phi_{\text{eff}}\,, \tag{1.11}$$

where $\mathbf{v}$ is the velocity of a star.

There are five points within the effective bar potential where $\nabla\Phi_{\text{eff}} = 0$, called Lagrange points ($L_1 \rightarrow L_5$, Binney & Tremaine 2008). We highlight their position

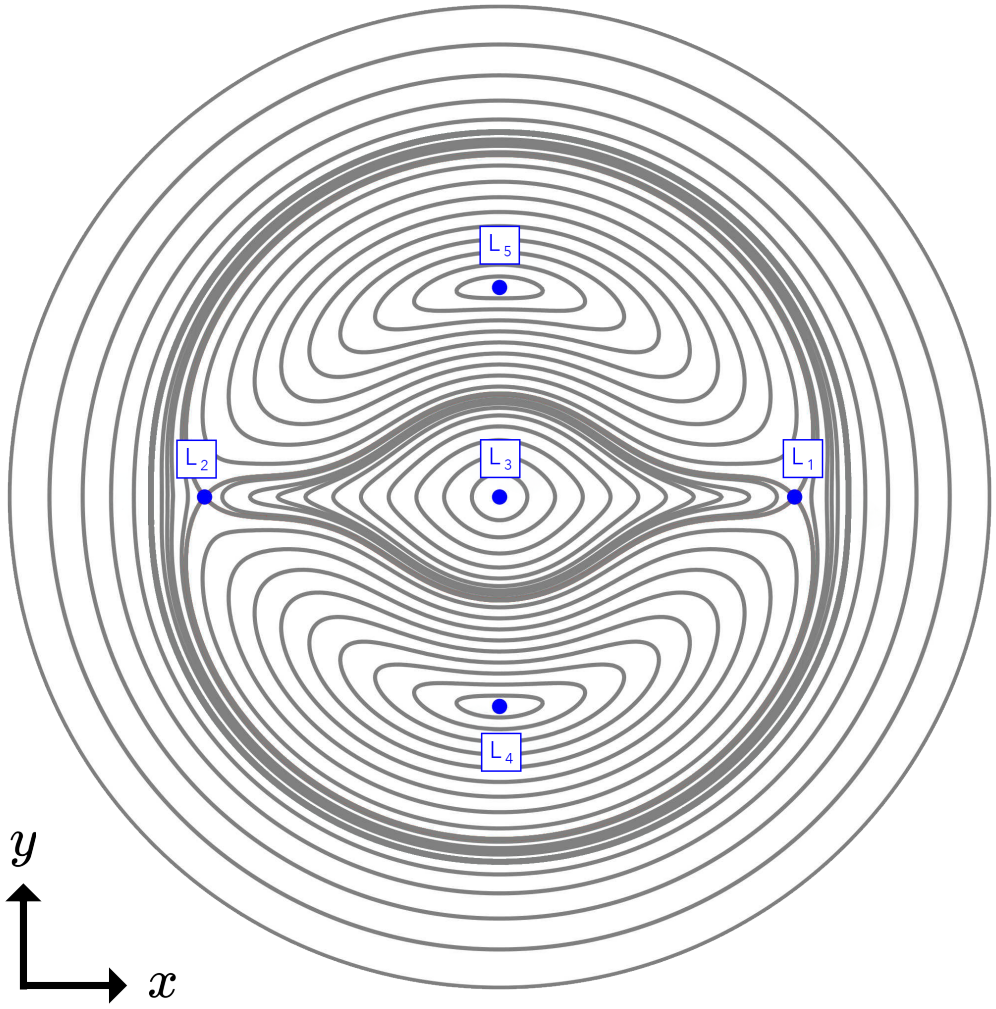

Figure 1.7: An example of a 2D bar potential presented in Jung & Zotos (2016) with the bar major axis aligned horizontally along the x-axis. The grey lines follow the contours of the effective potential. The five Lagrange points ($L_1 \rightarrow L_5$) are labelled on the potential. Image is adapted from Jung & Zotos (2016).

within a simple bar potential in Fig. 1.7. Lagrange points L_1, L_2 and L_3 lie along the major axis of the bar with L_3 being at the centre of the potential (the minimum of Φ_{eff}). L_1 and L_2 are saddle points. The L_4 and L_5 Lagrange points are coincident with the maximum of Φ_{eff}. It is possible for a star to orbit on a circular path in the rest frame at the L_1, L_2, L_4 and L_5 Lagrange points whilst appearing to be stationary in the rotating frame. Orbits at these points with the same rotational velocity are said to corotate with the potential. We can discern the regions in which stars with given Jacobi energies can occupy from Eqn. 1.11. Regions where $\Phi_{\text{eff}} > E_J$ are forbidden to the star of that energy (Binney & Tremaine 2008).

1.5.1.1 Regular Bar Orbits

We can consider closed orbits within a rotating frame as described in Section 1.4.1 in exploring orbits in a bar. Closed orbits retrace their path through the potential and are periodic (Sellwood & Wilkinson 1993; Binney & Tremaine 2008). However, numerical analysis of stars in bar potentials commonly shows that many orbits are not precisely periodic but liberating close to the path of a closed orbit. Such nearby orbits are referred to as regular or quasi-periodic (Valluri et al. 2016; Abbott et al. 2017). Stars on quasi-periodic orbits tend to oscillate about a 'parent' periodic orbit similar to a guiding radius. Therefore it is still helpful to explore the characteristics of periodic orbits to understand those which follow their distributions closely.

We adopt the naming conventions of Contopoulos when discussing periodic orbit families within the bar (*e.g.* Contopoulos & Papayannopoulos 1980; Contopoulos & Grosbol 1989). While the number of named orbits is extensive (Wang et al. 2022), we highlight only the primary families contributing to bar structure. Typical orbits within the bar follow a 2:1 ratio of radial to azimuthal excursions and are known as the x_i family of orbits where $i \in [1, 4]$.

The 'main' family, elongated parallel (with high eccentricity) to the bar major

axis (the x-axis in Fig. 1.7), is the x_1 family, the parent orbit supporting most stars contributing to the bar (Contopoulos & Papayannopoulos 1980; Contopoulos & Grosbol 1989; Athanassoula 1992; Skokos et al. 2002a,b). Non-periodic orbits that occupy the same region of the bar but are not bound by the x_1 orbit have higher energies and explore more extensive regions of the potential (Shen & Sellwood 2004). From their more rectangular paths in the rotating frame, they are commonly called 'box' orbits, though some librate close to x_1 family orbits ('boxlets') (Valluri et al. 2016).

The x_2 orbit is a stable orbit elongated perpendicular to the bar major axis, though it is close to circular, occupying a region between the galaxy centre and the ILR (Valluri et al. 2016). The existence of this family implies that for x_2 orbits to be stable, the disc's central density and bar pattern speed should be such that an ILR is present. The x_3 family, which is similar to yet more eccentric than the x_2 family, are always unstable and rarely found in the numerical modelling of bars (Valluri et al. 2016; Abbott et al. 2017). The retrograde x_4 family are highly circular with a slight elongation perpendicular to the major axis.

Within the bar potential, orbits around the L_4 and L_5 Lagrange points can be stable. Orbits close to the Lagrange point are energetic short-period orbits (SPO) which orbit like a radial epicycle where the Lagrange point is the guiding centre (Valluri et al. 2016). Long-period orbits (LPO) make larger excursions from L_4 and L_5 towards L_1 and L_2 but do not cross the major axis (Valluri et al. 2016). While SPOs and LPOs do not directly support the bar, they play other roles in shaping the central regions of discs, such as in the formation of lenses and rings (Kormendy & Kennicutt 2004).

Figure 1.8: M104 (the Sombrero galaxy), an SA spiral galaxy. Credit: NASA, ESA, and The Hubble Heritage Team (STScI/AURA).

1.6 Bulges

Thus far, we have focused primarily on the in-plane motions of stars. However, while most of the energy and motions of stars in a disc are within the plane, we cannot ignore a disc galaxy's vertical structure and kinematics. Observations of edge-on galaxies have shown that the bulges of disc galaxies have diverse morphologies (Gadotti & Sánchez-Janssen 2012). A common morphology observed in many disc galaxies is a 'smooth' spheroidal bulge often named in the literature as a 'classical' bulge, with a prominent example being the Sombrero galaxy M104 seen with the *Hubble Space Telescope (HST)* in Fig. 1.8.

These spheroidal bulges have smooth isophotes sharing many characteristics of elliptical galaxies. Their brightness profiles follow Sérsic (1968) functions defined as:

$$\log I(r) \propto r^{-1/n}\,, \tag{1.12}$$

where I is the light intensity, r is the radius from the centre, and n is the Sersic index which, for spheroidal bulges like M104, have values of $n \geq 2$. The kinematics of these bulges suggest that although they have some rotation, they have large

velocity dispersions meaning they are more pressure supported (Cappellari et al. 2007). From our understanding of disc formation through hierarchical assembly, this component of a galaxy would likely be formed by early merger activity (Gadotti 2009). Their similarity to elliptical galaxies, which undergo major mergers, supports this conclusion.

1.6.1 Box/Peanut Bulges

The spheroidal-shaped bulge was thought to be the primary morphology for the central regions of disc galaxies. As the quality of galaxy observations improved, other distinct structures with different kinematic properties became clear (Kormendy & Illingworth 1982; Davies & Illingworth 1983).

The second common bulge morphology is aptly named the box/peanut or 'X'-shaped bulge (commonly shortened to BP or BPX). The earliest reference in the literature to such a bulge was in Burbidge & Burbidge (1959) with an image of NGC 128 as one of "Three unusual S0 galaxies." In Fig. 1.9, we present their photographic plate alongside more modern images from the Sloan Digital Sky Survey (SDSS) presented in Ciambur & Graham (2016). In this galaxy, the bulge is not protruding out of the centre and is not spherical, resembling a peanut- or 'X'-shape instead.

The kinematics of box/peanut bulges display cylindrical rotation similar to that of discs and bars, contrary to the pressure-supported elliptical galaxies which spherical ('classical') bulges resemble (Kormendy 1993; Kuijken & Merrifield 1995; Bureau & Freeman 1999). The link between stellar bars and box/peanut bulges was theorised in observations (*e.g.*, Kormendy & Illingworth 1982) and later reinforced with numerical modelling (Combes et al. 1990; Sellwood 1993; Athanassoula & Misiriotis 2002). Box/peanut bulges are now thought to be produced through the secular evolution of bars.

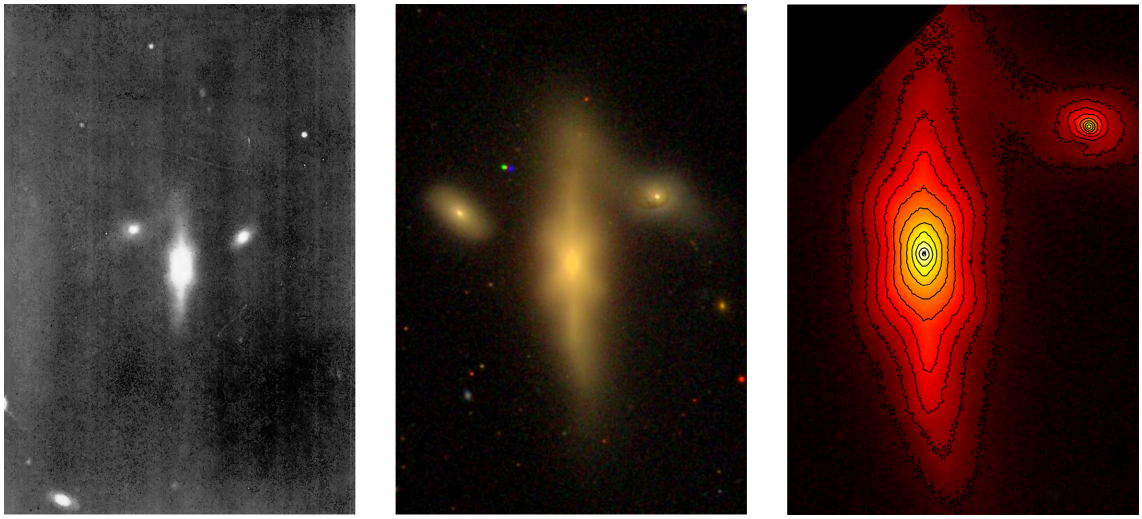

Figure 1.9: Left: Photographic plate from the 82-inch Otto Struve reflector at McDonald Observatory (University of Texas) presented in Burbidge & Burbidge (1959) of NGC 128 as one of "Three unusual S0 galaxies". Describing its bulge shape as "..unusual, as its maximum extent perpendicular to the major axis occurs not at the centre but at two points symmetrically spaced on either side of the centre. At the widest parts of the nuclear region there are four bulges of about equal size, coming out of the nucleus itself like a cross". This publication is the first noted description of a box/peanut or 'X'-shaped bulge. Middle: A combined *igr*-image of NGC 128 from the Sloan Digital Sky Survey (SDSS DR14) clearly shows that this galaxy is a box/peanut galaxy and has some indication of a double box/peanut structure. Right: SDSS r- band image of NGC 128 with iso-contours of luminosity, adapted from Ciambur & Graham (2016) where the authors concluded that NGC 128 likely has a second nested box/peanut structure in its inner regions slightly offset from outer formed from a second bar.

Early numerical models of barred galaxies showed that strong box/peanut features can appear as an X-shape when the bar is viewed edge-on, with its major axis perpendicular to the line of sight (LOS, Athanassoula & Misiriotis 2002; Athanassoula 2005). Observing the bar end-on (the major axis parallel to the LOS), box/-peanut bulges can appear weakly boxy or round, potentially being mistaken as a 'classical' bulge.

The key difference between classical and box/peanut bulges is that the former form early in a galaxy's evolution through early accretion and merger events; the latter form secularly (through internal dynamics) from the bar (see the reviews by Kormendy & Kennicutt 2004; Fisher & Drory 2016).

Observations of galaxies with their discs inclined to the LOS (not perfectly edge-on or face-on) offer insight into both their in-plane and vertical morphologies. For example, Erwin & Debattista (2017) showed that bars in inclined galaxies with box/-peanut bulges exhibit a 'box-spur' morphology from the projections of their bar and bulge to the LOS light distribution, further demonstrating their connection. In the local Universe, we find that the frequency of box/peanut bulges in barred galaxies depends on galactic parameters such as mass (Erwin & Debattista 2017). Box/-peanut bulges appear in up to 80% of local high mass ($\log(M_\star/\,\mathrm{M}_\odot) \gtrsim 10.4$) barred galaxies, a fraction which declines rapidly at lower masses (Erwin & Debattista 2017).

1.6.1.1 Buckling Instabillity

The large radial motions along a bar's major axis (such as those produced by the x_1 family of orbits) create large radial velocity dispersions. However, the disc and bar being initially thin compared to their radius means the vertical dispersion is low. Therefore the bar creates a largely anisotropic system and makes it susceptible to the buckling or 'fire hose' instability seen in other physical systems (*e.g.*, Collier

2020). The name comes from the analogy of a hose pipe at high pressure spraying water in one direction. If the end of the hose is untethered, small angles of flow direction are amplified, and the hose begins to bend and shake.

Numerical simulations have shown that buckling is common in bars (*e.g.* Raha et al. 1991; Debattista et al. 2005; Martinez-Valpuesta et al. 2006; Collier 2020), with cases of strong buckling being distinctive as their initial bending is not symmetric about the plane when viewed side-on. We present an example of strong buckling from the IllustrisTNG project (Pillepich et al. 2018b; Springel et al. 2018; Nelson et al. 2018; Naiman et al. 2018; Marinacci et al. 2018) in Fig. 1.10. In this galaxy, asymmetric features of the bar about the plane appear between redshift $0.17 \leq z \leq 0.2$ as the bar buckles. Sometime after the buckling event, the remaining distribution appears more symmetric about the plane in a box/peanut morphology. Buckling is typically a rapid, violent process experienced by strong bars (Raha et al. 1991; Merritt & Sellwood 1994; Debattista et al. 2006; Martinez-Valpuesta et al. 2006; Collier 2020; Łokas 2020). As buckling depends on anisotropy, thin discs and bars with low vertical velocity dispersion are more susceptible to buckling.

1.6.1.2 Resonant Trapping

The second mode of bar thickening is via the trapping of stellar orbits on vertical resonances, which occurs over longer timescales than buckling (Combes & Sanders 1981; Combes et al. 1990; Pfenniger & Friedli 1991; Skokos et al. 2002a; Quillen 2002; Quillen et al. 2014; Debattista et al. 2006).

A bar rotating with a pattern speed of $\Omega_{\rm b}$ creates a vertical perturbation in the disc. Stars respond in phase with the vertical perturbing force of the bar when they have vertical and circular frequencies which satisfy:

$$\nu \geq 2(\Omega - \Omega_{\rm b})\,, \tag{1.13}$$

where the right-hand term can also be expressed as $2\Omega_x$, the oscillation frequency

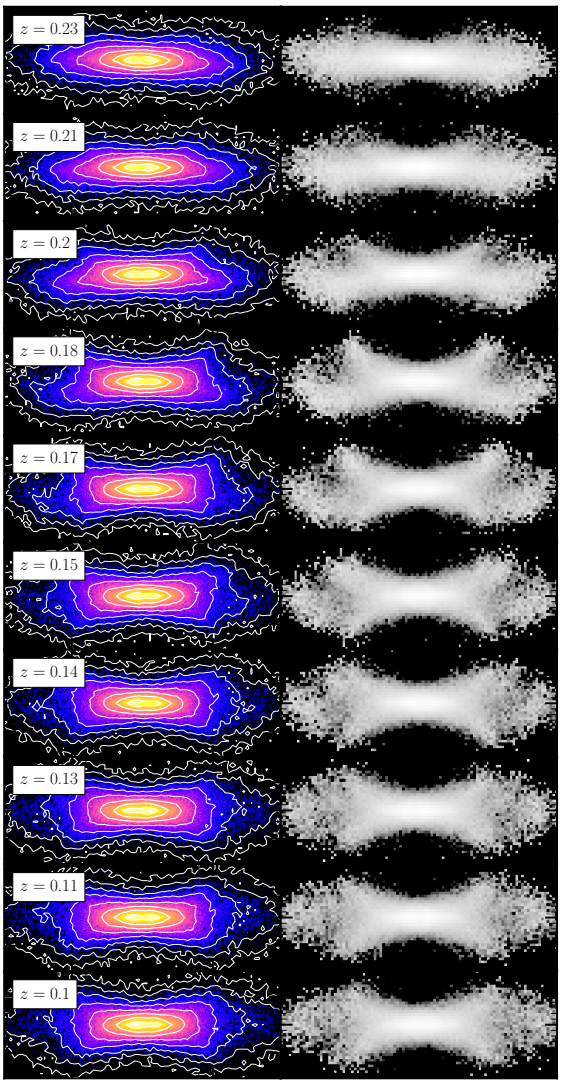

Figure 1.10: The edge-on projection of the bar region from a buckling barred galaxy (Subhalo ID **574037**) from the TNG50 simulation (Nelson et al. 2019a; Pillepich et al. 2019). In the left-hand column, we present the stellar surface density, and the right is an unsharp mask of the same distribution. Time moves towards the current epoch as we move down through each row. The corresponding redshift of each snapshot is shown in the top left-hand corner of each image. Note the asymmetric features about the plane present between redshift $0.17 \leq z \leq 0.2$ as a characteristic of the buckling event.

along the bar's major axis in the rotating bar frame. The resonance where $\nu = 2\Omega_x$ is referred to as the vertical-ILR (vILR). Bars can slow down by transferring angular momentum to the galaxy's dark matter halo (Weinberg 1985; Debattista & Sellwood 1998, 2000; Athanassoula 2002; O'Neill & Dubinski 2003). The slowing of the bar causes the location of corotation and the vILR to move outwards. With time, this 'sweeping' of the vILR would heat more populations at greater radii.

A comparison of three mechanisms for bar thickening was presented by Sellwood & Gerhard (2020). The first mechanism is the buckling instability, whereas the second two rely solely on the 2:1 vertical resonance. Stars can be heated as they pass over the vILR on short timescales (and remain heated), or the vILR can 'trap' stars at the resonance for extended periods (Quillen et al. 2014). The results of Beraldo e Silva et al. (2023) found, using numerical analysis of bar orbits in self-consistent simulations of barred galaxies, that stars rapidly pass the vILR whilst developing a long-lasting box/peanut morphology.

Recent work by Li et al. (2023) has demonstrated the close connection between the 2:1 vertical resonance and buckling in galaxies. They found stars being trapped by the resonance are coincident with a break in the vertical symmetry of the bar in their N-body simulation, *i.e.* the resonant excitation of stars triggers the buckling instability.

1.7 Kinematic Fractionation

1.7.1 The Milky Way Bulge

Studying the stellar populations within the bulges of external galaxies is challenging as we can only observe the integrated properties along the line of sight, rather than individual stars though it can still be inform understanding of galaxy dynamics (*e.g.*, Gadotti et al. 2020). Observing the Milky Way allows us to study in detail

the various components of a galaxy's bulge (such as a bar) by resolving individual stars. Though observing deep into the centre of our galaxy has its own challenges of dust obscuration and crowded fields, the Milky Bulge provides unique insights into the dynamics of galactic bulges.

A bar at the centre of the Milky Way was detected in early infrared studies from the *Cosmic Background Explorer (COBE)* satellite (Blitz & Spergel 1991; Dwek et al. 1995; Binney et al. 1997; Fux 1997, 1999). Photometric studies of stellar populations in the Milky Way bulge have found that it is primarily composed of stars older than 10 Gyr (Ortolani et al. 1995; Kuijken & Rich 2002; Zoccali et al. 2003; Ferreras et al. 2003; Sahu et al. 2006; Clarkson et al. 2008, 2011; Brown et al. 2010; Valenti et al. 2013; Calamida et al. 2014) with a small fraction of intermediate or young ages (*e.g.*, Bensby et al. 2011, 2013). A population of old, metal-poor RR Lyrae stars which trace an axisymmetric (or potentially weakly barred) distribution has been measured, suggesting the Milky Way has an accreted bulge component (Dékány et al. 2013; Du et al. 2020b).

In addition, many studies have traced the Milky Way bar and bulge using red clump (RC) giant stars as standard candles (*e.g.*, Stanek et al. 1994, 1997; Nikolaev & Weinberg 1997; Babusiaux & Gilmore 2005; Benjamin et al. 2005; Nishiyama et al. 2005; Rattenbury et al. 2007; Cao et al. 2013; Wegg & Gerhard 2013; Wegg et al. 2015; Clarke et al. 2019; Sanders et al. 2019). The RC spatial distribution within the bulge exhibits a bimodal distribution as a function of apparent magnitude (heliocentric distance) when observing latitudes away from the plane due to their box/peanut (X-shaped) morphology (McWilliam & Zoccali 2010; Nataf et al. 2010; Saito et al. 2011; Wegg & Gerhard 2013; Gonzalez et al. 2015). Kinematic data from spectroscopic surveys such as Bulge Radial Velocity Assay (BRAVA, Rich et al. 2007), Abundances and Radial velocity Galactic Origins Survey (ARGOS, Freeman et al. 2013) and Apache Point Observatory Galactic Evolution Experiment

(APOGEE, Zasowski et al. 2013), show that the Milky Way bulge is cylindrically rotating (Howard et al. 2008; Ness et al. 2013b, 2016a), which we expect for a bar and box/peanut bulge.

A vertical metallicity gradient close to the minor-axis (Galactic longitude, $l \sim 0$) has been measured in the Milky Way bulge (Zoccali et al. 2008; Gonzalez et al. 2011; Johnson et al. 2011, 2013). Metal-poor (old) populations are centrally concentrated with an axisymmetric spatial distribution. In contrast, the metal-rich population has a boxy distribution, consistent with an edge-on bar, and does not extend to large latitude (*e.g.*, Zoccali et al. 2017). The superposition of these populations produces a vertical metallicity gradient (see Fragkoudi et al. 2017c, and references therein). The box/peanut bulge also appears differently for chemically separated stellar populations. The bimodal density distribution appears strongly in more metal-rich populations than in metal-poor, where the density appears only weakly bimodal or at most a single density peak (Ness et al. 2012; Uttenthaler et al. 2012; Rojas-Arriagada et al. 2014; Lim et al. 2021).

Kinematic differences between stellar populations were suggested by Babusiaux et al. (2010), who found that metal-poor stars have velocities consistent with a spheroidal distribution. Metal-rich stars have motions typically associated with a bar morphology and high-velocity streaming motions. The velocity dispersions of both metal-rich and metal-poor populations decrease with increasing Galactic latitude. Metal-poor stars have larger velocity dispersions than metal-rich stars at low latitudes; however, the opposite is true at large latitudes (Babusiaux 2016; Zoccali et al. 2017).

The chemodynamical observations of the Milky Way bulge have also been reproduced in models (*e.g.*, Di Matteo 2016; Fragkoudi et al. 2018). These results have been interpreted to indicate that the Milky Way has a compound bulge, *i.e.*

a superposition of both a secularly built box/peanut bulge and an accreted 'classical' bulge component (Babusiaux et al. 2010; Hill et al. 2011; Zoccali et al. 2014) which can explain some observational trends such as the vertical metalicity gradient (Grieco et al. 2012). Compound bulges are also observed in external galaxies (*e.g.*, Méndez-Abreu et al. 2014; Erwin et al. 2015).

1.7.2 Bar Driven Evolution

Disentangling the dynamical history of a bulge like the Milky Way's is challenging from a theoretical perspective. As we showed above, the bar is a strong perturbing force within a galaxy's central regions. Box/peanut bulges are formed through secular processes in which stellar populations respond in phase with a bar's forcing.

Debattista et al. (2017) explored how populations with varying initial velocity dispersion respond to the bar (see also Athanassoula et al. 2017; Fragkoudi et al. 2017b). They found that stellar populations with the same spatial distribution but different initial in-plane kinematics separate due to the presence of the bar, referring to this behaviour as *kinematic fractionation*.

To demonstrate kinematic fractionation, Debattista et al. (2017) used an N-body simulation comprised of five superposed stellar discs with different initial kinematics. Each stellar disc was co-spatial with the same radial and vertical density profiles but different in-plane kinematics, where the radial velocity dispersions are a function of radius:

$$\sigma_R^2(R) = \sigma_{R,0}^2 \exp(-R/R_\sigma)\,, \tag{1.14}$$

where R_σ is a scaling factor and $\sigma_{R,0}$ is the central velocity dispersion. Because the vertical density profile was the same for each disc, their vertical velocity dispersion, σ_z, was also the same. The authors referred to these discs as D1→D5, with D1 being the 'hottest' kinematically (largest $\sigma_{R,0}$).

From these five discs, Debattista et al. (2017) produced a compound disc with an

equal combination of the original five to approximate a galaxy with a uniform star formation rate through its evolution, denoted as model CU (compounded uniformly, referenced earlier in this work as `741CU`). The compound disc was evolved for 5 Gyr, forming a bar and a box/peanut bulge.

Considering each population during their co-evolution in the compounded disc, the coolest (D5) grows a bar thus, its radial velocity dispersion rapidly increases. As a result, the bar strength increases until it buckles, rapidly increasing the vertical height and vertical velocity dispersion and simultaneously decreasing the radial velocity dispersion and bar strength. Disc D1 (the hottest disc) shows the most rapid increase in average vertical height as the bar forms but forms the weakest bar. All five populations increase their height and vertical velocity dispersion in exchange for bar strength and radial velocity dispersion; however, the absolute change in these quantities is larger for the coolest populations. We present the final distributions of each population in Fig. 1.11.

Bar strength is seen to anti-correlate with initial radial velocity dispersion. These results showed that the evolution of a population is heavily dependent on the initial radial velocity dispersion. For example, suppose a disc comprises both kinematically 'hot' and 'cold' populations. The hot component will thicken more rapidly to greater heights forming only a weak bar. Conversely, the cold component forms a stronger bar and increases radial velocity dispersion. As a result, the strong bar leads to the later thickening of cooler populations into box/peanut morphologies. This work showed that the initial radial velocities of stellar populations determine the populations' final bulge structure.

Debattista et al. (2017) also showed kinematic fractionation in a high-resolution star-forming simulation, which forms a barred spiral galaxy entirely from gas (described in detail in Chapter 3). This simulation forms a disc galaxy from a hot gas corona, eventually forming a strong bar, a nuclear disc and a box/peanut-shaped

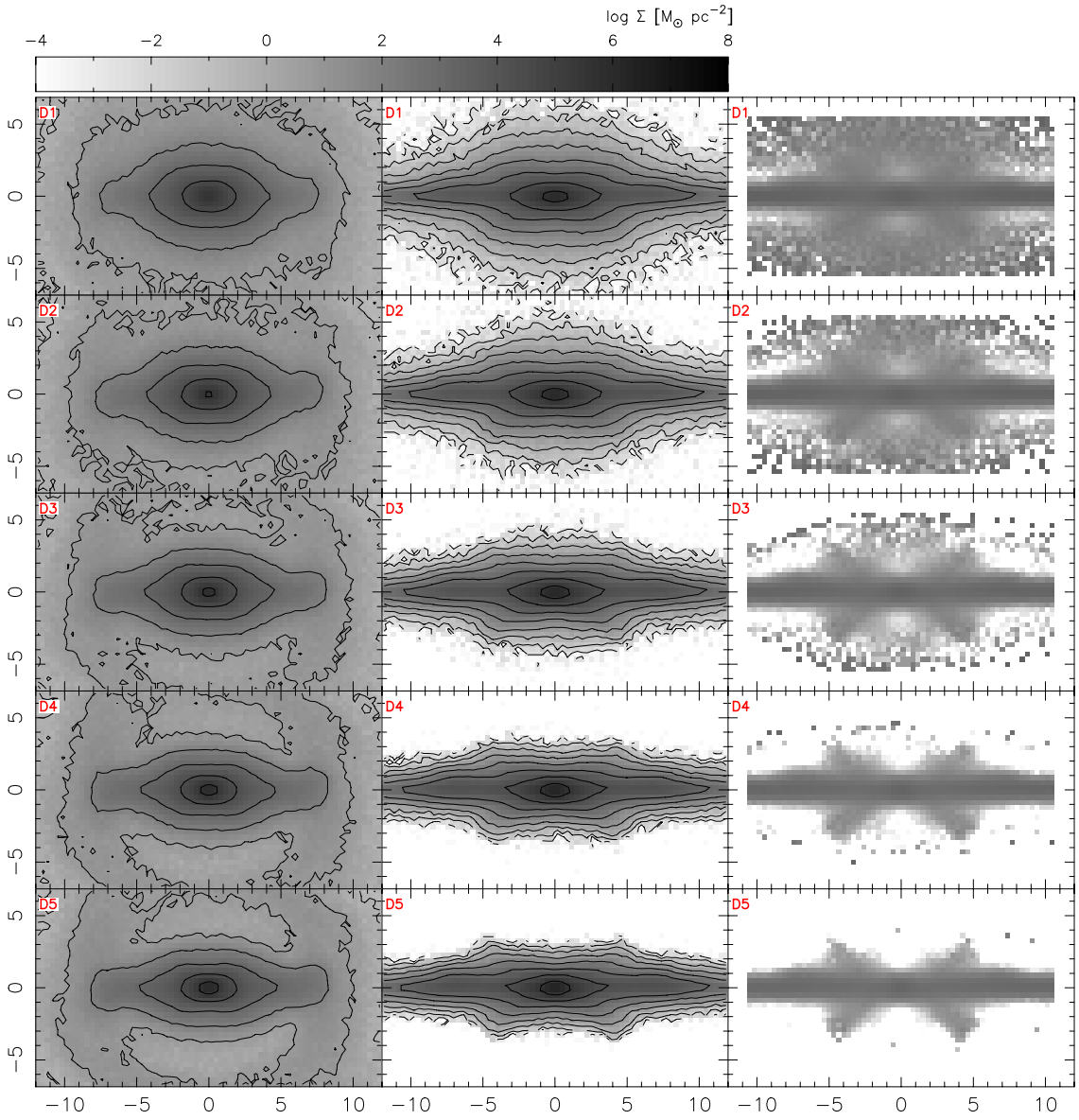

Figure 1.11: The face-on (left column) and edge-on (middle column) stellar surface density distributions of each individual population in model `741CU` from Debattista et al. (2017) (their figure 4). The right column shows unsharp masks of the edge-on distributions. From top to bottom, each row shows the initially radially hot population, D1, to the coolest population, D5. As the initial radial velocity dispersion decreases, the thinner the disc, the stronger the bar and the more pronounced the box/peanut bulge morphology observed.

bulge (Cole et al. 2014; Ness et al. 2014; Debattista et al. 2015, 2017). The model did not undergo strong buckling; however, its box/peanut bulge formed through a combination of weak buckling and resonant trapping. Stars in the model continuously form in the cold gas in the disc, producing a correlation between stellar age and birth radial velocity dispersion. Young stars are born with cooler kinematics than the older populations, which have heated.

From the same star-forming model after 10 Gyr of evolution, we split the populations into five equal quantiles of stellar age (Q1→Q5) and present their distributions in Fig. 1.12. Following the convention of Debattista et al. (2017), Q1 represents the oldest (hottest) population in the model, whereas Q5 represents the youngest (coolest). Qualitatively the trends between the N-body and star-forming models agree with old populations forming round bulges and weak bars due to being kinematically hot populations. Kinematically cooler and young populations form strong bars and box/peanut morphologies. The most striking difference between the N-body model and the star-forming model is that the latter forms a nuclear disc where young stars (bottom row of Fig. 1.12) can form from gas trapped on x_2 orbits within the bar (Cole et al. 2014).

Debattista et al. (2017) also showed using the star-forming model, which includes prescriptions for chemical enrichment (see Chapter 2), that there are relationships between initial radial velocity dispersion with age, metallicity and α-abundance before the bar formed. Therefore populations characterised by their chemical abundance or age as presented in Fig. 1.12 would exhibit different morphologies and would thus be kinematically fractionated.

The differences in final morphology between populations of varying initial radial velocity dispersion embed gradients of correlated stellar parameters within the central regions of disc galaxies, as seen in maps of the galaxy centre (for Milky Way

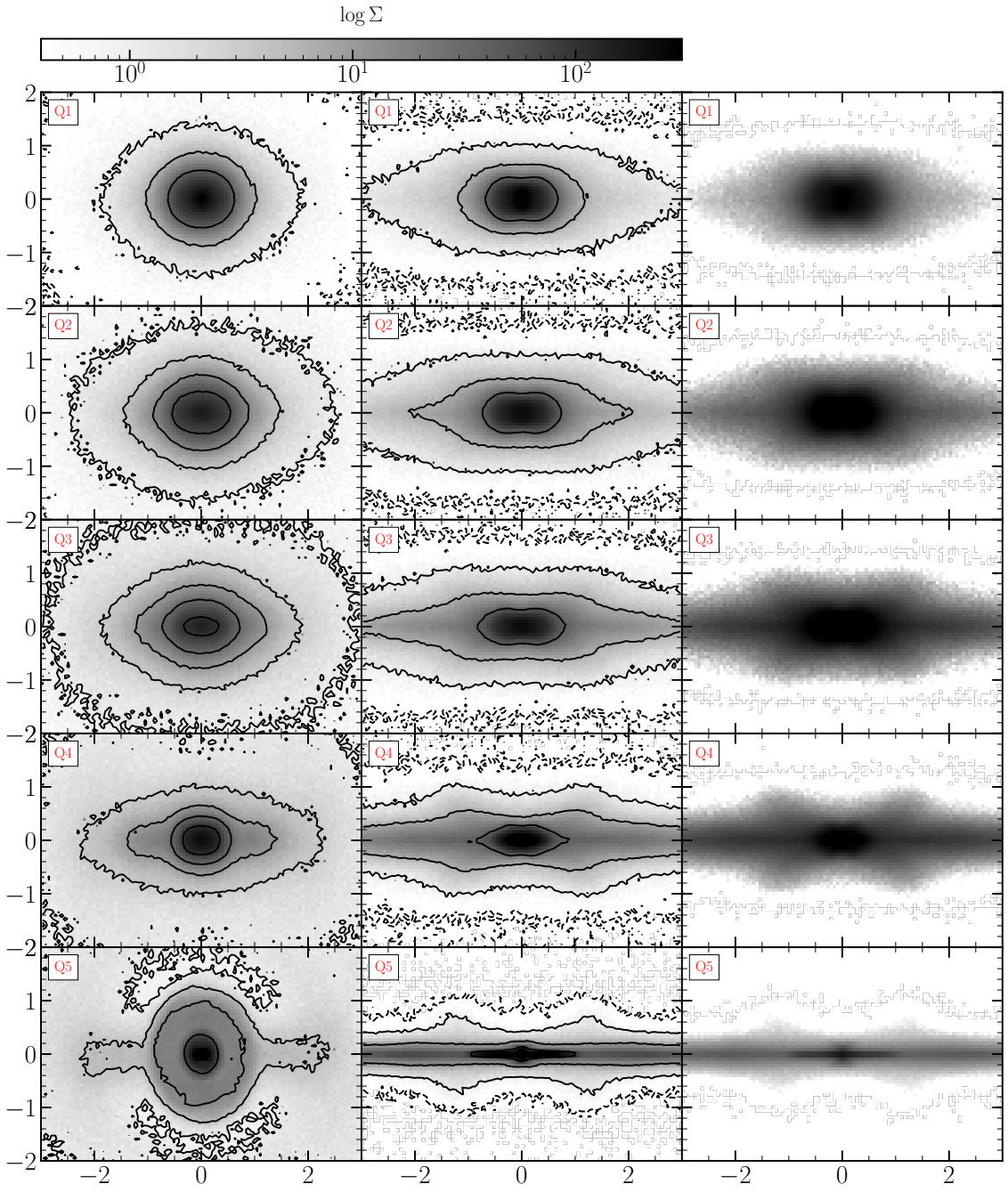

Figure 1.12: The face-on (left column) and edge-on (middle column) stellar surface density distributions of each age quantile in the star-forming model `708main` from Debattista et al. (2017) after 10 Gyr of evolution. The right column shows unsharp masks of the edge-on distributions. From top to bottom, each row shows the oldest population, Q1, to the youngest, Q5.

predictions, see figure 22-25 of Debattista et al. 2017). The work presented in Debattista et al. (2017) showed that bars are drivers of secular evolution within disc galaxies and are responsible for large-scale redistributions of matter within a galaxy.

Complementary to velocity dispersions, angle-action variables provide insights into the dynamics of gravitational potentials. However, they are typically only defined for axisymmetric (integrable) systems (Binney & Tremaine 2008). In the context of Hamiltonian mechanics, an action variable ($\mathbf{J}$) represents a constant of motion quantifying the magnitude of a periodic motion, while the angle variable (θ) represents the phase of the motion. Orbits with fixed action-angle variables are regular orbits. Angular momentum and actions are conserved in integrable potentials, while angle variables increase linearly with time.

Debattista et al. (2020) calculated the initial actions of stars in an N-body simulation of a disc galaxy and mapped the distributions of initial actions in the morphology of the galaxy after 5 Gyr of evolution. Despite the potential of the galaxy substantially changing as it forms spirals, bars and a box/peanut bulge, the initial actions of stars reliably predicted where they ended up in the galaxy by the final timestep.

For example, Debattista et al. (2020) presented the vertical profiles of average initial radial ($\langle \mathrm{J_{R,0}} \rangle$) and vertical ($\langle \mathrm{J_{z,0}} \rangle$) actions within the central region of their model for the first and final timestep, which we present here as Fig. 1.13. In the initial conditions, $\langle \mathrm{J_{z,0}} \rangle$ increases with vertical height out of the plane, whereas the profile of $\langle \mathrm{J_{R,0}} \rangle$ was primarily flat. By the final timestep, these relationships had reversed. By the final timestep, the $\langle \mathrm{J_{z,0}} \rangle$ profile had flattened, and $\langle \mathrm{J_{R,0}} \rangle$ increased linearly with absolute height. These results show that stars with the largest radial actions rise to the largest heights in the presence of a bar, confirming the results of Debattista et al. (2017).

Considering the chemical distribution of the Milky Way bulge, Debattista et al.

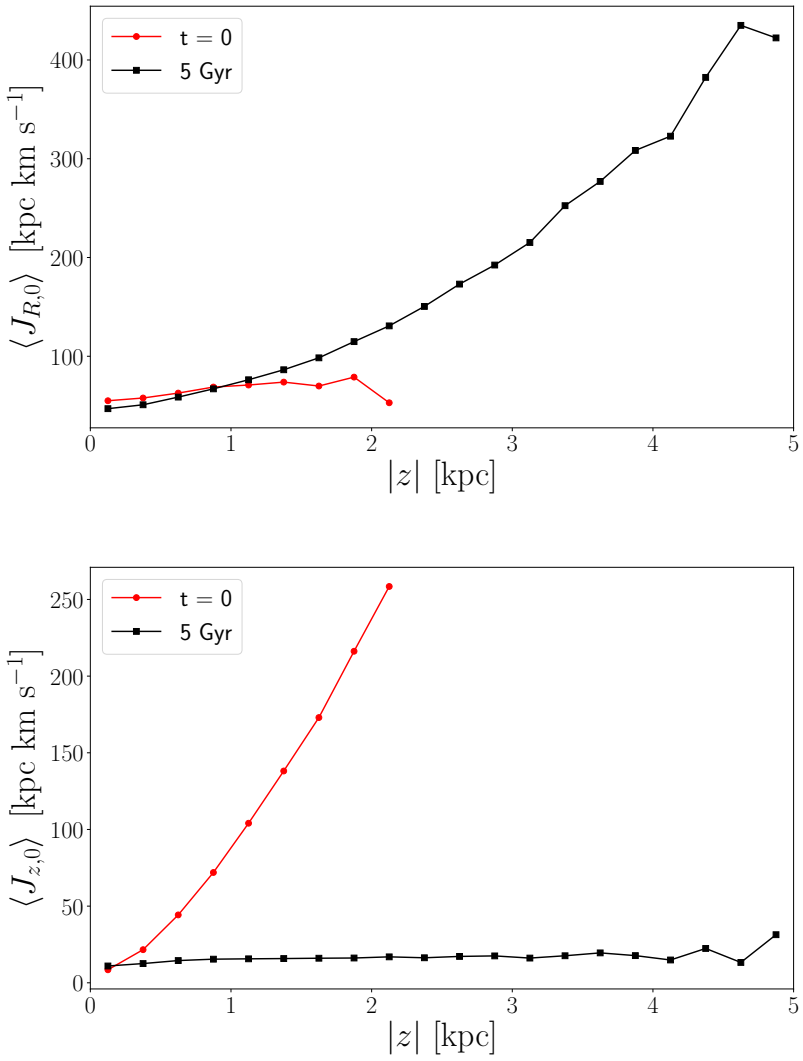

Figure 1.13: The change in the vertical profiles of $\langle \mathrm{J_{R,0}} \rangle$ (top row) and $\langle \mathrm{J_{z,0}} \rangle$ (second row) in model 2 of Debattista et al. (2020), an extract of their figure 9. The initial distributions at $t = 0$ are shown as (red) filled circles while the final distribution ($t = 5$) is shown as (black) filled squares (computed within $R_\mathrm{d} = 2.4\,\mathrm{kpc}$).

(2020) argued that, in a system in which the in-plane random motions are a function of age by the time the bar forms, radial metallicity gradients would become vertical gradients seen in the bulge. The main driver of this mechanism is $\langle J_{R,0} \rangle$; however, they demonstrate that this one component alone can not explain all trends observed in the Milky Way. All three action coordinates play a role in shaping the final distribution of stellar populations in the central structures of the galaxy (see also work by Di Matteo et al. 2015, 2019b; Di Matteo 2016; Fragkoudi et al. 2018).

1.8 Thesis Context

In simulations, stellar bars have been shown to separate stellar populations secularly (kinematic fractionation) within the central regions of disc galaxies (Debattista et al. 2017, 2019; Fragkoudi et al. 2018). This separation implies that different stellar populations with varying ages (and therefore chemical abundances) would exhibit different morphologies and kinematics. Distinct kinematics between populations has been shown observationally in the Milky Way (*e.g.*, Zoccali et al. 2017; Clarkson et al. 2018; Queiroz et al. 2021) and using simulations we can offer a theoretical interpretation of such observations and make predictions for future studies.

Constraining the bar in different populations within the Milky Way has led to contention on the age of the bar and how well these populations trace its structure. Previous studies have attempted to measure the bar length, strength, and orientation within bulge stellar populations, such as RR-Lyrae and red clump stars with different metallicities (Dwek et al. 1995; Binney et al. 1997; Stanek et al. 1997; Fux 1999; Bissantz & Gerhard 2002; Rattenbury et al. 2007; Cao et al. 2013; Wegg & Gerhard 2013; Wegg et al. 2015; Simion et al. 2017; Dékány et al. 2019; Du et al. 2020b).

One challenge of studying galactic evolution observationally is the non-trivial relationship between stellar age and chemical abundance. However, variable stars such as Miras have been shown to exhibit period-age relationships (Merrill 1923;

Feast 1963; Feast & Whitelock 2000). In this work, we study the utility of using Mira variables as age indicators for studying galaxy dynamics in the Milky Way. Previous studies have shown that Mira variables of different periods follow different structures within the Galactic centre (Grady et al. 2020a). Upcoming all-sky surveys, such as the Vera Rubin Observatory's Legacy Survey of Space and Time and future data releases from the *Gaia* satellite, open up opportunities for exploring large samples of variable stars. We study the latest *Gaia* data release (*Gaia* DR3) to define and characterise a sample of Mira variables in the catalogue.

The use of self-consistent, high-resolution and cosmological zoom simulations of disc galaxies has been shown to realistically capture the internal evolution of stellar bars (Kraljic et al. 2012; Scannapieco & Athanassoula 2012; Bonoli et al. 2016; Debattista et al. 2017, 2019, 2020; Fragkoudi et al. 2018, 2020; Buck et al. 2018, 2019; Di Matteo et al. 2019; Gargiulo et al. 2019; Walo-Martín et al. 2022). Simulations of isolated galaxies give us an unprecedented view of their internal dynamics at high resolutions. Fully cosmological simulations are instrumental in exploring the global properties of galaxy populations due to their large statistical samples. However, with larger volume sizes comes a compromise on the resolution of a simulation. Large-volume fully cosmological simulations are now reaching resolutions where they also realistically capture the dynamics of barred galaxies in a large sample size (*e.g.*, Du et al. 2020a; Zhao et al. 2020; Rosas-Guevara et al. 2022).

We utilise the latest generation of simulations in this work to study the secular evolutions of bars in a cosmological context. This allows us to compare the simulation to observations of the local Universe and understand the Milky Way in context. For example, ex situ populations are expected to be found within the Milky Way bulge but may be indistinguishable from old in situ populations (*e.g.*, Bonaca et al. 2017; El-Badry et al. 2018). Isolated simulations suggest that an ex situ population represents a small fraction of the bulge mass (Shen et al. 2010; Debattista et al.

2017). Using cosmological simulations, we can study the role ex situ populations play in forming box/peanut bulges to help constrain their contribution to the Milky Way.

We also use such simulations in this work to explore if the kinematics of stellar populations in a barred galaxy, observed at the current epoch ($z = 0$), can help constrain the evolutionary history of that galaxy. Using a statistically significant sample of barred galaxies, we also explore if stellar populations retain the dynamical memory of their bar formation epoch. In other words, is it possible to determine the epoch of bar formation only by observing the stellar populations at the current epoch?

Chapter 2

Numerical Methods

In the 17^{th} century, Newton's Philosophiae Naturalis Principia Mathematica firmly established the laws of gravitation between two objects, forming the foundation of classical mechanics. It also elegantly explains Kepler's laws of planetary motion, where two bodies orbit about their common centre of mass. However, a three-body system of point masses moving under mutual gravitation, such as the Sun, Earth and Moon, is not analytically solvable and became known as the 'three-body problem'. Solutions only appear under specific assumptions, such as one of the three bodies having negligible mass compared to the other two bodies (such as a spacecraft moving between the Sun and the Earth). Determining motions in $N > 2$ systems without these assumptions relies on numerical integration. While not a perfect solution, numerical integration can achieve accurate enough solutions to many astrophysical problems.

The first direct gravitational simulations were carried out by Erik Holmberg (Holmberg 1941) at the Lund Observatory. He presented a method for determining the forces between stars in encountering galaxies using the mathematical equivalence between the inverse square laws of light intensity and gravitational interaction. The stellar 'particles' of each 'nebula' (galaxy) were represented by 37 light bulbs at the positions of the stars. The force of gravity was calculated by equating it to

the measured fluxes of each star by a photocell. In remarkable resemblance to modern simulations, Holmberg (1941) studied the tidal tails of and spiral arms the galaxies developed during their encounter. von Hoerner (1960) ran the first completely computational N-body simulation using a direct summation scheme of $N = 16$ particles.

The earliest simulations investigated the dynamics of mass under gravity, studying the assembly of massive clusters (White 1976), and the development of large-scale structure (Aarseth et al. 1979; Efstathiou & Jones 1979). Simulations of ΛCDM systems match predictions of the large-scale distribution of dark matter. Modern simulations reach numbers of particles on the order of several trillion ($\sim 10^{12}$, Potter et al. 2017).

2.1 Gravitational Force Calculations

Many numerical methods exist for calculating gravitational forces in dynamical systems, and here we outline three approaches from this work. Vogelsberger et al. (2020) presented a comprehensive and more complete review of numerical methods for galaxy formation in cosmological simulations.

2.1.1 Direct Summation

To integrate the motions of particles in a system numerically, we must first numerically compute the forces acting on the particles. A simple method is to calculate the gravitational force between particles using Newton's law. The gravitational force on a particle, α (with mass m_α), in a system of N bodies can be calculated as the direct summation of the forces from all other bodies considered in the system ($\beta \in [2, N]$, $\alpha = 1$) as:

$$\mathbf{F}_\alpha = m_\alpha \sum_{\beta \neq \alpha} G m_\beta \frac{\mathbf{r}_\beta - \mathbf{r}_\alpha}{|\mathbf{r}_\beta - \mathbf{r}_\alpha|^3}\,, \tag{2.1}$$

where m_β is the mass of each body considered, $\mathbf{r}_\alpha$ and $\mathbf{r}_\beta$ are the position vectors of the corresping bodies. Due to the equivalence of opposite forces between two bodies ($\mathbf{F}_{\beta\alpha} = -\mathbf{F}_{\alpha\beta}$), the number of total evaluations of Eqn. 2.1 requires $\frac{1}{2}N(N-1)$ computations for all particles in the system and therefore scales as $\mathcal{O}(N^2)$ where $\mathcal{O}$ denotes the computational time complexity of the operation. Solving systems directly is now commonly referred to as particle-particle (PP) schemes. For small systems such as stellar clusters, this direct approach is not notably less efficient than other algorithms and is sufficient for small problems.

2.1.2 Tree Codes

As the number of particles in simulations increased from tens of particles to higher orders of magnitude, the $\mathcal{O}(N^2)$ cost of direct summation made it unfeasible, even with the improvements in computing technology. Considering the gravitational forces on a particle, α, from two distant particles in similar directions and at similar distances from α (β_1 and β_2, respectively), the distance between β_1 and β_2 is small compared to their distance to α. Therefore, their combined force on α is similar to a point mass equal to the combined mass of both particles (β_{1+2}), located at their combined centre of mass, *i.e.*:

$$\mathbf{F}_\alpha = \mathbf{F}_{\alpha\beta_1} + \mathbf{F}_{\alpha\beta_2} \approx \mathbf{F}_{\alpha\beta_{1+2}} \,. \tag{2.2}$$

This assumption forms the basis of the tree algorithm. For example, for the distribution of particles in a simulation, one can define a cube which encompasses all particles (the root). This root cube can then be subdivided into eight equal 'children' cubes (branches). Then each branch is subdivided iteratively until branches only contain one particle, making them a 'leaf', forming an oct-tree. Therefore considering any branch with more than one leaf within it, we can approximate the contained mass as the sum of the individual components acting at the centre of mass of the branch. Once the oct-tree is constructed (an $\mathcal{O}(N \ln N)$ process), it is relatively

efficient to query this structure. Considering forces on a particle α, traversing the oct-tree, we can define a condition on the ratio between the size of a branch (l) and the distance between α and the branch centre of mass (D) as:

$$l/D < \theta\,, \tag{2.3}$$

where θ is a dimensionless parameter called the opening angle. If the condition of Eqn. 2.3 is satisfied, all children of the branch are merged into a 'pseudo-leaf' and treated as a single particle. If the condition is not satisfied, the children of the branch are then considered iterating down the tree until the condition is again satisfied. This algorithm allows for fewer direct summation force calculations, especially in systems of large dynamic ranges and is adaptable to multiple system problems such as merging galaxies. Tree algorithms were first pioneered by Appel (1985) and Barnes & Hut (1986), with the latter being still a popular method implemented in modern simulation codes. The tree scheme improves the computational time complexity to $\mathcal{O}(N \log N)$.

The introduction of these algorithmic improvements to numerical force calculation allowed for a drastic increase in the number of simulated particles. Model `741CU` presented (with $N \approx 10^7$) above was evolved using the tree code PKDGRAV (Stadel 2001)[1].

2.1.3 Particle-Mesh (PM) Codes

For particle-mesh schemes, we build a regular mesh (grid) of N_c cubic cells in a spatial box. The box is then filled with N_P particles. Creating a mesh, similar to building a tree structure, has some computational overhead which scales as $\mathcal{O}(N_c \ln N_c)$. An appropriate mesh would be large enough to encompass all particles for the duration of the simulation and have sufficiently small cell sizes to capture gradients sufficiently, such as a galaxy's vertical density distribution.

[1] PKDGRAV implements a kd-tree structure similar to the oct-tree.

The true distribution of particle masses is assigned to the surrounding points on the mesh using algorithms such as the 'Cloud-In-Cell' (CIC) method. Instead of simply finding the nearest mesh point and adding a particle's mass, the CIC method assumes a particle has a volume the size of a cell and finds the nearest eight (in 3D implementations) mesh points. It then assigns a weighted part of the total particle mass from the particle's volume fraction in each neighbouring cell.

With densities assigned for each point on the mesh, the PM scheme then solves the discretised Poisson equation using a discrete Fourier transform to produce an algebraic expression of the potential and, therefore, the force at each point on the mesh. The acceleration of each particle can then be interpolated from the mesh grid to the particle's actual position. The position and velocities of all particles can then be advanced using numerical integration.

The challenge of PM schemes is that the mesh resolution is fixed, and systems with large dynamic scales would struggle to achieve high efficiency and high resolution in dense regions concurrently. Therefore, in some implementations, adaptive mesh approaches are used where a second higher-resolution mesh is defined in dense regions to capture the dynamics better.

A common implementation is to use large-scale PM schemes, such as cosmological volumes or galaxy clusters, and combine them with other gravity solvers, such as tree codes, in dense regions. For example, tree-particle-mesh (TreePM) codes have been successfully implemented in large-volume high-resolution cosmological simulations such as IllustrisTNG (see Chapter 5) using the simulation code AREPO (Springel 2010).

2.1.4 Force Softening

Stellar particles in galaxy and cosmological simulations typically have particle masses several orders of magnitude greater than real stars, due to computational limitations.

However, this can lead to unphysical interactions between massive particles during close passages. If two particles approach closely, the denominator of Eqn. 2.1 approaches zero, and the force between them diverges to substantial values. To better approximate the smooth potential of a real galaxy, it is common to add a 'softening' to the force calculation.

Because each particle represents a distribution of bodies, we can use the simple approximation of the particle having the potential of a Plummer sphere with scale length ϵ, referred to as a 'softening length'. Therefore the softening kernel takes the form:

$$S(r) = -\frac{1}{\sqrt{r^2 + \epsilon^2}}\,, \tag{2.4}$$

where $r = |\mathbf{r}_\beta - \mathbf{r}_\alpha|$. Thus for $r \gg \epsilon$, the solution tends back to Eqn. 2.1. However, the force tends smoothly to a constant for $r \leq \epsilon$. The choice of a value for ϵ is a trade-off between preventing unphysical interactions of particles and maintaining numerical resolution.

2.2 Numerical Integration

The integration of particle motion in simulations relies on numerically integrating differential equations of position and velocity of the form:

$$\mathbf{a}_i = \frac{\mathrm{d}\mathbf{v}_i}{\mathrm{d}t} = \frac{\mathrm{d}^2\mathbf{x}_i}{\mathrm{d}t^2}\,, \tag{2.5}$$

where $\mathbf{a}_i$, $\mathbf{v}_i$ and $\mathbf{x}_i$ are a particle's acceleration, velocity and position, respectively, at a given time step i. In stellar systems such as galaxies, the acceleration depends only on the mass distribution and can be calculated from the force using the methods above.

A typical integration scheme called leapfrog integration updates positions (drifts) and velocities (kicks) at staggered time intervals, 'leapfrogging' over each other. The 'kick-drift-kick' form of the leapfrog integrator updates the positions and velocities

from step i to $i+1$ through a time step, Δt, with the following algorithm:

$$\begin{aligned} \mathbf{v}_{i+1/2} &= \mathbf{v}_i + \left(\mathbf{a}_i \cdot \frac{\Delta t}{2}\right) \ -Kick \\ \mathbf{x}_{i+1} &= \mathbf{x}_i + \left(\mathbf{v}_{i+1/2} \cdot \Delta t\right) \ -Drift \\ \mathbf{v}_{i+1} &= \mathbf{v}_{i+1/2} + \left(\mathbf{a}_{i+1} \cdot \frac{\Delta t}{2}\right). \ -Kick \end{aligned} \tag{2.6}$$

Leapfrog integrators are used in many of the numerical methods outlined above.

2.3 (Magneto)-Hydrodynamics

The N-body gravity solvers above describe well the motions of dark matter and stars in the Universe. However, while dark matter and dark energy are the dominant components, we observe only the visible components, which are made up of baryonic matter. This baryonic matter was originally in the form of gas until the first stars were born.

On relatively small scales, baryonic matter not only follows motions due to gravity but must also satisfy hydrodynamical conditions. Therefore, more physics is required to capture their contributions to systems such as galaxies accurately. Several hydrodynamical schemes attempt to solve such physical processes in simulations numerically. For example, gas in simulations is typically described as inviscid ideal gases following the Eulerian equations. We outline two common schemes here.

2.3.1 Smooth Particle Hydrodynamics (SPH)

The first approach is a mesh-free Lagrangian method introduced by Gingold & Monaghan (1977) and Lucy (1977) where the continuous gas distribution is traced with particles of a given mass. The physical parameters of any particle are computed over a kernel function by summing the relevant properties of $N_{\rm smooth}$ particles that lie within $2h$ (where h is the 'smoothing length'); thus, changing $N_{\rm smooth}$ allows

for the resolution to be adjusted. In systems such as galaxies, we are interested in both the gravity and hydrodynamics of matter within them; thus, the particle-based nature of smooth particle hydrodynamics (SPH) allowed for easy integration into gravity force solvers mentioned above.

Because the hydrodynamical computations are calculated over nearest neighbours, it works well in systems with large-density contrasts. SPH schemes have been developed and applied to large cosmological simulations such as Romulus25 (Tremmel et al. 2017) run using the Tree+SPH code ChaNGa (Menon et al. 2015).

2.3.2 Moving Mesh Finite Volume (MMFV)

Hydrodynamical systems can be numerically integrated using a mesh-based approach. Some of the most common approaches include finite volume, finite difference and finite element methods. However, the large dynamic range needed in galaxy and cosmological simulations typically requires adaptive meshes, leading to the development adaptive-mesh-refinement schemes. Nevertheless, this also leads to another problem that mesh codes face. In fixed mesh schemes, computational time is spent in regions of very low density; therefore, allowing the mesh to move with high-density regions also can make the methods more efficient.

Moving meshes can also be deformed from their Cartesian structure to allow for the change in particle density (*e.g.*, Gnedin 1995). Modern moving mesh schemes have used unstructured meshes, such as a mesh generated from the Voronoi tessellation of a set of discrete points (Springel 2010). This approach allows the mesh to deform without twisting, thereby continuously adjusting its resolution to the particle density.

The Voronoi cells of the mesh track conserved quantities of the hydrodynamical fluid such as mass, momentum and energy. In cases where the simulation integrates magnetic fields (*i.e.* magneto-hydrodynamics) the average field strength can also

be calculated within the Voronoi cells. Moving mesh schemes can also operate in conjunction with gravity solvers.

The magneto-hydrodynamics code Arepo (Springel 2010) implemented a moving-mesh finite-volume approach with a tree+PM gravity solver and was used to produce the large-scale and relatively high-resolution cosmological simulations of the IllustrisTNG project (Pillepich et al. 2018b; Springel et al. 2018; Nelson et al. 2018; Naiman et al. 2018; Marinacci et al. 2018).

2.4 Sub-Grid Physics

Simulations typically do not resolve individual stars or gas clouds. Therefore they do not resolve physical processes which occur in individual stars, such as their birth, evolution, and eventual death. To compensate, we define sub-resolution (sub-grid) implementations to approximate astrophysical processes.

Gas in different phases, such as cold and dense, warm and diffuse, and ionised states dissipates its internal energy through cooling processes such as collisional excitation and ionisation, inverse Compton, recombination, free-free emission and metal line cooling. These processes are typically expressed as analytical approximations.

Stars form out of cold and dense gas, represented in simulations as gas particles. Therefore gas particles transform a portion of their mass into collisionless star particles (star-formation), representing a single stellar population (SSP) described by an adopted initial stellar mass function and the chemical abundance of the gas particle. The fraction of the gas particle mass converted into a stellar particle, M_f, is a tunable parameter that can control the star formation rate. Criteria for star formation commonly apply limits to the density and temperature of the gas particle (usually restricting gas to the molecular phase), which also has to be part of a converging flow (*i.e.* $\nabla \cdot \mathbf{v} < 0$, Stinson et al. 2006). A probabilistic sampling scheme converts eligible gas into stars, making most star-forming simulations stochastic in

nature. The probability, p, of forming a stellar particle in a time step, Δt, can be formulated as:

$$p = M_f(1 - e^{-c^* \Delta t / t_{\rm dyn}}) \tag{2.7}$$

where c^* is a constant factor as a parameter for 'star-forming efficiency', and $t_{\rm dyn}$ is the dynamical time (Stinson et al. 2006).

Stellar particles in simulations are typically not removed once formed. However, as explored in Section 1.3, stellar evolutionary processes such as stellar winds and supernovae return mass, energy and heavy elements to the gaseous interstellar medium. This 'feedback' of energy heats and redistributes the gas, regulating star formation. The stellar feedback is generally assigned from tabulated mass and metal yields derived from stellar evolution models. Typically supernovae are short-lived processes and are not captured correctly within the cadence of galaxy simulations. Therefore prescriptions for feedback are implemented at the sub-grid level where surrounding gas is prevented from cooling for a period of time or the gas is heated probabilistically. Supermassive black hole feedback also injects energy into the galactic environment and, combined with stellar feedback, can drive galactic scale outflows.

Chapter 3

Bulge Proper Motion Rotation Curves

The following chapter is a paper published in the *Monthly Notices of the Royal Astronomical Society* as Gough-Kelly et al., 2022, *MNRAS*, 509, 4829-4848. entitled:

Predicted Trends in Milky Way Bulge Proper Motion Rotation Curves: future Prospects for *HST* and LSST

presented by the following authors:

Steven Gough-Kelly[1], Victor P. Debattista[1], William I. Clarkson[2], Oscar A. Gonzalez[3], Stuart R. Anderson[1], Mario Gennaro[4], Annalisa Calamida[4], Kailash C. Sahu[4]

[1]Jeremiah Horrocks Institute, University of Central Lancashire, Preston PR1 2HE, UK

[2]Department of Natural Sciences, University of Michigan-Dearborn, 4901 Evergreen Road, Dearborn, MI 48128, USA

[3]UK Astronomy Technology Centre, Royal Observatory, Blackford Hill, Edinburgh EH9 3HJ, UK

[4]Space Telescope Science Institute, 3700 San Martin Drive, Baltimore, MD 21218, USA

CHAPTER 3

Abstract

We use an N-body+smoothed particle hydrodynamics simulation of an isolated barred galaxy to study the age dependence of bulge longitudinal proper motion (μ_l) rotation curves. We show that close to the minor axis ($|l| \sim 0°$) the relatively young stars rotate more rapidly than the old stars, as found by *Hubble Space Telescope* in the Milky Way's (MW's) bulge. This behaviour would be expected also if the MW were unbarred. At larger $|l|$ a different behaviour emerges. Because younger stars trace a strong bar, their galactocentric radial motions dominate their μ_l at $|l| \sim 6°$, leading to a reversal in the sign of $\langle \mu_l \rangle$. This results in a rotation curve with forbidden velocities (negative $\langle \mu_l \rangle$ at positive longitudes, and positive $\langle \mu_l \rangle$ at negative longitudes). The old stars, instead, trace a much weaker bar and thus their kinematics are more axisymmetric, resulting in no forbidden velocities. We develop metrics of the difference in the $\langle \mu_l \rangle$ rotation curves of young and old stars, and forbidden velocities. We use these to predict the locations where rotation curve reversals can be observed by *HST* and the Vera Rubin Telescope. Such measurements would represent support for the amplitude of the bar being a continuous function of age, as predicted by kinematic fractionation, in which the bar strength variations are produced purely by differences in the random motions of stellar populations at bar formation.

3.1 Introduction

More than half of the galaxies in the local Universe host a bar (Eskridge et al. 2000; Menendez-Delmestre et al. 2007; Barazza et al. 2008; Aguerri et al. 2009; Gadotti 2009). Bars play an important role in driving the dynamics and structural properties within the central regions of galaxies via secular processes, including the formation of bulges (see the review by Kormendy 2013). Two bar-driven processes can vertically

thicken a bar. The higher radial velocity dispersion due to orbital motion along the bar's major axis makes the bar susceptible to the buckling instability (Raha et al. 1991; Merritt & Sellwood 1994; Debattista et al. 2006; Martinez-Valpuesta et al. 2006; Collier 2020; Łokas 2020). The buckling instability causes the bar to thicken very rapidly. The second mode of vertical thickening is via the trapping of orbits on vertical resonances (Combes & Sanders 1981; Combes et al. 1990; Pfenniger & Friedli 1991; Quillen 2002; Skokos et al. 2002a; Debattista et al. 2006; Quillen et al. 2014). This symmetric form of vertical thickening has recently been demonstrated explicitly in N-body simulations (Sellwood & Gerhard 2020). Unlike the buckling instability, heating by orbit trapping is a slow process.

In both mechanisms, the resulting bulge morphology is boxy or peanut shaped. Such bulges are commonly referred to as boxy/peanut- (B/P) or X-shaped bulges. Stronger features can appear as an X-shape when the bar is viewed edge-on, with its major axis perpendicular to the line of sight (LOS) (Athanassoula & Misiriotis 2002; Athanassoula 2005). B/P bulges appear in up to 80 per cent of local high mass (*i.e.* those with characteristic stellar mass $\log(M_\star/\mathrm{M}_\odot) \gtrsim 10.4$) barred galaxies, a fraction that declines rapidly at lower masses (Erwin & Debattista 2017). This characteristic mass appears to have remained unchanged since redshift $z \sim 1$ (Kruk et al. 2019).

The *in situ* separation of different populations within a B/P bulge as presented in Debattista et al. (2017) demonstrates that co-spatial populations with varying initial radial velocity dispersions evolve separately in a growing bar. As a result, kinematically cooler populations form a strong bar and strongly peanut-shaped bulge, whereas hotter populations form a weaker bar, and are more vertically heated. They termed this process kinematic fractionation. Correlations between kinematics and

stellar properties such as age and metallicity during bar formation then result in gradients developing in the final morphology of the B/P bulge and bar (see also Fragkoudi et al. 2018; Debattista et al. 2019). Gonzalez et al. (2017) demonstrated that the metallicity distribution of NGC 4710 is more peanut-shaped than the density, as predicted by kinematic fractionation. An alternative mechanism for producing a vertical metallicity gradient relies on the transition between a metal-rich thin disc and a metal-poor thick disc (Bekki & Tsujimoto 2011; Di Matteo 2016). This led Di Matteo et al. (2019) to argue that, in addition to the radial velocity dispersions, the vertical dispersion also played a key role in the vertical thickening of populations. However, Debattista et al. (2020) showed vertical thickening is a monotonic function of the initial radial action of a given stellar population. Consequently, a thick disc can produce a vertical gradient largely because it has a higher radial velocity dispersion.

The Milky Way (MW) is now understood to host a B/P bulge. Early evidence for this shape was the bimodal density distribution of red clump (RC) stars in the bulge (McWilliam & Zoccali 2010; Saito et al. 2011) along the line of sight (LOS) to the Galactic Centre. This bimodality is produced by the two arms of an X-shape. This structure can be seen directly in the infrared by observing towards the Galactic Centre with *Wide-field Infrared Survey Explorer* (Ness & Lang 2016). Various lines of evidence for kinematic fractionation having occurred in the MW have been obtained. Ness et al. (2012) demonstrated that the double RC is only traced by metal-rich stars, which was later confirmed with data from *Gaia*-ESO DR1 and VISTA Variables in Via Lactea (VVV, Rojas-Arriagada et al. 2014) and more recently by Lim et al. (2021) in the Blanco DECam Bulge Survey (BDBS). The behaviour of the RC is the Solar-perspective equivalent of the strongly peanut-shaped metallicity distributions found in external galaxies. Zoccali et al. (2017) showed that the 3D density distributions of MW metal-rich and metal-poor stars

are boxy and spheroidal, respectively. Catchpole et al. (2016) demonstrated an age dependence of the bar strength by considering Mira variables of different periods, showing that the younger Miras trace a stronger bar. Grady et al. (2019) also found a similar dependence of bulge morphology on stellar age, with the youngest Miras showing a strong bar with a peanut distribution, which is not seen in the oldest stars. Grady et al. (2019) estimated that the bar formed $\sim 8 - 9$ Gyr ago, roughly 5 Gyr after the MW formed.

Kinematic studies of the bulge have shown indications of bar streaming motions at low latitudes in both LOS velocities and proper motions (Babusiaux et al. 2014). The correlation between the two components, as measured by vertex deviation, indicates the presence of elongated stellar orbits (Babusiaux et al. 2010; Hill et al. 2011; Vásquez et al. 2013). Measurements of the vertex deviation in Baade's Window show clear non-zero values in metal-rich stars, indicating their stronger bar structure (Portail et al. 2017; Debattista et al. 2020). The dependence of bulge kinematics on chemistry is also seen in the radial velocity dispersion. Metal-rich stars have lower dispersion than metal-poor stars (Zoccali et al. 2017) except close to the plane ($b \lesssim 1°$), which has been attributed to the central density peak observed by Valenti et al. (2016). The radial velocity dispersion of metal-rich stars decreases steeply away from the centre whereas the gradient in metal-poor stars is much shallower (Kunder et al. 2012; Ness et al. 2013b). For a review of the chemodynamics of the MW bulge, see Barbuy et al. (2018) and references therein. These kinematic differences have been interpreted as further evidence of kinematic fractionation in the bulge (Debattista et al. 2017, 2019), although the metal-poor stars require a contribution from the stellar halo to explain the observations completely.

Clarkson et al. (2018, hereafter C18) studied proper motions in the well-observed *Sagittarius Window Eclipsing Extrasolar Planet Search* (SWEEPS) field (see also Sahu et al. 2006; Clarkson et al. 2008) imaged by the *Hubble Space Telescope* (*HST*).

C18 used proper motions calculated by Calamida et al. (2014) from observations collected over a 10-year baseline with the Advanced Camera for Surveys/Wide Field Camera (ACS/WFC) onboard *HST* and derived photometric parallaxes for main-sequence stars. They also used photometry from the Bulge Treasury Survey (BTS, Brown et al. 2010) to tag photometric metallicities to the stars within the field, allowing them to construct a metal-rich and a metal-poor population of main-sequence stars. They found that the longitudinal proper motion rotation curves (*i.e.* $\langle \mu_l \rangle$ as a function of distance) were distinct for the two populations. Metal-rich stars exhibited larger amplitude proper motions, with a steeper gradient through the zero point in distance (approximately the Galactic Centre). C18 suggested that this could be the signature of orbital differences as predicted by kinematic fractionation.

Proper motion rotation curves therefore have the ability to constrain the different kinematic states of bulge populations, and therefore the formation of the bulge. The study of C18 represents a deep 'pencil-beam' along a single LOS close to the bulge's minor axis, but provides little insight into how the proper motion rotation curves vary across the entire bulge. Therefore, in this paper, we explore the trends expected for proper motion rotation curves of different populations in the bulge. We study the proper motions in a star-forming simulation which forms a B/P bulge to predict and interpret trends in the rotation curves across the MW's bulge. The model we use is the same as that in Debattista et al. (2017) which they showed had experienced kinematic fractionation. Therefore, our study will predict the expected trends for proper motion rotation curves if this mechanism has been the main process responsible for the distribution of the MW's stellar populations.

The paper is organized as follows. We describe the model used in this study in Section 3.2. In Section 3.3, we explore the separation of rotation curves in the SWEEPS field along with a metric we define for quantifying the separation amplitude and present an interpretation of the observed trends with galactocentric

velocity maps. In Section 3.4, we explore the SWEEPS field in greater detail and compare our results with MW observational data to test the robustness of our separation amplitude measurement. We also provide predictions for the rotation curves in key lines of sight within the MW bulge. In Section 3.5, we explore how galactocentric velocities project onto longitudinal proper motions and define a second measurement of kinematic separation between populations. Section 3.6 presents our comparison to a second model with a weaker bar and B/P. Finally, in Section 3.7, we discuss the implications of our findings and predictions for future work.

3.2 Simulation

We analyse a high-resolution N-body+smoothed particle hydrodynamics (SPH) star-forming simulation which forms a barred spiral galaxy from a hot gas corona embedded in a live dark matter halo. The model has been described numerous times in earlier works where it has been compared to both the MW and external galaxies (Cole et al. 2014; Gardner et al. 2014; Ness et al. 2014; Gonzalez et al. 2016, 2017; Debattista et al. 2017). Debattista et al. (2017) demonstrated that the model underwent kinematic fractionation, and has different bulge (and bar) properties for older (metal-poor) and younger (metal-rich) populations. The resulting trends are comparable to those seen in the MW.

The initial conditions are comprised of a hot gas corona inside a dark matter halo. The dark matter halo is comprised of 5 million particles having a force softening of $\epsilon = 103\,\mathrm{pc}$, virial radius $r_{200} = 198\,\mathrm{kpc}$ and virial mass $M_{200} = 9.0 \times 10^{11}\,\mathrm{M}_{\odot}$. The gas corona consists of 5 million gas particles with a force softening of $\epsilon = 50\,\mathrm{pc}$. The gas corona has angular momentum $L_z \propto R$ with spin $\lambda \approx 0.041$.

The simulation is evolved using the N-body+SPH code GASOLINE (Wadsley et al. 2004) with a base time step of 10 Myr. The gas in the corona cools and settles to the centre forming a disc. The formation of a stellar particle happens when gas reaches

densities greater than 100 amu cm^{-3} with a temperature of $T < 15\,000$ K. 10% of gas in this state forms stars with 35% the mass of the initial gas particles, corresponding to $\approx 9.4 \times 10^3\,\mathrm{M}_\odot$. Gas particles in this state will continue to trigger star formation until their mass falls to below 21% of their initial mass. Then the remaining mass is redistributed to its nearest neighbours, and the gas particle is removed. Each stellar particle is a representation of a Miller & Scalo (1979) initial mass function. Feedback from type Ia and type II supernovae is modelled using the blastwave prescription of Stinson et al. (2006). Stellar winds of asymptotic giant branch stars using the theoretical yields for iron and oxygen from Woosley & Weaver (1995) also enrich the interstellar medium. This simulation does not include the diffusion of metals between gas particles (Loebman et al. 2011) producing the undesirable effect of forming low metallicity stars at all ages, broadening the metallicity distribution.

After 10 Gyr of evolution $\sim$ 11 million star particles have formed, with a total mass of $\sim 6.5 \times 10^{10}\,\mathrm{M}_\odot$. The resulting disc has a scale length $R_d \approx 1.7$ kpc (Cole et al. 2014). The bar forms between $2 - 4$ Gyr, after which it continues to grow secularly. We define the bar radius, r_{bar}, as the mean of the radii where the amplitude of $m = 2$ Fourier moment reaches half its peak value (Debattista & Sellwood 2000) and that where the $m = 2$ phase angle changes by 10° from constant. At 10 Gyr, $r_{bar} \sim 3$ kpc (Cole et al. 2014).

3.2.1 Comparing With the Milky Way

As shown by Debattista et al. (2017), this model provides insights into trends in the MW, and makes predictions which can be tested against current and future observations. By scaling the $t = 10$ Gyr time-step as in Debattista et al. (2017), we can produce a bar of about the right size with roughly the correct kinematics. Here we describe how we scale the model and qualitatively compare to the MW.

We spatially scale up the simulation by a factor of 1.7, in line with recent measurements for the MW's bar length, $r_{bar} = 5.0 \pm 0.2$ kpc (Wegg et al. 2015). After rescaling, the model's bar length is $r_{bar} = 4.85 \pm 0.55$ kpc. The velocities are scaled by 0.48 to match the velocity dispersion in the MW bulge (see Debattista et al. 2017). We place the observer at 8 kpc from the galactic centre in the mid-plane with the bar aligned to 27° from the LOS of the observer to the galactic centre (Wegg & Gerhard 2013; Qin et al. 2018), with the near side of the bar at positive longitude.

In order to increase our resolution in the bulge region, we assume the simulation to have mid-plane symmetry; therefore, we project stars below the plane onto above the plane with an inverted vertical velocity ($z' = -z$; $v'_z = -v_z$, for $z < 0$). We then calculate galactic longitude, latitude, and LOS distance (l, b, D) along with longitudinal proper motions (μ_l) for each star from the solar perspective, in the galactic rest frame. Coordinate transformations in this work were computed using the PYTHON package GALPY (Bovy 2015).

We define the bulge region as follows: $|l| \leq 20°$, $2° \leq |b| \leq 10°$, and $5.75 \leq D/\,\mathrm{kpc} \leq 10.25$. This is larger than previous studies which usually constrain longitude to $|l| < 10°$. Considering that the bar is inclined by 27°, at $l = +20°$, we sample ~ 3.5 kpc along the near side of the bar encapsulating a larger extent of the B/P component. Our range is also larger than the proposed footprint of the Vera Rubin Observatory, Legacy Survey of Space and Time (LSST) bulge observations allowing for predictions for this and additional future survey missions (see Section 3.7.1).

The lack of chemical mixing in this model results in an excess of stars with low metallicities at all ages. Debattista et al. (2017) circumvented this problem by considering stellar populations defined by age, rather than by metallicity. Likewise, here we also define populations based on stellar ages. The cumulative distribution of ages within the model's bulge is shown in Fig. 3.1. Using this distribution, we

define a young population as those stars with age < 7 Gyr (mean age $= 5.8$ Gyr) and an old population with stellar ages > 9 Gyr (mean age $= 9.6$ Gyr). This results in a sample of 361 131 relatively young stars and 1 341 922 old stars within our defined bulge region, representing 14 and 51 per cent of all bulge stars, respectively. Since the simulation was run for only 10 Gyr the majority of ages are lower than would be expected for the MW; none the less, the ordering of the stellar ages would remain intact. These age ranges allow us to qualitatively compare the simulation with populations separated by metallicities in the SWEEPS field (Bernard et al. 2018) and the MW bulge in general. We also note that the distribution of ages in this model is consistent with the picture of a largely old bulge in the MW (Kuijken & Rich 2002; Zoccali et al. 2003; Clarkson et al. 2008, 2011; Brown et al. 2010; Valenti et al. 2013; Renzini et al. 2018), as discussed in Debattista et al. (2017). The model also has a similar fraction of stars younger than 5 Gyr observed in the MW ($\sim 3\%$ of the bulge population Renzini et al. 2018). While we refer to a young population in the model's bulge, we mean this in a relative sense: even excluding that the model is only evolved for 10 Gyr, a large majority of the young stars are old with $\sim 50\%$ of them formed during the bar's formation.

We verify that the vertical structure of our rescaled model is a reasonable analogue of the MW's B/P bulge by considering the variation of the distance bimodality as a function of latitude, as viewed from the Sun. In particular, we consider the double RC as a function of latitude. Following the similar prescription of Gonzalez et al. (2015) and Debattista et al. (2017), we assume that the RC stars follow the same density as the model in general. We therefore set the absolute magnitude of all stars to the average of the RC, $M_K = -1.61$, and convert this to apparent magnitudes, m_K, based on their distance from the solar position (8 kpc). We then convolve each m_K with a Gaussian kernel of $\sigma = 0.17$ mag to approximate the width of the RC magnitude distribution (Gerhard & Martinez-Valpuesta 2012). We

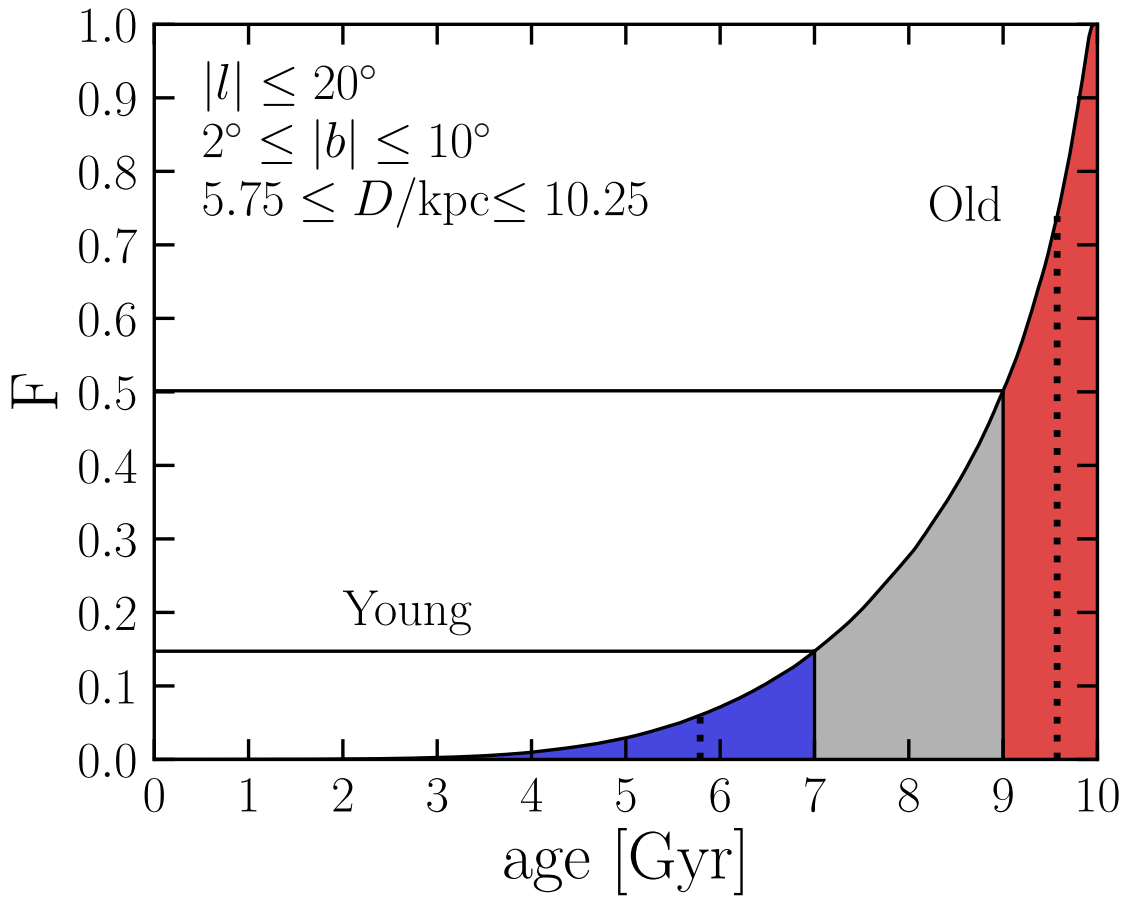

Figure 3.1: The cumulative distribution of ages within the model's bulge region at $t = 10$ Gyr. The spatial cuts used are given at the top left-hand side. We define the young (blue) and old populations' (red) age cuts as 7 and 9 Gyr, respectively. The mean ages for the two populations (vertical black dashed lines) are 5.8 = and 9.6 Gyr, respectively.

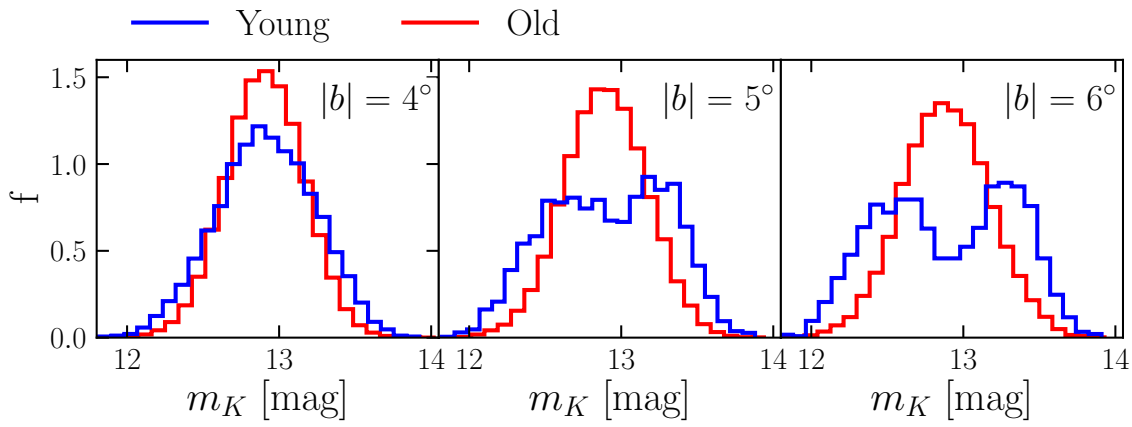

Figure 3.2: Unextincted apparent magnitude distributions of simulated RC stars along the LOS within $|l| < 4°$ for $|b| = 4°$ (left-hand panel), 5° (middle panel) and 6° (right-hand panel) with $\delta|b| = 0.25°$. Young (age < 7 Gyr) and old (age > 9 Gyr) stars are represented by the blue and red histograms, respectively. The magnitude distributions have been convolved with a Gaussian of width $\sigma = 0.17$ mag to represent the width of the RC. As in the MW, a bimodality is first evident at $|b| \simeq 5°$.

present the magnitude distribution of simulated RC stars split by our age cuts in Fig. 3.2. The distribution of young stars is single peaked at $|b| = 4°$ and bimodal above that, in agreement with the bimodality found by Ness et al. (2012). The old population is single peaked at all latitudes.

3.3 Separation of Rotation Curves

The combined field from SWEEPS+BTS data studied in C18 was approximately $3.4 \times 3.4\,\mathrm{arcmin}^2$ centred at $(l, b)_{J2000.0} \approx (+1.26°, -2.65°)$. We compare the rotation curves of young and old stars in the model's equivalent of the SWEEPS+BTS field,

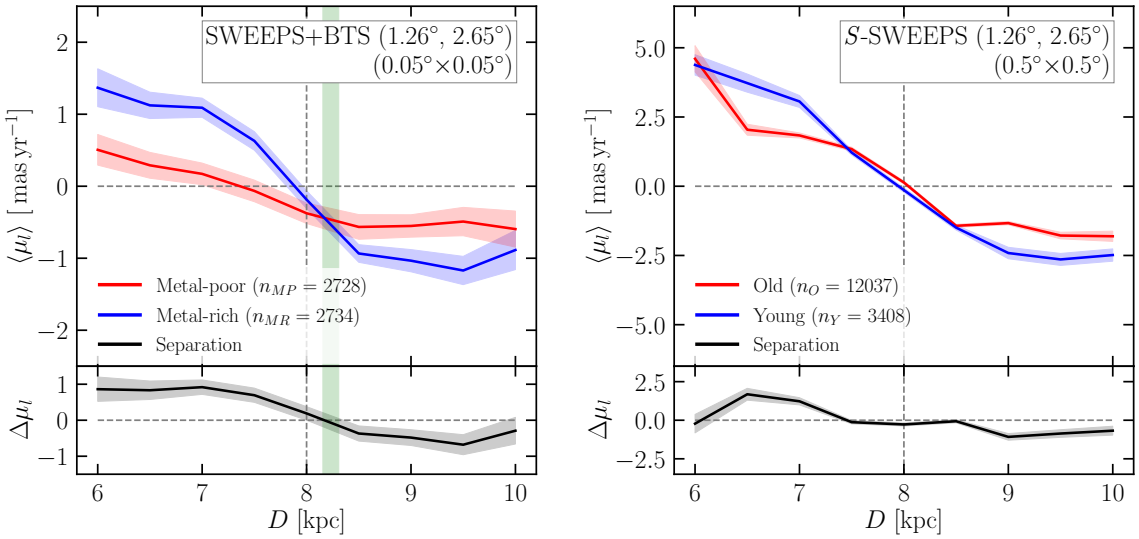

Figure 3.3: Left-hand panel: Average longitudinal proper motion rotation curves for metal-rich and metal-poor main-sequence stars of the SWEEPS+BTS field, centred on $(l, |b|) = (+1.26°, 2.65°)$ with an FOV of $0.05 \times 0.05\,\mathrm{deg}^2$ (C18). The vertical green shaded region show the range of estimates of $R_\odot$ from the GRAVITY consortium. Right-hand panel: Average longitudinal proper motion rotation curves for young and old stars, and the separation between them, of the simulated *S*-SWEEPS field, centred on $(l, |b|) = (+1.26°, 2.65°)$ with an FOV of $0.5° \times 0.5°$. The number of star particles in each population is listed in the legends.

hereafter *S*-SWEEPS[1]. Although the model has a large number of star particles, the overall number is still small compared to the real MW; therefore our field of view (FOV) is increased to $30 \times 30\,\mathrm{arcmin}^2$ to increase the number of particles. As mentioned in Section 3.2.1, we constrain our distance measurements within the bulge to between 5.75 to 10.25 kpc. Taking bins along the LOS, we calculate the mean longitudinal proper motion for young and old stars, $\langle \mu_l \rangle_Y$ and $\langle \mu_l \rangle_O$, within each bin, with the standard error given by

$$e_{\langle \mu_l \rangle} = \frac{\sigma_{\mu_l}}{\sqrt{n_\star}}. \tag{3.1}$$

The rotation curve separation between the young and old populations is then simply $\Delta\mu_l = \langle \mu_l \rangle_Y - \langle \mu_l \rangle_O$ in each bin and the uncertainty, $e_{\Delta\mu_l}$, is propagated through addition in quadrature.

We explore the SWEEPS+BTS data using the same binning as described above. The left-hand panel of Fig. 3.3 presents the sample from C18 (their figure 8), showing the average longitudinal proper motion as a function of LOS distance for their metal-rich versus metal-poor main-sequence populations. The distances are estimated from photometric parallax, using as reference the median distance modulus $(m - M)_0 = 14.45$ of the SWEEPS+BTS field main-sequence (Calamida et al. 2014), which, taken literally, corresponds to a physical distance of $D_0 = 7.76$ kpc. This is the distance of the median well-measured population that survives their kinematic cut for bulge objects ($\mu_l < -2$ mas yr^{-1}), and thus naturally lies closer to the observer than the Galactic Centre. The offset between the proper motion zeropoints $\mu_l = 0$ in the two panels arises because the SWEEPS+BTS proper motions are measured relative to the median well-measured (majority-bulge) stellar population in the FOV (with median distance closer than 8 kpc; see C18 and Calamida et al. 2014 for more on this issue), whereas for our simulated samples, $\mu_l = 0$ at the galactic centre by

[1]We use the prefix "*S*-" throughout this paper to denote simulated equivalents of observed *HST* fields.

construction. This offset in proper motion zeropoint does not impact our results in any way.

The identification of photometric parallax with physical distance gains some support when we consider the distance at which the 'metal-rich' and 'metal-poor' rotation curves cross, which is approximately the same as the recent measurement of the Galactic Centre distance by the GRAVITY experiment, at $R_{\odot} \approx 8.156 - 8.308\,\mathrm{kpc}$ (Gravity Collaboration et al. 2019, 2021), shown as the green shaded region in the left-hand panel of Fig. 3.3.

The rotation curves from the *S*-SWEEPS field are shown in the right-hand panel of Fig. 3.3. For both the simulation and observations we show the rotation curve separation, $\Delta\mu_l$ below each panel. In both the young and old populations, $|\langle\mu_l\rangle|$ rises on either side of the galactic centre. The peak value of $|\langle\mu_l\rangle|$ on the near side is larger than that on the far side, by a factor of about 2 for both populations, which is expected because of perspective. The ratio of peak amplitude of young stars to old stars is also ~ 2. The largest $\Delta\mu_l$ is at $\sim 1\,\mathrm{kpc}$ from the galactic centre. These results are qualitatively similar to those of C18 for the metal-rich vs. metal-poor main-sequence populations shown in the left-hand panel.

3.3.1 Separation Amplitude

Given that the model matches the trends found by C18, we consider the behaviour of the rotation curves of young and old stars across the model's bulge, to predict trends that can be tested in future studies.

The top panel of Fig. 3.4 shows, in Galactic coordinates $(l, |b|)$, the density distribution of stars in the two populations. The distribution of young population (blue contours) is more pinched at high latitude, resembling a peanut, whereas the old population (red contours) appears more boxy. The young stars are also more concentrated to the mid-plane, demonstrating there are fewer young stars at

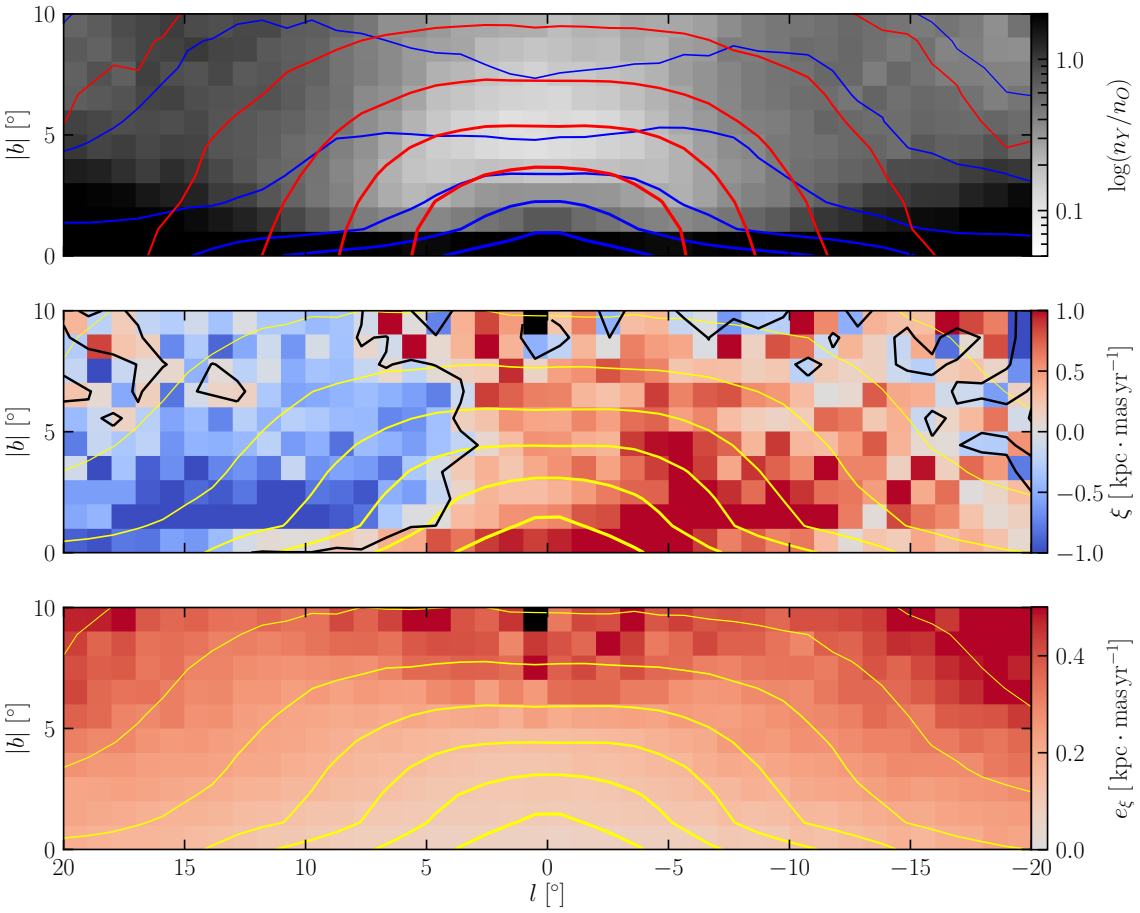

Figure 3.4: Top panel: fractional distribution of young to old stars within the bulge of the model. Blue and red contours follow young and old population densities, respectively. Middle panel: separation amplitude, ξ, for each pixel representing a $1 \times 1\,\mathrm{deg}^2$ field. Bottom panel: uncertainty on ξ for each field. In the bottom two panels, the yellow contours follow the density of all bulge stars. Black pixels are fields for which ξ could not be measured reliably.

higher latitudes, similar to the metallicity distributions (Zoccali et al. 2017) and the distribution of long-period (young) Miras (Grady et al. 2019) within the MW.

To quantify the separation between the young and old rotation curves, we integrate the separation along the LOS, to obtain a separation amplitude. Binned by distance, we define the separation amplitude ξ, as the LOS integral of $\Delta\mu_l(D) = \langle\mu_l\rangle_Y(D) - \langle\mu_l\rangle_O(D)$ as

$$\xi = \delta D \cdot \sum_{D=d_1}^{d_2} \Delta\mu_l(D), \tag{3.2}$$

where D is each distance bin centre with width $\delta D = 0.5\,\mathrm{kpc}$ and ξ has units of $\mathrm{kpc}\cdot\mathrm{mas\,yr^{-1}}$. We set $d_1 = 6\,\mathrm{kpc}$, $d_2 = 10\,\mathrm{kpc}$, respectively, as the limits of the model's bulge region.

We map ξ across the entire bulge of the model, using fields of $1 \times 1\mathrm{deg}^2$. This represents a much larger FOV than those sampled by deep bulge fields in the MW, but is necessary to attain reasonable particle numbers at higher latitudes. For each $(l, |b|)$ bin, we repeat the analysis applied to the *S*-SWEEPS field, producing $\langle\mu_l\rangle$ rotation curves for the young and old populations using the same binning along each LOS.

The middle panel of Fig. 3.4 shows a map of $\xi(l, |b|)$ for the model. We focus on the region $|b| > 2^\circ$ to avoid the thin disc and the nuclear disc found below this latitude in our model (Cole et al. 2014; Debattista et al. 2015, 2018). Along the minor axis, $|l| \lesssim 5^\circ$, ξ is mostly positive up to large latitudes with relatively low amplitudes, $0 < \xi/\,\mathrm{kpc}\cdot\mathrm{mas\,yr^{-1}} < 0.5$. These rotation curves have qualitatively similar separation profile to the *S*-SWEEPS field (Fig. 3.3) which is more or less antisymmetric with distance from the galactic centre, resulting in relatively small ξ values. The small positive values of ξ on the minor axis arise largely because of perspective.

As we show below, some rotation curves of fields away from the minor axis are not anti-symmetric, resulting in separation profiles that are everywhere positive or

negative; for these rotation curves, ξ will be larger. Almost all fields with longitudes $l < 5^\circ$ have positive ξ values, whilst for longitudes $l > 5^\circ$ ξ has mostly negative values. Away from the minor axis, there is a slight vertical gradient with higher amplitude ξ values at low latitude which decreases with increasing latitude.

The number of young stars decreases rapidly with increasing height, and above $|b| \gtrsim 8^\circ$ some fields have too few young stars to measure a reliable rotation curve. We calculate the uncertainty of the separation amplitudes, e_ξ, for each field as

$$e_\xi = \delta D \cdot \left(\sum_{D=d_1}^{d_2} e_{\Delta\mu_l}(D)^2 \right)^{1/2}, \tag{3.3}$$

where $\delta D = 0.5\,\mathrm{kpc}$ is the bin width.

The distribution of e_ξ, presented in the bottom panel of Fig. 3.4, loosely traces the density distribution of young stars (blue contours in the top panel), highlighting that the number of star particles along an LOS is a limiting factor in this measurement. The uncertainties are lowest on the minor axis and on the near side of the bar.

3.3.2 Galactocentric Velocities

In order to interpret the ξ map, including the asymmetries between positive and negative longitudes, we consider the difference in the bulge's intrinsic (galactocentric cylindrical) kinematics, *i.e.* the galactocentric radial velocity, v_R and galactocentric tangential velocity, v_ϕ. Fig. 3.5 first presents the vertically averaged heliocentric longitudinal proper motions for the bulge's young and old populations in the (X, Y) plane, along with the corresponding galactocentric cylindrical velocities. We only consider stars in the vertical slice $0.5 < |z|/\,\mathrm{kpc} < 1.0$, equivalent to $4^\circ < |b| < 7^\circ$ at 8 kpc, to avoid the effect of the nuclear disc as discussed in Section 3.3.1 and regions where the uncertainty in ξ is largest. The left-hand and middle columns of Fig. 3.5 show the velocity distributions of the young and old populations respectively. The right-hand column shows the difference between the young and old velocity

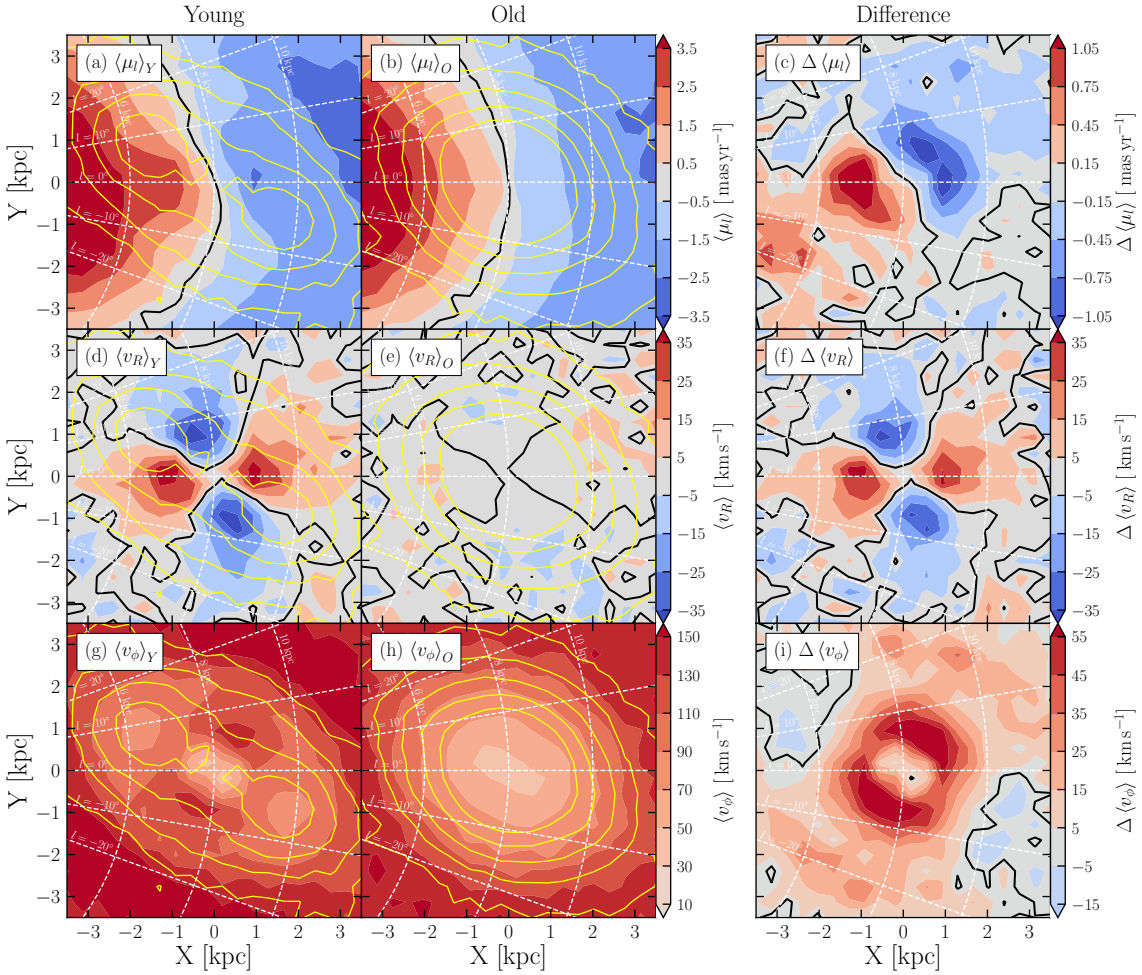

Figure 3.5: Average velocity fields in the (X, Y) plane for stellar particles at $0.5 < |z|/\,\mathrm{kpc} < 1.0$. The left-hand column presents the kinematics of the young population while the middle column shows those of the old. The difference in the velocity fields between young and old stars is shown in the right-hand column. The top row shows heliocentric longitudinal proper motions, the middle row shows galactocentric radial velocities and the bottom row shows galactocentric tangential velocities. Yellow contours follow log densities of the corresponding population. Black contours indicate where each velocity component equals zero. White circular dashed lines outline distances 6, 8 and 10 kpc, while the white straight dashed lines mark longitudes between 20° and −20° in 10° intervals. The observer is at $X = -8\,\mathrm{kpc}$ in this figure.

distributions. Within each panel, a thick black contour traces the zero amplitude line of each velocity component and where the difference between populations is also zero. The density of the two populations, indicated by the yellow contours in the left-hand and middle panels, shows that the young stars trace a strongly barred morphology, which has two peaks on either side of the galactic centre. The peaks are the lower layer of the X-shape in the B/P bulge, as also seen in the MW (Sanders et al. 2019, their figure 19). The old population, instead, is considerably less elongated, supporting only a weak bar, as shown by Debattista et al. (2017).

Panels (a) and (b) show that as a result of the much stronger bar in the young population, their average heliocentric proper motions ($\langle\mu_l\rangle_Y$) exhibit a stronger longitudinal variation relative to the Sun than those of the old stars. The $\langle\mu_l\rangle_Y$ distribution has two high-amplitude regions along the $l = 0°$ direction, 1 kpc in front of, and 1 kpc behind the galactic centre. The black contour in the $\langle\mu_l\rangle_Y$ profile is twisted towards the bar major axis, away from the $d_\odot = 8$ kpc line, unlike the $\langle\mu_l\rangle_O = 0$ contour which traces the 8 kpc line more closely at central longitudes. Fig. 3.5(c) shows the difference in the distribution of $\langle\mu_l\rangle$ between the two populations. This panel shows that most of the signal in $\Delta\langle\mu_l\rangle$ comes from regions where the amplitude of $\langle\mu_l\rangle_Y$ peaks, close to $l = 0°$. The near peak has a tail towards negative longitude whereas the far peak has a tail to positive longitude. A field close to the minor axis will intersect both the near and far peaks of $\Delta\langle\mu_l\rangle$ which have positive and negative values respectively, resulting in $\xi \sim 0$. From the (X, Y) perspective, we can see that lines of sight away from the minor axis only intersect one of these $\Delta\langle\mu_l\rangle$ peaks, and therefore have larger $|\xi|$ values.

We then turn to the intrinsic kinematics in galactocentric cylindrical coordinates, which is the natural frame of the bar, removing the effects of perspective. In the middle row of Fig. 3.5 we present the distributions of galactocentric radial velocity, $\langle v_R\rangle$. The young population (Panel d) exhibits a quadrupole pattern, with zero

velocity lines (black contours) aligned with the bar major and minor axes. The amplitude of $\langle v_R \rangle$ peaks at $\sim \pm 45^\circ$ relative to the bar indicating bar-aligned motions along either side of the galactic centre. The old population has no quadrupole pattern and near-zero $\langle v_R \rangle$ values, reflecting its weaker bar morphology. The resulting difference map, $\Delta\langle v_R \rangle$ (Panel f), therefore also has a strong quadrupole pattern.

The bottom row of Fig. 3.5 presents the distribution of the galactocentric tangential velocity, $\langle v_\phi \rangle$. For the old population (Panel h), the distribution of $\langle v_\phi \rangle_O$ is mildly elongated along the bar. In contrast, the $\langle v_\phi \rangle_Y$ distribution (Panel g), is elongated more strongly whilst also exhibiting a complex inner structure. The lower levels of the X-shape, identified by the density contours, coincide with regions of low $\langle v_\phi \rangle$ positioned approximately 3 kpc along the bar major axis. The lowest values of $\langle v_\phi \rangle_Y$ are at the very centre. Peak values of $\langle v_\phi \rangle_Y$ are along the bar's minor axis, as expected for streaming motions in a highly elongated population. Consequently, the difference between the two populations, $\Delta\langle v_\phi \rangle$ (Panel i), exhibits two peaks along the minor axis. Regions of $\Delta\langle v_\phi \rangle < 0$ appear slightly beyond 2 kpc along the bar major axis, where the young stars are reaching the apocentre of their elongated orbits and the old population has comparable or larger velocities.

Taken as a whole, these differences in the intrinsic kinematics are as expected for the two populations, one strongly tracing the bar (the young one) and one that traces it weakly (the old one). From the Solar perspective, the proper motion rotation curves are then a position-dependent combination of these two motions. The differences between the velocity distributions can be understood largely in terms of the different bar strengths, which themselves are a result of the different random motions of stars at the time of the bar's formation (Debattista et al. 2017).

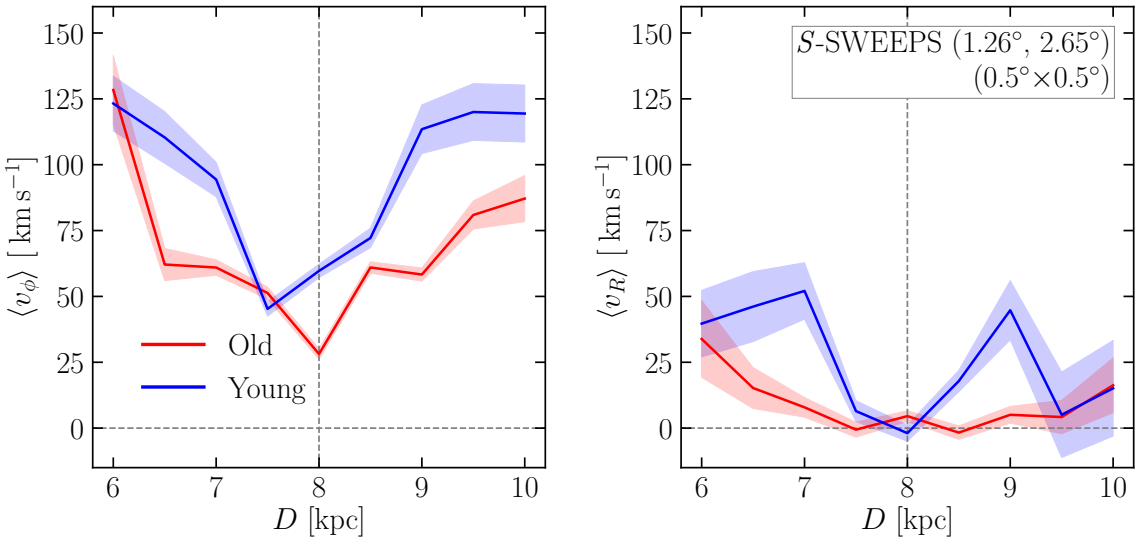

Figure 3.6: LOS profiles of galactocentric $\langle v_\phi \rangle$ (left-hand panel) and $\langle v_R \rangle$ (right-hand panel) for the *S*-SWEEPS field in the model.

3.4 Interpretation of the SWEEPS Field

We now explore the simulated *S*-SWEEPS field (Fig. 3.3) in greater detail. Using Eqn. 3.2 we calculate the separation amplitude of the *S*-SWEEPS field to be $\xi = 0.05 \pm 0.48\,\mathrm{kpc \cdot mas\,yr^{-1}}$, commensurate with the regions surrounding this LOS in Fig. 3.4. We use the insight derived from Fig. 3.5 to interpret this value in terms of the intrinsic velocities and the resulting rotation curves. Furthermore, we directly compare our model with MW data to test the level of confidence of our model as an approximation of the MW.

For the *S*-SWEEPS LOS, Fig. 3.6 shows the distance profiles of galactocentric tangential $\langle v_\phi \rangle$ and galactocentric radial $\langle v_R \rangle$ velocities using the same distance bins as the rotation curves. Both populations have their lowest $\langle v_\phi \rangle$ close to 8 kpc, increasing away from the centre. At almost every distance bin, the young population has the higher $\langle v_\phi \rangle$. In Fig. 3.5, we showed that the young population has a stronger bar and kinematics consistent with elongated bar orbits; the peaks of $\langle v_R \rangle$ seen in the right-hand panel of Fig. 3.6 support this, and indicate stars moving away

from the galactic centre. The old population has low values of $\langle v_R \rangle$ along the LOS, which reflects their more axisymmetric distribution. These profiles show that the differences in rotation curves between the young and old populations are a consequence of differences in both $\langle v_\phi \rangle$ and $\langle v_R \rangle$ because only the young population is strongly barred.

3.4.1 Monte Carlo Simulation of MW Data

To compare the separation amplitude of the *S*-SWEEPS field with observational data, we apply our methodology to the SWEEPS+BTS data presented in C18. We note here that the populations within the model represent the ends of the age distribution (see the coloured regions in Fig. 3.1), whereas C18 split the photometric metallicity distribution within their data using auto-GMM clustering. The estimated mean metallicities of the 'metal-rich' and 'metal-poor' samples are $[\mathrm{Fe/H}]_0 \approx -0.24$ and $[\mathrm{Fe/H}]_0 \approx +0.18$, respectively (see section 3.5 of C18). As a consequence of their methodology and the nature of separating by metallicity, the age distributions of their sub-samples may partially overlap.

We use the C18 data, which the authors used to produce their Fig. 8, showing that metal-rich stars have higher amplitude $\langle \mu_l \rangle$ rotation curves than metal-poor stars. For their metal-rich and metal-poor populations, we bin the data in distance following the prescriptions in Section 3.3 and calculate the separation amplitude using the same method as we used for the model.

To determine the effect of observational uncertainties on the calculated values and the robustness of the uncertainty estimates (e_ξ), we run a Monte Carlo (MC) simulation of our separation amplitude measurement. We assume that the uncertainty of the observed longitudinal proper motion to be $\sigma_{\mu_l} = 0.08\,\mathrm{mas\,yr^{-1}}$ (Fig. 17 of C18). The photometric parallax used in the distance determination has an estimated uncertainty of 0.119 and 0.153 mag for the metal-rich and metal-poor

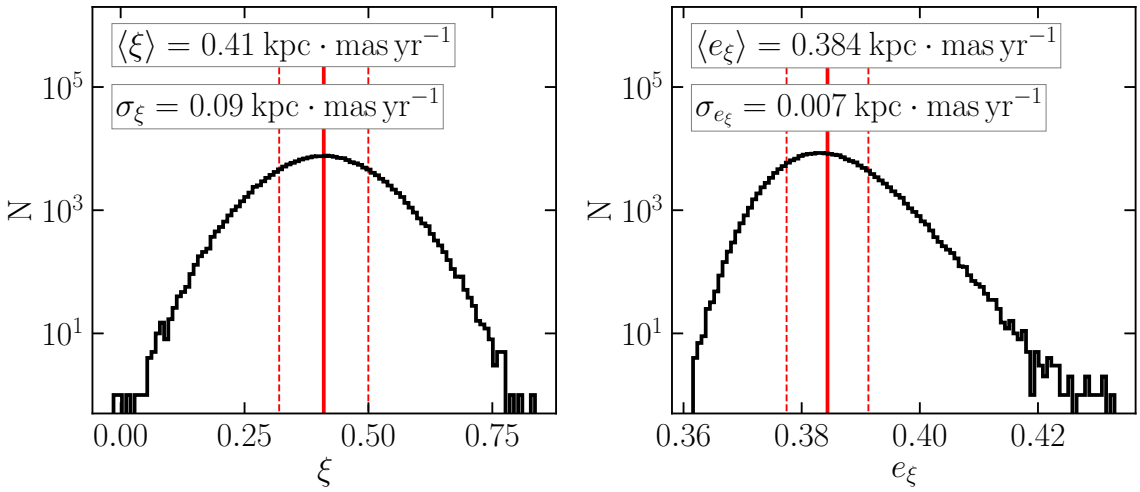

Figure 3.7: Results of the Monte Carlo runs to calculate the separation amplitude for the SWEEPS+BTS data from C18. Thick red lines show the mean ξ and e_ξ values. Red dashed lines denote 1σ deviation. At this field, the fiducial model predicts $\xi = 0.05 \pm 0.48$ kpc · mas yr^{-1}.

sample, respectively (Table 11 of C18). For each run of the MC, we add random errors to the magnitudes and proper motions of each star in the SWEEPS+BTS sample, assuming the error distributions are Gaussian. We then recalculate ξ and e_ξ for each run. Our MC of 200 000 runs produces the distributions of ξ and e_ξ shown in Fig. 3.7. The mean separation amplitudes and errors from the MC runs are $\langle\xi\rangle = 0.41$ kpc · mas yr^{-1} and $\langle e_\xi\rangle = 0.384$ kpc · mas yr^{-1}. The value of $\langle e_\xi\rangle$ is relatively large as in the model, however it is well constrained with a standard deviation of $\sigma_{e_\xi} = 0.007$ kpc · mas yr^{-1}. The definition of e_ξ from Eqn. 3.3 corresponds to the sum in quadrature of the uncertainties for each distance bin, where the uncertainty in each bin is given by the proper motion dispersion and the number of stars in the bin. Since the number of stars within the whole distance range ($5.75 - 10.25$ kpc) does not change substantially between MC iterations, and the μ_l uncertainty is low overall, this leads to $\langle e_\xi\rangle$ being well constrained, with a small standard deviation.

Comparing the ξ values of the observational data to our model, we can see that

they agree within the uncertainty. Although this is a comparison for a single field on the minor axis, it demonstrates that our metrics can applied to observational data and the model provides a reasonable basis for comparing to the MW. For the SWEEPS+BTS field, the profile is antisymmetric resulting in a low value of ξ. Our model has a value of ξ closer to zero and a larger associated error than the MW data. We stress, however, that there are many differences between the observational and simulated measurements so we limit our comparisons to qualitative trends.

3.4.2 Other Fields

We now expand our analysis to fields for which data are available from *HST*-BTS observations. The three remaining BTS fields that can be used for a study similar to that of C18 are *Stanek's Window*, *Baade's Window* and the OGLE29 field (Brown et al. 2010; Renzini et al. 2018). We explore comparable fields within our model, which we refer to as *S-Stanek's Window*, *S-Baade's Window* and the *S*-OGLE29 field. We also suggest three further regions of interest, which sample areas of negative ξ away from the minor axis and large latitude; we refer to these as Field A, Field B and Field C. We increase the field size in regions of larger statistical uncertainty, allowing us to sample sufficient number of star particles to provide reasonable predictions. The on-sky positions and sizes of each region of interest are shown in the top panel of Fig. 3.8. For each field, we produce $\langle \mu_l \rangle$ rotation curves, following the same method as above. The results are presented in the bottom panels of Fig. 3.8.

The two BTS fields close to the *S*-SWEEPS field, *S-Stanek's Window* and *S-Baade's Window*, only a few degrees apart, have similar ξ values, with anti-symmetric profiles, as in the *S*-SWEEPS field. Both *S-Stanek's Window* and *S-Baade's Window* have $\langle \mu_l \rangle$ profiles with increasing amplitude away from the galactic centre, and have similar peak young/old, and a near/far ratio of ~ 2.

The *S*-OGLE29 field is at the highest latitude of the BTS fields and is further

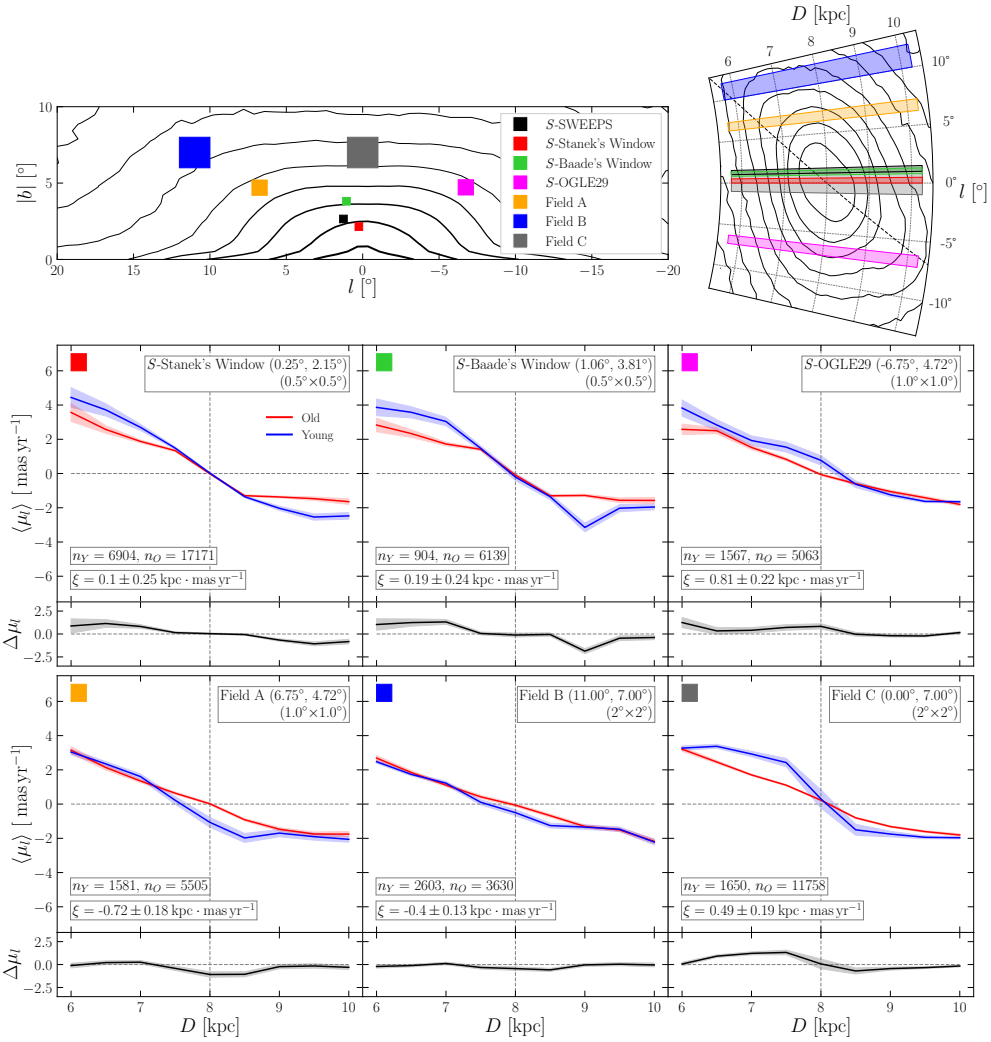

Figure 3.8: Top left-hand panel: the positions of the six fields of interest within the model's bulge from the heliocentric perspective. The coloured squares correspond to the sizes used in our simulated fields to capture enough star particles. Black contours follow the log density of all bulge stars. Top right-hand panel: the six fields of interest presented in a top-down view of the model's bulge. The bar major axis is indicated by the dashed line. Black contours follow the log density of all bulge stars. Bottom panel: average longitudinal proper motion rotation curves and the separation for the fields of interest. The field names and FOV are labelled at the top right-hand side. The number of star particles in both populations is also listed along with the calculated separation amplitude, ξ.

away from the minor axis in a region where $\xi > 0$. This field has a different separation profile: while the rotation curve of the old population remains similar to those previously described, the rotation curve of the young stars crosses the $\langle \mu_l \rangle = 0$ line beyond 8 kpc. The minimum separation between the young and old population occurs in the furthest distance bins. We can understand this behaviour by referring back to the top row Fig. 3.5. Along longitude $l \approx -7^\circ$ the nearest distance bins pass through the region where young stars have high positive $\langle \mu_l \rangle$ values, where they are streaming at high velocity along the bar edge. The direction of the velocity here is closer to perpendicular to the LOS, which results in the higher $\langle \mu_l \rangle$ peak. At the furthest distance bins, we are observing the far end of the bar. The direction of the velocities here are angled more closely parallel to the LOS; therefore, younger stars have a lower $\langle \mu_l \rangle$ amplitude, comparable to the value for old stars in the same region. This results in a ξ value larger than the other three BTS fields.

We define Field A to explore the asymmetry in ξ. Its location is mirrored across the minor axis from the *S*-OGLE29 field, at the same latitude and with the same FOV, within a region where $\xi < 0$. Again the old stars have a rotation curve of increasing $\langle \mu_l \rangle$ from the galactic centre. The young stars in this field show little separation in the nearest and furthest distance bins. However, at 7.5 kpc, the young population's rotation curve crosses the $\langle \mu_l \rangle = 0$ line and decreases to negative $\langle \mu_l \rangle$ more steeply than the older stars, and converges to that of the older population beyond 9 kpc. At this longitude, the nearest distance bins are within the central bar region, but beyond ~ 8 kpc the LOS passes through the far edge of the bar, where stars are streaming towards negative longitude. Both the *S*-OGLE29 field and Field A demonstrate the effect of observing the proper motions of an angled bar, which we explore further in Section 3.5.

Field B also explores an area where $\xi < 0$ but at larger latitude and longitude. At these higher latitudes, e_ξ is larger due to the limited vertical extent of the young

population, requiring us to increase the field size considerably. A largely linear profile is seen in both young and old population rotation curves. However, between 8 and 9 kpc the young population deviates to more negative $\langle \mu_l \rangle$, similar to Field A. We attribute this deviation to the same effect discussed for Field A, but the separation is smaller here due to being located further away from the minor axis and at higher latitude.

Field C covers a region of high latitude on the minor axis. We see an antisymmetric profile similar to the *S*-SWEEPS field; however the young stars have a flatter profile away from the galactic centre. The young stars still have a higher amplitude $\langle \mu_l \rangle$ with a steeper gradient through the galactic centre. The central bins have very few young stars, since the young population is peanut shaped. The ξ value is much larger here due to the effect of perspective.

3.5 Projection of Intrinsic Velocities

The rotation curves of the *S*-OGLE29 field and Field A demonstrate the clear effect of a non-axisymmetric structure within the bulge region. To illustrate how the galactocentric radial and tangential velocities project onto the observed longitudinal proper motions we now project each galactocentric velocity component individually onto $\hat{l}$, the unit vector in the direction of increasing longitude, *i.e.* the tangential direction to the LOS from the Sun. Lines parallel to $\hat{l}$ follow concentric circles centred on the Sun. As these velocity projections are position dependent, not all regions of high-amplitude galactocentric velocity contribute to large proper motions.

We present the projections onto $\hat{l}$ in the (X, Y) plane in Fig. 3.9. We denote the v_R and v_ϕ projections, respectively, as

$$\mu_{l,R} = \alpha \frac{v_R}{D} \frac{\sin(\phi - l)}{\cos b}, \tag{3.4}$$

$$\mu_{l,\phi} = \alpha \frac{v_\phi}{D} \frac{\cos(\phi - l)}{\cos b}, \tag{3.5}$$

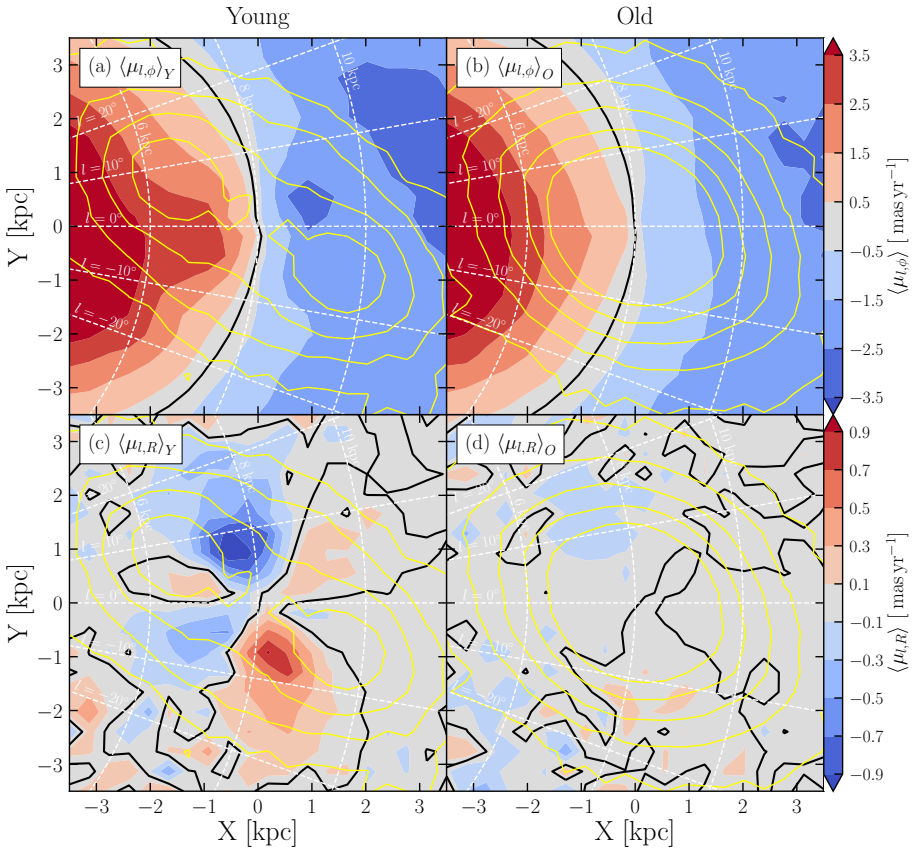

Figure 3.9: Projections of the galactocentric intrinsic velocities onto μ_l in the (X, Y) plane for star particles at $0.5 < |z|/\,\mathrm{kpc} < 1.0$. The left-hand column column presents the kinematics of the young population while the right-hand column shows those of the old. The top row shows the projection of galactocentric $\langle v_\phi \rangle$ onto longitudinal proper motions, the bottom row shows the projection of galactocentric radial velocities $\langle v_R \rangle$ onto longitudinal proper motions. Yellow contours follow log densities of the corresponding population. Black contours indicate where each velocity component equals zero. White circular dashed lines outline distances 6 kpc, 8 kpc and 10 kpc, while the white straight dashed lines mark longitudes between 20° and −20° in 10° intervals. The observer is at $X = -8$ kpc in this figure.

where $\alpha \approx 0.210\,\mathrm{kpc\,s\,km^{-1}}$ and ϕ is a star's cylindrical polar angle in the galactocentric frame.

Unsurprisingly, $\langle v_\phi \rangle$ contributes to $\langle \mu_l \rangle$ of both the young and old populations as seen in Panels (a) and (b) of Fig. 3.9. In an axisymmetric disc, this would be the only contribution to $\langle \mu_l \rangle$ because then $\langle v_R \rangle = 0$. The $\langle v_\phi \rangle$ contribution to the old population's proper motions, shown in Fig. 3.9(b), has a distribution not much different from that of an axisymmetric disc. Conversely, the young population has stronger rotation closer to the galactic centre, with pronounced twists in the $\langle \mu_{l,\phi} \rangle$ contours. The regions of low $\langle v_\phi \rangle$ manifest in the young stars' $\langle \mu_{l,\phi} \rangle$ distribution as deviations of the velocity contours from being parallel to $\hat{l}$. In an axisymmetric system, the general trend of increasing velocity dispersion of stellar populations with age would give rise to a separation of the rotation curves purely from $\langle v_\phi \rangle$, with no contribution from $\langle v_R \rangle$. However, a stationary axisymmetric system cannot produce a non-zero $\langle \mu_{l,R} \rangle$. Instead, a bar produces a quadrupolar $\langle v_R \rangle$ distribution, and hence peaks in $\langle \mu_{l,R} \rangle$ as seen in the bottom left-hand panel of Fig. 3.9. Moreover, the orientation of the MW's bar is such that two of the regions of large $\langle v_R \rangle$ project almost perfectly into the $\hat{l}$ direction, at positive longitude on the near side and at negative longitude on the far side of the galactic centre. In these regions, the observed longitudinal proper motion has a strong contribution from $\langle v_R \rangle$. The other two high amplitude $\langle v_R \rangle$ regions lie at $|l| \lesssim 2^\circ$ and therefore $\langle v_R \rangle$ in these regions projects only a small component in the $\hat{l}$ direction. Comparing Panels (a) and (c) of Fig. 3.9, it is evident that the main peaks in $\langle \mu_{l,R} \rangle$ contribute to the total $\langle \mu_l \rangle$ with opposite sign to the $\langle \mu_{l,\phi} \rangle$ for the young population. For example, the peak of negative $\langle v_R \rangle_Y$ centred near $(X, Y) = (-0.5, 0.5)\,\mathrm{kpc}$ in Panel (c) is within a region of positive $\langle v_\phi \rangle_Y$ in Panel (a). The old population has everywhere relatively low $\langle v_R \rangle$; therefore, its longitudinal proper motion is everywhere dominated by $\langle v_\phi \rangle$. The young population, having a strong bar, has a strong quadrupolar $\langle v_R \rangle$. Consequently,

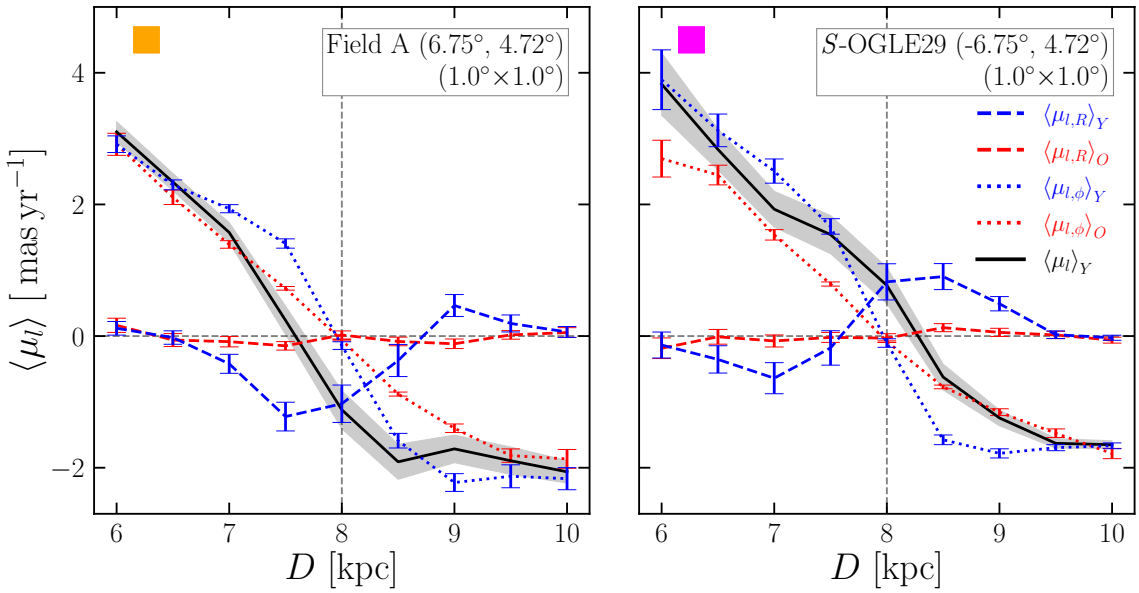

Figure 3.10: The contributions of galactocentric $\langle v_R \rangle$ (dashed lines) and $\langle v_\phi \rangle$ (dotted lines) to the average longitudinal proper motion rotation curves for young (blue lines) and old stars (red lines) for the simulated Field A (left-hand panel) and the OGLE29 field (right-hand panel). We plot the sum of the two young components, the total observed $\langle \mu_l \rangle_Y$ as a black line. The old population has no substantial $\langle v_R \rangle$ contribution therefore the $\langle \mu_l \rangle_O$ line would lie on top of the $\langle \mu_{l,\phi} \rangle_O$ line; we thus do not display it. The coloured squares correspond to the field locations indicated in Fig. 3.8.

the effect of the bar will be most evident in the kinematics of the young population in the regions where $|\langle v_R \rangle|$ peaks.

The competing effects of the $\langle v_R \rangle$ and $\langle v_\phi \rangle$ contributions to the $\langle \mu_l \rangle$ rotation curves give rise to interesting behaviours. We now demonstrate how these two components project onto the rotation curves of the *S*-OGLE29 field and Field A. In the left-hand panel of Fig. 3.10 we can see that the $\langle \mu_{l,\phi} \rangle$ component of both populations in Field A follow an antisymmetric profile. However, for the young stars, $\langle \mu_{l,R} \rangle_Y$ provides a substantial negative contribution slightly short of 8 kpc. This contribution acts in opposition to the positive contribution from $\langle \mu_{l,\phi} \rangle$; as

a result, the total $\langle \mu_l \rangle_Y$ for Field A (black line) crosses $\langle \mu_l \rangle = 0$ at $\sim 7.5\,\mathrm{kpc}$. Therefore, the radial contribution leads to a sign reversal in the proper motions of young stars and a rotation curve with 'forbidden' velocities. We term non-zero velocities at the galactic centre as forbidden because they would not be present in an axisymmetric system. Our usage echos the use of the term for describing gas kinematics at the Galactic Centre (*e.g.* Weiner & Sellwood 1999)

The young stars in the *S*-OGLE29 field also have a rotation curve with forbidden velocities but with a sign reversal from negative to positive. The radial contribution comes somewhat beyond the galactic centre, where the $\langle v_\phi \rangle$ component is negative, and the $\langle v_R \rangle$ velocities are positive. The total $\langle \mu_l \rangle_Y$ rotation curve crosses $\langle \mu_l \rangle = 0$ at $\sim 8.25\,\mathrm{kpc}$.

The young stars in both of these fields reverse the sign of their proper motions due to the contribution of the radial velocity. The age dependence of bar strength and their resulting velocity profiles demonstrated above are a prediction of kinematic fractionation, where younger populations with lower initial in-plane random motions are less vertically heated, form a stronger bar and a more peanut-shaped bulge (Debattista et al. 2017).

3.5.1 Quantifying the Effect of Kinematic Fractionation

We now develop a second metric to quantify the signature of kinematic fractionation within the bulge which is less reliant on deep observations with highly accurate distance determinations. We define a large spatial bin located at $D = 8\,\mathrm{kpc}$ with a width of 1 kpc, allowing for larger distance uncertainties, then calculate the difference in $\langle \mu_l \rangle$ between the young and old populations, *i.e.*

$$\delta\mu_l = \langle \mu_l \rangle_{Y,8\,\mathrm{kpc}} - \langle \mu_l \rangle_{O,8\,\mathrm{kpc}}. \tag{3.6}$$

Large positive values of $\delta\mu_l$ correspond to rotation curves where the young population have larger positive $\langle \mu_l \rangle$ than the old population within this central bin, which

are forbidden velocities at negative longitude. We use $\delta\mu_l$ to measure forbidden velocities in the bulge whilst also taking into account the expected observational distance uncertainties. Following from our previous analysis, we expect to measure positive $\delta\mu_l$ values in the direction of the OGLE29 field and negative values in the direction of Field A. We assume every star in the model is an RC star with absolute magnitude $M_K = -1.61$, and calculate their apparent magnitudes as we did in Section 3.2.1 to more closely approximate observations. We assume extinction to be uniform across the bulge region for simplicity. Reproducing this work observationally would rely on extinction corrections being made for the tracer populations used. We then define the magnitude range equivalent to 8 ± 0.5 kpc, which is $12.75 - 13.05$ mag, a bin width of 0.3 mag. We present $\delta\mu_l$ in the $(l, |b|)$ plane in Fig. 3.11, under three different assumptions for the distance uncertainty, $\sigma_{\rm mag}$: no uncertainty, SWEEPS field uncertainties and RC uncertainties. For the SWEEPS uncertainties, we assume the metal-rich and metal-poor magnitude uncertainties from C18 apply to our young and old populations respectively, $\sigma_{\rm mag,Y} = 0.119$ and $\sigma_{\rm mag,O} = 0.153$. For the RC uncertainties, we apply the width of the RC distribution, as in Section 3.2.1, $\sigma_{\rm mag,RC} = 0.17$ to both populations. To estimate the uncertainty in $\delta\mu_l$, we add in quadrature the $\langle\mu_l\rangle$ uncertainty for the young and old populations.

In the top panel of Fig. 3.11, we present $\delta\mu_l$ across the bulge assuming no magnitude uncertainties. The distribution of $\delta\mu_l$ has a left/right asymmetry with negative values for fields $l > 0^\circ$ and positive values at $l < 0^\circ$. The peaks in the amplitude of $\delta\mu_l$ occur around $(|l|, |b|) = (6^\circ, 5^\circ)$. Along the minor, axis we expect $\delta\mu_l \sim 0$ as there is only a small contribution from galactocentric radial velocities in this region. Away from the minor axis, close to the locations of the OGLE29 field and Field A, we find large values $|\delta\mu_l|$. Regions with $\delta\mu_l > 0$ are present near the OGLE29 field at negative longitude, while regions of $\delta\mu_l < 0$ surround a large area around Field

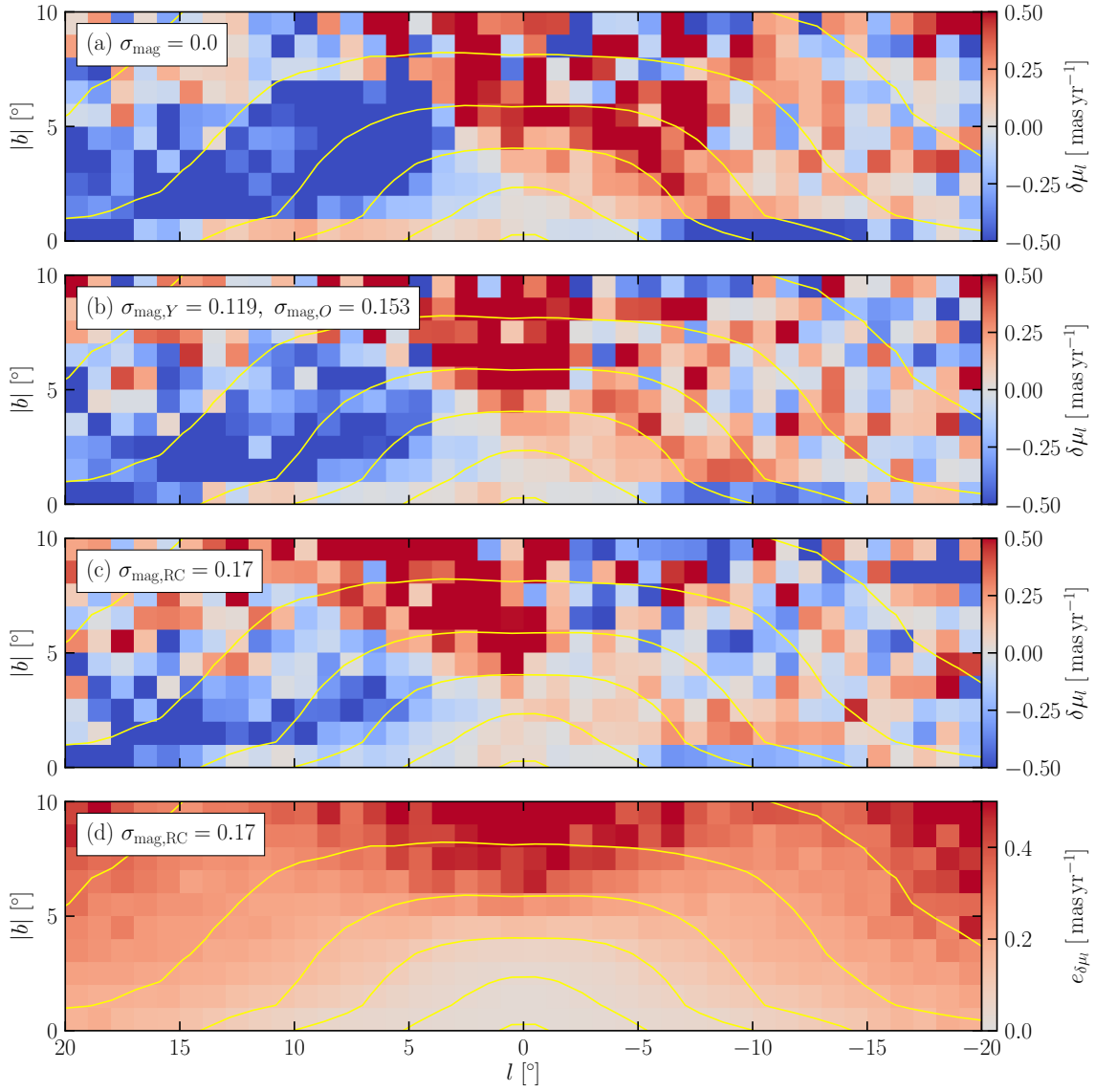

Figure 3.11: Top panel: the $\delta\mu_l$ distribution in the bulge region defined as the difference in $\langle\mu_l\rangle$ between the young and old populations at ~ 8 kpc. Middle top panel: the same as above but with young and old stars apparent magnitudes convolved with C18 uncertainties of $\sigma_{\rm mag,Y} = 0.119$ and $\sigma_{\rm mag,O} = 0.153$. Middle bottom panel: the same as above but with both populations convolved with the width of the RC, $\sigma_{\rm mag,RC} = 0.17$. Bottom panel: the calculated error for each field when applying the RC magnitude uncertainties.

A, at positive longitude. Regions of positive $\delta\mu_l$ at high latitude on the minor axis are due to the bin centre being at a cylindrical radius closer than the galactic centre at this latitude, worsened by large bin width used.

With increasing distance uncertainties, as in the two middle panels of Fig. 3.11, the peaks near $(|l|, |b|) = (6^\circ, 5^\circ)$ become weaker, with smaller $\delta\mu_l$ values in general. The overall distributions still retain a left/right asymmetry but with more fields having small $\delta\mu_l$ indistinguishable from $\delta\mu_l = 0$. In all panels, the negative $\delta\mu_l$ region is larger and has higher amplitude than the positive one, due to the bar's orientation. In the direction of the OGLE29 field and Field A typical values of $|\delta\mu_l| > 0.5\,\mathrm{mas\,yr^{-1}}$ at 8 kpc correspond to $\approx 20\,\mathrm{km\,s^{-1}}$ difference in heliocentric tangential velocities.

We present the $e_{\delta\mu_l}$ map for the RC magnitude uncertainties in the bottom panel of Fig. 3.11. The variation in $e_{\delta\mu_l}$ between the three levels of magnitude uncertainties is minimal and retains the general trends. Similar to e_ξ, the $e_{\delta\mu_l}$ distribution is peanut shaped with the region of the largest uncertainty at high latitude on the minor axis, again because of the lower number of young stars there.

The map of $\delta\mu_l$ is in good agreement with the map of ξ, in as much as large separations in velocities are observed in regions away from the minor axis. We have demonstrated here that large amplitude values of $\delta\mu_l$ are a result of rotation curves with forbidden velocities (see Fig. 3.10), which are the result of radial velocity contributions from bar supporting orbits.

3.6 Comparison With a Weaker B/P Model

We briefly explore a second model (hereafter Model 2) which forms a bar later in its evolution; the bar is weaker and produces a weaker B/P bulge than the fiducial model. The initial conditions from Section 3.2 remain the same; however, Model 2 has different subgrid physics and forms a bar of length ~ 2.5 kpc between $4 - 6$ Gyr

(versus ~ 3 kpc, forming at $2-4$ Gyr). To directly compare with the fiducial model, we scale and align Model 2 following the same procedures outlined in Section 3.2.1 but with a spatial scaling factor of 2 instead of 1.7. Owing to the stochasticity inherent in bar evolution (Sellwood & Debattista 2009), the two bars do not evolve in the same way. The bar length at 10 Gyr in Model 2 after scaling is $r_{bar} = 4.80 \pm 0.90$ kpc, and the double RC appears only weakly at $|b| = 6^\circ$ as a result of its more limited B/P growth compared to the fiducial model. We plot the radial profiles of the $m = 2$ Fourier moment amplitude and phase along with the evolution of the global bar amplitude for both models in Appendix A. The cumulative distribution of ages within Model 2's bulge reveals that it has a lower star formation rate at the beginning of the simulation; our cut of old stars at age > 9 Gyr therefore represents a smaller fraction of the bulge population. The selection of young stars (age < 7 Gyr) samples a higher fraction of stars born before and during the formation of the bar (85%), which lowers the overall bar strength of this population.

We measure our metrics of kinematic separation, ξ and $\delta\mu_l$, across the bulge of Model 2, which we present in Appendix A. Our measurements show the same global trends as in the fiducial model. The map of ξ is asymmetric about the minor axis with $\xi < 0$ at positive longitudes and $\xi > 0$ at negative longitudes. The amplitudes of ξ are lower than in the fiducial model with a steeper decreasing gradient with increasing latitude. Model 2 has similar values of the uncertainty, e_ξ, however, its distribution is less peanut shaped. The map of $\delta\mu_l$ also matches the general trends of the fiducial model's with a left-right asymmetry, $\delta\mu_l < 0$ at positive longitude and $\delta\mu_l > 0$ at negative longitude but also has generally lower amplitude values. The $e_{\delta\mu_l}$ distribution is also more box shaped.

We present a comparison of each model's rotation curves for the simulated *S*-SWEEPS and *S*-OGLE29 fields along with Field A and Field C in Fig. 3.12, where now we have used magnitude bins of 0.3 mag. instead of distance. We use the

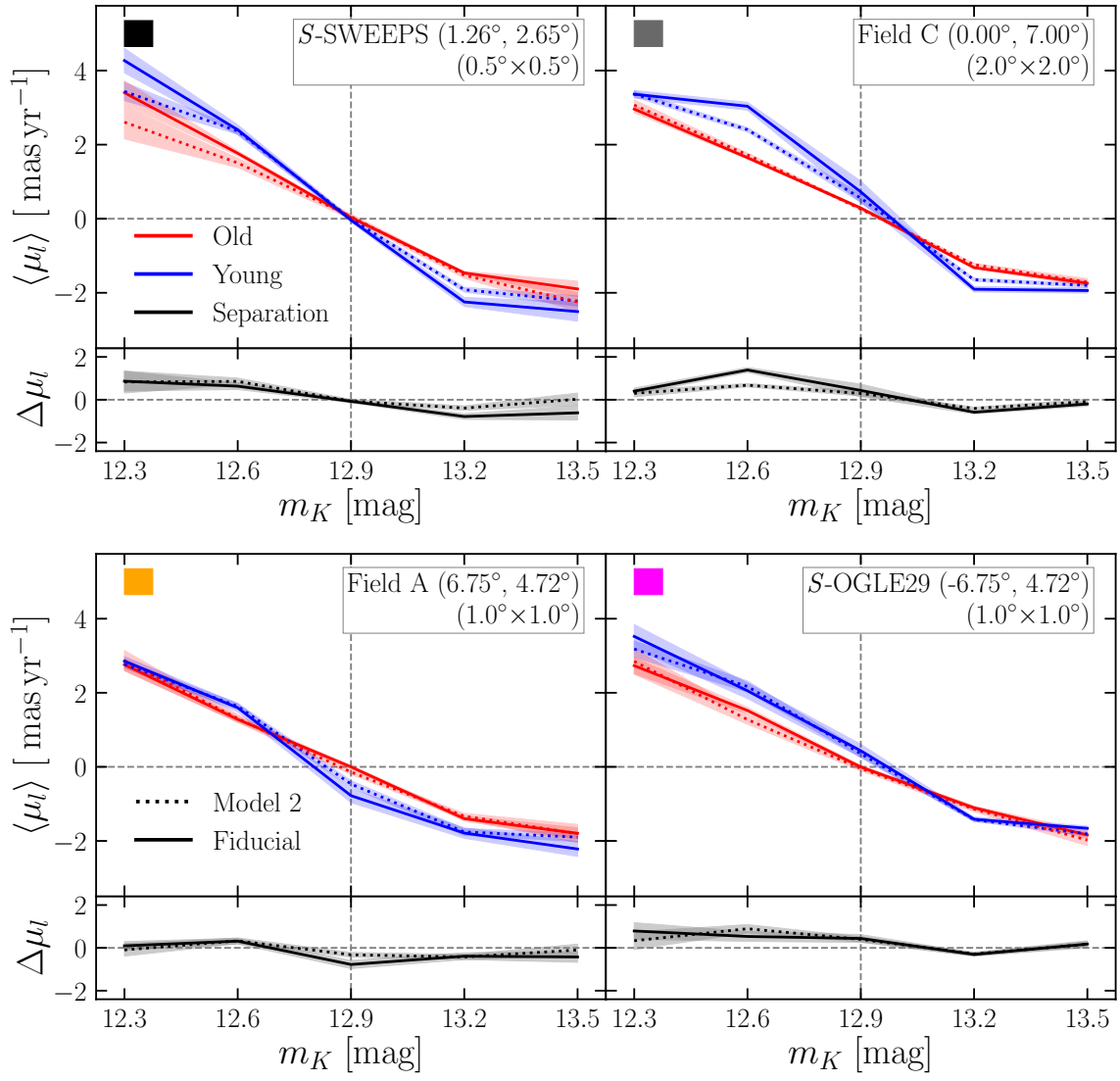

Figure 3.12: Average longitudinal proper motion rotation curve for young and old stars, and the separation between them using magnitude bins for four key fields in the bulge. The rotation curves and separation from the fiducial model are plotted as dotted lines whereas Model 2 is plotted as solid lines. The field name, location, and FOV are labelled in the top right-hand of each panel. The coloured squares correspond to the field locations indicated in Fig. 3.8.

Field	Model	ξ	e_ξ	$\delta\mu_l$	$e_{\delta\mu_l}$
S-SWEEPS	Fiducial	0.005	0.091	-0.073	0.068
S-SWEEPS	Model 2	0.188	0.093	-0.065	0.084
Field C	Fiducial	0.217	0.055	0.435	0.293
Field C	Model 2	0.117	0.037	0.295	0.118
Field A	Fiducial	-0.177	0.064	-0.776	0.192
Field A	Model 2	-0.092	0.068	-0.322	0.111
S-OGLE29	Fiducial	0.245	0.076	0.439	0.183
S-OGLE29	Model 2	0.226	0.076	0.398	0.117

Table 3.1: Calculated values of ξ and e_ξ (with units of $\mathrm{kpc}\cdot\mathrm{mas\,yr^{-1}}$), $\delta\mu_l$, and $e_{\delta\mu_l}$ (with units of $\mathrm{mas\,yr^{-1}}$) for the simulated *S*-SWEEPS, *S*-OGLE29, Field A, and Field C in the fiducial model and Model 2.

magnitude range equivalent to span $5.75 - 10.25$ kpc to present predictions of ξ and $\delta\mu_l$ simultaneously for these key fields (*i.e.* $\delta\mu_l$ is the $\langle\mu_l\rangle$ difference in the central bin at 12.9 mag.). This also allows us to test our metrics using a methodology closer to MW observations. ξ and $\delta\mu_l$ for these fields are shown in Table 3.1.

Although now binning in magnitude, the rotation curve profiles in both models qualitatively match those presented in Fig. 3.8. Here, we discuss only the differences between the two models.

In the *S*-SWEEPS fields, the amplitudes of $\langle\mu_l\rangle$ are lower for both the young and old populations in Model 2 than the fiducial model. However, considering the separation profile, Model 2 has similar separation on the near side but has weaker separation beyond the galactic centre resulting in a larger ξ value. As expected for a central longitude, the *S*-SWEEPS field has very low $\delta\mu_l$ in both models.

Field C in Model 2 also has lower $\langle\mu_l\rangle$ amplitudes. The old population rotation curves in the two models overlap each other. However, there is a large difference between the rotation curves of the young populations in the two models: in the

fiducial model, the rotation curve is steeper at the galactic centre. Model 2 also has lower separation in the nearest bins resulting in a lower ξ. Field C is at a large latitude on the minor axis and as a result there is a small perspective effect contributing to $\delta\mu_l$. At this latitude, the central (8 kpc) bin is located in front of the galactic centre by ~ 0.16 kpc, which results in both populations crossing the $\langle\mu_l\rangle = 0$ line beyond the central bin, and thus a positive $\delta\mu_l$ results. This effect is also seen in the bottom right-hand panel of Fig. 3.8.

Field A in both models has similar rotation curves with the main difference being in the degree of deviation into forbidden velocities. Model 2 has lower separation at the central bin resulting in lower ξ and $\delta\mu_l$ values. The two models differ very little in the *S*-OGLE29 field, with a slightly larger $\delta\mu_l$ in the fiducial model.

The combined effects of later bar formation and the weaker bar and B/P in Model 2 result in longitudinal proper motion rotation curves that are qualitatively similar in profile but have lower separations and forbidden velocities as measured by both the ξ and the $\delta\mu_l$ metrics. Thus, the separation amplitudes and the global trends of ξ and $\delta\mu_l$ provide important information on the relative bar strength of each population and may be useful in constraining the MW's bar and bulge.

3.7 Discussion

Kinematic differences between different populations in the MW's bulge have been explored in many studies. Metallicity is most often used to separate bulge stellar populations. Metal-rich bulge stars typically have higher radial velocity dispersion than metal-poor stars (Rich 1990; Sharples et al. 1990; Minniti 1996) and the metal-poor population has a shallower velocity dispersion gradient with latitude (Ness et al. 2013a,b, 2016b; Zoccali et al. 2017). Observations at Baade's Window have shown that metal-rich stars have non-zero vertex deviation, whereas that of the metal-poor stars is nearly zero (Soto et al. 2007; Babusiaux et al. 2010; Hill et al.

2011; Vásquez et al. 2013). Even amongst the (old) RR Lyrae (RRL), metallicity separates different populations. Du et al. (2020b) and Kunder et al. (2020) found that metal-rich RRL trace a (weak) bar and have angular velocities slightly larger than metal-poor RRL, which do not trace any bar. Populations can also be separated by their α-abundance. Queiroz et al. (2021) explored the chemo-dynamics of the bulge using APOGEE and *Gaia* data. They found two distinct components when considering the v_ϕ vs Galactocentric radius distribution. One component is a low-α population with high rotational velocities and the other has high-α concentrated at small radii and with near-zero or negative v_ϕ. However, the single chemical track of the bulge implies that separating populations by the $\alpha-$abundance is similar to separating by metallicity.

In summary, these observational results point to stronger barred streaming motions in metal-rich stars, which is borne out by models and simulations (Portail et al. 2017; Debattista et al. 2020). However, the origin of each component within the bulge is still a matter of debate. Whilst it is possible for (part of) the metal-poor component to be a classical bulge formed through mergers, most of it may also have formed *in situ*. Indeed, using the same fiducial model as here, Debattista et al. (2017) showed that the velocity dispersions of stars separated by age qualitatively match the above trends in the ARGOS data provided a halo-like population was added to the very oldest, most metal-poor stars. Observationally stars with metallicity [Fe/H] < -1 represent only $\sim 5\%$ of all bulge stars (Ness & Freeman 2016), with no more than 1/3 of stars with metallicity [Fe/H] ≤ -0.8 potentially being an accreted population (Horta et al. 2021). Recent studies of zoom-in simulations of MW-like galaxies by Fragkoudi et al. (2020) suggest that the bulge contains a negligible fraction of accreted stars (see also Buck et al. 2019). Isolated simulations also showed that such a component could not be larger than $\sim 8\%$ of the disc mass (Shen et al. 2010).

CHAPTER 3

An efficient way to probe the kinematics of bulge stellar populations as a function of distance was presented by C18 for a sample of just under ten thousand main-sequence stars in a deep *HST* field combining SWEEPS and BTS data. Separating these by relative photometric metallicity, C18 produced longitudinal proper motion rotation curves of 'metal-rich' and 'metal-poor' samples. They found that metal-rich stars have larger amplitude longitudinal proper motions. In this paper, we have simulated the SWEEPS+BTS field (*S*-SWEEPS) using an isolated, star-forming model scaled to approximate the MW. Our young and old populations match the trends of the MW metal-rich and metal-poor main-sequence stars in as much as the young (metal-rich) stars having a larger amplitude $\langle \mu_l \rangle$ along the LOS than the old (metal-poor) ones. The amplitude between the young and old populations differs by roughly a factor of 2, in good agreement with the observations of C18. Thus we conclude that the trends in the rotation curves of the bulge can be reproduced without the need for an accreted population.

To help prepare for future studies, we have quantified the difference between the rotation curves of the two populations by defining a separation amplitude, ξ, as the sum of the difference between averages of longitudinal proper motion in distance bins along an LOS. We have demonstrated, using Monte Carlo resampling to account for distance and velocity uncertainties, that ξ is similar between our model and the SWEEPS+BTS C18 data, despite the differences in sample selection between the model and observations. We have measured ξ across the entire bulge region covering $|l| \leq 20°$, $2° \leq |b| \leq 10°$, and $5.75 \leq D/\,\mathrm{kpc} \leq 10.25$. Both the distribution of ξ within the bulge and the rotation curves of key fields indicate that the rotation curve profiles change with longitude and latitude. We interpret these variations as differences in the intrinsic velocity distributions of the two populations.

The galactocentric cylindrical velocities of (relatively) young stars match the expected signature of stars on strongly barred orbits; in contrast, the old stars trace

a weaker bar. Here we have selected stars based on their age. While not a perfect match for metallicity, our results suggest that the bar should be more metal-rich than the rest of the bulge population. The different velocity profiles reflect the underlying density distributions and relative bar strengths of the populations. Recent studies have indeed shown that the bar is more metal-rich than the off-bar regions (Wegg et al. 2019; Queiroz et al. 2021) (but see Bovy et al. 2019, for a different view).

We have studied how the intrinsic velocities of stars on bar orbits project onto longitudinal proper motions by considering the radial as well as tangential velocity components separately in both galactocentric and heliocentric coordinates. We find, in the young population, regions of high galactocentric radial velocities in the (X, Y) plane as a quadrupole rotated by $\sim 45°$ relative to the bar axes. With the MW bar inclination angle of $\sim 27°$, two of these regions project onto longitudinal proper motions at lines of sight away from the minor axis ($|l| \approx 6°$). Fields which intersect these regions have rotation curve profiles quite different to those of the SWEEPS field and other fields on the minor axis. The galactocentric radial velocity contribution is in the opposite direction to the contribution from the galactocentric tangential velocity, resulting in a rotation curve with 'forbidden velocities': negative $\langle \mu_l \rangle$ at positive longitudes, and positive $\langle \mu_l \rangle$ at negative longitudes. The *S*-OGLE29 field is one such case, and as a result, the young stars have a rotation curve that changes sign (crosses the $\langle \mu_l \rangle = 0$ line) beyond 8 kpc. The old population shows no such deviations as a result of much lower galactocentric radial velocities produced by their weaker bar. Since the forbidden velocities would not be present in an axisymmetric system, they are the best probe of the variation of the bar strength. Thus the minor axis is not the ideal probe of the bar in proper motion rotation curves. We have analysed only two bar models; therefore we defer a deeper quantification of the relationship between intrinsic kinematics and bar strength to a future study.

3.7.1 Future Prospects

We have predicted the lines of sight which have rotation curves with large galactocentric radial velocity contributions acting in opposition to galactocentric tangential velocity in the same region, resulting in forbidden velocities. These regions provide clear indications of kinematic differences due to a stronger bar in the relatively young populations. We consider the difference in velocities between model young and old stars within a magnitude bin equivalent to 1 kpc at $R_{\odot} = 8$ kpc, denoted as $\delta\mu_l$, assuming the stars have fixed absolute magnitude. We find regions centred near $(|l|, |b|) = (6^{\circ}, 5^{\circ})$ show the largest separation, with higher amplitudes of $|\delta\mu_l|$ at positive longitude (owing to the bar orientation). These would be very fruitful targets for future observations.

The predictions in this study provide a framework for the observational testing of evolutionary pathways of the MW bulge and bar, such as the time of bar formation. While the separation of populations in these models has used stellar ages, a similar separation can be achieved in chemical ([Fe/H]) space, as demonstrated in the SWEEPS field by C18. The remaining *HST*-BTS fields offer an opportunity to test the predictions in Fig. 3.8 and Fig. 3.12. Proper motions are publicly available for the remaining fields, and we plan to use the same method adopted by C18 for the SWEEPS field to determine the photometric metallicity and distances for main-sequence stars in the OGLE29, *Stanek's* and *Baade's* windows (Clarkson et al. *in preparation*). The derived rotation curves for populations split by metallicity will be compared to those in this paper for the relatively young and old stars. The comparison of the OGLE29 window would be the most critical test of the results presented here as it has a distinct rotation curve profile with forbidden velocities. Although we find stronger signals at positive longitude in field A (see Fig. 3.11), the OGLE29 field presents an opportunity to test our predictions with data already available.

The *Nancy Grace Roman Space Telescope* (*RST*) promises to provide high-precision astrometry for $\sim$ 100 million stars within the bulge (WFIRST Astrometry Working Group et al. 2019). A shallow, multiepoch survey with *RST* directed at the key fields identified in this paper would be very useful to constrain the bulge/bar rotation curves. On the other hand, an All-Sky near-IR astrometric space mission (GaiaNIR, Hobbs et al. 2021) would provide homogeneous proper motions, parallaxes, and NIR magnitudes down to the Main Sequence Turn-Off (MSTO) in regions close to Galactic plane, thus facilitating the study of proper motion rotation curves as presented in this work, as probes for the formation of the bulge, and its dynamical evolution.

Future ground-based spectroscopic surveys (e.g. APOGEE-2, MOONS, 4MOST) (Zasowski et al. 2017; Gonzalez et al. 2020; Bensby et al. 2019) will collect high-resolution spectra for millions of bulge red giant stars, measuring metallicity, elemental abundances, and radial velocities. These large samples, when combined with the 2D motions from extensive photometric surveys such as VVV and *Gaia*, have the potential to facilitate the investigation of rotation curves of chemically distinct populations. It is thus critical that surveys deliver sufficiently large samples in key lines of sight for the measurement of statistically significant kinematic separations, after decomposing in chemical and distance space.

The Vera C. Rubin Observatory/LSST has the potential to produce a one-of-a-kind synoptic data set to test the predictions presented in this study. In particular, a multiepoch survey of the Galactic bulge region, deep enough to reach the MSTO, would provide the ideal data set to measure both ages and proper motions (Gonzalez et al. 2018, LSST bulge white paper) and apply the methods used here. A key output of LSST data would be a homogeneous, wide-field map of these properties (similar to the map in Fig. 3.4 and Fig. 3.11). This 'definitive map' would allow us to characterize the morphologies of different stellar populations of the bulge and bar in

unprecedented detail, answering fundamental questions about the formation of the MW bar.

3.7.2 Summary

We summarize our main conclusions as follows:

1. We have shown that the longitudinal proper motion rotation curves of old and (relatively) young stars are distinct, with the rotation curves of young stars generally having larger amplitudes. Our results are in agreement with observations of the SWEEPS field within the MW, which showed that the metal-rich population has a higher amplitude proper motion rotation curve than the metal-poor one (C18). This result does not require the presence of an accreted population (see Section 3.3).

2. We have presented maps of the intrinsic kinematics of each population to help understand the observations. The galactocentric cylindrical velocities of young stars are consistent with bar aligned orbits, in contrast to the nearly axisymmetric velocity distributions of old stars, which reflect their respective underlying density distributions. We demonstrate how the intrinsic velocities project onto longitudinal proper motions. Large galactocentric radial velocity contributions (in the young populations) produce rotation curves with forbidden velocities, which would not be present in an axisymmetric system (see Section 3.3.2).

3. We have defined two metrics to quantify the difference between the rotation curves of young and old populations, and predict their variation across the bulge. We show that the rotation curves of young and old populations in fields which intersect the bar away from the minor axis have non-antisymmetric separation profiles. These effects are due to the large galactocentric radial

velocities of young stars which, along these lines of sight, project into forbidden proper motions (see Sections 3.3.1 and 3.5.1).

4. We have demonstrated that the rotation curve separations can be explained by the distinct kinematics of populations separated by an evolving bar, as predicted by kinematic fractionation (Debattista et al. 2017), without the need for an accreted component. However, rotation curve separation would also naturally be present in an axisymmetric system because of the increasing asymmetric drift with population age. Therefore, it is the longitudes with forbidden velocities, which probe the variation of the bar's strength with age. (See Section 3.5.)

5. Finally, we present predictions of our two metrics and the profiles of rotation curves for key fields within the MW Bulge (see Section 3.6). These will allow for follow-up study with *HST*-BTS data (Clarkson et al. *in preparation*) along with future survey missions such as *RST* and LSST. We recommend deep observations of fields away from the minor axis, close to the regions of $(|l|, |b|) = (6^\circ, 5^\circ)$ where we have demonstrated rotation curves have forbidden velocities.

Acknowledgements

VPD is supported by STFC Consolidated grant # ST/R000786/1. SGK is supported by the Moses Holden Studentship, with particular thanks to Patrick Holden. The simulations used in this paper were run at the High Performance Computing Facility of the University of Central Lancashire. This work is based partially on observations made with the NASA/ESA *Hubble Space Telescope (HST)* and obtained from the data archive at the Space Telescope Science Institute (STScI). The *HST* comparisons reported in this paper rely on products from *HST* Guest Observer programs 9750, 12586 and 13057 (P.I. Sahu), 12020 (P.I. Clarkson), 11664 and 12666 (P.I. Brown),

support for which was provided by NASA through grants from STScI. STScI is operated by the Association of Universities for Research in Astronomy, Inc., under NASA contract NAS 5-26555 The authors are grateful for the anonymous referee's comments which helped to clarify and improve this paper. The analysis in this paper made use of the `PYTHON` packages `NUMPY, SCIPY, PANDAS, GALPY, PYNBODY` and `JUPYTER` (Harris et al. 2020; Virtanen et al. 2020; Wes McKinney 2010; Bovy 2015; Pontzen et al. 2013; Kluyver et al. 2016). Figures in this work were produced using the `PYTHON` package `MATPLOTLIB` (Hunter 2007).

3.8 Appendix A: Separation of Kinematics in Model 2

Here, we present the properties of Model 2, a simulation with the same initial conditions to our fiducial model but different subgrid physics to those outlined in Section 3.2.1. The following figures compare the properties of the bar and bulge populations of Model 2 with those of the fiducial model. We also present the equivalent maps of our ξ and $\delta\mu_l$ metrics for Model 2.

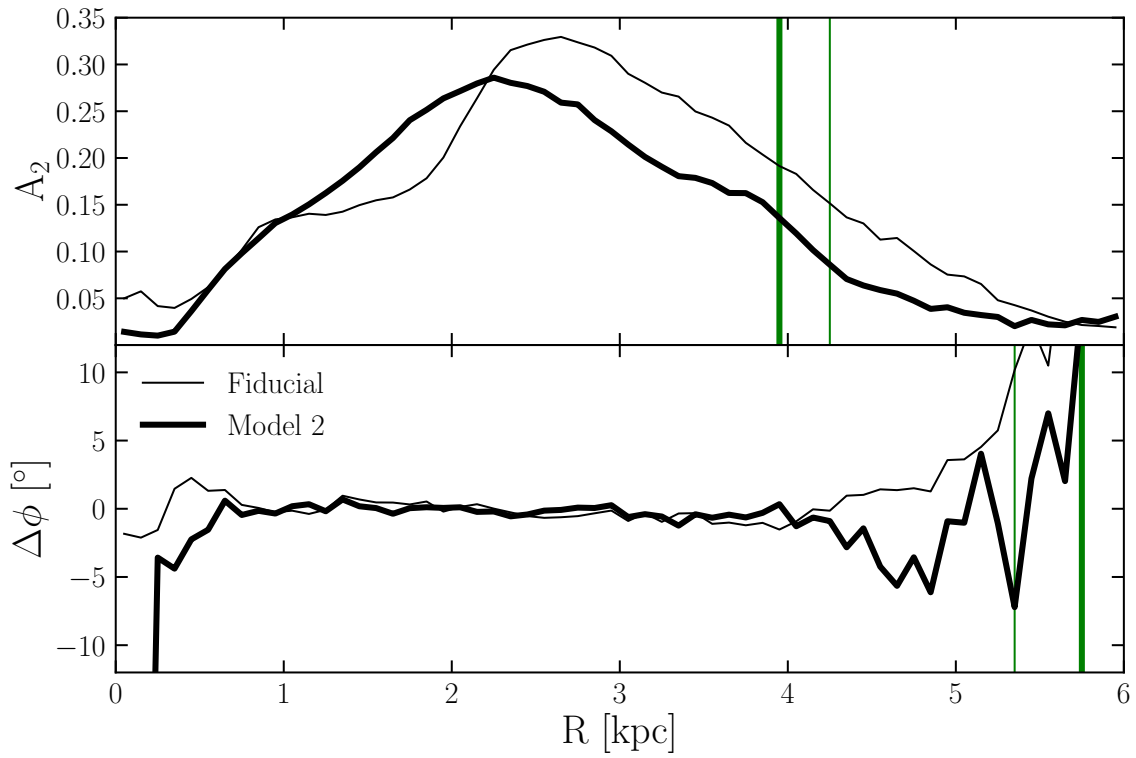

Figure 3.13: Top panel: the radial profile of the A_2 Fourier amplitude at time $t = 10\,\mathrm{Gyr}$ of the fiducial model and Model 2. Bottom panel: the change in phase angle of the $m = 2$ mode with radius at $t = 10\,\mathrm{Gyr}$. Vertical green lines indicates where A_2 reaches its half maximum value and $|\Delta\phi| > 10°$ for each model. Averaging these two values results in bar radial extents of $4.85 \pm 0.55\,\mathrm{kpc}$ and $4.80 \pm 0.90\,\mathrm{kpc}$ for the rescaled fiducial model and Model 2 respectively.

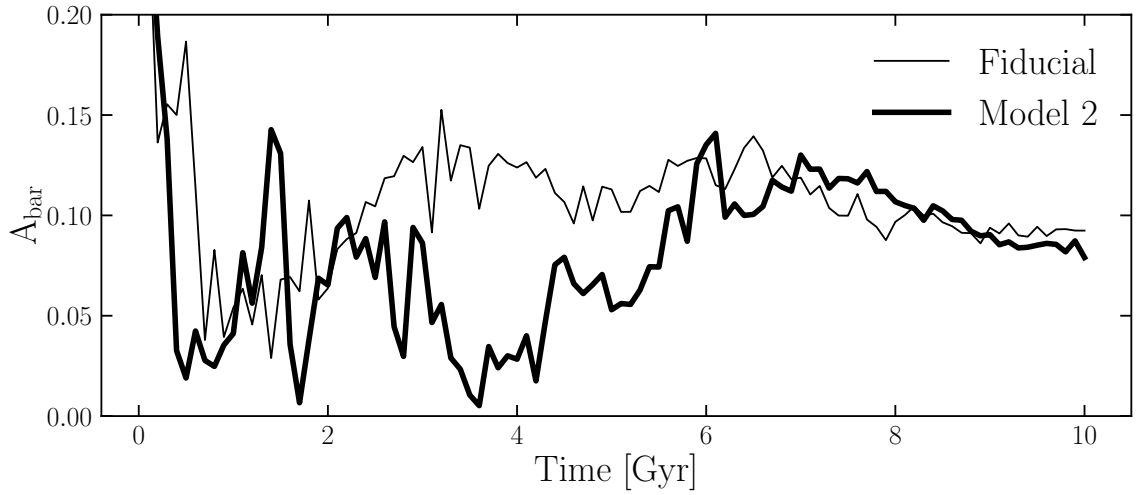

Figure 3.14: The global bar amplitudes of the fiducial model and Model 2 versus time. The major growth period for the fiducial model is between 2 and 4 Gyr, and 4 and 6 Gyr for Model 2.

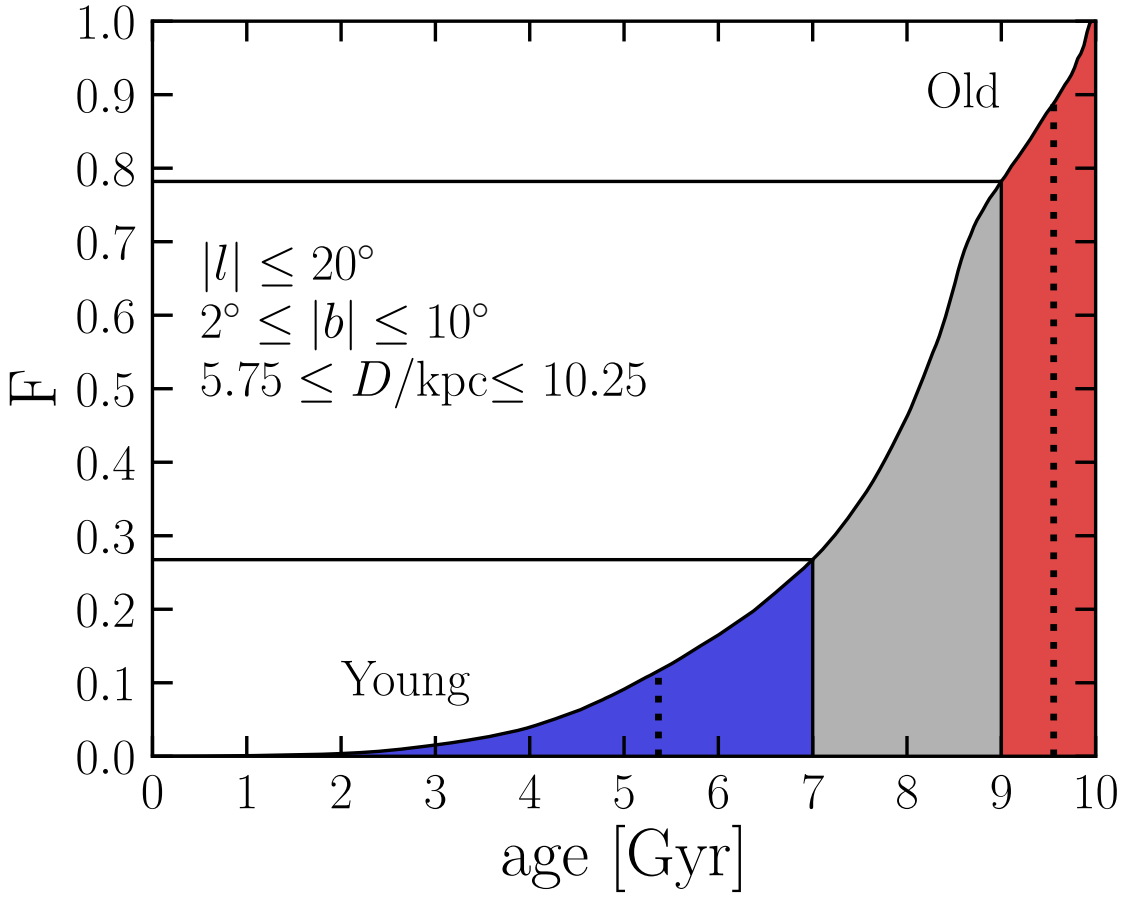

Figure 3.15: The cumulative distribution of ages within Model 2's bulge region, defined at top left-hand side, and our definition of the young (blue) and old population (red). The average age for the two populations (vertical black dashed lines) is 5.4 and 9.6 Gyr, respectively.

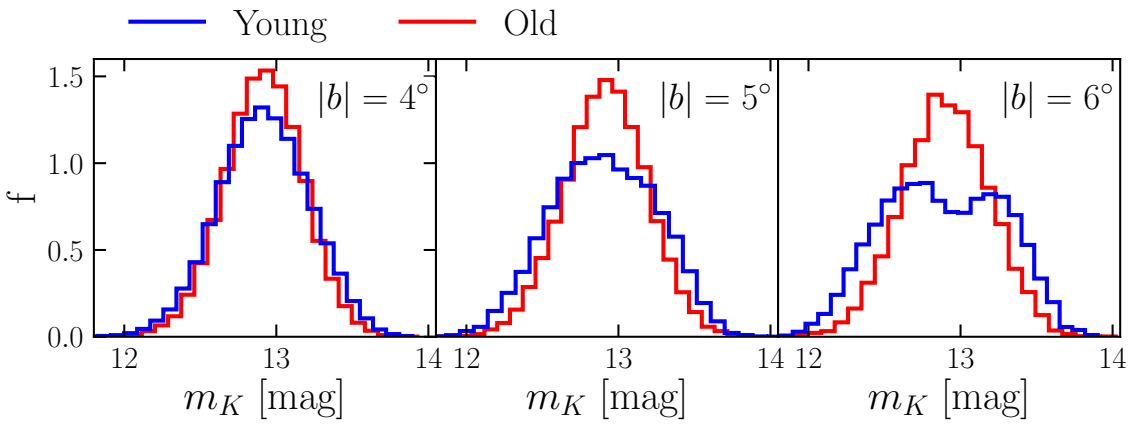

Figure 3.16: Unextincted apparent magnitude distributions of simulated RC stars along the LOS within $|l| < 4°$ for $|b| = 4°$ (left-hand panel), 5° (middle panel) and 6° (right-hand panel) with $\delta|b| = 0.25°$ in Model 2. Young (age < 7 Gyr) and old (age > 9 Gyr) stars are represented by the blue and red histograms, respectively. The magnitude distributions have been convolved with a Gaussian of width $\sigma = 0.17$ mag to represent the width of the RC. In the fiducial model (Fig. 3.2), a bimodality is first evident at $|b| \simeq 5°$ whereas in Model 2 the distribution is only split at $|b| \simeq 6°$.

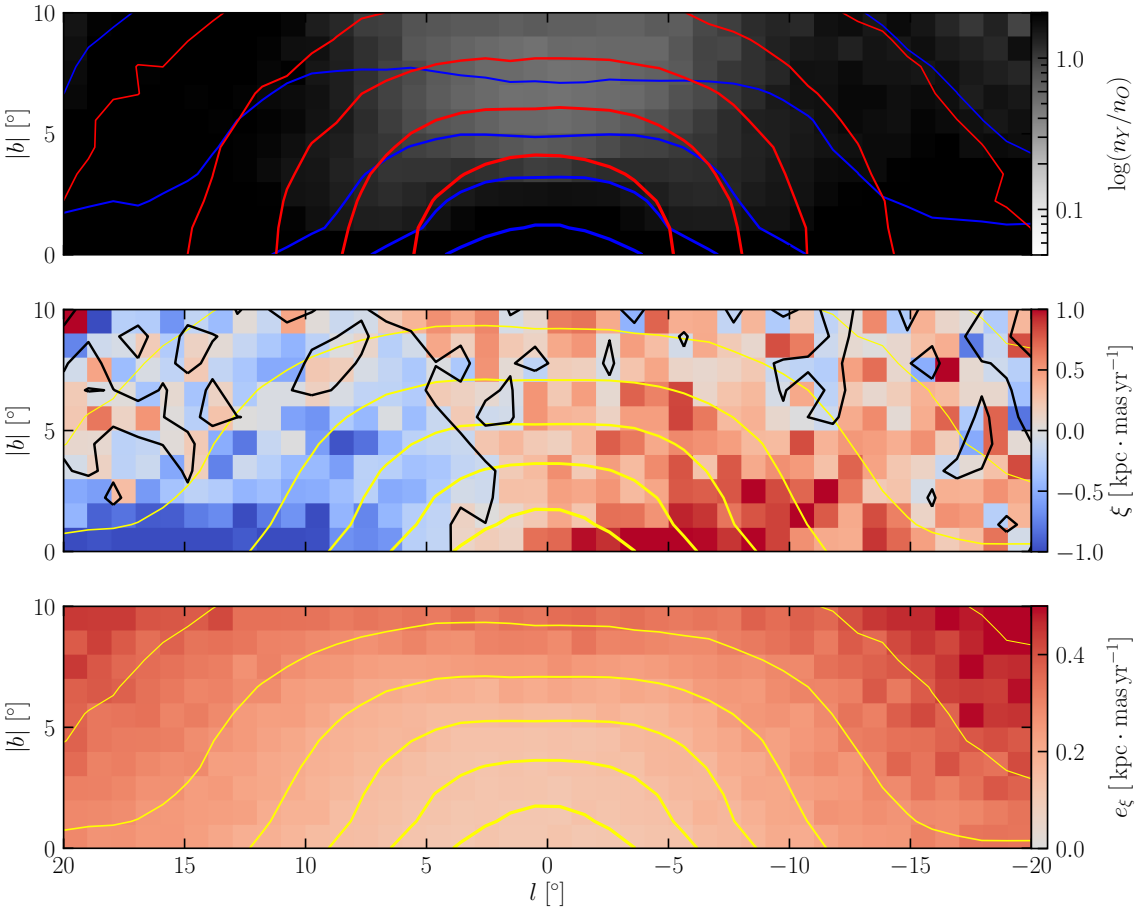

Figure 3.17: Top panel: density distribution of bulge stars in Model 2. Blue and red contours follow young and old population densities, respectively. Middle panel: separation amplitude, ξ, for each pixel representing a 1×1 deg^2 field. Bottom panel: model uncertainty on the separation amplitudes for each field. In the bottom two panels, the yellow contours follow the density of all bulge stars.

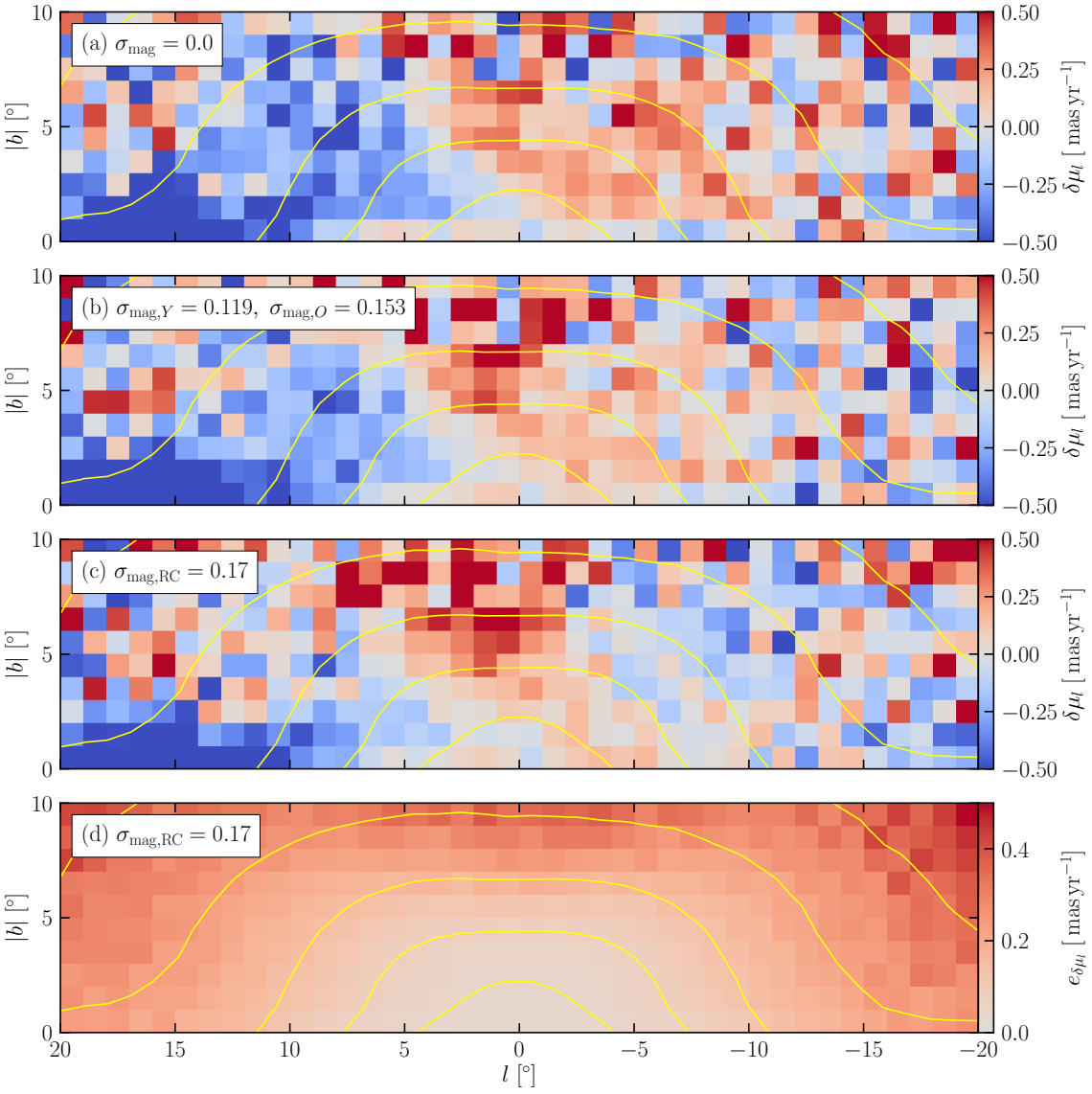

Figure 3.18: Top panel: the $\delta\mu_l$ distribution in the bulge region of Model 2 defined as the difference in $\langle\mu_l\rangle$ between the young and old populations at ~ 8 kpc. Middle top panel: the same as above but with young and old stars apparent magnitudes convolved with C18 uncertainties of $\sigma_{\rm mag,Y} = 0.119$ and $\sigma_{\rm mag,O} = 0.153$. Middle bottom panel: the same as above but with both populations convolved with the width of the RC, $\sigma_{\rm mag,RC} = 0.17$. Bottom panel: the calculated error for each field when applying the RC magnitude uncertainties.

Chapter 4

Gaia dR3 Ages from Variables for galactIc Dynamics (GRAVID)

4.1 Introduction

Stellar variability refers to changes in the brightness of a star over time. Over their lifetimes, stars pass through various phases of variability as they age. For this work, we focus primarily on long-period variables (LPVs), referring to the group of stars that vary periodically (or quasi-periodically) on timescales from tens of days up to thousands of days. LPVs are thermally-pulsating cool (red) giants or supergiants that lie on the red giant brand (RGB) and asymptotic giant branch (AGB) of the Hertzsprung–Russell diagram. Therefore, they typically have low- to intermediate-mass (0.5 – 8 $M_{\odot}$). AGB stars have depleted the hydrogen in their cores and are in the later stages of their evolution. As a result, the star expands and contracts during the pulsation cycle, causing its outer layers to cool and heat up, leading to periodic brightness and colour changes.

One of the earliest LPVs to be identified in the late 16^{th} century was named 'Mira' by Johannes Hevelius and pulsated with a primary period, changing brightness by a

whole magnitude. Subsequent observations by fellow astronomers Ismail Bouillaud and Johannes Holwarda estimated the period to be $\approx$ 330 days. Mira variables are named after the prototype star Mira and represent LPVs with large variability amplitudes. However, they can also exhibit long secondary periods (*e.g.*, Nicholls et al. 2009; Pawlak 2023).

Other classifications of LPVs include semi-regular (SRVs) and irregular variables, small amplitude red variables (SARV) and OGLE[1] small amplitude red giants (OSARGs), which all have secondary periods (first, second, or third overtones) or are less periodic. Many of the less regular LPVs pulsate in more than one mode.

4.1.1 Period Relations

Early observations of Mira variables in the Large Magellanic Cloud (LMC) demonstrated that they follow a tight period-luminosity relation (e.g. Glass & Evans 1981; Wood et al. 1999; Groenewegen 2004), allowing them to be used as standard candles. The period-luminosity relation is typically calibrated empirically using Mira variables in the LMC (see recent work by Yuan et al. 2017; Bhardwaj et al. 2019; Iwanek et al. 2021). However, few theoretical models of stellar evolution reproduce the observed period-luminosity relations of fundamental mode pulsation (Trabucchi et al. 2021a,b) and further work is needed to constrain these relations further.

In the Solar Neighbourhood, empirical studies, such as those of Merrill (1923) and Feast (1963), found that Miras with short periods have hotter kinematics (larger velocity dispersions) and larger vertical extents out of the plane (Feast & Whitelock 2000). This relation is usually interpreted as the period correlating with the age of a Mira variable where short periods (and hotter kinematics) are associated with older stellar populations and the opposite for long-period Miras. We present in Fig. 4.1 four empirically derived period-age relations from recent studies of Mira Variables

[1]Optical Gravitational Lensing Experiment (OGLE).

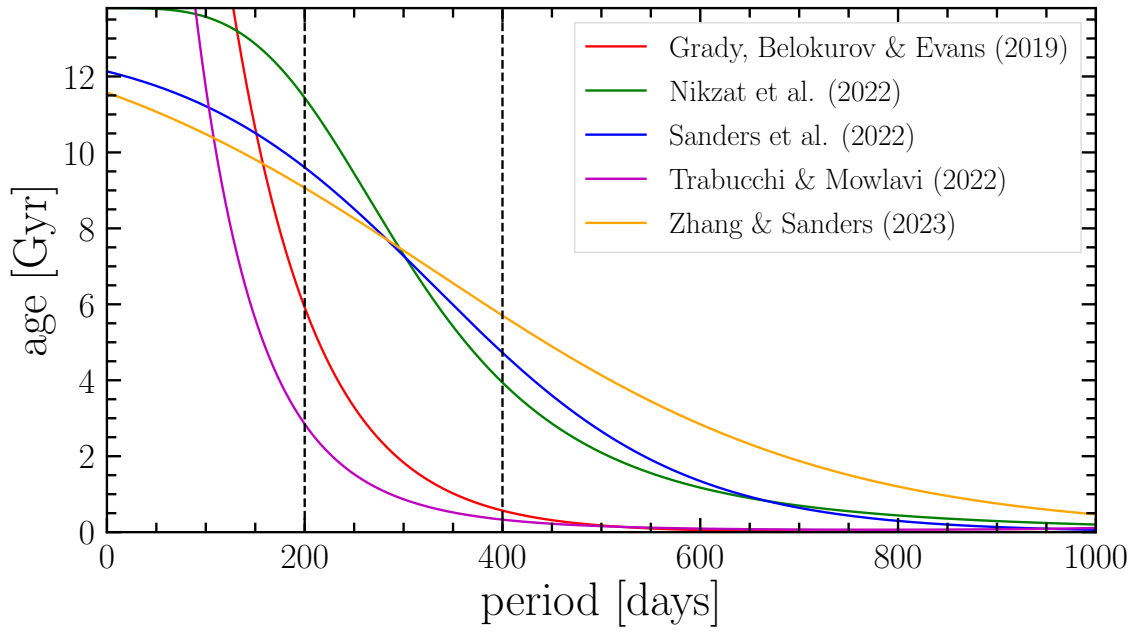

Figure 4.1: The period-age relations for Milky Way Mira variables from Grady et al. (2019, red), Nikzat et al. (2022, green), Sanders et al. (2022, blue), Trabucchi & Mowlavi (2022, magenta) and Zhang & Sanders (2023, orange). Uncertainties in the relations have not been plotted but can be significant (see Trabucchi & Mowlavi 2022). We use the vertical black dashed lines later in section 4.6.2 to define relatively young and old Miras in the Milky Way.

in the Milky Way. It is clear that there is a considerable disagreement between the ages of Miras for a given period. Indeed the uncertainties (not shown) predicted in the relations from Trabucchi & Mowlavi (2022) can be significant. Using theoretical pulsation models, the authors found there is a 3 Gyr range of ages for Miras with a 350 day period. Despite this uncertainty and contention between relations (Fig. 4.1), populations of Miras with varying periods can still be used as age indicators within the Milky Way and in external galaxies (*e.g.*, Catchpole et al. 2016; Grady et al. 2019, 2020a).

This chapter introduces key surveys of variables stars in the Milky Way in Section 4.2. Then, in Section 4.3, we summarise the contents of *Gaia* Data Release 3

(DR3) and present the methods of extracting LPVs from the catalogue. We also highlight the effects of large variability amplitude on photometric and astrometric solutions within *Gaia* and other multi-epoch surveys in Section 4.4. Next, we define a sample of LPVs in the LMC and present methods for extracting Mira candidates in Section 4.5. We then apply these methods to a Milky Way LPV sample in Section 4.6, exploring the spatial and kinematic distributions of Mira candidates as a function of the period after applying dust corrections to obtain 5D coordinates for the Milky Way sample and 6D coordinates for a subset with radial velocities. Finally, we summarise our findings in Section 4.7.

4.2 Variable Star Surveys

Surveys that revisit the same regions of the sky are naturally able to detect stellar variability. However, the periods they can resolve are limited by the cadence (the frequency of repeat observations) as well as the length of the mission. Several large-scale multi-epoch surveys have been conducted since the 1990s, providing significant leaps in our understanding of stellar evolution and variability, namely, the All-Sky Automated Survey (ASAS, Pojmanski 1997), the Optical Gravitational Lensing Experiment (OGLE, Udalski et al. 1992), the Panoramic Survey Telescope and Rapid Response System (Pan-STARRS, Chambers et al. 2016), the Zwicky Transient Facility (ZTF, Bellm et al. 2019), the Massive Compact Halo Objects Project (MACHO, Cook et al. 1992) and the VISTA Variables in the Via Lactea Survey (VVV, Saito et al. 2012). In addition, modern observatory facilities dedicated to detecting exoplanets through the transit method, such as the Wide Angle Search for Planets (WASP, Pollacco et al. 2006), *Kepler* (Borucki et al. 2010), and *Transiting Exoplanet Survey Satellite* (*TESS,* Ricker et al. 2014), produce data sets suitable for measuring and detecting variable stars. All-sky astrometric surveys also provide multi-epoch data on a large sample of stars over large timescales (Eyer &

Mowlavi 2008). We outline two important missions here.

4.2.1 *Hipparcos*

One of the early and most extensive surveys of variable stars was carried out by the European Space Agency (ESA), HIgh Precision PARallax COllecting Satellite or, more commonly, *Hipparcos* (Perryman 1986). Launched in 1989, *Hipparcos* measured the parallax of $\sim$ 120 000 bright stars in the solar neighbourhood. The mission's primary goal was to measure the parallax of stars with an unprecedented precision of 2 milli-arc-seconds (mas). *Hipparcos* was also able to determine the proper motions of stars with an accuracy of 2 mas yr^{-1}, achieved by measuring each star on average 100 times during the mission lifespan of over three years. A by-product of repeating measurements of the same stars was that it provided the light curves of variable stars with periods as short as one hour. Many new periodically variable stars were discovered as a result of the *Hipparcos* mission.

4.2.2 *Gaia*

The successor to the *Hipparcos* mission, the *Gaia* satellite, is also an ESA mission (Gaia Collaboration et al. 2016). Its goal is to create the most extensive, most precise three-dimensional map of the Milky Way by surveying $\sim$ 1% of the Galaxy's $\sim$ 200 billion stars. *Gaia* was launched in 2013 with routine operations commencing in July of 2014 and is expected to operate until 2025. The spacecraft is designed for astrometry: measuring stars' positions, distances and motions with an unprecedented sub-milliarcsecond (<mas) precision.

Gaia targets objects brighter than 20.7^{th} mag. in a broad photometric band (G) that covers the extended visual range between near-UV and near-infrared. The astrometry instrument (Astro) precisely determines the positions of stars and - by combining the measurements for each individual star over the five-year mission -

determines their parallax. Therefore its distance and proper motion (the velocity of the star projected on the plane of the sky) can also be measured.

In addition to the broad white light photometric G-band, there is the spectro-photometer (BP/RP). The blue and red spectro-photometry, BP and RP, respectively, help determine stellar properties such as temperature, mass, age and colour. In addition, prisms provide low-resolution spectra[2].

The Radial-Velocity Spectrometer (RVS) is primarily used to determine the velocity of objects along the line of sight by acquiring high-resolution spectra in the spectral band $847 - 874$ nm (field lines of calcium ion). The RVS reveals a star's velocity along the line of sight by measuring the Doppler shift of absorption lines in a 'high-resolution' ($\lambda/\Delta\lambda \sim 11\,500$) spectrum for stars brighter than apparent magnitudes of 17.5. Radial velocities are measured with precisions between $1\,\mathrm{km\,s^{-1}}$ ($V = 11.5$ mag.) and $30\,\mathrm{km\,s^{-1}}$ ($V = 17.5$ mag.), though there are more significant uncertainties for large amplitude LPVs and fainter sources (see Section 4.4).

Given all the aforementioned attributes, *Gaia* is particularly suited to conduct an all-sky survey of Mira variables in the Milky Way and Local Group galaxies.

4.3 *Gaia* DR3

The initial set of data released as *Gaia* Early Data Release 3 (EDR3) (Gaia Collaboration & et al. 2021) on December 3$^{\mathrm{rd}}$, 2020, included observations of G-band magnitudes for ≈ 1.8 billion sources with G_{BP} and G_{RP} magnitudes for ≈ 1.54 billion and ≈ 1.55 billion sources, respectively. A full astrometric solution: positions on the sky (α, δ), parallax (ϖ), and proper motions (μ_α, μ_δ) for approximately 1.46 billion sources were also included with a limiting magnitude of $G \approx 21$ mag. and a bright limit of $G \approx 3$ mag. The astrometric solution had several new quality

[2]The BP-band covers wavelengths from 330 to 680 nm, while the RP-band covers 640 to 1050 nm over ≈ 25 pixels and ≈ 30 pixels, respectively.

indicators discussed in Section 4.4.2.

The full *Gaia* DR3 complemented the above data set with new products released on June 13$^{\text{th}}$, 2022 (Gaia Collaboration et al. 2022). *Gaia* defined a celestial reference frame, allowing us to account for our motion through the Galaxy with ≈ 1.61 million reference frame sources included in DR3 (Gaia-CRF3). In addition, astrometric cross-matches between Gaia (E)DR3 sources and other Milky Way surveys such as *Hipparcos*, Two Micron All Sky Survey (2MASS) Point Source Catalog and Extended Source Catalog (PSC & XSC), the Sloan Digital Sky Survey (SDSS), the Pan-STARRS were also included (Marrese et al. 2019).

These products also included object classifications for 1.59 billion sources and astrophysical parameters (*e.g.*, effective temperature, chemistry, extinction, distance) from BP/RP spectra for 470 million objects. Other astrophysical parameters from the BP/RP spectra for smaller subsets of the sources include mass, age and spectral types. In addition, *Gaia* DR3 released mean RVS spectra for 1 million objects, mean radial velocities for 33 million stars and mean magnitudes for 32 million objects with $G_{\text{RVS}} \lesssim 14$ mag. with effective temperatures (T_{eff}) in the range of $\sim 3\,100$ to $14\,500$ K.

Variability analysis of the epoch photometry for ≈ 10.5 million sources provided additional parameters for measuring the sources' brightness variation and classified them into 24 variability classes. The *Gaia* team performed detailed variability analysis on several classes, and the results were published in separate data sets (Eyer et al. 2022). Candidate LPVs from the Specific Object Study (SOS) have published generalised Lomb–Scargle periods and Fourier amplitudes for their primary period if it lies in the range of 35 day to 1039 days[3]. The *Gaia* DR3 release included 1 720 588 long-period variable sources, providing a remarkable and unique data set to study the Milky Way's structure, kinematics and the Galaxy's evolutionary history.

[3]The duration of the *Gaia* mission at the DR3 release.

Data for this work were extracted from the University of Heidelberg *Gaia* TAP service as part of the Data Processing and Analysis Consortium (DPAC) using `TOPCAT` (Taylor 2005)[4]. In Table 4.1, we summarise common quantities from the *Gaia* DR3 archive used in this chapter.

4.3.1 *Gaia* DR3 LPV Sample

We describe here the prescriptions we impose to select a clean sample of LPVs from the *Gaia* archive.

We are interested in studying LPVs that are not part of binary or multiple systems. Therefore, we use the condition `non_single_star = 0` from the `gaia_source` table. We also ensure quality data is included by removing duplicate sources (`duplicated_source = 'FALSE'`) from the same table.

We extract LPVs using the classifier results of the variability pipeline (Lebzelter et al. 2023) by specifying sources that have the highest classification score to be LPV from the `vari_classifier_result` table, conditioning the parameter `best_class_name = 'LPV'`. The sources must also appear in the `vari_long_period_variable` table[5]. From the LPV table, we also require that the frequency has been modelled successfully and therefore `frequency IS NOT NULL`).

Carbon-rich LPVs have a period-luminosity relation that is more uncertain than their oxygen-rich counterparts (*e.g.*, Whitelock et al. 2008). Lebzelter et al. (2023) describe a method to distinguish between the two classes by utilising the low-resolution RP spectra. The surface chemical signatures between carbon-rich (C) and oxygen-rich (O) LPVs have distinct C/O ratios, resulting in fundamentally different spectra. Spectra of O-rich red giants (top panel of Fig. 4.2) have wide absorption features due to high abundances of TiO (Titanium Oxide). However, the spectra

[4]With particular thanks to Mark Taylor and Jon Juaristi Campillo.

[5]*i.e.*, `vari_long_period_variable.source_id IS NOT NULL`

Symbol	Database Entry	Archive Table	Description
Photometry			
G	phot_g_mean_mag	gaia_source	Weighted mean G-band flux on the CCD, converted into magnitude.
G^{FoV}	mean_mag_g_fov	vari_summary	G-band flux converted to magnitudes and the unweighted mean magnitude (Field-of-View, FoV, Eyer et al. 2022).
Variability			
ν	frequency	vari_long_period_variable	The primary frequency of the Fourier model fit to the light curve.
σ_ν	frequency_error	vari_long_period_variable	The uncertainty of ν.
A_{model}	amplitude	vari_long_period_variable	The half peak-to-peak magnitude of the Fourier model fit to the light curve.
σ_G^{FoV}	std_dev_mag_g_fov	vari_summary	The standard deviation of the G^{FoV} mean magnitude.
Amp	See Eqn. 4.5		The square root of the signal variance.
	$\hookrightarrow$ phot_g_mean_flux	gaia_source	
	$\hookrightarrow$ phot_g_mean_flux_error	gaia_source	
	$\hookrightarrow$ phot_g_n_obs	gaia_source	

Table 4.1: Summary of common quantities used in this chapter from the *Gaia* DR3 archive.

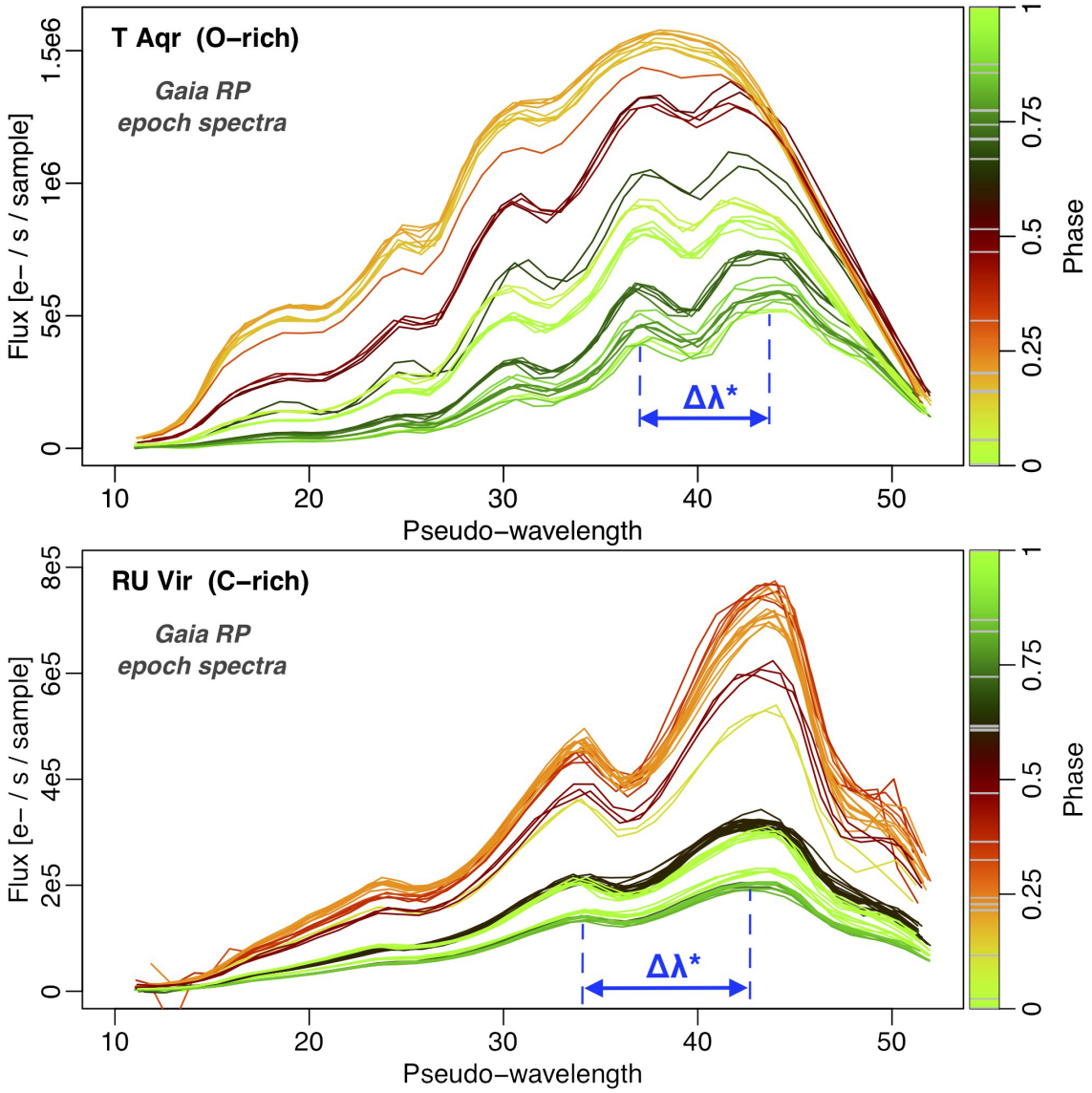

Figure 4.2: Epoch RP spectra of the O-rich Mira star T Aqr (top panel, pulsation period of 203 days) and the C-rich Mira star RU Vir (bottom panel, pulsation period of 425 days) coloured by the various phases of their pulsation cycle. The horizontal axis represents an arbitrary, dimensionless pseudo-wavelength covering the 640 to 1100 nm wavelength range. Image credits: ESA/Gaia/DPAC, Nami Mowlavi, Isabelle Lecoeur-Taïbi, Maria Süveges, Thomas Lebzelter, Francesca De Angeli, Laurent Eyer, Dafydd Evans, Michal Pawlak, and the Gaia CU7 Geneva and CU5 Cambridge teams.

of C-rich giants (bottom panel of Fig. 4.2) show wide absorption features due to the presence of CH (Methylidyne) and C_2 (Diatomic Carbon). Therefore, the width of the absorption features is larger for C-rich stars, while O-rich stars show more absorption features. From these low-resolution spectra of each LPV, the pseudo-wavelength separation between the two highest flux peaks detected in the spectrum, $\Delta\lambda_{RP,i}$ at each epoch i, is taken as a proxy for the spectral absorption width. For each LPV the median separation is computed, $\langle\Delta\lambda_{RP}\rangle$ where Lebzelter et al. (2023) define C-rich LPVs as those with $\langle\Delta\lambda_{RP}\rangle > 7$. Thus O-rich LPVs have lower separation with $\langle\Delta\lambda_{RP}\rangle \leq 7$. When the automated routines cannot distinguish between the two classifications, the `is_cstar` flag in the `vari_long_period_variable` table is set to `'NULL'`. Therefore, to extract only confident O-rich LPVs, we use the condition `is_cstar = 'False'`.

We also require infrared photometric measurements acquired from the 2MASS PSC (Skrutskie et al. 2006) using the cross-matching algorithm (Marrese et al. 2019) provided by *Gaia* DPAC[6]. Finally, we combine the above conditions to construct the following ADQL query, which we used to extract single star and oxygen-rich LPVs from the *Gaia* DR3 archive:

```
SELECT gs.*,lpv.*, claslpv.*, n.*, j.*, tmass.*
FROM gaiadr3.gaia_source AS gs
JOIN gaiadr3.vari_classifier_result
    AS claslpv USING (source_id)
JOIN gaiadr3.vari_long_period_variable
    AS lpv USING (source_id)
JOIN gaiadr3.tmass_psc_xsc_best_neighbour
    AS n USING (source_id)
```

[6]The naming conventions for external catalogues, `extcat.twomass`, are unique to the University of Heidelberg *Gaia* TAP service.

```
JOIN gaiadr3.tmass_psc_xsc_join
    AS j USING (clean_tmass_psc_xsc_oid)
JOIN extcat.twomass AS tmass
     ON j.original_psc_source_id = tmass.mainid
WHERE gs.non_single_star = 0
AND gs.duplicated_source = 'FALSE'
AND (claslpv.best_class_name = 'LPV'
OR lpv.source_id IS NOT NULL)
AND lpv.frequency IS NOT NULL
AND lpv.is_cstar = 'FALSE'
```

where the above query returns 321 581 LPV sources[7].

Further selection criteria beyond this point were applied to the results of running the ADQL query above. Conceivably, the following selections can be joined to a larger query[8].

For our analysis, we require the 2MASS K_s-band and H-band magnitudes, thus removing an additional 45 sources where values of magnitudes are `'NULL'`. To also ensure we use the best possible cross-matched sources, we also filter on the following parameters:

```
xm_flag = 8
number_of_neighbours < 2
number_of_mates < 1
```

found in the `tmass_psc_xsc_best_neighbour` table. These conditions filter sources with multiple matches with the 2MASS catalogue, removing 4 124 sources. Finally, we separate Milky Way LPVs from satellites and Local Group galaxies using

[7]A query with the same selection conditions but not including the cross-match with 2MASS PSC returns 322 751 sources (1 170 additional sources).

[8]Applying all of the selections in one query causes the request to time out.

Satellite	Number of LPV Sources
LMC	12 325
SMC	1 485
M31	32
M33	14
Fornax dSph	5
NGC 6822	9
Total	13 870

Table 4.2: The number of *Gaia* DR3 LPV sources associated with Milky Way satellites and Local Group galaxies.

the definitions from Gaia Collaboration et al. (2021) (their table C.2) and Lebzelter et al. (2023) (their section 2.1) with the number of sources associated with each satellite presented in Table 4.3.1 below. Therefore, we are left with a sample of 303 542 *Gaia* DR3 Milky Way single star, oxygen-rich LPV sources with good cross-matching with the 2MASS PSC.

4.3.2 LPV Variability Amplitudes

When studying LPVs, we consider the Field-of-View (FoV) magnitude, G^{FoV}, which is calculated without a weighting procedure (`mean_mag_g_fov`, see Eyer et al. 2022). We define the amplitude of variability for LPVs to be the standard deviation of the G^{FoV} mean magnitude, σ_G^{FoV}, (`std_dev_mag_g_fov`) defined in the `vari_summary` table.

The variability and SOS pipelines implemented in *Gaia* DR3 use a Fourier decomposition approach, assuming the light curve is mono- or multi-periodic (Eyer et al. 2022) fitting a single period and amplitude to light curves. The `amplitude` of the model (A_{model}) quoted in `vari_long_period_variable` table is calculated

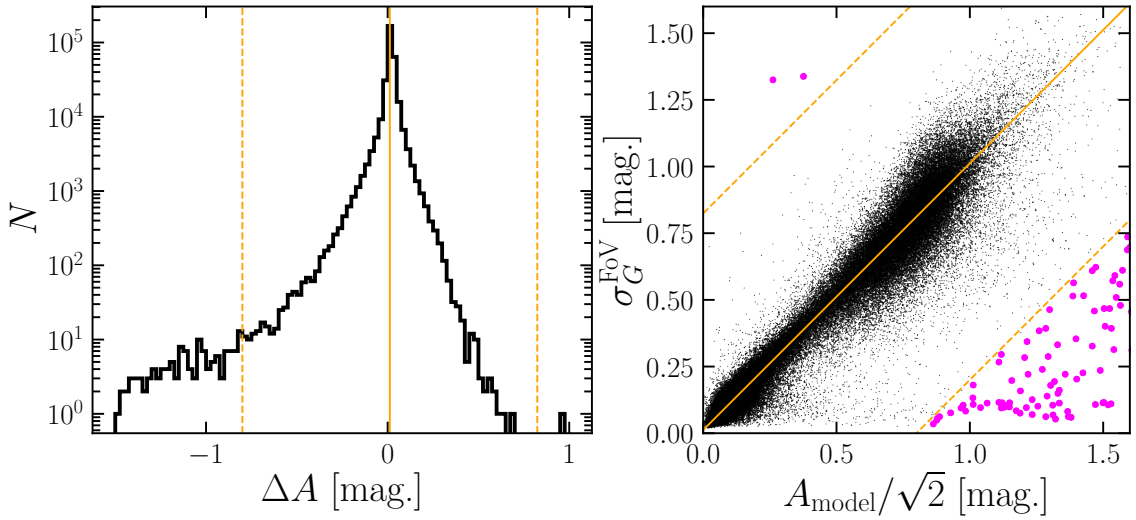

Figure 4.3: Left: the distribution of ΔA, the difference between variability amplitudes calculated via the Fourier model ($A_{\rm model}$) and via standard deviation of the FoV magnitude ($\sigma_G^{\rm FoV}$) (Eqn. 4.3) for LPV sources. The vertical orange line denotes the mean difference, $\langle \Delta A \rangle$, between amplitude metrics, and the vertical dashed orange lines denote the region between $\pm 5\sigma_{\Delta A}$ of $\langle \Delta A \rangle$ (Eqn. 4.4). Right: the distribution of $A_{\rm model}$ against $\sigma_G^{\rm FoV}$. The orange and dashed lines trace the same regions as in the left panel. Sources with differences beyond 5σ are plotted as magenta points.

as the half peak-to-peak magnitude of the light curve. In signal processing (Smith 1999), the peak-to-peak amplitude ($A_{\rm pp}$) of a sine wave relates to the standard deviation of the variability, σ, as:

$$A_{\rm pp} = 2\sigma\sqrt{2}\,. \tag{4.1}$$

Therefore comparing the model amplitude, $A_{\rm model}$ ($A_{\rm pp}/2$) with the standard deviation of the FoV magnitude, $\sigma_G^{\rm FoV}$ in a noise-free environment, we expect to find the following relation:

$$A_{\rm model}/\sqrt{2} = \sigma_G^{\rm FoV}\,. \tag{4.2}$$

We know, however, that there is noise in the observations, and thus $\sigma_G^{\rm FoV}$ is

the sum of $\sigma_{\rm signal} + \sigma_{\rm noise}$ which leads to an overestimate of the amplitude. In the right-hand panel of Fig. 4.3, we show the relation between $A_{\rm model}/\sqrt{2}$ and $\sigma_G^{\rm FoV}$ for the LPVs, which follows the 1:1 relation closely but has an apparent vertical offset. Furthermore, we show the difference between the two metrics:

$$\Delta A = \sigma_G^{\rm FoV} - A_{\rm model}/\sqrt{2}\,, \tag{4.3}$$

in the left-hand panel of Fig. 4.3. We calculate a mean difference of $\langle \Delta A \rangle = 0.012$ mag. and a standard deviation of $\sigma_{\Delta A} = 0.16$ mag., indicating good agreement between the amplitude measurements. We find that the model amplitude is slightly larger than the $\sigma_G^{\rm FoV}$ validating the empirical relation between metrics. However, we also find several sources with substantial values for $A_{\rm model}$ in comparison to $\sigma_G^{\rm FoV}$ highlighted in the right-hand panel of Fig. 4.3. Therefore we examine the light curves of extreme cases where:

$$|\Delta A - \langle \Delta A \rangle\,| > 5\sigma_{\Delta A}\,. \tag{4.4}$$

The primary reason for this discrepancy is that the data coverage of the maxima and minima is sparse for these sources. The fitting procedures of the light curves struggle to determine the true amplitude of variability because the light curve is incomplete, and $\sigma_G^{\rm FoV}$ underestimates the total variance of the brightness. However, reasonable periods may still be identified by the Fourier model. Therefore we exclude sources with the above condition (Eqn. 4.4) from further analysis.

4.4 Effects of Large Variability Amplitude

Observations of stars typically combine multiple images to achieve greater signal-to-noise, to measure motions on the sky, or to measure parallax. In the case of *Gaia*, it attempts to do all three. Multiple pointings are typically averaged to achieve higher signal-to-noise in measurements, weighting by the uncertainties from each

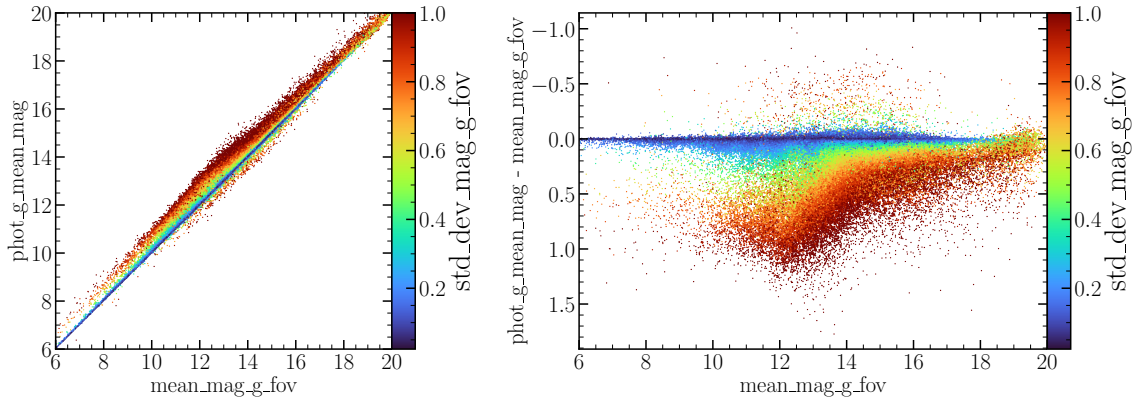

Figure 4.4: Left: comparison between G-band mean magnitude measurements for LPVs. Right: the difference between the G-band mean magnitude measurements as a function of the FoV mean magnitude. Both panels are coloured by the standard deviation of the FoV magnitude.

image. This procedure improves the quality of measurements for most standard (non-variables) sources. However, large amplitude oscillators vary their brightness considerably, image to image, and thus the assumed uncertainties also change, biasing weighting procedures. Here we explore the effects of large variability amplitude on the uncertainties of different photometric and astrometric parameters in *Gaia* DR3.

4.4.1 Photometry

There are several estimators of the mean magnitude for different objects of interest in the *Gaia* archive. For the LPVs, there are two: `gaia_source.phot_g_mean_mag` and `vari_summary.mean_mag_g_fov`. The first is the weighted mean G-band flux on the CCD, converted into magnitude. The second is the G-band flux converted to magnitudes and the unweighted mean magnitude (Field-of-View, FoV).

The light curves of large amplitude variables change their brightness by up to

3 mag., and when weighting each observation by the uncertainty of the flux[9], more weight is given to the fainter data points leading to an underestimate of the mean magnitude of the variable.

We demonstrate this effect for LPVs in Fig. 4.4. LPVs with low variability amplitude (standard deviation of the FoV magnitude, $\sigma_G^{\rm fov}$) follow the 1:1 relation of `phot_g_mean_mag` to `mean_mag_g_fov`. However, large amplitude LPVs have larger values of `phot_g_mean_mag` than `mean_mag_g_fov`, resulting in them appearing above the 1:1 relation in the left-hand panel. We highlight this effect in the right-hand panel of Fig. 4.4 by presenting the difference between mean magnitude metrics as a function of the FoV magnitude and colouring by $\sigma_G^{\rm fov}$. For the largest amplitude LPVs, differences between the mean magnitudes reach 1.0 *mag.* with `phot_g_mean_mag` again underestimating the brightness of the source.

These biases for sources with large variability amplitude also impact estimates of the amplitude itself. In the literature, the amplitude is estimated by calculating the square root of the signal variance, *e.g.*:

$$\text{Amp} = \sqrt{N_{\rm obs}}\frac{\sigma_F}{F}, \tag{4.5}$$

where $N_{\rm obs}$ is the number of observations, and F is the weighted mean flux (*e.g.*, Belokurov et al. 2017; Deason et al. 2017; Mowlavi et al. 2018; Iorio et al. 2018; Grady et al. 2020a). In *Gaia* DR3 this is calculated using the `phot_g_n_obs`, `phot_g_mean_flux_error` and `phot_g_mean_flux` fields from the `gaia_source` table, therefore F in Eqn. 4.5 becomes $\overline{I_G}$.

In Fig. 4.5, we present comparisons between three metrics of variability amplitude Amp, $\sigma_G^{\rm fov}$ and $A_{\rm model}$. It is clear that there is a strong bias visible in the square root of the signal variance as an estimate for amplitude. We showed in Section 4.3.2 that $\sigma_G^{\rm fov}$ correlates strongly with the model amplitude, and here we see no relationship with the mean magnitude. However, bright and large amplitude LPV sources have

[9]Calculated as 1/uncertainty^2, where uncertainty is Poisson noise, *i.e.* $\sigma = \sqrt{\text{flux}}$.

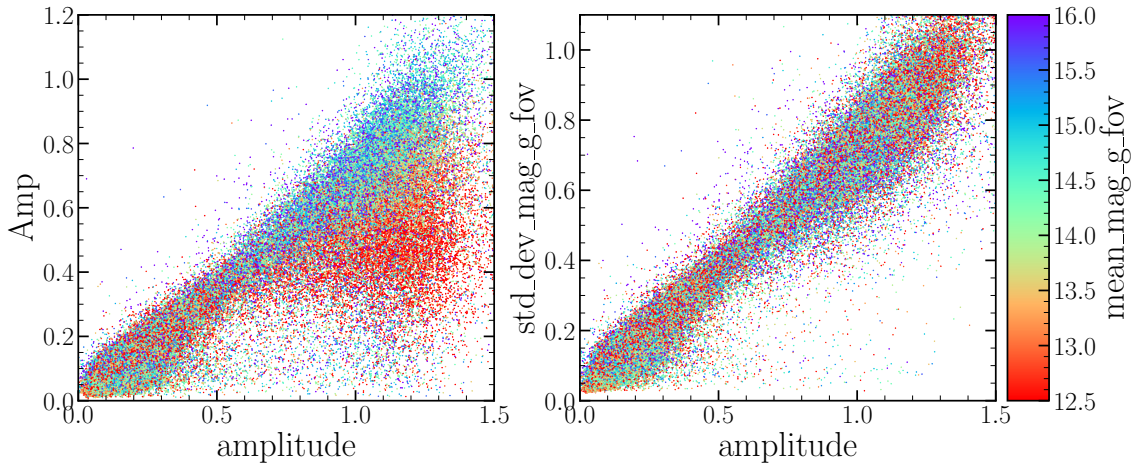

Figure 4.5: Left: the comparison between the square root of the signal variance (Eqn. 4.5 labeled as Amp, and the `amplitude` of the model quoted in the `vari_long_period_variable` table. Right: the comparison between the `std_dev_mag_g_fov` defined in the `vari_summary` table and model amplitude. Both panels are coloured by the `mean_mag_g_fov`.

their amplitude underestimated by the square root of the signal variance (Eqn. 4.5). Therefore, such a parameter is not a suitable amplitude proxy for LPVs.

We also show that other measured parameters of the unweighted magnitudes (FoV), such as the `range_mag_g_fov`, correlate well with the model amplitude and highlight the bias of using the square root of the signal variance. Finally, we present the comparisons between metrics in Fig. 4.6. We find good correlations with the model amplitude for the parameters: `std_dev_mag_g_fov`, `range_mag_g_fov` and `trimmed_range_mag_g_fov`.

4.4.2 Astrometric Solution

Sources with large variability can have more significant uncertainties for their astrometric solution for the same reason as having larger biases in their mean magnitude.

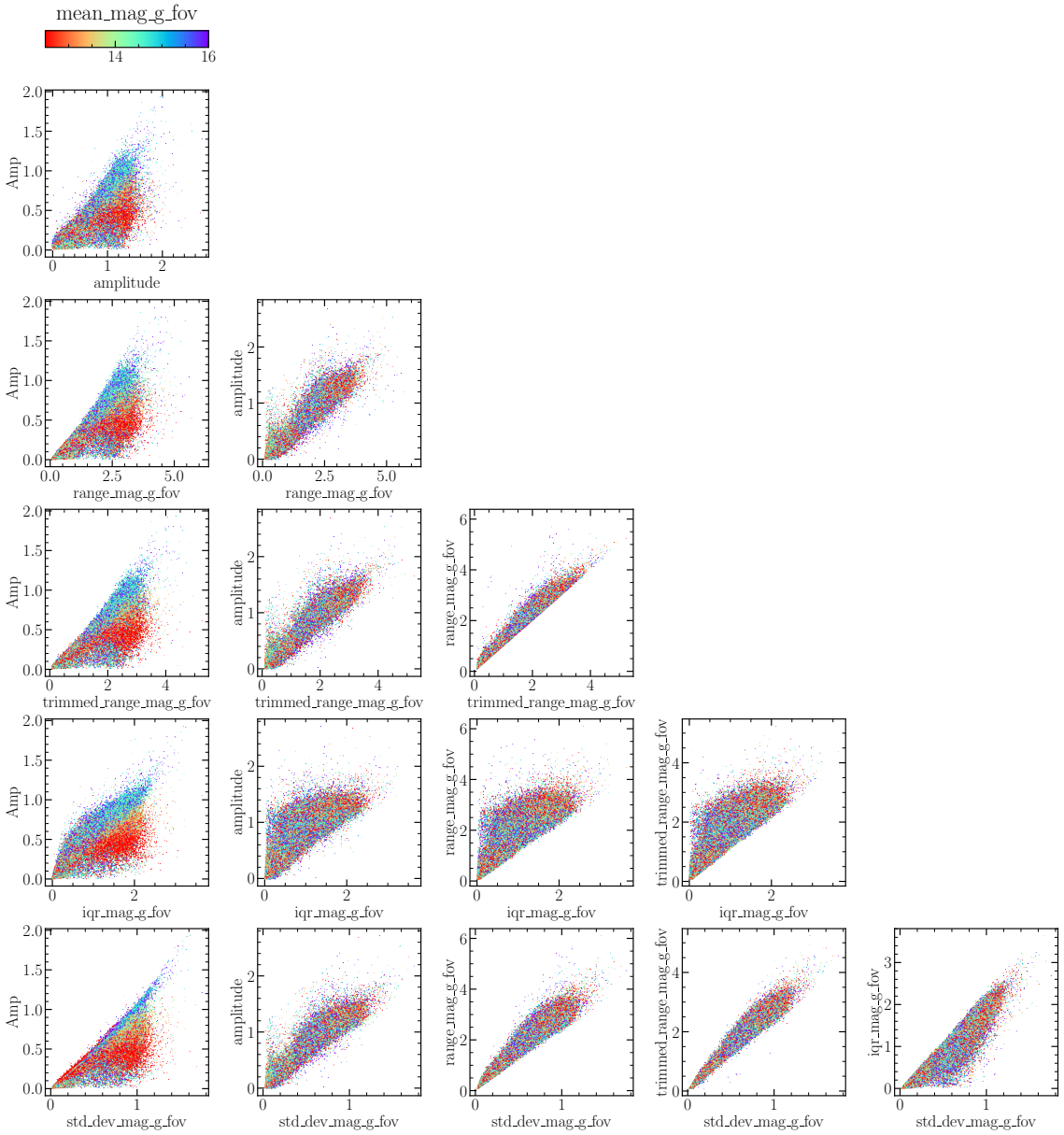

Figure 4.6: Comparisons between stellar variability amplitude estimates with axis labelled by their *Gaia* archive entry from the `vari_summary` and `vari_long_period_variable` tables for the Milky Way LPV sample. The `std_flux_over_mean_flux` refers to the square root of the signal variance (Eqn. 4.5). All points are coloured by their weighted mean magnitude.

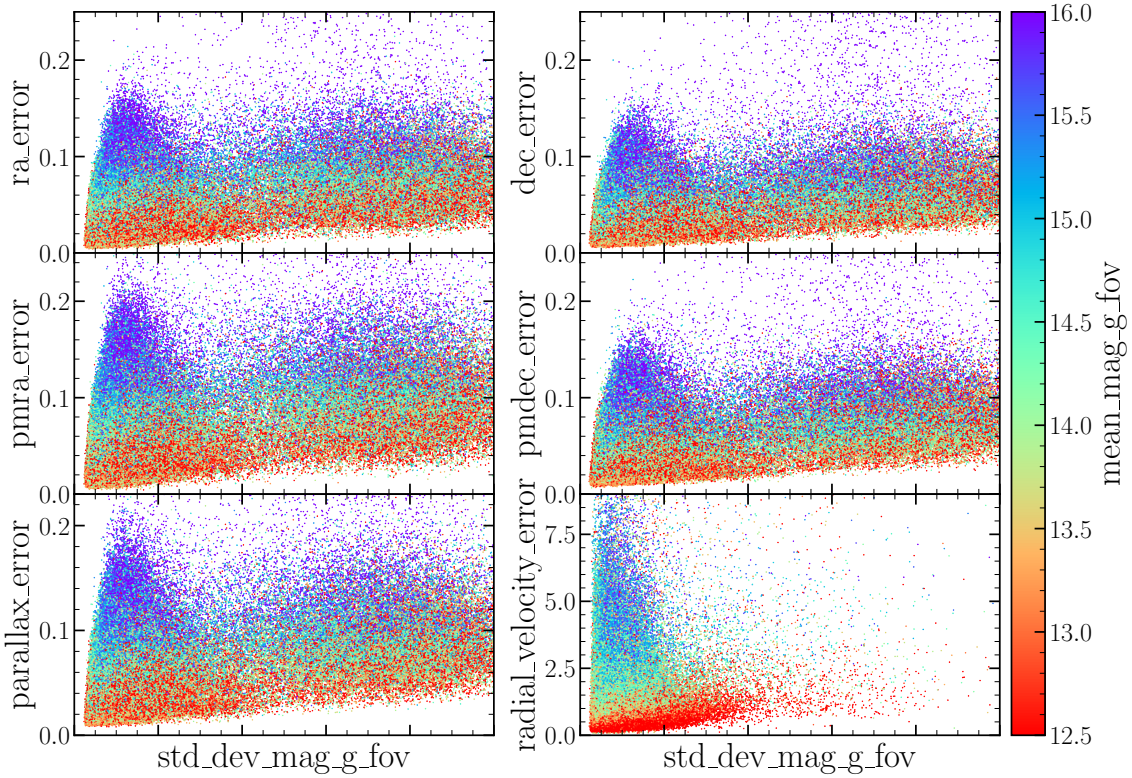

Figure 4.7: Distributions of uncertainties of astrometric parameters as a function of stellar variability amplitude for LPV sources in the Milky Way. Points in each panel are coloured by their FoV mean magnitude.

Weighting positions based on their uncertainty, typically derived from their brightness at each epoch, can lead to biases as a variable star oscillates. This results in an increase of uncertainties for the Right Ascension and Declination (α, δ), on-sky Right Ascension and Declination proper motions (μ_α, μ_δ), parallax (ϖ) and radial velocity (for those LPVs with RV measurements). We present the distributions of astrometric uncertainties as a function of stellar variability amplitude `std_dev_mag_g_fov` in Fig. 4.7. We find a clear increasing trend in astrometric uncertainty in each component with increasing variability amplitude. As expected, vertical gradients of increasing astrometric uncertainty for fainter sources are also evident.

The `ruwe` parameter released as part of *Gaia* DR3 can be used as a proxy for the

combined error of the astrometric solution. Initially described in DPAC document code GAIA-C3-TN-LU-LL-124-01 (see also Lindegren et al. 2018) is a Re-normalised version of the Unit Weight Error (UWE). Single star sources with good astrometric solution are expected to have a UWE close to 1.0. However, this is not the case for bright sources and those with extreme colour index, which have exaggerated uncertainties for stars such as those on the red giant branch (like Miras). Re-normalising UWE by accounting for the magnitude and colour of the source allows for a single parameter selection for good sources. This quantity helps identify sources with observations consistent with a five-parameter astrometric solution, indicating a well-defined position and uniform motion across the sky. We can also remove sources whose observations are not consistent with such a solution, where the discrepancy could, for example, be binary or multiple systems. This single quantity encapsulates the effects of uncertainty in the astrometric solution.

We present the distribution of `ruwe` as a function of stellar variability amplitude in Fig. 4.8 for the Milky Way LPVs (see Section 4.6). The combined effect of variability amplitude on the uncertainties of individual parameters does not seem to introduce strong dependencies on the value of `ruwe`; however, there is still some indication that high amplitude LPVs have larger `ruwe` values on average. Although less clear than in the individual components, vertical gradients of increasing `ruwe` for fainter sources are also evident.

4.5 Mira Variables in the LMC

We require a large sample at a fixed distance to define a method for separating Mira Variables from other LPVs. Therefore, we consider the 12 325 LPVs in the direction of the LMC. In Section 4.3.1, we cut the LMC solely with on-sky positions to ensure they are completely removed from the Milky Way sample of LPVs. Here, we take the spatially selected LMC LPVs and refine this cut by performing the proper motion

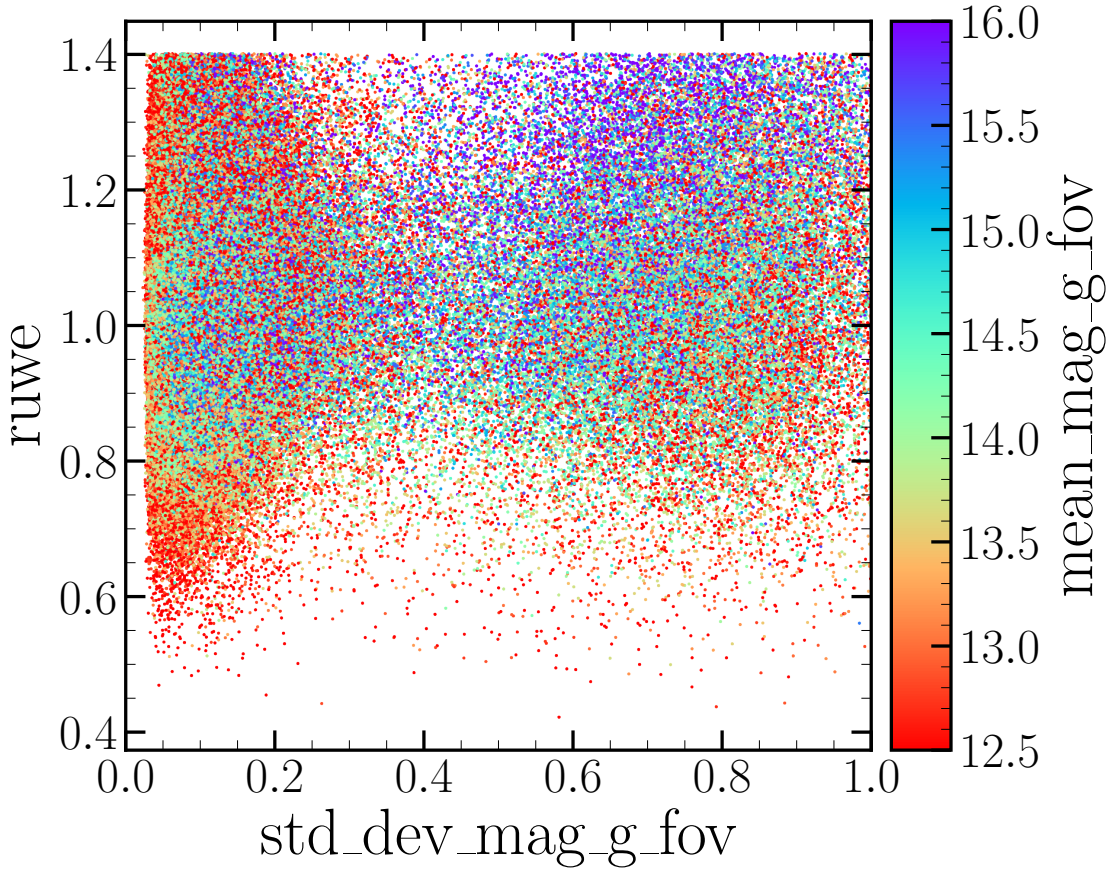

Figure 4.8: The distribution of `ruwe` as a function of stellar variability amplitude for LPV sources in the Milky Way. Points are coloured by their FoV mean magnitude.

selections presented in section 2 of Gaia Collaboration et al. (2021) (see also Gaia Collaboration et al. 2018), removing 493 stars. We also apply the above amplitude difference cut (Eqn. 4.3), leaving 11 803 stars in the final LMC LPV sample.

4.5.1 Identifying Track C

In Fig. 4.9, we present the period-magnitude plane for the LMC LPVs, where we find the variability tracks clearly identifiable. We identify the tracks by comparing them to previous studies of the LMC (Spano et al. 2011; Lebzelter et al. 2023) and label them accordingly. Miras are large amplitude oscillators; therefore, we can identify the Mira track by colouring this plane by the variability amplitude, σ_G^{FoV}, which highlights Track C.

We use the empirical period-luminosity relation of O-rich Miras from Yuan et al. (2017) to calculate the expected absolute magnitudes (M_{K_s}) of the LPVs:

$$M_{K_s} = -6.9 - 3.77 \times (\log(P) - 2.3) - 2.23 \times (\log(P) - 2.3)^2 - 0.17\,, \tag{4.6}$$

where P is the period of variability. Applying the distance modulus equation, assuming a distance to the LMC to be $d = 50\,\mathrm{kpc}$, we calculate the apparent magnitude as:

$$m_{K_s} = M_{K_s} + 5\log(d) + 10\,. \tag{4.7}$$

The expected apparent magnitudes of the LPVs as a function of the period also trace the Mira track. We use this period-luminosity relation as a guide and select stars that lie reasonably close to it[10], which we present in Fig. 4.10. We knowingly allow some over-spill onto the neighbouring tracks to capture as many Mira candidates as possible.

[10]Determined using the `PYTHON` package `SHAPELY` to calculate the geometric distance ($\mathcal{S}$) of LPVs from Eqn. 4.6 in the $m_{K_s} - P$ plane where $|\mathcal{S}| < 1.2$.

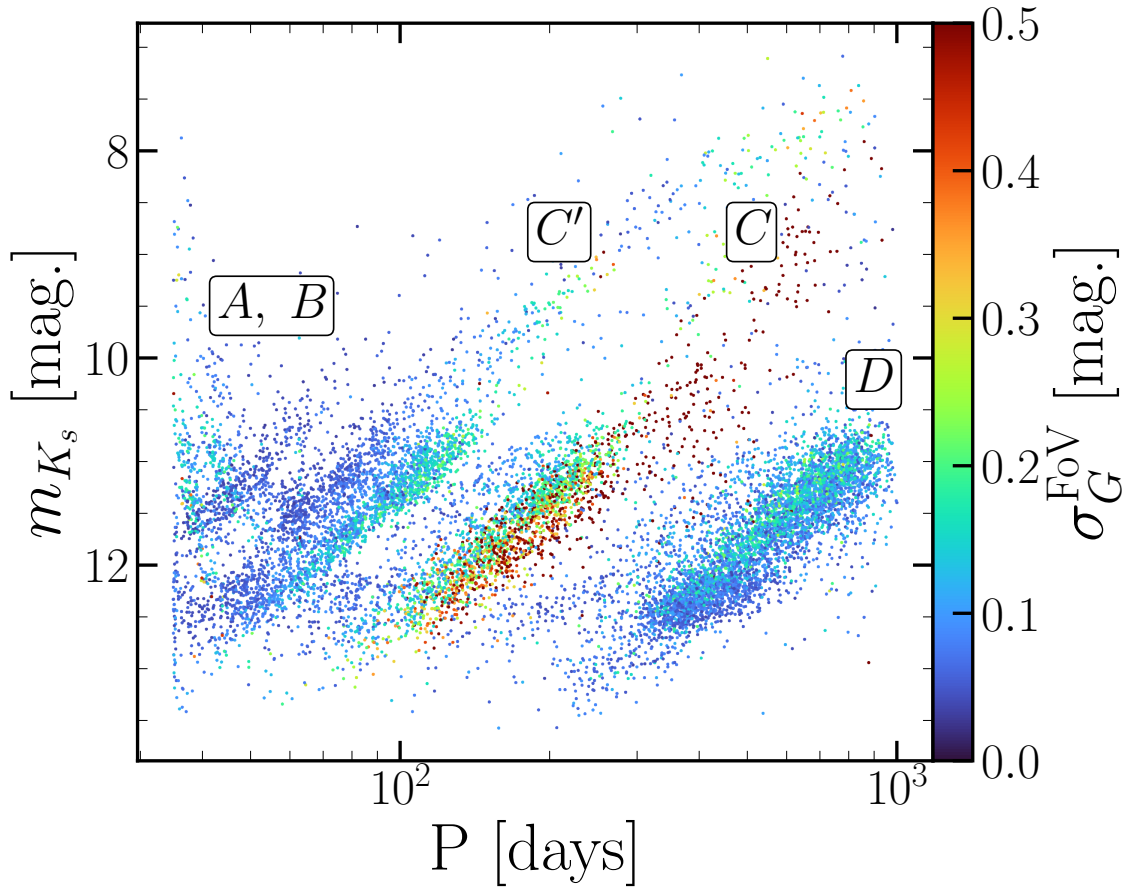

Figure 4.9: The 2MASS K_s-band apparent magnitudes of LPV sources in the LMC. Variability tracks are visible and labelled following Spano et al. (2011) and Lebzelter et al. (2023). Points are coloured by the standard deviation of the FoV magnitude ($\sigma_G^{\rm FoV}$, variability amplitude). The Mira track (Track C) is identifiable by the large variability amplitudes.

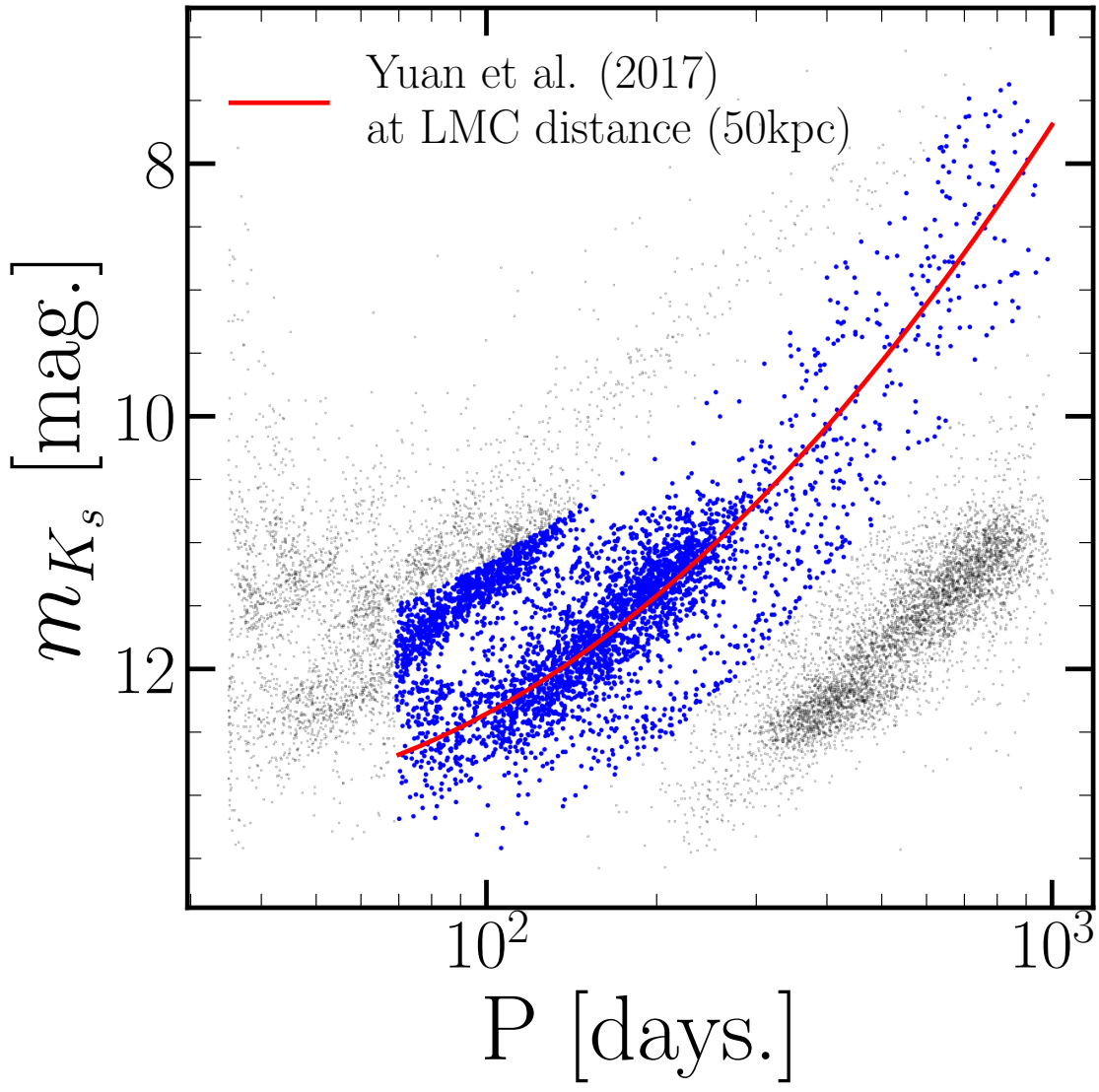

Figure 4.10: The 2MASS K_s-band apparent magnitudes of LPV sources in the LMC plotted as grey points with the period-luminosity relation of O-rich Miras from Yuan et al. (2017) plotted as the red line. Blue points are those geometrically close to this relation (we purposefully allow for a wider area to be captured as we refine our selection of Miras using other methods).

4.5.2 Relative Frequency Error

Miras oscillate mono-periodically compared to the multi-periodic oscillations of SRVs. Typically, separations between Miras and SRVs rely on amplitude-based cuts to distinguish between them. Trabucchi et al. (2021a) showed that SRVs with strong fundamental modes could also be used as distance indicators. Therefore, a more physically appropriate criterion to select fundamental mode oscillators should also include separations based on pulsation periods. Along Track C, we expect to find Mira variables and SRVs, with SRVs typically having larger amplitude secondary periods. As the *Gaia* variability pipeline only fits a single frequency model to the light curve, stars that oscillate with a strong fundamental mode will have a better fit than those with more significant secondary modes. Therefore we use the error generated by the frequency model to distinguish Mira variables and SRVs with only small amplitude secondary frequencies. We define a dimensionless relative frequency error, e_ν, as:

$$e_\nu = \sigma_\nu / \nu, \tag{4.8}$$

where σ_ν and ν are defined in the *Gaia* `vari_long_period_variable` table as `frequency_error` and `frequency`, respectively. We plot $\log(e_\nu)$ as a function of $\log(P)$ where P is the period $(1/\nu)$ of the models frequency in Fig. 4.11.

Sources with higher $\log(e_\nu)$ as a function of their period will also be sources where the single frequency modelling of the *Gaia* variability pipeline will return larger uncertainties in the frequency estimate, seen as a track in the right-hand panel of Fig. 4.11. Fundamental mode oscillators like Miras (which also have a large variability amplitude) occupy lower regions of this space, shown by the distribution on the left-hand panel of Fig. 4.11.

To find a quantitative threshold between the low and high relative error regimes, we fit a straight line to the distribution of the LMC LPVs, excluding Track C, to get the relation between $\log(e_\nu)$ and $\log(P)$ calculated to be $\log(e_\nu) = 0.882 \log(P)$. We

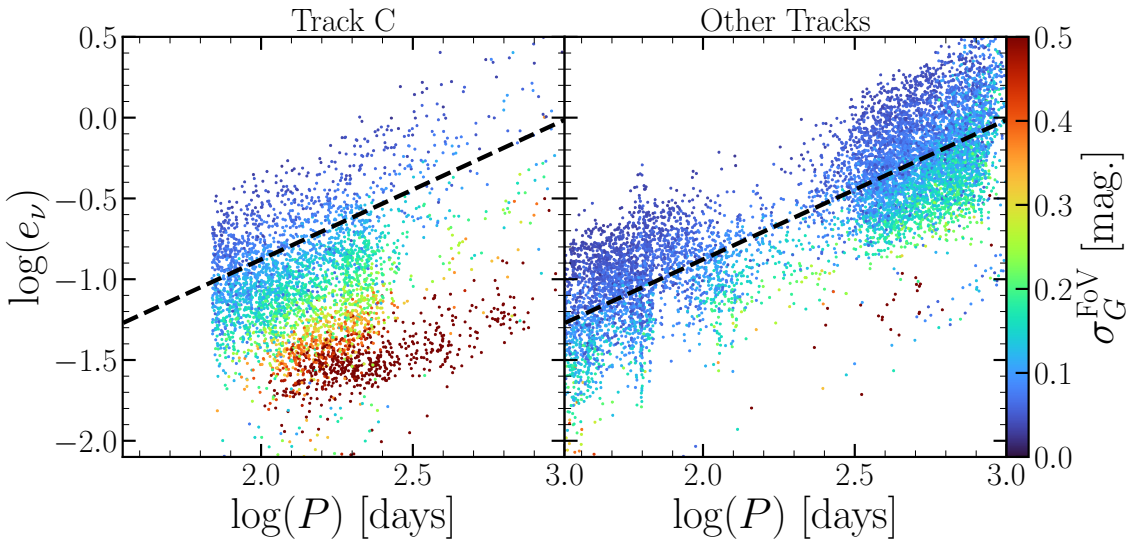

Figure 4.11: The log relative frequency error, $\log(e_\nu)$, as a function of log period, $\log(P)$, for LMC LPVs on the Mira track (Track C, left-hand panel) and those which are not (right-hand panel). Points are coloured by the variability amplitude, σ_G^{FoV}. The black dashed line is a linear fit to the stars not on Track C (right-hand panel) to get the gradient of the relation between $\log(e_\nu)$ and $\log(P)$ calculated to be $\log(e_\nu) = 0.882\log(P)$.

use this gradient and consider LPVs on Track C, iterating through intercept values and defining two samples above and below the intercept (*i.e.*, high and low relative frequency error). We then apply a two-sample Kolmogorov–Smirnov (KS) test to the two sample distributions of σ_G^{FoV} for that intercept (presented in the left-hand panel of Fig. 4.12). We attempted to find an intercept value that best separates the distributions into low and high variability amplitude. The null hypothesis of the two-sample KS test is that both distributions were sampled from populations with identical distributions. Thus tests for any violation of that null hypothesis – indicate that the distributions are different. We find a minimum in the KS statistic $\mathcal{D}$ where the two samples have the most significant difference. This results in an intercept value of $c = -3.18$ being the best separator of low and high amplitude variables on Track C.

Therefore we select fundamental mode variables in the LMC to be those stars on Track C where:

$$\log(e_\nu) < 0.882 \times \log(P) - 3.18, \tag{4.9}$$

In the right-hand panel of Fig. 4.12, we show that the intercept defined above follows the lower edge of the LMC $\log(e_\nu)$-$\log(P)$ relation from Tracks excluding Track C. Therefore, stars on Track C, also above this line, have a relative frequency error no smaller than other SRVs. We note some contamination from stars with low relative frequency error and low variability amplitude. We find fewer sources with large amplitude and high relative frequency error. Therefore, relying on a classification based solely on this metric is insufficient.

4.5.3 Mira Amplitude Distinction

As we shown in Fig. 4.13, there is still some overlap in the distributions of σ_G^{FoV} for the low and high relative frequency error regimes. Therefore, it is also prudent to also apply a threshold on variability amplitude to obtain a clean sample of Mira

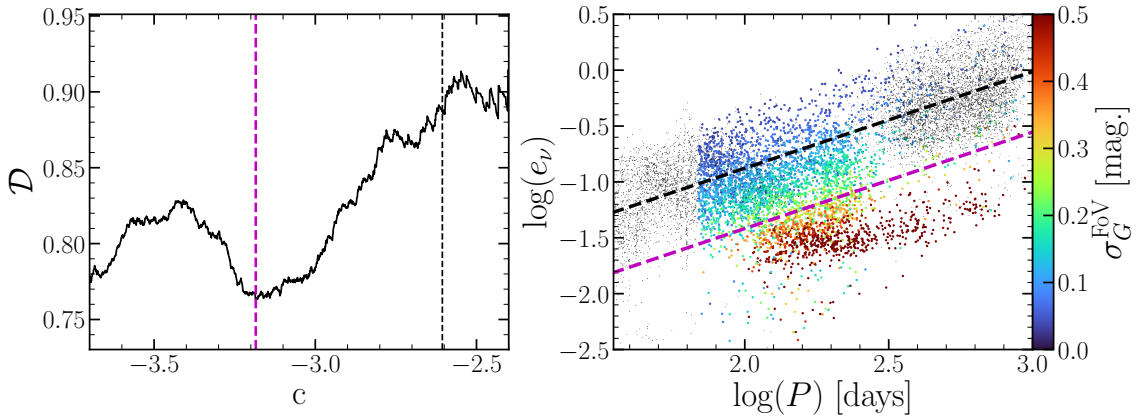

Figure 4.12: Left: results from KS tests for varying values of the $\log(e_\nu)$-$\log(P)$ relation intercept. The dashed black line denotes the initial linear fit to the LMC LPVs excluding Track C (right-hand panel of Fig. 4.11). The vertical dashed magenta line shows the location of the minimum KS statistic ($\mathcal{D}$), where we find the optimal intercept to be $c = -3.18$. Right: the black points show the LMC $\log(e_\nu)$, $\log(P)$ distribution for all LPVs. The $\log(e_\nu)$, $\log(P)$ distribution for Track C are coloured by σ_G^{FoV}. The black dashed line is a linear fit to the stars, not on Track C. The magenta dashed line is the linear fit with optimal intercept (identified in the left-hand panel, Eqn. 4.9). The magenta line separates low-amplitude SRVs from the fundamental variables below this line.

stars. Canonically, Mira variable definitions have relied on cuts in amplitude and colour. Since we can determine the variability tracks in the LMC and have defined a threshold between the low and high relative frequency error regimes, we can also find a variability amplitude cut that best separates Miras from SRVs. We must find the crossover region of the largest amplitude variables with high relative frequency error and the lowest amplitude fundamental mode oscillators (low relative frequency error). Taking the classification from relative frequency error as the 'truth' of whether a star is a Mira or a SRV (Eqn. 4.9), we can consider a varying threshold cut in amplitude, σ_G^{FoV} to make a 'predictive' classification of each star with Miras having larger amplitudes.

For each value of a threshold σ_G^{FoV}, we calculate the mean square contingency coefficient, r_ϕ[11] which is a measure the correlation of binary classification methods (Yule 1912; Matthews 1975). We then find the maximum value, which results in the closest match to the relative frequency error classification. The r_ϕ value for each threshold value is also presented as the right-hand axis in Fig. 4.13. We find a critical value of $\sigma_G^{\mathrm{FoV}} = 0.282$ mag. resulting in an r_ϕ value of 0.835 and overall accuracy (number of true positives and negatives as a fraction of all classifications) of 93.3% at reproducing the relative frequency error classification. The confusion matrix using this critical value is presented in the top right of Fig. 4.13.

While we expect to find good agreement between relative frequency error and amplitude cuts from the distributions presented in Fig. 4.12, we apply both cuts to the LMC LPVs, resulting in a sample of 966 LMC Mira variables, representing 8.2% (966 / 11 803) of the LMC LPV sample.

[11] $r_\phi = [(\mathrm{TP} \times \mathrm{TN}) - (\mathrm{FP} \times \mathrm{FN})]/\sqrt{(\mathrm{TP}+\mathrm{FP})(\mathrm{TP}+\mathrm{FN})(\mathrm{TN}+\mathrm{FP})(\mathrm{TN}+\mathrm{FN})}$, where TP = number of true positives, TN = number of true negatives, FP = number of false positives and FN = number of false negatives for each value of σ_G^{FoV} evaluated.

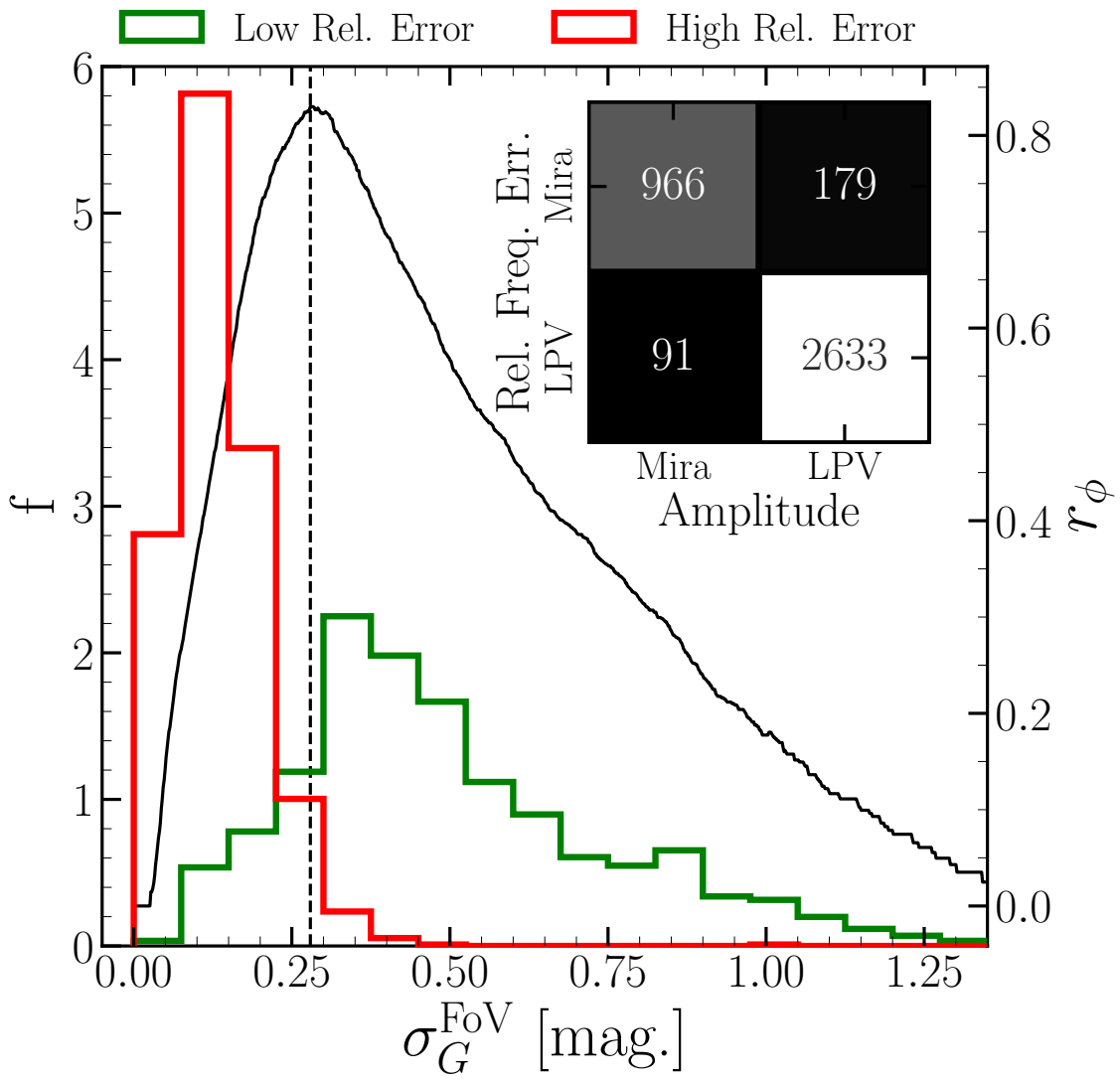

Figure 4.13: The normalised distributions of variability amplitude, $\sigma_G^{\rm FoV}$, for the low and high relative frequency error regimes (left-hand axis, green and red histograms, respectively) for stars on Track C in the LMC. The mean square contingency coefficient (r_ϕ) calculated at each value of $\sigma_G^{\rm FoV}$ is presented as the black line (right-hand axis). The vertical black dashed line shows the location of the maximum value of r_ϕ, giving the critical amplitude. The confusion matrix between definitions based on $\sigma_G^{\rm FoV}$ and relative frequency error for the critical amplitude ($\sigma_G^{\rm FoV} = 0.282$ mag.) is presented in the top right-hand corner.

4.6 Milky Way Mira Variables

We start with the base sample of 303 542 LPVs from the *Gaia* DR3 catalogue with the satellites removed (section 4.3.1). Then, we apply some further quality cuts in defining a Milky Way sample. The first is `gaia_source.ruwe` < 1.4 (Lindegren et al. 2021b), which is applied to remove 22 859 sources with bad astrometric solutions[12]. We also apply the same method presented in Section 4.3.2 to remove sources with large differences ($|\Delta A - \langle \Delta A \rangle| > 5\sigma_{\Delta A}$) in variability amplitude between the model amplitude and $\sigma_G^{\rm fov}$ for Milky Way LPVs. These quality cuts result in a clean sample of Milky Way LPVs of 283 063 sources.

We apply the relative frequency cut defined for the LMC (Section 4.5.2, Eqn. 4.9) to the Milky Way LPVs to separate fundamental mode oscillators from SRVs presented in Fig. 4.14. As a result, the large amplitude Mira candidates in the Milky Way clearly have lower relative frequency error and sit below the main distribution of SRVs.

In Fig. 4.15, we show the distributions of $\sigma_G^{\rm fov}$ for the low and high relative frequency error LPVs in the Milky Way. We again use the same definition of the critical amplitude from the LMC $\sigma_G^{\rm fov} \geq 0.282$, which separates these two distributions in the Milky Way. Therefore, Mira variables are LPV sources with low relative frequency and large amplitudes, which from the confusion matrix in the top right-hand corner of Fig. 4.14 gives a sample of 45 075 Miras in *Gaia* DR3. A further 4 306 sources have amplitudes above the critical value but also have significant secondary periods resulting in larger relative frequency error, and 6 047 LPVs have low relative frequency error but amplitudes below the critical value.

[12]We discussed in Section 4.4.2 the dependence of variability on the astrometric solution, which could bias us away from large-amplitude long-period Miras if a more stringent cut in `ruwe` is applied.

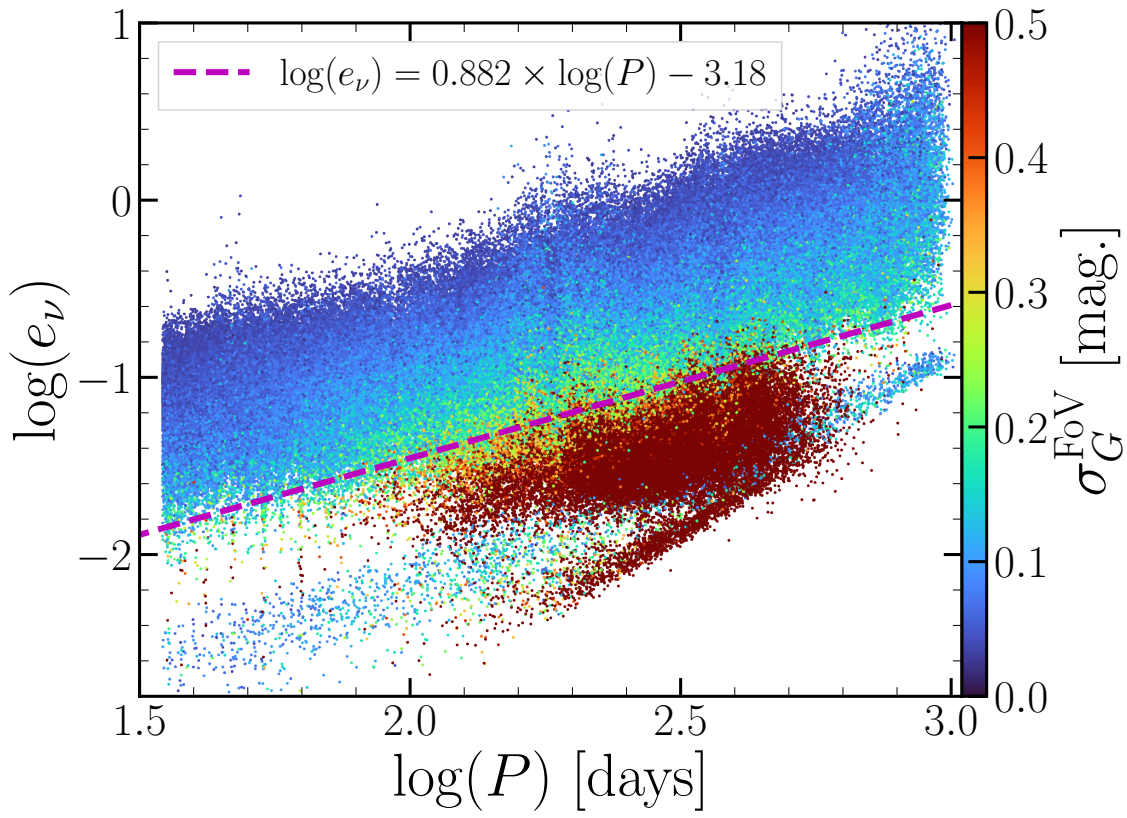

Figure 4.14: The log relative frequency error, $\log(e_\nu)$, as a function of log period, $\log(P)$, for Milky Way LPVs. Points are coloured by the variability amplitude σ_G^{FoV}. The magenta dashed line is the $\log(e_\nu)$-$\log(P)$ relation (Eqn. 4.9) derived in Section 4.5.2 for the LMC.

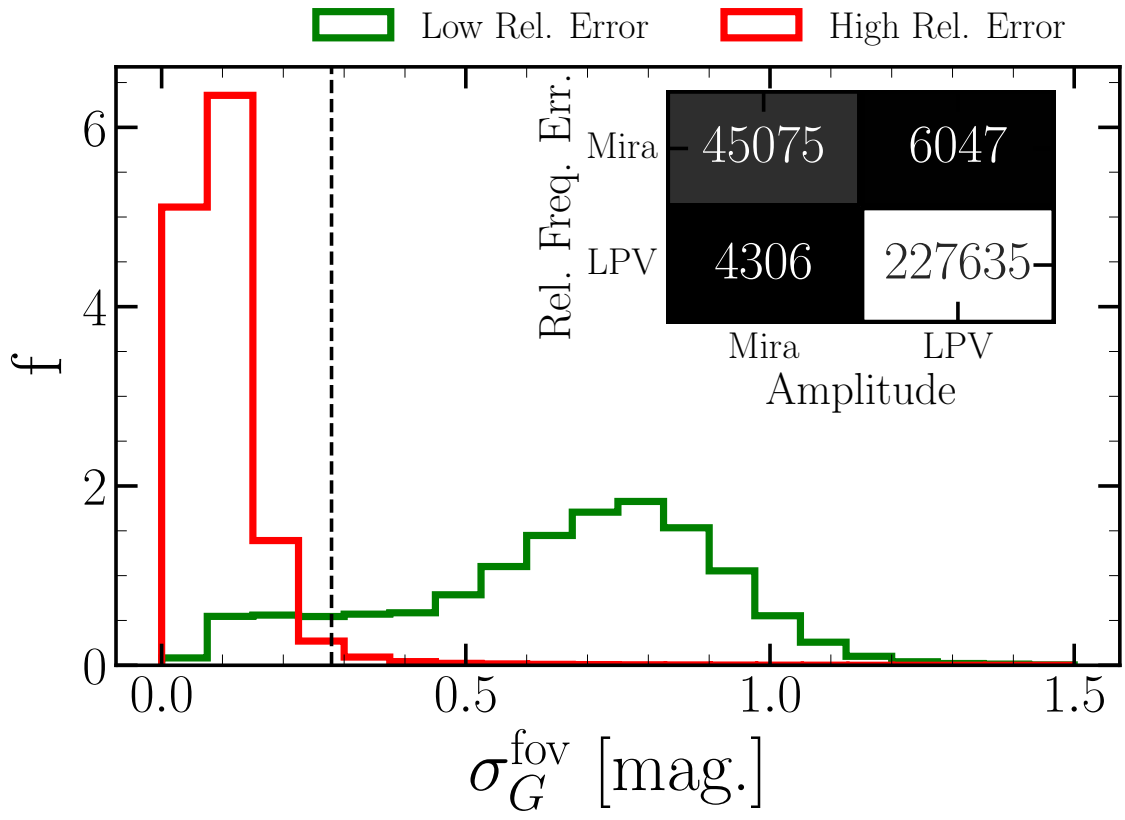

Figure 4.15: The normalised distributions of variability amplitude, $\sigma_G^{\rm FoV}$, for the low and high relative frequency error regimes (green and red histograms, respectively) for the Milky Way LPV sources. The vertical black dashed line shows the critical amplitude defined from the LMC (Section 4.5.3). The confusion matrix between definitions based on $\sigma_G^{\rm FoV}$ and relative frequency error for the critical amplitude ($\sigma_G^{\rm FoV} = 0.282$ mag.) is presented in the top right-hand corner.

4.6.1 Distance Estimates For Dust Correction

To determine the spatial distribution of Miras in the Milky Way, we must first correct their apparent magnitudes for dust. Using the same period-luminosity relation from Section 4.5.1 (Eqn. 4.6), we can calculate an absolute magnitude without correcting for dust and determine a distance (in kpc) using the distance modulus:

$$D_{\rm PL} = 10^{\left(\frac{m_{K_S} - M_{K_S}}{5} - 2\right)}, \tag{4.10}$$

where m_{K_S} is the 2MASS K_S-band measured apparent magnitude and M_{K_s} is the absolute magnitude calculated from the period of the Mira variable. We explore independent distance metrics to correct for the 3D dust distribution that would affect this relation. In Fig. 4.16, we present the distributions of distance from the period-luminosity relation against three other distance metrics. The first being the most straightforward approach of taking the inverse of parallax $(1/\varpi)$[13] which, as expected, does not show clear a monotonic relationship beyond a few kpc away from the Sun. The second two distances are derived from Bayesian inference of the parallax solution (`r_med_geo`) and Bayesian inference of the parallax and photometry (`r_med_photogeo`) from Bailer-Jones et al. (2021).

From these comparisons, it is clear that although there is only a weak correlation between period-luminosity distance and `r_med_photogeo` ($\rho = 0.35$), the latter represents the best independent measure of distance. We use this quantity to query 3D maps of the dust extinction in the Milky Way. For the Miras, we calculate the magnitude of extinction in the K_s-band, E_{K_s}, using the `combined19` dustmap (Drimmel et al. 2003; Marshall et al. 2006; Green et al. 2019) of the `PYTHON` package `MWDUST` (Bovy et al. 2016) and Bailer-Jones et al. (2021) parallax and photometry distance estimates.

Therefore the corrected distances, $D^*_{\rm PL}$, are calculated using the absolute magnitude from the period-luminosity relation (see Eqn. 4.6, Yuan et al. 2017) and the

[13]Calculated after applying parallax zero-point correction from Lindegren et al. (2021b).

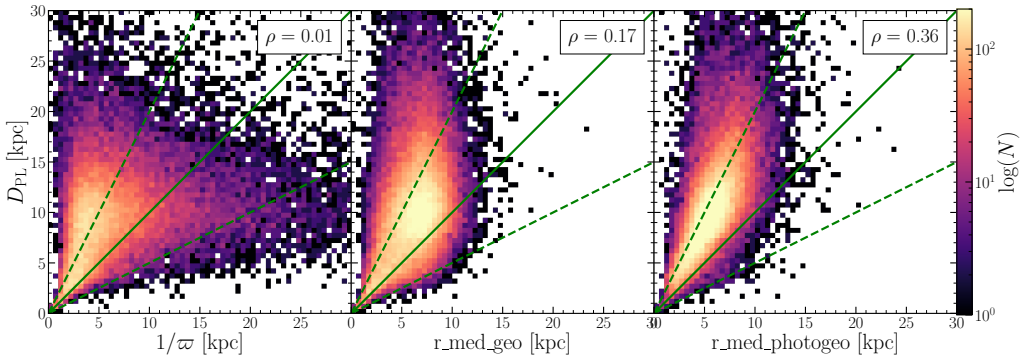

Figure 4.16: The number density distributions of distances derived from the uncorrected (for extinction) period-luminosity relation against distances derived from parallax (left-hand panel), Bayesian inference of the parallax solution (middle panel) and Bayesian inference of the parallax and photometry (right-hand panel). The Pearson correlation coefficients (ρ) for each combination are presented in the top right-hand corner of each panel. The green line denotes the 1:1 relation, whereas the dashed green lines show the 2:1 and 1:2 relations.

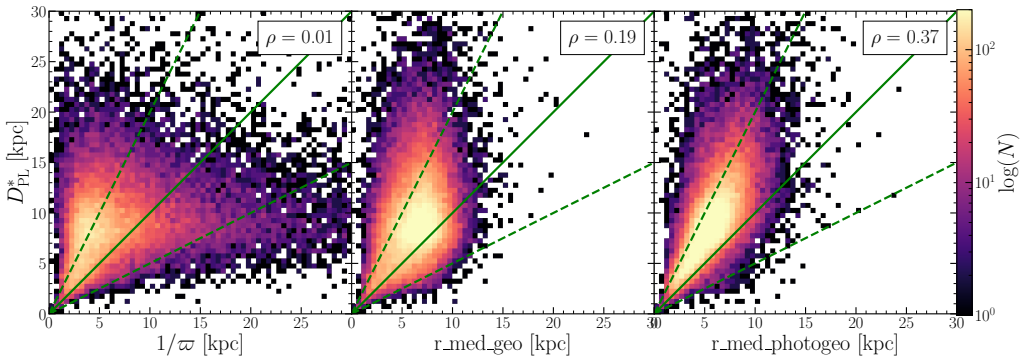

Figure 4.17: The same as Fig. 4.16 but for distances derived from the dust corrected period-luminosity relation (Eqn. 4.11).

distance modulus equation now including the K_s-band extinction:

$$D^*_{\rm PL} = 10^{\left(\frac{m_{Ks} - E_{Ks} - M_{Ks}}{5} - 2\right)}. \tag{4.11}$$

From Fig. 4.17, we can see an improvement in the correlations between the distances derived from the period-luminosity relation and those from parallax and photometry Bayesian inference. The distribution of Miras shifts downwards and towards the 1:1 relation in the figure, showing that without the dust corrections, the period-luminosity relation is overestimating their distances.

We are therefore left with 45 075 Mira variables in the Milky Way with 3D spatial coordinates $(\alpha, \delta, D^*_{\rm PL})$ and 2D on-sky Right Ascension and Declination proper motions, (μ_α, μ_δ) and therefore a 5D coordinate solution. We find that 3 231 Miras in our sample also have radial velocity measurements[14], so they have full 6D coordinates (RV sample).

4.6.2 Spatial and Kinematic Distributions

We now conduct a brief exploration of the Miras sample within the Milky Way. In Fig. 4.18, we show the distribution of Miras in galactocentric coordinates where the Sun is positioned at $x_\odot = -8.232$ kpc (Gravity Collaboration et al. 2019, 2021). The bar within the Milky Way is visible as a large over-density at the Galactic centre orientated clockwise away from x-axis (the line of sight between the Sun and the Galactic centre). The near side of the bar is seen at positive Galactic longitude. In the (x, z) and (y, z) projections, the effect of crowding and extinction in the plane is apparent, with fewer sources observed at low Galactic latitudes. The radial velocity sample (RV) is smaller than the full Milky Way sample as expected, but we still obtain coverage across the Galaxy, including the bulge and disc.

Referring back to the period-age relations presented in Section 4.1.1, we can determine period ranges to sample the extreme ends of the age distribution of Miras

[14] `gaia_source.radial_velocity`

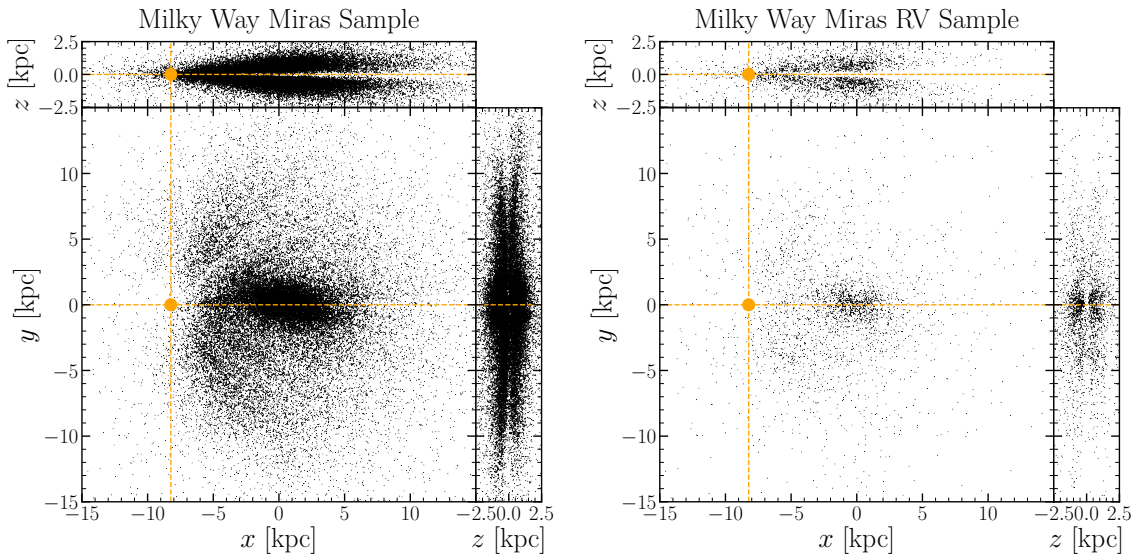

Figure 4.18: The spatial distribution in galactocentric projections of the Milky Way Miras sample (left-hand panels) and the distribution of Milky Way Miras with radial velocity measurements (right-hand panels). The orange point and orange dashed lines represent the solar position $(x, y, z)_{\odot} = (-8.232, 0.0, 0.0)$.

regardless of the relation employed. Relatively old and young Miras are selected as those with periods, $P < 200$ days and $P > 400$ days, respectively. We present the distribution of old and young Miras in Fig. 4.19 where we can observe the bar in long-period (young) Miras, which are also constrained to the plane. In contrast, the short-period Miras are centrally concentrated and are at greater vertical heights in the disc. In the (y, z)-projection, we can also see a more box-shaped central region in the young Miras compared to the more roundly distributed old Miras consistent with the findings of Grady et al. (2020a) and expected when considering the spatial distributions of differently aged populations in the Milky Way (*e.g.* Debattista et al. 2017; Fragkoudi et al. 2017c).

However, in the (x, z) projection, we do not see a clear 'X' or peanut shape. This may be due to a combination of the selection function of *Gaia* DR3 and uncertainties on the distance estimate, broadening the distribution of Miras towards the bulge.

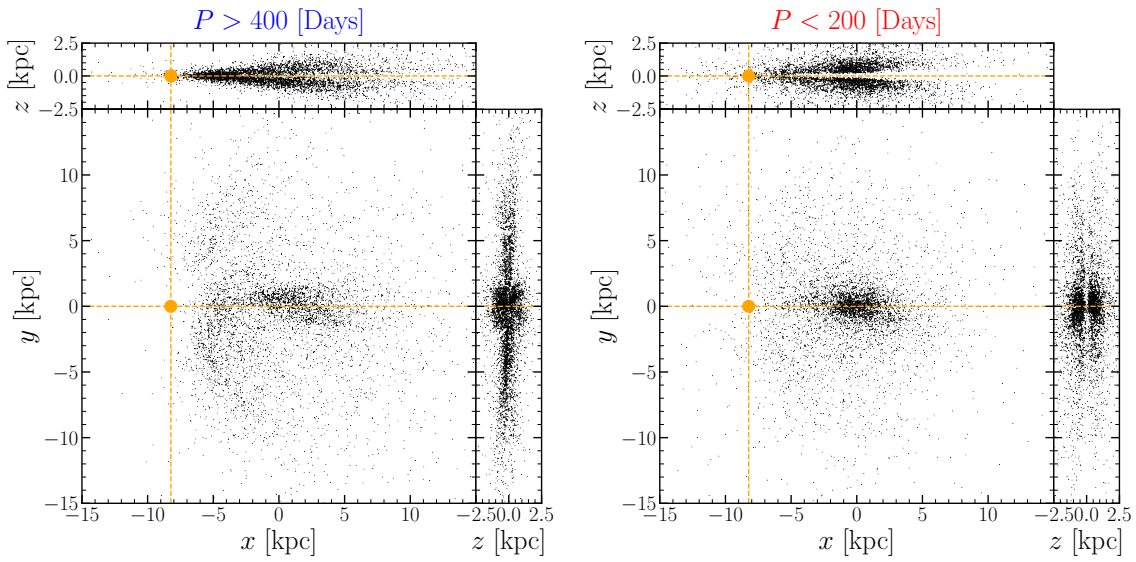

Figure 4.19: The spatial distribution in galactocentric projections of long-period Miras (young, left-hand panels) and short-period Miras (old, right-hand panels). The orange point and orange dashed lines represent the solar coordinates solar position $(x, y, z)_\odot = (-8.232, 0.0, 0.0)$.

Adjusting the selection to more favourable criteria, such as increasing the period threshold selecting younger Miras and spatially selecting those close to the y-axis (*i.e.*, $P > 500$ days and $|y| < 0.5$) results in too few Miras to observe the BP bulge within their distribution.

We use a Toomre diagram to determine Mira populations' contributions to different structures within the Milky Way, which we present in the top panel of Fig. 4.20. Here, v_R, v_ϕ and v_z are the cylindrical galactocentric velocities calculated using the coordinate transformation routines of `GALPY` (Bovy 2015) for the RV sample. Such diagrams have been widely used to distinguish between structures in the Milky Way by defining them kinematically (*e.g.*, Venn et al. 2004; Altmann et al. 2004; Qu et al. 2011; Yan et al. 2019), through the stellar populations' relative velocity compared to the Local Standard of Rest (LSR). Stars in the Milky Way thin disc typically have velocities such that $|\mathbf{V} - V_\odot| < 100\,\mathrm{km\,s^{-1}}$ (*e.g.*, Venn et al. 2004; Bensby et al.

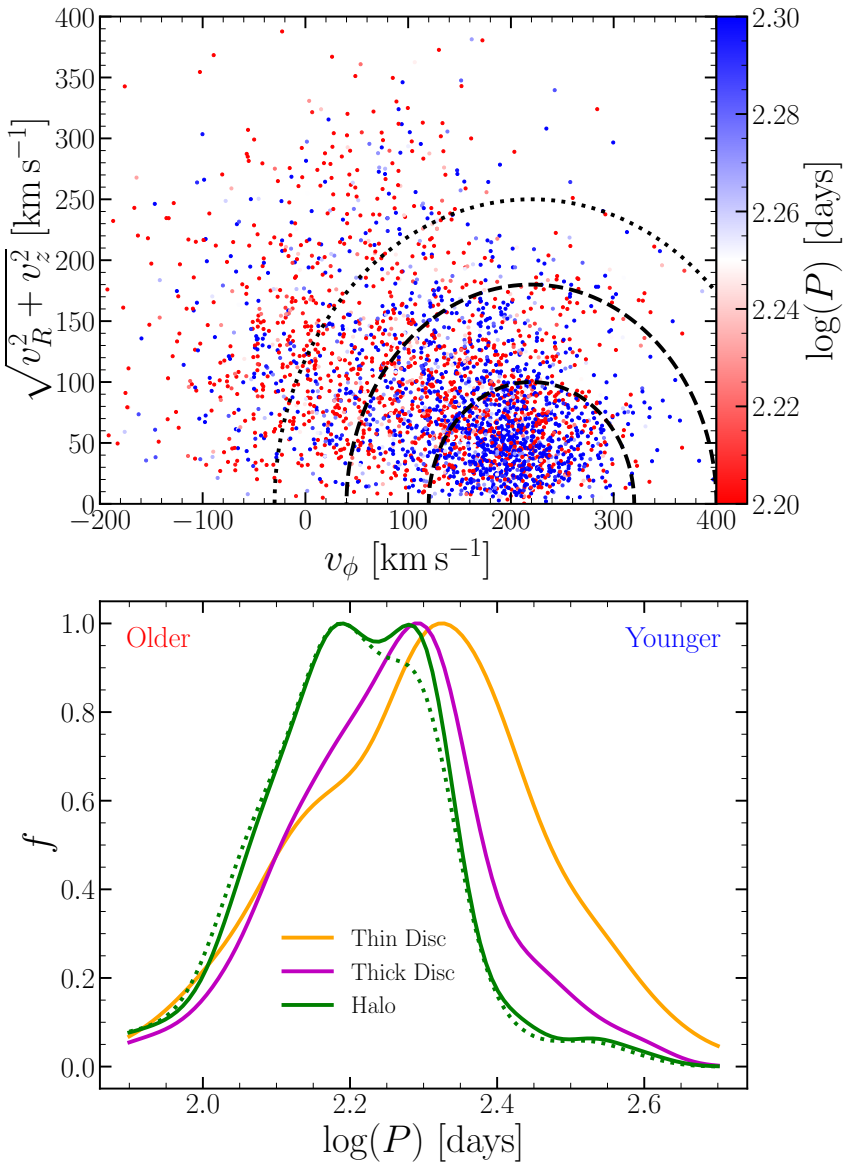

Figure 4.20: Top: a Toomre diagram of the Milky Way Miras RV sample coloured by the period, log(P). The black dashed lines denote the region where $|\mathbf{V} - V_\odot| = 100\,\mathrm{km\,s^{-1}}$ and $|\mathbf{V} - V_\odot| = 180\,\mathrm{km\,s^{-1}}$ for the inner and outer lines, respectively. The black dotted line defines the region of a purer halo population with $|\mathbf{V} - V_\odot| > 250\,\mathrm{km\,s^{-1}}$ (Koppelman & Helmi 2021). Bottom: the normalised distribution functions (f) of periods for Galactic stellar components defined in the Toomre diagram, the thin disc (orange), thick disc (magenta) and halo (green lines) where the dotted line follows the pure halo definition from above.

2014; Limberg et al. 2021) where $\mathbf{V}$ is the total velocity and of a star $V_\odot$ is the Solar tangential velocity ($V_\odot \approx 220\,\mathrm{km\,s^{-1}}$). Thick disc stars are defined in the interval $100 < |\mathbf{V}-V_\odot|/\,\mathrm{km\,s^{-1}} < 180$ and stars with velocities beyond $|\mathbf{V}-V_\odot| > 180\,\mathrm{km\,s^{-1}}$ are typically associated with the halo, but still contain over 15% of stars with thick disc kinematics. (*e.g.*, Amarante et al. 2020).

We find an ordering of increasing average period and distribution of the Milky Way RV Miras as we consider the structures of decreasing relative velocity, halo→thick disc→thin disc. Considering the average period of these structures, they follow what is expected from period-age relations but also highlight the evident uncertainty in this relation as there is much overlap in the distribution functions (bottom panel of Fig. 4.20). We define a purer sample of Mira halo stars following Koppelman & Helmi (2021) ($|\mathbf{V} - V_\odot| > 250\,\mathrm{km\,s^{-1}}$), which has a more prominent short-period peak in the bottom panel of Fig. 4.20. However, there is still considerable overlap in the period distribution of the thin and thick discs.

4.7 Conclusions

We have successfully extracted a sample of oxygen-rich LPVs from *Gaia* DR3 cross-matched with the 2MASS PSC. We utilise a sample of LPVs in the LMC to define novel methods for extracting Mira candidates using data-motivated cuts on their relative frequency error and variability amplitude, minimising contamination from SRVs. We have justified our cut on amplitude by deriving the threshold between Miras with high relative frequency error and low amplitude SRVs with low relative frequency error. The lowest amplitude Miras in our sample may be classified as SRVs, yet to be included in our sample; they must have strong fundamental mode oscillations and amplitudes larger than the rest of the SRVs in the LPV sample.

We then apply these methods to a Milky Way LPV sample to generate a catalogue of 45 075 Mira variables with dust corrections and 5D coordinates (full 6D

for 3 231 sources). Exploring the spatial and kinematic distributions of these Mira candidates as a function of the period, we find they follow expected trends for the distributions of the differently aged populations within the Milky Way. Therefore, Mira variables are good tracers for Galactic dynamics.

Our brief exploration of the kinematics of our Milky Way Miras sample highlights their utility in studying Galactic dynamics in the disc. However, there are still many challenges in studying the Milky Way bar and bulge. Such studies with older data releases of *Gaia* have begun to constrain properties of the bar, such as its age, using Mira variables (*e.g.*, Grady et al. 2020b). Recent studies have shown that large statistical samples of stars with varying chemistry (and inferably age) are able to confirm predictions from theoretical models, such as those presented in Chapter 3 (Marchetti et al. 2023). The more limited statistics of Miras within the bulge make similar kinematic signatures harder to detect. Further work will explore how this sample can be used to explore the dynamics of the Milky Way bulge and to prepare for future data releases of the *Gaia* mission.

Looking beyond the bar and bulge of the Milky Way, the Miras sample offers insight into the ages of stars in the outer disc. Stars in this region are a combination of stars formed at that radius and those that have migrated to that radius through secular processes, resulting in complex age and metallicity distribution functions (Roškar et al. 2008; Kubryk et al. 2013; Di Matteo et al. 2013; Grand et al. 2015; Loebman et al. 2016). The radial distribution of Miras of varying periods can also provide a novel approach to understanding the migration of stars in the Milky Way (Fiteni et al. 2024, *in prep.*).

From these samples, we have also characterised the effect of large variability amplitude on increasing the uncertainty in photometric and astrometric solutions within *Gaia* with implications for other multi-epoch surveys. This work has highlighted the importance of custom data pipelines for LPV sources and understanding

the photometric, astrometric and variability models for large amplitude variables. Future *Gaia* data releases will also include fits of multi-periodic solutions to the light curves of LPVs, allowing for a more sophisticated approach to separating Miras from SRVs.

Chapter 5

Box/Peanut Bulges in Cosmological Simulations

The following chapter is comprised of extracts of contributions to a paper submitted to the *Monthly Notices of the Royal Astronomical Society* as Anderson et al. (2023), entitled:

The interplay between accretion, downsizing and the formation of box/peanut bulges in TNG50

presented by the following authors:

Stuart Robert Anderson,[1], *Steven Gough-Kelly*,[1] Victor P. Debattista,[1,2] Min Du,[3], Peter Erwin,[4,5] Virginia Cuomo,[6] Joseph Caruana,[7,2] Lars Hernquist[8] and Mark Vogelsberger[9]

[1]Jeremiah Horrocks Institute, University of Central Lancashire, Preston, PR1 2HE, UK

[2]Institute of Space Sciences & Astronomy, University of Malta, Msida MSD 2080, Malta

[3]Department of Astronomy, Xiamen University, Xiamen, Fujian 361005, China

[4]Max-Planck-Insitut für extraterrestrische Physik, Giessenbachstrasse, 85748 Garching, Germany

CHAPTER 5

[5]Universitäts-Sternwarte München, Scheinerstrasse 1, D-81679 München, Germany

[6]Instituto de Astronomía y Ciencias Planetarias, Universidad de Atacama, Avenida Copayapu 485, 1350000 Copiapó, Chile

[7]Department of Physics, Faculty of Science, University of Malta, Msida MSD 2080, Malta

[8]Harvard–Smithsonian Center for Astrophysics, 60 Garden Street, Cambridge, MA 02138, USA

[9]Department of Physics and Kavli Institute for Astrophysics and Space Research, Massachusetts Institute of Technology, Cambridge, MA 02139, USA

5.1 Introduction

The stellar bar of disc galaxies are key drivers of secular evolution (Weinberg 1985; Debattista & Sellwood 1998; Athanassoula 2002; Athanassoula & Misiriotis 2002; Athanassoula 2003; Kormendy & Kennicutt 2004; Holley-Bockelmann et al. 2005; Debattista et al. 2006; Ceverino & Klypin 2007; Dubinski et al. 2009). Box/peanut bulges (BPs) are the vertically extended regions of galactic bars and are common in barred galaxies such as the Milky Way (Erwin & Debattista 2017, hereafter ED17). Stellar populations in the Milky Way that form over a range of ages trace barred and box/peanut-shaped structures in the bulge. Red clump stars within the Milky Way bulge exhibit a bimodal distribution as a function of apparent magnitude (distance) through the box/peanut bulge (McWilliam & Zoccali 2010; Nataf et al. 2010; Saito et al. 2011; Wegg & Gerhard 2013; Gonzalez et al. 2015).

In external galaxies, ED17 studied 84 local barred galaxies from the Spitzer Survey of Stellar Structure in Galaxies (S^{4}G, Sheth et al. 2010), finding the fraction of BPs amongst barred galaxies to be a strong function of stellar mass, and that above a stellar mass $\log(M_\star/\mathrm{M}_\odot) \simeq 10.4$, approximately 79% of barred galaxies host BP bulges. In context, the Milky Way has a mass of $\log(M_\star/\mathrm{M}_\odot) = 10.69 - 10.86$ (Licquia & Newman 2015); therefore is not unusual to have a BP bulge.

Furthermore, Gadotti et al. (2020) found a fraction of 62% BPs in a sample of 21

massive barred galaxies from the Time Inference with MUSE in Extragalactic Rings (TIMER) project (Gadotti et al. 2019). Marchuk et al. (2022) also found an upturn in BP fraction at $\log(M_\star/\mathrm{M}_\odot) \simeq 10.4$ in their sample of 483 edge-on galaxies from the Dark Energy Spectroscopic Instrument (DESI, DESI Collaboration et al. 2016) survey.

The formation and evolution of BP bulges have been studied in detail using numerical simulations (*e.g.*, Raha et al. 1991; Athanassoula & Misiriotis 2002; Berentzen et al. 1998; Bureau & Athanassoula 2005; Martinez-Valpuesta et al. 2006; Saha & Gerhard 2013; Fragkoudi et al. 2017b; Debattista et al. 2017; Saha et al. 2018; Łokas 2019; Ciambur et al. 2021; Anderson et al. 2023). As discussed in Section 1.6.1 of the thesis introduction, we find there are two mechanisms for forming as BP bulges, the buckling instability (Raha et al. 1991; Merritt & Sellwood 1994; Martinez-Valpuesta & Shlosman 2004; Smirnov & Sotnikova 2019) and the heating of stars by vertical resonances (Combes & Sanders 1981; Combes et al. 1990; Pfenniger & Friedli 1991; Skokos et al. 2002a; Quillen 2002; Quillen et al. 2014; Debattista et al. 2006; Sellwood & Gerhard 2020) and potential combinations of the two (see also Li et al. 2023).

Work on BP bulges in a cosmological context has been conducted using Zoom simulations. Examples of BP have been found in the Auriga suite of Milky Way-Like models (Grand et al. 2017, 2019) by Blázquez-Calero et al. (2020) and Fragkoudi et al. (2020) who found BP fractions of 19% and $\sim 30\%$ of barred galaxies respectively. These fractions are considerably lower than what is observed in the local Universe.

For this work, we use the highest resolution run of the IllustrisTNG (Pillepich et al. 2018b; Springel et al. 2018; Nelson et al. 2018; Naiman et al. 2018; Marinacci et al. 2018) suite of simulations. We define and extract disc galaxies from the TNG50 simulation (Nelson et al. 2019a,b; Pillepich et al. 2019) to investigate galaxies with

bars and BPs at $z = 0$. TNG50 offers an unrivalled opportunity to investigate BP galaxies with reasonably high resolution but for a significantly larger self-consistent sample of BP galaxies than has previously been possible. In this work, we define novel metrics for determining the BP strength of a galaxy and use them to discern the BP formation mechanism. From these methods, we are also able to determine the time of bar and BP formation.

5.2 TNG50

IllustrisTNG (Pillepich et al. 2018b; Springel et al. 2018; Nelson et al. 2018; Naiman et al. 2018; Marinacci et al. 2018) is a suite of advanced cosmological simulations within the ΛCDM framework that employs magneto-hydrodynamics described in detail in Weinberger et al. (2017) and Pillepich et al. (2018a). TNG50 simulated 2×2160^3 dark-matter particles and gas cells within a volume of side-length $35/h$ or ~ 50 c Mpc. Alongside a baryonic mass resolution of $8.5 \times 10^4\,\mathrm{M}_\odot$ and gravitational softening length for stellar particles of $\epsilon = 288$ pc ($1 \geq z \geq 0$) the simulation also achieves gas cell sizes as small as 70 pc in dense star-forming regions. This results in a large statistical sample of galaxies at 'zoom'-like resolution including many disc galaxies (Nelson et al. 2019b; Pillepich et al. 2019).

Dark matter halos within IllustrisTNG are identified using the friends-of-friends algorithm (Davis et al. 1985); subhalos within each halo were identified using the `SUBFIND` algorithm (Springel et al. 2001; Dolag et al. 2009). Gravitationally bound stellar masses within a halo or subhalo are defined as Galaxies. We extract all the bound particles within a (sub)halo associated with a galaxy and place the centre of the potential at the origin. We align the angular momentum vector within two effective radii ($2R_{\mathrm{eff}}$) of the stellar disc with the z-axis, resulting in the stellar disc being in the (x, y)-plane. For each galaxy, we extract the main leaf progenitor branch (Rodriguez-Gomez et al. 2015) to study their evolutionary history.

Symbol	Description
$R_{\rm eff}$	Cylindrical radius containing half the total stellar mass.
$M_\star$	Stellar mass of a galaxy (within a spherical radius $r \leq 10R_{\rm eff}$).
$K_{\rm rot}$	Measure of the fraction of kinetic energy attributed to rotational motion, defined in Section 5.3 (within cylindrical radius $R \leq 30\,{\rm kpc}$)).
$\mathcal{B}$	'Strength' of the BP bulge, measured as described in Section 5.5.
$t_{\rm bar}(z_{\rm bar})$	Time (redshift) of bar formation, assessed as described in Section 5.4.
$t_{\rm BP}(z_{\rm BP})$	Time (redshift) of BP formation, assessed as described in Section 5.8.
$t_{\rm buck}(z_{\rm buck})$	Time (redshift) of buckling, assessed as described in Section 5.5.1.

Table 5.1: Summary of notation used in this chapter.

For the purpose of our study, we seek barred-disc galaxies at the current epoch (*i.e.* $z = 0$). We do not consider galaxies which may have been disc or barred at earlier epochs that do not survive until $z = 0$. To ensure our sample is resolved enough with sufficient stellar particles, we restrict our sample to galaxies with $\log(M_\star/{\rm M}_\odot) \geq 10.0$. For the reader's convenience, we present a list of the notation we use in this chapter for various metrics and parameters of the galaxies in Table 5.1.

5.3 Barred Galaxies

Disc galaxies were selected at $z = 0$ following the method used by Zhao et al. (2020) with TNG100: we select those galaxies with stellar masses $M_\star \geq 10^{10}\,{\rm M}_\odot$ within a spherical radius of 30 kpc. We align the galaxy onto the (x, y)-plane using the angular momentum vector as described in Section 5.2. Disc galaxies are those with stellar kinematics dominated by ordered rotation using the $K_{\rm rot}$ parameter (Sales

et al. 2010):

$$K_{\rm rot} = \frac{1}{M} \sum_k \frac{m_k v_{\phi,k}^2}{v_{x,k}^2 + v_{y,k}^2 + v_{z,k}^2}, \tag{5.1}$$

where the sum is over all stellar particles k within the 30 kpc sphere, and M is the total stellar mass within the sphere. $K_{\rm rot}$ measures the fraction of stellar kinetic energy committed to in-plane rotation. Disc galaxies are defined as those having $K_{\rm rot} \geq 0.5$ (Zhao et al. 2020). These cuts result in a sample of 608 disc galaxies at $z = 0$. We refer to this as the 'disc sample'. For this sample, the number of stellar particles within $10R_{\rm eff}$ is $(1.7 - 96.0) \times 10^5$ (median 4.0×10^5) and the number of gas particles ranges from just 221 to 2.0×10^6 (median 2.1×10^5) at $z = 0$. From this point on, metrics are computed with a spherical radius of $10R_{\rm eff}$ unless otherwise noted.

Since a bar is a bisymmetric deviation from axisymmetry, we define the global bar strength, $A_{\rm bar}$, as the amplitude of the $m = 2$ Fourier moment of the stellar particle surface density distribution, projected onto the (x, y)-plane. We calculate the global bar amplitude as:

$$A_{\rm bar} = \left| \frac{\sum_k m_k e^{2i\phi_k}}{\sum_k m_k} \right|, \tag{5.2}$$

where ϕ_k and m_k are the azimuthal angle and mass of each star particle. We compute the radial profile of a bar's amplitude as:

$$a_2(R) = \left| \frac{\sum_{k,R} m_k e^{2i\phi_k}}{\sum_{k,R} m_k} \right|, \tag{5.3}$$

where now the sum runs over all stellar particles within a given cylindrical annulus of radius R. We also calculate the phase of the $m = 2$ Fourier moment within each annulus. Within the region where the $m = 2$ phase is constant to within 10°, we define the maximum of $a_2(R)$ as $a_{2,\rm max}$. We consider a galaxy to be barred if $a_{2,\rm max} > 0.2$. This results in a sample of 266 barred galaxies (44% of the disc sample).

Many methods have been devised for measuring bar lengths, each having advantages and disadvantages (e.g. Aguerri et al. 2000; Athanassoula & Misiriotis 2002; Erwin 2005; Michel-Dansac & Wozniak 2006; Cuomo et al. 2021). At each time step in the simulation for each barred galaxy identified above, we compute the bar's radius, $R_{\rm bar}$, as the average of the cylindrical radius at which the amplitude of the $m = 2$ Fourier moment reaches half its maximum value (so $a_{2,\rm max}/2$) after its peak, and the cylindrical radius at which the phase of the $m = 2$ component deviates from a constant by more than 10° beyond the peak in $a_2(R)$ (the median of half the difference between the two measures is $\sim 20\%$ of the bar radius).

While TNG50 has a large number of galaxies modelled, the large force softening means that the force resolution is comparable to the disc thickness. Therefore density and bending waves (such as those involved in the buckling instability) are not well resolved (Merritt & Sellwood 1994). Hence dynamical processes are not fully resolved for small bars. Hence, we restrict our attention to those BPs whose extent is at least twice the softening length (288 pc at $z = 0$) to be secure in our recognition of BPs. In their study of 84 moderately inclined local barred galaxies ED17 found that the range of sizes of the BP as a fraction of the bar radius is $0.25 - 0.76$ (see also Lütticke et al. 2000). In ED17, the authors determined the BP 'extent' visually from sky-plane density isophotes, taking it as the radius beyond which spurs, rather than boxy, isophotes dominate. To determine a minimum bar radius cut with respect to the softening length of the simulation, we assume BPs in TNG50 would manifest isophotes in the same manner, hence that we can use the same ratio. Hence, we require a minimum bar radius of ~ 2 kpc, and so we exclude galaxies with $R_{\rm bar} < 2$ kpc. We argue in Section 5.5.2 for a more stringent cut of $R_{\rm bar} < 2.6$ kpc. This more stringent cut eliminates 75 of the 266 barred galaxies, resulting in a final sample of 191 barred galaxies out of 608 ($\sim 31\%$) disc galaxies.

We refer to this as the 'barred sample'. We emphasize that it includes only those

galaxies with bars at $z = 0$, whose radius is ≥ 2.6 kpc, having $a_{2,\max} > 0.2$, and not those which may have formed bars which dissolved (or shrank to a radius < 2.6 kpc or weakened to below $a_{2,\max} = 0.2$) before $z = 0$.

Rosas-Guevara et al. (2022) studied barred galaxies in TNG50 with total stellar mass $\log(M_\star/\mathrm{M}_\odot) \geq 10$, defined as the mass enclosed within $10R_{\rm eff}$. Disc particles were defined as those with circularity parameter[1] $\varepsilon \geq 0.7$, and disc galaxies were defined as those with disc/total mass fraction $> 50\%$. Using this method, and a different bar length cutoff criteria than used in this study (RG used a bar radius limit based on softening length), they found 349 discs and 105 (30%) bars, compared to this study's 608 discs and 191 (31%) bars. The method used in this paper captures the same fraction of bars, but in greater numbers, and to enhance statistics, we retain the use of $K_{\rm rot}$ to identify disc galaxies.

Fig. 5.1 shows the stellar mass distributions at $z = 0$ for the disc (608 galaxies), all barred (266 galaxies), barred with $R_{\rm bar} \geq 2.6$ kpc (191 galaxies) and unbarred galaxies. The stellar mass distribution of the barred sample is similar to the mass distribution of all (*i.e.* including those with $R_{\rm bar} < 2.6$ kpc) barred galaxies.

5.4 Time of Bar Formation

Following Algorry et al. (2017), we track the evolution of the $m = 2$ Fourier amplitude for the barred sample, and set the threshold of bar formation at $a_{2,\max} = 0.2$. We consider the bar to have formed when we detect at least four consecutive snapshots with $a_{2,\max} > 0.2$, taking the formation time as the first step where this occurs. We denote this time as $t_{\rm bar}$. Once this is identified, we compare with the evolution of $A_{\rm bar}$. Since during bar formation the bar amplitude grows exponentially, after

[1] $\varepsilon = J_z/J(E)$, where J_z is the specific angular momentum of the particle around the z-axis, and $J(E)$ is the maximum specific angular momentum possible at the specific binding energy of a stellar particle.

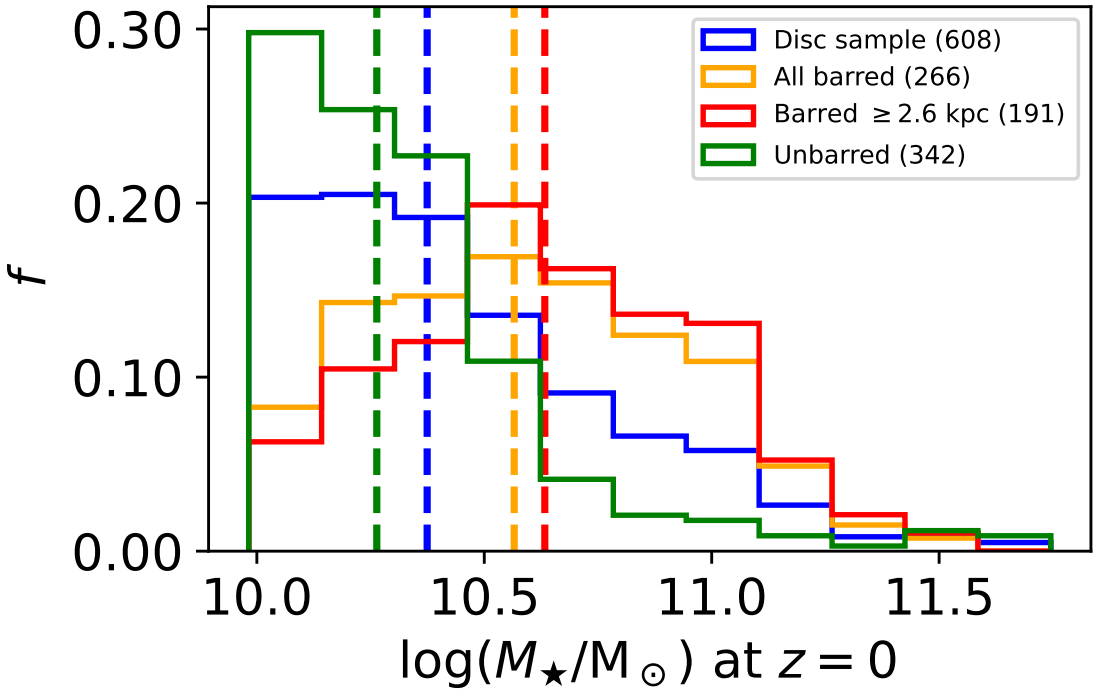

Figure 5.1: The distribution of stellar mass at $z = 0$ for all disc galaxies (disc sample – 608 galaxies, blue line), for all galaxies in the disc sample with bars ($a_{2,\max} > 0.2$, 266 galaxies, orange line) and for the galaxies in the disc sample without bars (342 galaxies, green line) at $z = 0$. The red line shows the distribution for all bars within the disc sample with $R_{\rm bar} \geq 2.6\,{\rm kpc}$ (191 galaxies, see Section 5.3). The vertical dashed lines show the median stellar masses in each group.

the instability has saturated we expect to see, at most, a slower secular growth. Therefore, we inspect the evolution of $A_{\rm bar}$ for each galaxy as a check on the reasonableness of the derived $t_{\rm bar}$. Examples of this procedure are shown in Fig. 5.2, where $A_{\rm bar}$ stabilises within two or three snapshots after $t_{\rm bar}$. This Figure also shows that bars can continue to grow after $t_{\rm bar}$.

This method works well in 161 (84%) of the 191 barred galaxies, as confirmed by visual inspection of the density profiles. However, in 30 (16%) barred galaxies, the evolution of $A_{\rm bar}$ and $a_{2,\rm max}$ is too noisy to find $t_{\rm bar}$ within the algorithm's rules. In these cases, we inspect the (x, y) density distributions at each redshift and set $t_{\rm bar}$ manually. Note that 14 (7%) of the bars have $t_{\rm bar}$ earlier than $z = 2$.

5.5 Quantification of BP Strength

The strength of a BP is a challenging concept to define, but is important for our analysis. Previous methods of determining the BP strength have included using the median height (*e.g.*, Fragkoudi et al. 2020), mass excesses when modelling the bulge as a spheroidal component (*e.g.*, Abbott et al. 2017) and m-fold deviations from a pure ellipse in edge-on views (*e.g.* Ciambur et al. 2021).

In this work we measure the fourth order Gauss-Hermite moment of the vertical velocity distributions (Gerhard 1993; van der Marel & Franx 1993) along the bar's major axis. The fourth order term in this series, h_4, measures how peaked the distribution is compared to a Gaussian. If the distribution has $h_4 > 0$ at a particular point, then it is more sharply peaked than a Gaussian. If $h_4 < 0$ then the distribution is flatter than a Gaussian. Debattista et al. (2005) demonstrated that a BP bulge, when viewed face-on, produces two deep minima in the h_4 profile, on either side of the galactic centre along the bar major axis. This was confirmed observationally by Méndez-Abreu et al. (2008) in NGC 98. The minima appear because the vertical velocity distribution of stars is broadened by the presence of a BP. As did Debattista

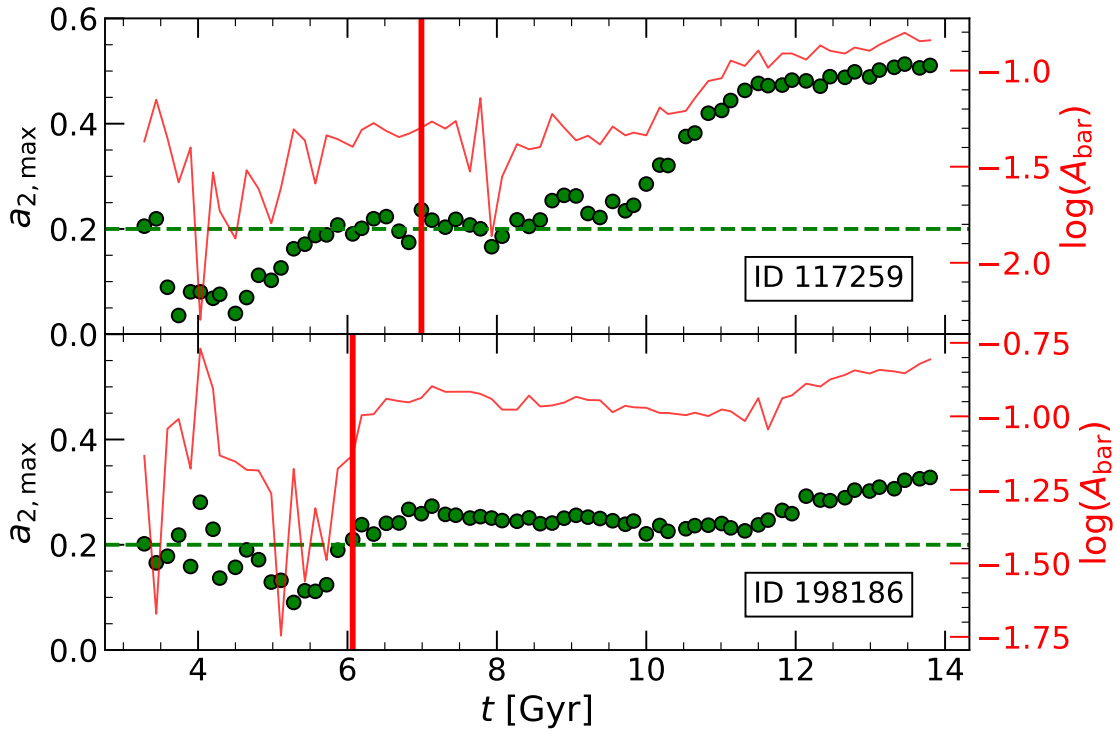

Figure 5.2: Bar formation time identification for two TNG50 barred galaxies. The horizontal green dashed line shows the $a_{2,\mathrm{max}}$ threshold and the green points show $a_{2,\mathrm{max}}$ values at each timestep. The solid red line shows $\log(A_{\mathrm{bar}})$ at each step. The thick red vertical lines indicate the time of bar formation, defined in Section 5.4. The galaxies are labelled with their TNG50 Subhalo IDs.

et al. (2005), in addition to the h_4 profile, we also examined the fourth order Gauss-Hermite moment of the height distribution along the bar major axis (d_4), but found this to be noisier and more challenging to constrain than h_4. Thus for our BP strength metric we rely solely on h_4.

We calculate the h_4 profile of v_z along the bar major axis (we continue to use a cut of $|y| \leq 0.3R_{\rm bar}$) for each barred galaxy at every redshift, and identify the minima in h_4 on either side of $x = 0$, if present. A high signal-to-noise (S/N) ratio is required to compute accurate Gauss-Hermite moments. To achieve this, we bin along the bar major axis with an adaptive number of bins (found by experimentation) based on the particle count within the cut. We compute the S/N ratio as $\sqrt{N_p}$, where N_p is the particle count within each bin (Du et al. 2016). If we find minima in the resulting h_4 profile, we broaden the bins until we reach S/N ≥ 50 at the location of the minima. To aid in detecting the peaks and valleys, we smooth the resulting h_4 profiles using a second order Butterworth filter (Butterworth 1930) and interpolate using a cubic spline. We use the `SIGNAL` module of the `PYTHON SCIPY` library to search for peaks and valleys in the profiles, setting a limit λ on the number of extrema per kpc in the profile, rejecting any profile which has too many peaks or valleys per kpc as being too noisy. After some experimentation we set $\lambda = 1.75\,\mathrm{kpc}^{-1}$. A profile without a valley on each side of $x = 0$ is deemed to be a non-BP profile. We avoid valley locations too close to the galactic centre (within 10% of the bar radius from the centre), and too close to the end of the bar (within 10% of the end). Selecting the deepest valley on each side of $x = 0$, we compute their mean, and denote this as $\overline{h_{4,\rm valley}}$. We take the peak in h_4 between these two valleys, denoted as $\overline{h_{4,\rm peak}}$, and use the difference as the peak−valley amplitude $\mathcal{B}$:

$$\mathcal{B} = \overline{h_{4,\rm peak}} - \overline{h_{4,\rm valley}}\,. \tag{5.4}$$

We use this dimensionless quantity as the BP strength metric, akin to its prominence. Its growth indicates large vertical excursions along the bar region, *i.e.* a BP bulge.

We use the term 'prominence' as one can observe BP bulges which are large in physical size (radius) but appear as a weakly defined peanut, or smaller BPs in radius but with strongly defined 'X' shapes. So $\mathcal{B}$ measures how well-defined the BP is. Hereafter, we use the term 'BP strength' throughout, on the understanding that this is a strength metric based on kinematics. Debattista et al. (2005) demonstrated a strong correlation between the 4th-order moment of the velocity and density, so we are satisfied with its suitability as a measure of BP strength. Uncertainties on $\mathcal{B}$ are computed using the differences between the raw and smoothed h_4 profiles at the valleys and peak, added in quadrature.

Many bars without BPs have no detectable valleys in their h_4 profiles, and therefore have $\mathcal{B} = 0$.

5.5.1 Buckling Versus Weak/Non-Buckling BPs

It is generally accepted that BPs can form via two principal mechanisms. The first is the most morphologically obvious – the buckling instability (Raha et al. 1991; Merritt & Sellwood 1994; Martinez-Valpuesta & Shlosman 2004; Erwin & Debattista 2016; Smirnov & Sotnikova 2019), a large deviation from vertical symmetry, followed by a rapid rise in vertical thickness in the inner regions of the bar. Li et al. (2023) showed that the buckling instability results in the resonant trapping of planar and vertical stellar orbits. The second pathway is a BP which grows also via the resonant trapping of stars, albeit more gradually (Combes & Sanders 1981; Combes et al. 1990; Quillen 2002; Sellwood & Gerhard 2020). This can be difficult to distinguish from weak buckling. However, it is possible that some galaxies can form and grow their BP bulge through a mixture of buckling and resonant trapping which is difficult to disentangle. We distinguish those BP bulges which experienced a strong buckling episode in their history and those which did not. In isolated simulations, buckling happens rather rapidly, in $\sim 0.5-1$ Gyr (e.g. Martinez-Valpuesta & Shlosman 2004;

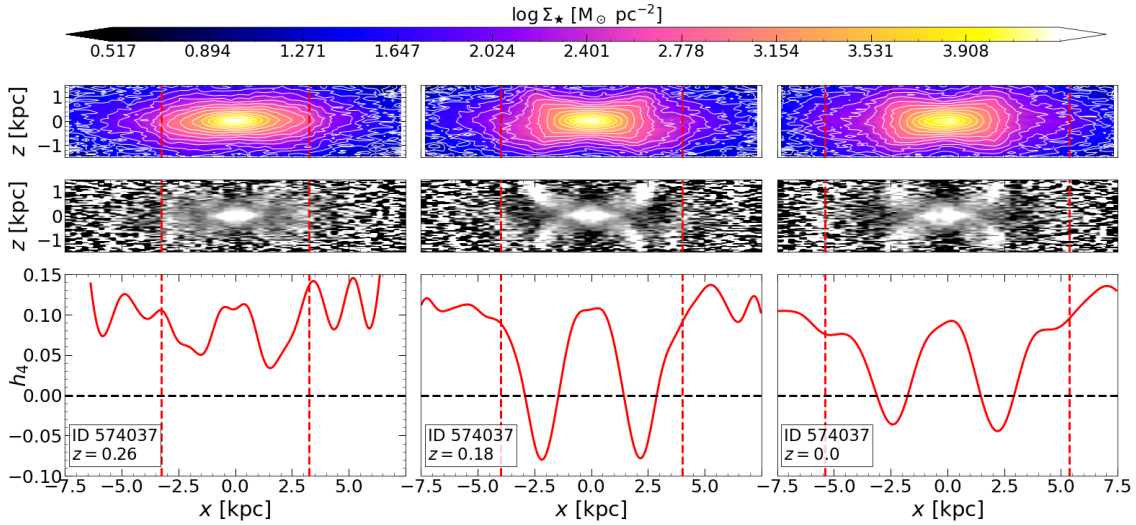

Figure 5.3: Example of a buckling galaxy, Subhalo ID **574037**, before, at and after its buckling redshift, $z = 0.18$. Top row: stellar surface density in the (x, z)-plane. Middle row: unsharp mask of the surface density in the (x, z)-plane. Bottom row: smoothed h_4 profiles along the bar major axis. Columns represent, from left to right, $z = 0.26, 0.18$ and 0.0. The bar radius is indicated by the vertical red dashed lines. The black dashed line shows $h_4 = 0$ for reference. Each panel uses the cut $|y| < 0.3R_{\rm bar}$.

Martinez-Valpuesta et al. 2006; Łokas 2019; Cuomo et al. 2022; Li et al. 2023). This seems consistent with observations (e.g. Erwin & Debattista 2016). The minimum, maximum and median difference between snapshots in TNG50 from $z = 2$ to 0 are 87, 236 and 159 Myr, respectively, thus providing good temporal resolution for detecting strong buckling. We note that strong buckling is obvious in (x, z) density distributions and unsharp mask images. It is accompanied by a strong signature in the h_4 profile (two deep valleys appear on either side of $x = 0$), and hence a rapid increase in the BP strength, $\mathcal{B}$.

For each galaxy with a BP at $z = 0$, we examine unsharp mask images and density plots, noting if vertical asymmetry in the (x, z)-plane surface density map

appears suddenly at any time, alongside the development of an asymmetric 'X' shape in the unsharp masks. If it does, and this is accompanied by the prompt formation of two deep valleys in the h_4 profile, and a steep rise in the evolution of $\mathcal{B}$, then we deem the galaxy to have experienced strong buckling. We label the time at which this occurs as $t_{\rm buck}$ and denote these galaxies as the 'BCK sample'. An example is shown in Fig. 5.3 where the vertical asymmetry of galaxy **574037**, at the time of buckling, stands out in the stellar density, and the 'X' shape is visible in the unsharp mask. Note the evolution of the h_4 profile (bottom row) where we see the clear formation of two deep valleys on either side of $x = 0$ at buckling. After buckling, there is a reduction in the depth of the valley in h_4.

We investigated the use of other buckling indicators, such as $A_{\rm buck}$ (Debattista et al. 2006) and A_{1z} (Li et al. 2023), but found these to be very noisy in TNG50, unlike in isolated simulations. In TNG50, we found a sharp increase in $\mathcal{B}$ (see the example in the top left panel of Fig. 5.10) to be a much more reliable indicator of buckling, because it is insensitive to small misalignments of galaxy inclination (up to $\sim 30°$).

While strong buckling is obvious, we may miss examples of weak buckling, possibly classifying BPs which had weak (possibly recurrent) buckling episodes in their history as having formed via resonant capture. We define those BPs where we did not detect strong buckling as the weak/non-buckling ('WNB') sample.

Fig. 5.4 shows three h_4 profiles at $z = 0$ which we identify as BCK, WNB and non-BP barred galaxies. Note the deep minima with $h_4 < 0$ in the BP galaxy which has undergone buckling (consistent with the findings of Sellwood & Gerhard 2020). The minima in the WNB galaxy are not as deep, but still prominent. The non-BP h_4 profile still has some peaks and valleys, but is considerably flatter in the central regions than the BP galaxies.

We illustrate the evolution of the h_4 profiles, from redshift $z = 1.5$ to $z = 0$, in

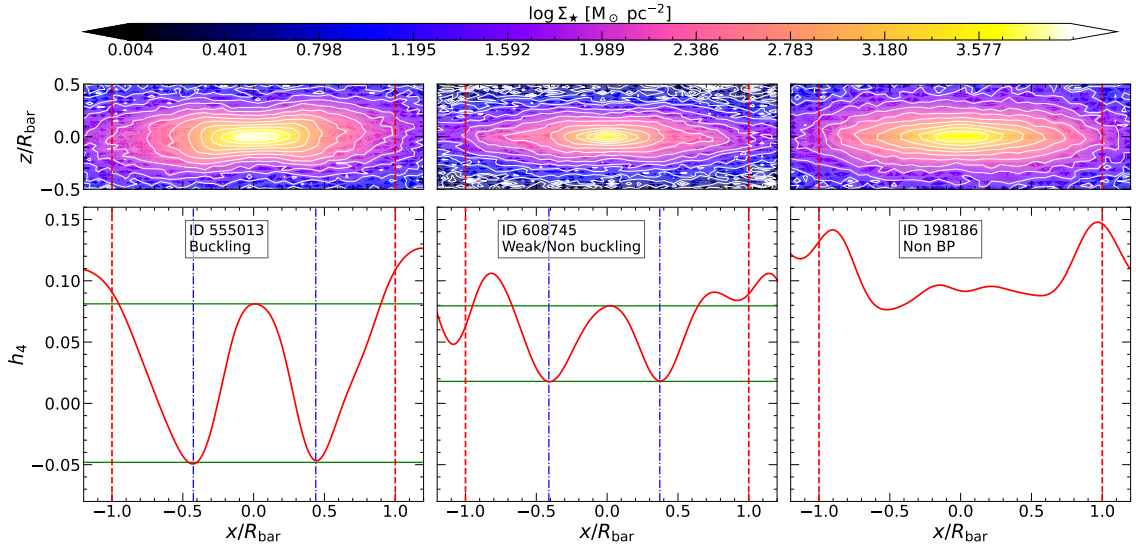

Figure 5.4: h_4 profiles along the bar major axis (bottom panels) for three galaxies at $z = 0$: a buckled BP galaxy (left column), a galaxy with a BP but which has no major buckling episode (middle column) and a barred galaxy without a BP (right column). The top panels show the stellar surface density in the (x, z) plane (vertical scale is shown as $z/R_{\rm bar}$). All panels are shown for $|y| < 0.3R_{\rm bar}$. The smoothed profiles are shown in solid red lines. The bar radius is indicated by the vertical red dashed lines. The two deep minima detected by the BP algorithm (blue vertical dot-dash lines) are present in the buckling galaxy, shallower ones in the weak/non-buckling galaxy, and the galaxy without a BP has a profile with shallow valleys. The green horizontal lines represent the mean valley and peak h_4 levels. The galaxies are labelled with their TNG50 Subhalo IDs.

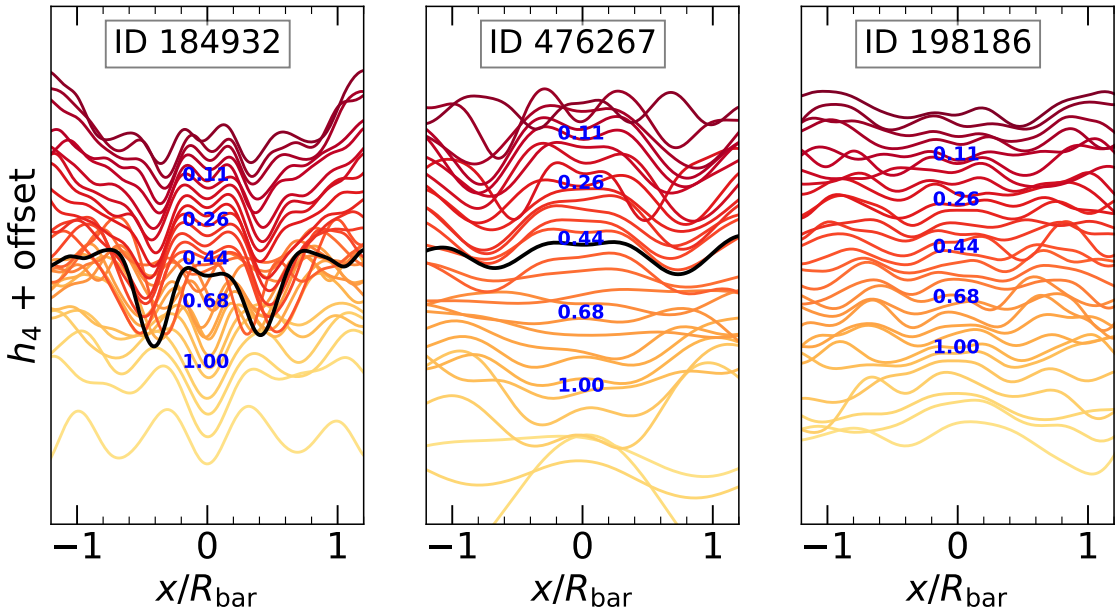

Figure 5.5: Examples of the evolution of the h_4 profiles along the bar major axis for three representative galaxies, a BCK (left panel), WNB (middle panel) and non-BP barred (right panel) galaxy. Time progresses upwards towards the darker colours, and we plot every other redshift from $z = 1.5$ for clarity. We apply a constant offset to separate the profiles vertically and every fifth time step, we label the redshift in blue. The profiles in solid black lines are those at the time of BP formation (Section 5.8). The galaxies are labelled with their TNG50 Subhalo IDs.

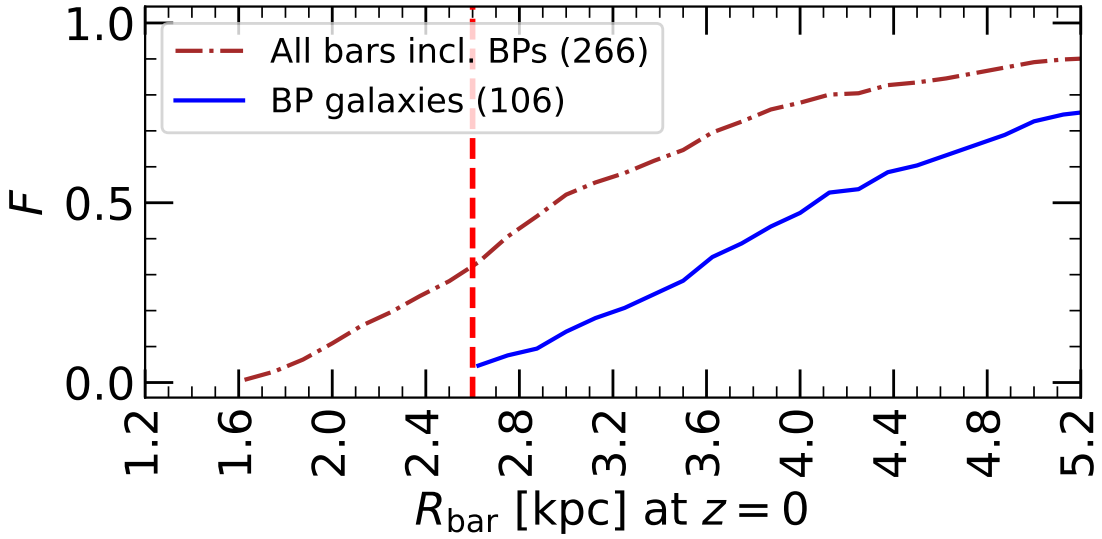

Figure 5.6: The cumulative distribution of $R_{\rm bar}$ for all barred galaxies (those with $a_{2,\rm max} > 0.2$ but with no cut in $R_{\rm bar}$) (brown dot-dashed line), and BP galaxies amongst them (blue solid line). To show details at small radius, the x-axis limit is set to ~ 5 kpc. The vertical dashed red line marks our bar cut, $R_{\rm bar} = 2.6$ kpc.

Fig. 5.5 for representative BCK, WNB and non-BP barred galaxies. In the BCK and WNB galaxies, clear minima in h_4 are present after the BP forms, while the non-BP galaxy shows no such feature. The minima in buckling galaxies appear suddenly, and are deeper than in the WNB profiles.

5.5.2 $R_{\rm bar}$ Cut Refinement

Our initial bar radius cut was 2 kpc, based on arguments presented in Section 5.3. Fig. 5.6 shows the cumulative distribution of $R_{\rm bar}$ for BP and non-BP bars, which includes all bars with $a_{2,\rm max} > 0.2$. We see that a cut of 2.6 kpc marks the radius where both cumulative fractions begin to rise linearly in a reasonably consistent way. Therefore, we select those bars with $a_{2,\rm max} > 0.2$ and $R_{\rm bar} \geq 2.6$ kpc as the barred sample. Compared to using a cut at $R_{\rm bar} \geq 2$ kpc, this eliminates a further 58 barred and 5 BP galaxies.

Recent work by Frankel et al. (2022) concluded that TNG50 bars appear in general to be too short.

Observational data from the Spitzer Survey of Stellar Structure in Galaxies (S^4G, Sheth et al. 2010), taken from Erwin (2018), is a distance- and magnitude-limited sample of barred galaxies. From the images, the bar radius is determined from its deprojected semi-major axis length. We exclude galaxies in the S^4G sample with $\log(M_\star/\mathrm{M}_\odot) < 10.0$ to match the TNG50 sample. In Fig. 5.7 (Figure 17 in A23), we present the $(\log(M_\star/\mathrm{M}_\odot), R_{\mathrm{bar}})$-plane at $z = 0$ for the TNG50 sample and overlay in blue circles the S^4G sample.

From this figure, it is clear that at $z = 0$, TNG50 does not produce excessively long bars compared to the observations. In TNG50 at $z = 0$, the median $R_{\mathrm{bar}} = 3.5^{+1.5}_{-0.8}$ kpc after the exclusion of bars smaller than 2.6 kpc, and $3.0^{+1.6}_{-0.8}$ kpc without excluding small bars (16th and 84th percentiles). The observational sample has bar lengths $4.0^{+2.1}_{-1.0}$ kpc after the exclusion of bars smaller than 2.6 kpc, and $2.7^{+2.3}_{-1.1}$ kpc for all bars. However, as mentioned above, TNG50, with its limited resolution, may not accurately capture the dynamics of small bars. Therefore, we maintain our cut of 2.6 kpc and we apply the same limits when comparing to observational samples.

After this cut, the visual inspection and BP strength determination results in a population of 106 BPs out of 191 galaxies in the barred sample ($\sim 55\%$) at $z = 0$. We refer to those galaxies with a BP at $z = 0$ as the 'BP sample', while the remaining barred galaxies without BPs at $z = 0$ constitute the 'non-BP sample' (85 galaxies).

5.6 Control Sample

To help investigate the conditions which lead some barred galaxies to form BPs and others not, we produce a sample of non-BP barred galaxies which match the stellar mass distribution of our BP sample. For each BP galaxy, we select a barred but non-BP galaxy which is closest in terms of total stellar mass at $z = 0$. Although the

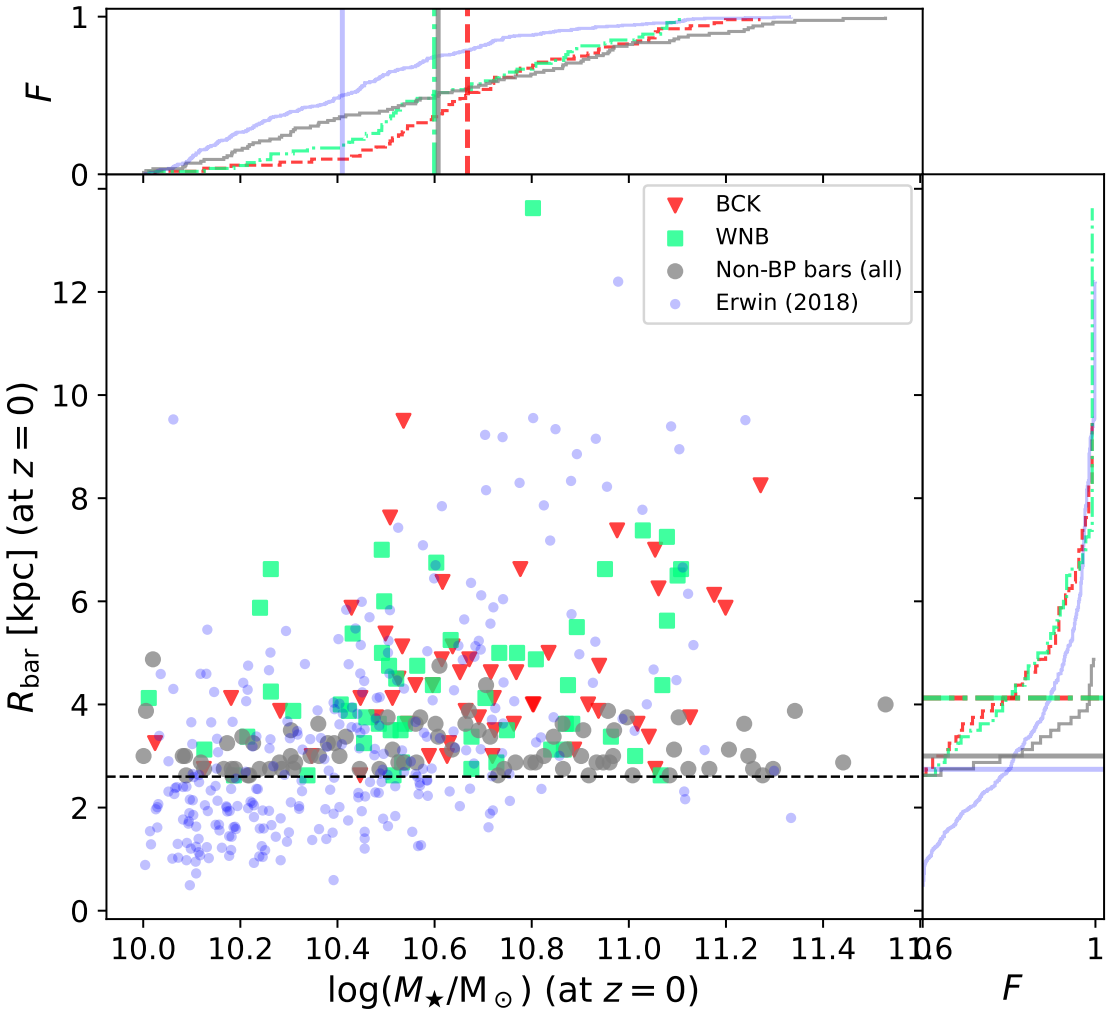

Figure 5.7: The distribution of barred galaxy samples in the $(\log(M_\star/\mathrm{M}_\odot), R_{\rm bar})$-plane at $z = 0$, identifying BCK, WNB and non-BP galaxies. The side panels represent cumulative distributions of the parameter on the respective axis, with their median shown in vertical (top) and horizontal (right) panels. We overlay in light blue circles observational data from Erwin (2018), with a cut on $\log(M_\star/\mathrm{M}_\odot) \geq 10.0$ to match the TNG50 sample (but without a cut on $R_{\rm bar} \geq 2.6$ kpc). For these data, $R_{\rm bar}$ is the deprojected semi-major axis length of the bar. For the (Erwin 2018) data, to match the TNG50 sample, we show cumulative lines only for $R_{\rm bar} \geq 2.6$ kpc. The horizontal black dashed line represents $R_{\rm bar} = 2.6$ kpc.

matching is rather simple, it helps illuminate key differences in galaxy parameters, giving us insight into why those barred galaxies without BPs do not form them.

To construct the control sample, for every galaxy in the BP sample, we iterate through every galaxy in the non-BP barred sample to form combinations of each BP and a non-BP galaxy. For each combination, we calculate $\Delta M_\star/M_\star$, the fractional difference between the stellar masses at $z = 0$. These combinations are then sorted in ascending order by $\Delta M_\star/M_\star$ for matching. Since we have 84 non-BP galaxies (we exclude one which is in the process of buckling at $z = 0$), and 106 BP galaxies, we must pair some controls with more than one BP. To maximize the match in stellar mass, we allow each control to be used up to twice, *i.e.* pairing is done *with replacement*. 60 of 84 (71%) unique control galaxies are paired amongst the BP galaxies. We refer to the population of control galaxies as 'the control sample'.

Fig. 5.8 shows the distribution of $M_\star$ for BP and control galaxies. The BP galaxy and control stellar mass distributions have a two-sample KS test p-value of 0.38, signifying negligible differences between the two distributions. There are much larger differences between the BP sample and the population of non-BP bars ($p = 0.008$). Using this approach, 14 controls are paired once, 46 twice. The median fractional difference in $M_\star$ between BP galaxies and controls is 0.99%. We find 96% of BP galaxies have a fractional difference in stellar mass with their control of less than 5%. Thus, when comparing BP and control galaxies, $M_\star$ is reasonably well controlled for.

5.7 BP Sample Validation

We use the BP strength metric, $\mathcal{B}$, to perform a quantitative test of the BP sample obtained through visual inspection, since $\mathcal{B}$ may be noisy, for example in cases of galaxies which experience interactions. We calculate the median of $\mathcal{B}$ in the final five snapshots for each galaxy, $\widetilde{\mathcal{B}_5}$, for the BP and non-BP samples and present their

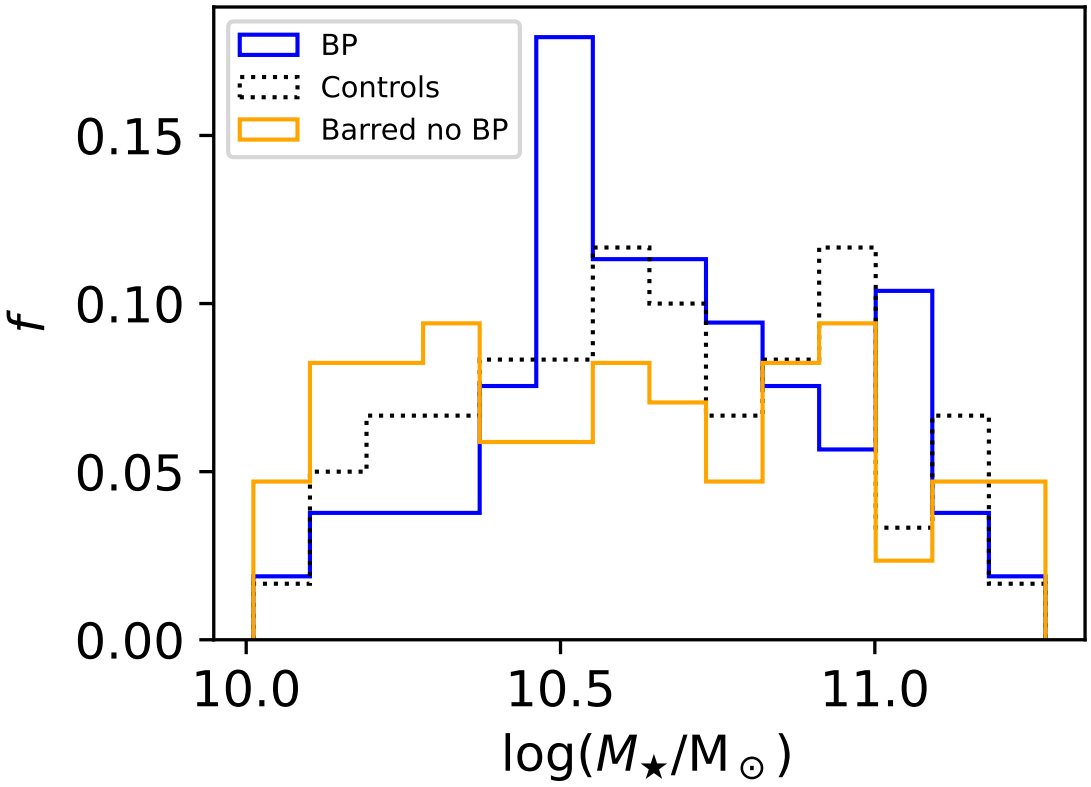

Figure 5.8: Distribution of $\log(M_\star/\mathrm{M}_\odot)$ for the BP (blue) and control (dotted black) samples at $z = 0$ and for comparison, all barred galaxies without BPs (orange). A good match between BP and control samples is achieved with a two-sample KS test having $p = 0.38$, signifying negligible difference in their distributions.

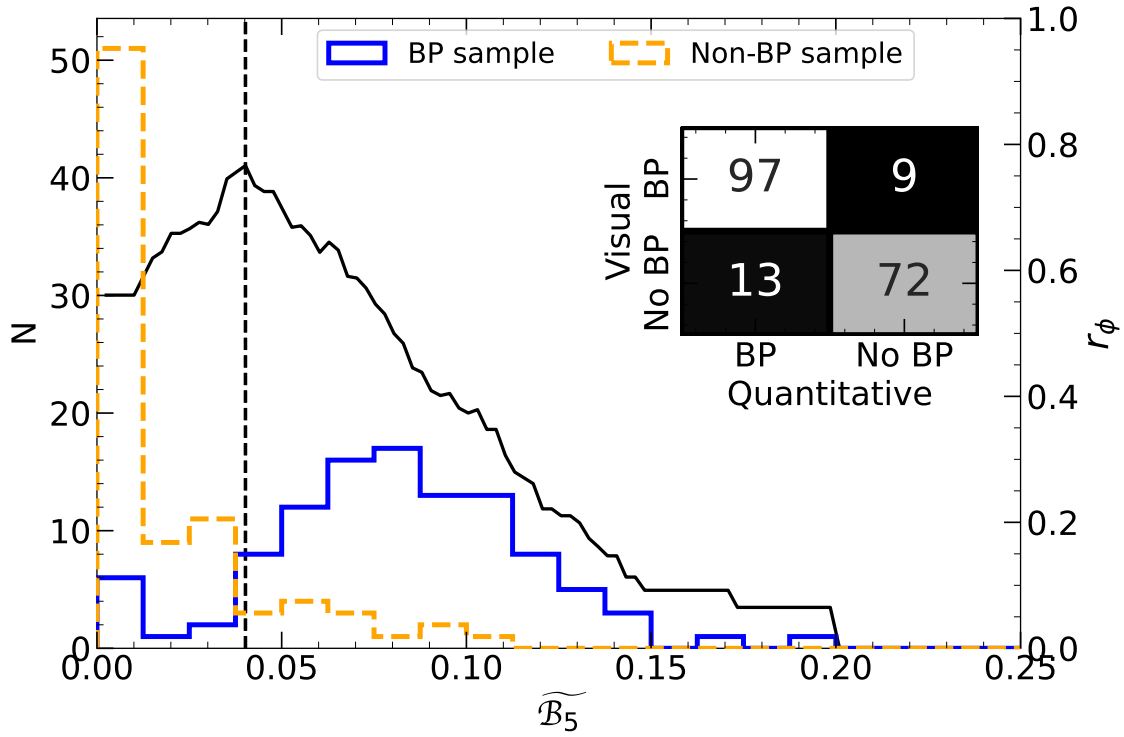

Figure 5.9: The distributions of the median of $\mathcal{B}$ for the last five time steps, $\widetilde{\mathcal{B}_5}$, for the BP (blue) and non-BP samples (orange) (left axis). The black line (right axis) shows r_ϕ, the 'phi coefficient' of Yule (1912); Matthews (1975), a correlation coefficient between the binary classifications methods, as a function of $\widetilde{\mathcal{B}_5}$ which is used for the threshold value of BP classification. The confusion matrix in the top right corner is a comparison of the visual and quantitative classifications using the $\mathcal{B}_{\rm crit}$ (maximum r_ϕ) value indicated by the vertical dashed line.

distributions in Fig. 5.9 (left axis). As expected, non-BP galaxies have near zero values of $\widetilde{\mathcal{B}_5}$, with a tail to larger values (some galaxies have transient large values of $\mathcal{B}$). The BP sample clearly has overall larger values of $\widetilde{\mathcal{B}_5}$ than the controls, with a large range. However, the distributions overlap. Using a single critical value of $\mathcal{B}$ to classify barred galaxies as BP or non-BP would therefore introduce confusion in the classifications. We compare the visual and quantitative classifications based on applying a threshold $\mathcal{B}_{\rm crit}$, taking the visual classification to be the 'truth'. We use the $\mathcal{B}_{\rm crit}$ value to make a 'predictive' classification of each galaxy solely using each galaxy's value of $\widetilde{\mathcal{B}_5}$ (a BP being present if $\widetilde{\mathcal{B}_5} \geq \mathcal{B}_{\rm crit}$).

We compute the mean square contingency coefficient[2], r_ϕ, a correlation coefficient between binary classification methods (Yule 1912; Matthews 1975), as a function of $\mathcal{B}_{\rm crit}$, then finding the value which results in the closest match to the visual classification. The r_ϕ value for each threshold value is also presented in Fig. 5.9 (right axis, black line). We find that a critical value of $\widetilde{\mathcal{B}_5} = 0.040$ results in an r_ϕ value of 0.735, and an overall accuracy (number of true positives and negatives as a fraction of all classifications) of 86.9% at reproducing the visual classification. The confusion matrix using this critical value is presented in the top right of Fig. 5.9. This demonstrates that the $\mathcal{B}$ metric captures the BP component of the bulge well, with some uncertainty in the individual values as well as uncertainty in our visual classifications. While comparing BP classifications between authors gives minimal disagreement, this test demonstrates the challenge of identifying BPs with an automated routine even in simulations.

[2] $r_\phi = [(\mathrm{TP} \times \mathrm{TN}) - (\mathrm{FP} \times \mathrm{FN})]/\sqrt{(\mathrm{TP}+\mathrm{FP})(\mathrm{TP}+\mathrm{FN})(\mathrm{TN}+\mathrm{FP})(\mathrm{TN}+\mathrm{FN})}$, where TP = number of true positives, TN = number of true negatives, FP = number of false positives and FN = number of false negatives for each value of $\mathcal{B}_{\rm crit}$ assessed.

5.8 Measuring the Time of BP Formation

We use the BP strength $\mathcal{B}$ to determine the time of BP formation. We calculate $\mathcal{B}$ at each time step, and set a threshold of $\mathcal{B}_{\rm crit} = 0.040$ found in Section 5.7, considering that a BP is present when $\mathcal{B} > \mathcal{B}_{\rm crit}$. We find the earliest time step with no more than four subsequent consecutive time steps with $\mathcal{B}$ below the threshold (or no value for $\mathcal{B}$). We consider this to be the time when the BP formed, which we denote as $t_{\rm BP}$. The constraint on the reasonably contiguous nature of $\mathcal{B}$ avoids early transient signals (perhaps caused by interactions) and spurious signals caused by poor alignment. It sets $t_{\rm BP}$ at an epoch around which a BP is firmly established. That is, a few 'missing' time steps with $\mathcal{B} < 0.040$ would not cause us to discount a time step being $t_{\rm BP}$, unless this condition were protracted.

Fig. 5.10 shows examples of the evolution of $\mathcal{B}$ for an example buckling (BCK) galaxy, two WNB galaxies and a non-BP galaxy, with their identified $t_{\rm BP}$. We mark in green those points sufficiently contiguous in $\mathcal{B}$ (and larger than $\mathcal{B}_{\rm crit}$) for us to consider them a suitable measure of BP strength. We see a sudden, rapid increase in $\mathcal{B}$ at $t_{\rm buck}$ followed by a period of approximately linear decline in the buckled galaxy whose BP formed ~ 1 Gyr before buckling. The decline in $\mathcal{B}$ is typical of buckling galaxies in TNG50, but varies across the sample. Sellwood & Gerhard (2020) noted an initially negative h_4 value immediately after buckling in their N-body models, which increased to around zero by the end of the evolution. The evolution of $\mathcal{B}$ in the BCK galaxies is consistent with their result.

The evolution of $\mathcal{B}$ in the WNB sample is more varied, as exemplified by the two WNB panels. Some exhibit an evolutionary pattern in $\mathcal{B}$ similar to buckling galaxies (although in the unsharp masks and density we were unable to see evidence of any strong buckling in them), others show a steady increase in $\mathcal{B}$ with time. Still others show a steady decrease in $\mathcal{B}$ after an initial rise at $t_{\rm BP}$, highlighting the difficulty in disentangling weak buckling from resonant capture-built BPs. We also verify

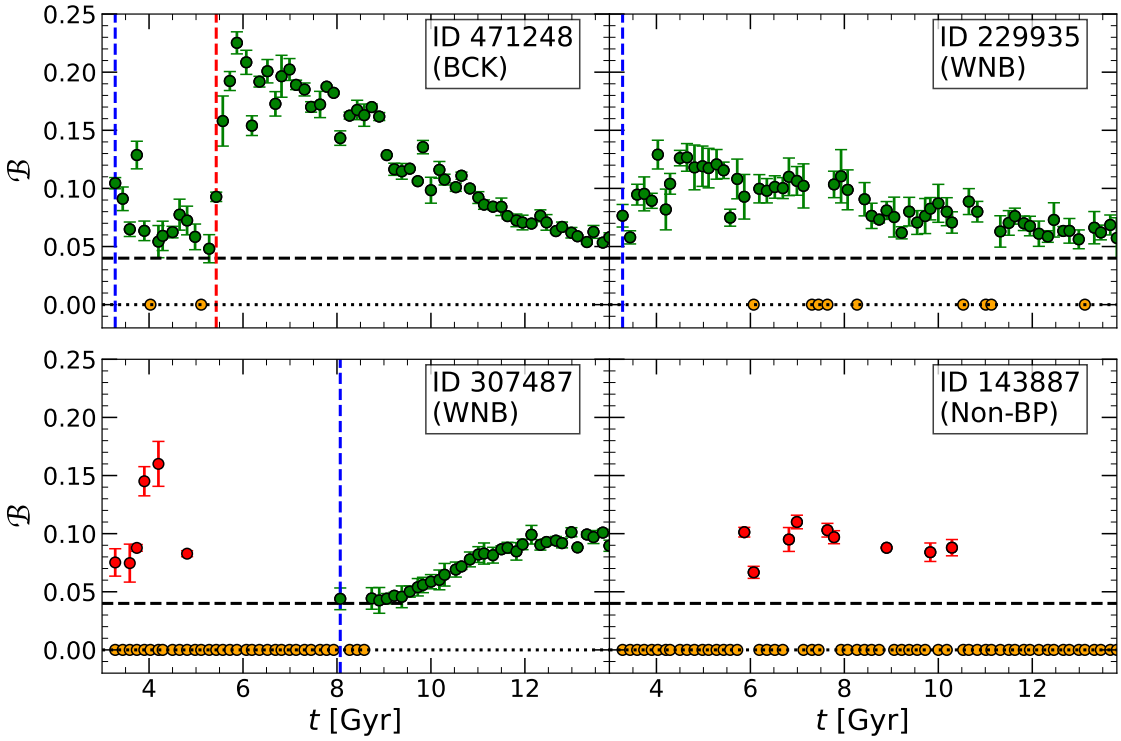

Figure 5.10: BP strength $\mathcal{B}$ for four galaxies, one buckling, two WNB and one non-BP galaxy. The black dashed horizontal line shows $\mathcal{B}_{\rm crit}$. Green points are those which meet our contiguity and threshold requirements for a BP, red those which do not (Section 5.8). The blue vertical dashed line marks $t_{\rm BP}$, the time of BP formation (by definition, the non-BP galaxy has no BP at $z = 0$). The red dashed vertical line marks the time of buckling. The redshifts where the algorithm calculates no $\mathcal{B}$ value are shown by the orange points along the x axis, and we mark $\mathcal{B} = 0$ with a dotted black horizontal line. The galaxies are labelled with their TNG50 Subhalo IDs.

the reasonableness of $t_{\rm BP}$ by visually inspecting the (x, z) density distributions and unsharp masks, ensuring a BP is discernible at this time.

For the non-BP galaxies, there is usually no pattern in the evolution of $\mathcal{B}$, and often no value could be calculated owing to a lack of a substantial h_4 peak−valley structure. Three controls do have some periods of contiguous evolution of $\mathcal{B}$ before $z = 0$, but $\mathcal{B} < \mathcal{B}_{\rm crit}$ at $z = 0$. They have indications of having had BPs in the past, but no longer at $z = 0$. Five controls have contiguous values of $\mathcal{B} > \mathcal{B}_{\rm crit}$ up to $z = 0$ but no discernible BPs in the density plots and unsharp masks.

We check the consistency of $t_{\rm BP}$ and $t_{\rm bar}$, checking those galaxies where $t_{\rm BP}$ was more than 1 Gyr before $t_{\rm bar}$. This occurs in 3 galaxies and we reinspect these galaxies' h_4 and density plots. We amend $t_{\rm BP}$ forward manually a few time steps in these cases.

5.9 Summary and Conclusions

We have defined a sample of 608 disc galaxies with $\log(M_\star/{\rm M}_\odot) \geq 10.0$, in the TNG50 run of the IllustrisTNG simulation suite at $z = 0$. We have examined these galaxies for the presence of bars and box/peanut (BP) bulges and summarised our findings in Table 5.2. From the disc sample, we find 191 (32%) have bars with $R_{\rm bar} \geq 2.6\,{\rm kpc}$ at $z = 0$ (Section 5.3). Of these, 106 (55%) have BPs at $z = 0$. We have identified bars using a canonical metric, the $m = 2$ Fourier moment of the stellar surface density. We have tracked the bar strengths temporally to determine the epoch of bar formation. To identify BP bulges we have studied the fourth-order Gauss-Hermite moments (h_4) of the stellar vertical velocity distributions along the bar's major axis. We use a metric derived from the profile of h_4 to measure a BP's 'strength' (how well-defined it is), which we can also measure through time. This allows us to determine the time of BP formation and the time of major buckling if it occurs. These quantitative metrics are also reinforced by the inspection of images

Classification	Number
Disc galaxies	608
$\hookrightarrow$ All barred galaxies (incl. short bars)	266
$\hookrightarrow$ Barred galaxies ($R_{\rm bar} \geq 2.6\,{\rm kpc}$)	191
$\hookrightarrow$ BP galaxies	106
$\hookrightarrow$ Strongly buckling galaxies (BCK)	52
$\hookrightarrow$ Weak/non-buckling galaxies (WNB)	54

Table 5.2: Sample sizes of TNG50 galaxy classifications.

of the stellar surface density and unsharp masks.

We are able to discern between formation mechanisms of a BP by studying their evolutionary history to find 52 (49%) have strongly buckled in the past, and 54 (51%) have never strongly buckled.

We identify one galaxy which appears to be in the process of buckling at $z = 0$ (Subhalo ID **608386**). We also find five galaxies that appear to have buckled but do not have a BP at $z = 0$ but remain barred. Another two galaxies did not buckle strongly but had a BP that is no longer discernible by $z = 0$, yet also remain barred. A detailed analysis of the redshift evolution of disc, barred and BP galaxies is outside the scope of this work but is certainly worth further study.

In A23, we studied the variation of BP fraction in barred galaxies ($f_{\rm BP}$) as a function of stellar mass. We found a similar dependence to that of observations of local galaxies such as those of ED17 and Erwin, Debattista & Anderson (submitted; hereafter EDA23) studying local barred galaxies from the Spitzer Survey of Stellar Structure in Galaxies (S^4G, Sheth et al. 2010). The BP fraction in TNG50 is low in low-mass galaxies, similar to the results of ED17. However, as shown by Fig. 5.11, we see a rapid increase of $f_{\rm BP}$ for increasing $M_\star$ until the fraction plateaus at $\log(M_\star/{\rm M}_\odot) \sim 10.5$ at a fraction of ~ 0.6. Observations also show a platue but

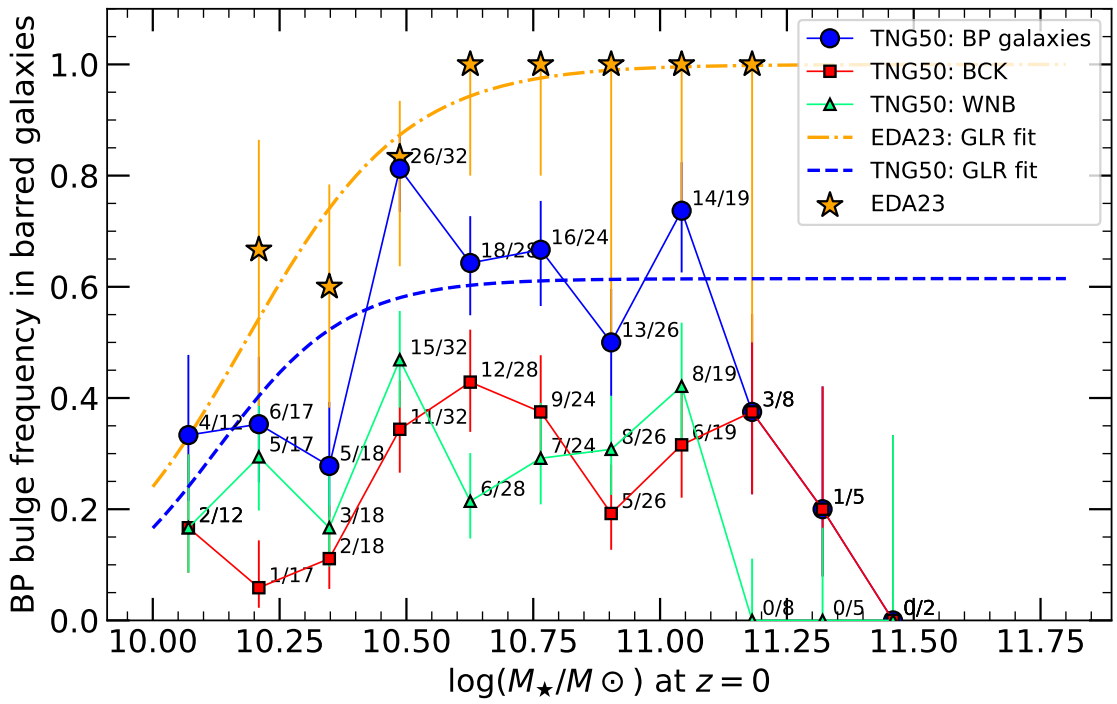

Figure 5.11: Dependence of the BP fraction on stellar mass at $z = 0$ for the sample of 191 barred galaxies (solid blue) in A23 (their figure 1). They split the BP population into the BCK (red) and WNB (green) populations. The fractions next to each point show the number of BP galaxies/number of barred galaxies in each mass bin. The blue dashed line represents a generalized logistic regression (GLR) fit to the data for all TNG50 BPs. The orange stars and dot dashed line represent the logistic regression fit to the observational data of EDA23 (restricted to bars of radius ≥ 2.6 kpc to match our selection, and limited to the same mass range as in this paper's barred sample). Error bars are the 68% (1σ) confidence limits from the Wilson (1927) binomial confidence interval. TNG50 appears to significantly under-produce BP bulges, particularly at higher mass.

they tend to saturate at $f_{\rm BP} = 1$ at high mass ($\log(M_\star/{\rm M}_\odot) \gtrsim 11.2$ in ED17 and $\log(M_\star/{\rm M}_\odot) \gtrsim 10.6$ in EDA23).

While applying a cut on the bar size in this work will artificially increase the fraction of BPs by mass, for both the TNG50 results and observations, A23 showed that these small barred-galaxies typically have low stellar mass. This bias will affect our measured values for the transition mass and the platue value of the BP fraction quantitatively, but not the qualitative comparison and conclusions of this work. Having the bar sizes of galaxies from an observational sample, we are able to make the same cut, and thus make a direct comparison with TNG50 with this bias applied to both.

A23 concluded that the low $f_{\rm BP}$ at low $M_\star$ could be attributed to the youth of the bars, which is a consequence of downsizing. At high mass, the plateau value being $\sim 60\%$ compared to 100% saturation in observations is due to excessive heating in TNG50 from merger activity and the numerical effects of lower resolutions. As a result, the main driver of whether a bar hosts a BP in TNG50 is not the galaxy mass, but how long and strong the bar is.

Chapter 6

Kinematic Fractionation in TNG50 Barred Galaxies

6.1 Introduction

Galactic bars are non-axisymmetric structures commonly found in massive disc galaxies. Bars, which started forming as early as $z = 2$ (see Guo et al. 2023; Le Conte et al. 2023), are important drivers of secular evolution (Kormendy & Kennicutt 2004, and references therein). The kinematics of the bars and their vertically thickened bulge regions have been explored in detail in isolated simulations (Debattista et al. 2017; Fragkoudi et al. 2017b, 2018; Di Matteo et al. 2019; Debattista et al. 2020), cosmological zoom simulations (Kraljic et al. 2012; Scannapieco & Athanassoula 2012; Bonoli et al. 2016; Buck et al. 2018, 2019; Debattista et al. 2019; Gargiulo et al. 2019; Fragkoudi et al. 2020; Walo-Martín et al. 2022) and in the highest-resolution fully-cosmological volumes (Rosas-Guevara et al. 2022; Anderson et al. 2023).

The *in situ* separation of different populations within a barred galaxy presented in Debattista et al. (2017) demonstrates that initially co-spatial populations with

varying initial radial velocity dispersions (and therefore initial radial action, Debattista et al. 2020) evolve separately in a growing bar: kinematically cooler populations form a strong bar and a strongly boxy/peanut-shaped (BP) bulge, whereas hotter populations form a weaker bar, and are more vertically thickened. They termed this behaviour *kinematic fractionation*. Since hotter populations are older, and age correlates with chemistry, bar evolution results in gradients of these properties in the final morphology of the bar and BP bulge (see also Athanassoula et al. 2017; Fragkoudi et al. 2017b,c, 2018, 2020; Buck et al. 2019). Such spatial variations of stellar properties must also be reflected in the kinematics of different populations (*e.g.*, Gough-Kelly et al. 2022). Thus relatively young populations must have more eccentric orbits in order to support a stronger bar, while older populations have less rotational support and are more dispersion dominated, producing a rounder distribution. Evidence of such variations was shown in the Milky Way by Queiroz et al. (2021) for populations split by metallicity and α-abundance.

In principle, these variations in the density and kinematics of different stellar populations within a bar may provide clues about the age of a bar. Because bars grow by trapping stars from the disc, their stellar populations include stars that are both older and younger than the bar itself. This makes measuring the age of bars difficult. One fruitful approach to constraining bar ages is to measure the ages of stars in their nuclear discs, which form because bars drive gas to the centre (*e.g.* Gadotti 2009; Kim et al. 2012; Cole et al. 2014; Sormani et al. 2015; Emsellem et al. 2015, and references therein). Since the formation of a nuclear disc or ring follows that of the bar's formation, the age of the nuclear disc (when one is present) provides a lower limit on that of the bar (Gadotti et al. 2015; Baba & Kawata 2020; de Sá-Freitas et al. 2022). How delayed nuclear disc formation is once a bar is formed is not well known but is thought to depend in part on the central concentration of the density (Baba & Kawata 2020). Similarly, the formation of a BP bulge follows

that of the bar and might also be used to constrain the bar's age (*e.g.*, Pérez et al. 2017; Buck et al. 2018). Buck et al. (2018), using a Milky Way analogue from the Numerical Investigation of a Hundred Astronomical Objects (NIHAO) project (Wang et al. 2015), proposed a method for determining the age of the bar and BP bulge using the age variation of the separation between the near- and far-side arms of the bulge along the line-of-sight through the bulge. In the Milky Way, variations in the separation bimodality produced by BP bulge have been shown to be a function of metallicity (*e.g.* Ness et al. 2013a; Gonzalez et al. 2015; Lim et al. 2021). Buck et al. (2018) also showed that populations contributing to the bar structure and those of the surrounding disc within the bulge have similar age and chemical distributions, making them hard to distinguish, except with full kinematic information. This is not unexpected from a bar which forms within a disc.

Large-volume fully cosmological hydrodynamical simulations are now reaching resolutions where they begin to capture the secular evolution of disc galaxies within the larger context, producing large samples of self-consistent barred galaxies (Rosas-Guevara et al. 2022; Anderson et al. 2023). In this chapter, we use one such simulation to explore whether the stellar populations of barred galaxies retain a dynamical 'memory' of the bar formation epoch. We use the highest resolution run of the IllustrisTNG project (Pillepich et al. 2018b; Springel et al. 2018; Nelson et al. 2018; Naiman et al. 2018; Marinacci et al. 2018), TNG50 (Nelson et al. 2019a,b; Pillepich et al. 2019). We study the sample for barred galaxies presented in Anderson et al. (2023, hereafter A23). In Section 6.2, we briefly describe the TNG50 simulation, the sample selection of barred galaxies, and in Section 6.3 our method for subsampling the stellar populations. In Section 6.4, we explore how the bar strength varies as a function of a stellar population's age relative to the age of the bar with metrics based on density and kinematics. In Section 6.5, we investigate signatures of kinematic fractionation in bulges. Finally, we discuss our results and present our summary in

Section 6.6.

6.2 TNG50 Sample Selection

The TNG50 run of the gravo-magneto-hydrodynamical cosmological suite of simulations, IllustrisTNG, is its highest resolution realization. The IllustrisTNG simulations are evolved with the moving mesh code AREPO (Springel 2010) within the ΛCDM framework, including subgrid prescriptions for star formation and chemical evolution, gas cooling, feedback and black hole formation, and evolution. These prescriptions are described fully in Weinberger et al. (2017) and Pillepich et al. (2018b). The free parameters of the model were chosen to reproduce observed integrated trends of galactic properties, particularly their stellar content at $z = 0$, star formation rate densities, black hole masses, gas fraction and stellar effective radii. Because it represents a large cosmological volume, TNG50 produces a large sample of galaxies at resolutions approaching those of zoom-in and isolated simulations of individual galaxies. The resolution means that the simulations capture aspects of the secular evolution of individual disc galaxies. TNG50 achieves a baryonic mass resolution of $8.5 \times 10^4\,\mathrm{M}_\odot$ and gravitational softening length for stellar particles of $\epsilon = 0.288\,\mathrm{kpc}$ (at $z = 0$). Gas cell sizes are as small as 70 pc in star-forming regions.

Galaxies bound to dark matter halos (or subhalos) within TNG50 are identified within the simulation at each timestep using the friends-of-friends (Davis et al. 1985) and `SUBFIND` (Springel et al. 2001; Dolag et al. 2009) algorithms. In this work, we use the sample of TNG50 barred galaxies identified in A23 but focus solely on the final time step of the simulation ($z = 0$). These galaxies are centred, and we align their discs with the angular momentum vector within two effective radii ($2R_\mathrm{e}$) along the z-axis, which places the stellar disc in the (x, y)-plane.

Here we briefly describe the selection criteria for obtaining the barred sample of galaxies; for full details, see Chapter 5 (Appendix A of A23). First, we impose a

stellar-mass cut at $z = 0$ of $\log(M_\star/M_\odot) \geq 10$ within a spherical radius of 30 kpc. This cut ensures that the galaxies in our sample are traced by a significant number of particles ($N_\star \geq 10^5$). We then select disc galaxies by taking a cut on the $K_{\rm rot}$ parameter, which measures the fraction of kinetic energy committed to in-plane rotation (Sales et al. 2010). Disc galaxies are identified as those with $K_{\rm rot} \geq 0.5$ also within 30 kpc (Zhao et al. 2020).

A23 measured bar length and strength through the Fourier decomposition of the stellar surface density distribution. The bar being a strong bisymmetric deviation from axisymmetry implies that the $m = 2$ amplitude peaks within the bar radius, where the $m = 2$ phase is roughly constant (to within 10°). Therefore we can quantify the bar strength by the peak amplitude of the $m = 2$ component as a function of the cylindrical radius, $a_{2,\rm max}$. We can also use these profiles to define the bar radius, $R_{\rm bar}$, by taking the mean of the outer radius at which the $m = 2$ amplitude drops to half the maximum value and the radius at which the phase angle deviates from constant by more than 10°. We can also define the bar strength as the sum of the $m = 2$ amplitude within the bar radius ($A_{\rm bar}$). In Section 5.5.2 of Chapter 5 (Appendix A4.2 of A23), we motivate a further cut on bar radius of $R_{\rm bar} \geq 2.6$ kpc, which removes small bars which are over-produced in TNG50 and are poorly resolved (*e.g.* Zhao et al. 2020). The final selection criteria for TNG50 barred galaxies in A23 are $\log(M_\star/M_\odot) \geq 10$, $K_{\rm rot} \geq 0.5$, $a_{2,\,\rm max} > 0.2$ and $R_{\rm bar} > 2.6$ kpc, resulting in a sample of 191 barred galaxies at $z = 0$.

The evolution of the bar strength is tracked throughout the evolution of each galaxy in the sample, allowing us to determine the epoch of bar formation as described in Section 5.4 of Chapter 5 (Section A2 of A23). We consider the age of the bar at the current epoch ($z = 0$), which we denote as $\mathcal{A}_{\rm bar}$, and present the cumulative distribution function (CDF) of bar ages in Fig. 6.1; we note bars form throughout the simulation from $z \approx 3$ to the current epoch.

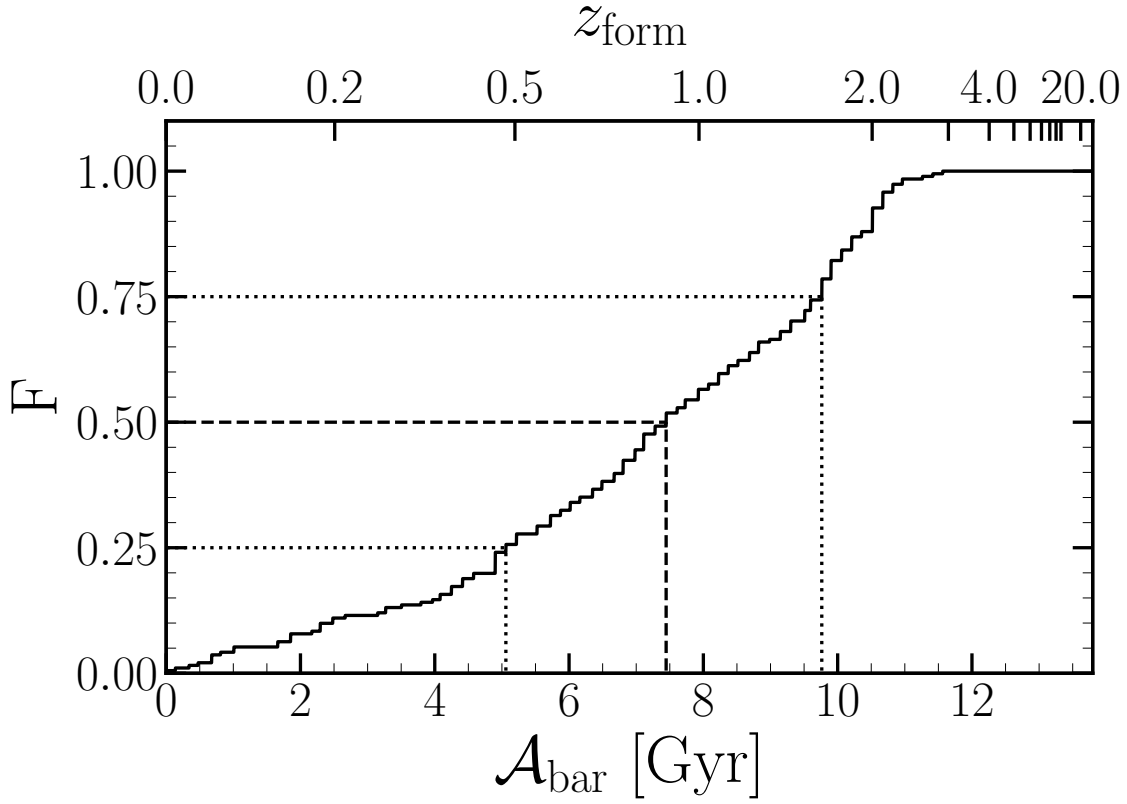

Figure 6.1: The CDF of bar ages in TNG50, derived as described in Section 5.4 of Chapter 5 (Appendix A of A23). The dashed line denotes the median $\mathcal{A}_{\rm bar}$ while the dotted lines denote the $25^{\rm th}$ and $75^{\rm th}$ percentiles. The earliest bars formed ~ 11 Gyr ago at $z \approx 3$.

6.3 Age Dissection

For each galaxy in the barred sample, we construct the CDF of stellar ages ($\mathcal{A}_\star$) within a cylindrical radius and height equal to the bar radius ($R \leq R_{\rm bar}$ and $|z| \leq R_{\rm bar}/2$). These CDFs differ between galaxies due to the variation in star formation histories. To account for this variability, we do not attempt to separate the populations within a galaxy by fixed age bins; instead, we split a galaxy's CDF of ages into eight quantiles, each with the same number of star particles. This allows us to sample the full age range while ensuring quantiles have sufficient particles to be representative of a population of stars when comparing galaxies. We present an example of the CDF sub-sampling method applied to galaxy **414917** in Fig. 6.2, where we split the age CDF into the eight quantiles from young to old, labeled A-H. Each quantile, referred to hereafter as a 'sub-population', contains 12.5 percent of all stars within the bar region. For galaxy **414917**, each sub-population has 141 348 stellar particles from a total of 1 130 784 in the bar region. We then calculate the mean age of each sub-population, $\mathcal{A}_{{\rm pop},\,i}$, which we use as the single age value to represent all stars within that sub-population when comparing between galaxies. In other words, we treat a sub-population as though it were a mono-age population.

We explore the variation in $\mathcal{A}_{\rm pop}$ between barred galaxies by comparing the distributions of sub-populations in order of formation. For example, we explore the distribution of mean ages in the youngest sub-population, 'A', in all the barred galaxies. Across the sample of 191 barred galaxies, sub-population 'A' has a median age of $\langle \mathcal{A}_{\rm pop,A} \rangle = 4.19\,{\rm Gyr}$ with a lower quartile of 2.26 Gyr and upper quartile of 5.98 Gyr. The full range of $\langle \mathcal{A}_{\rm pop,A} \rangle$ is $0.24 - 11.34\,{\rm Gyr}$, highlighting the wide variation in stellar assembly history amongst the galaxies in the sample. Fig. 6.3 shows violin plots of the distributions of $\mathcal{A}_{{\rm pop},\,i}$ within each labeled sub-population (A-H) for the barred galaxies. The vertical lines of each violin represent the median, the $25^{\rm th}$ and $75^{\rm th}$ percentiles, and the full range of values. The shaded area of

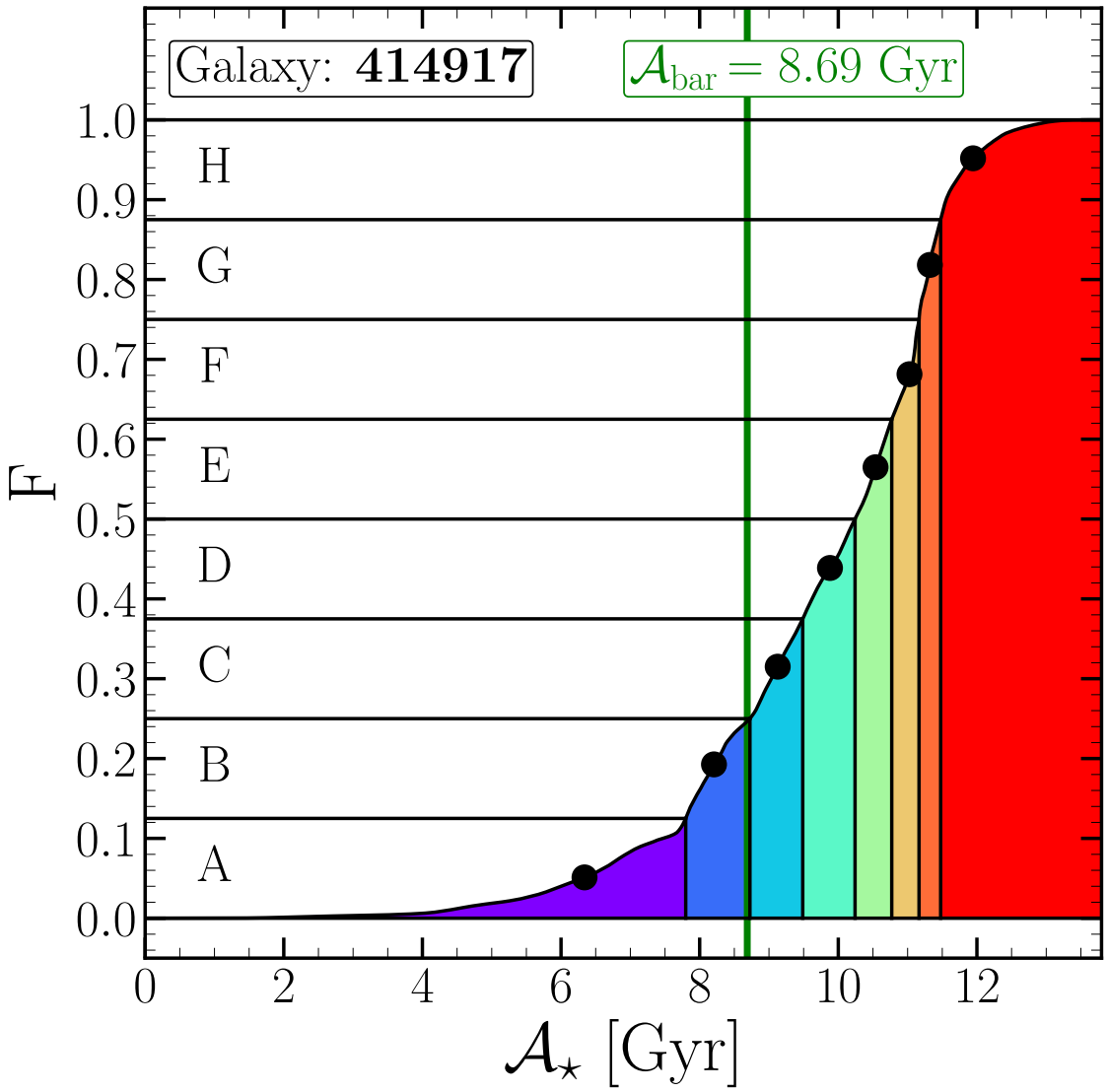

Figure 6.2: The cumulative distribution of stellar particle ages within the bar region of the TNG50 galaxy **414917** at $z = 0$. Black points denote the mean age of each sub-population. The green vertical line indicates the age of the bar in this galaxy.

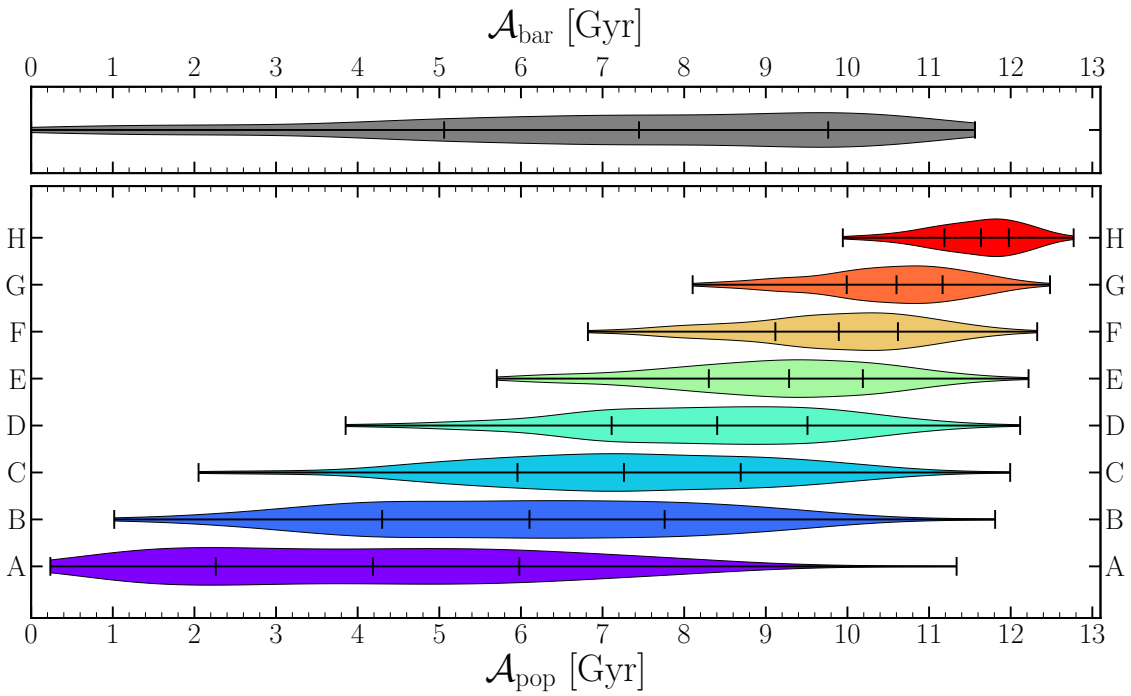

Figure 6.3: The distributions of average ages for each labeled sub-population (A-H) of each of the 191 barred galaxies (lower panel). Each row is the distribution of 191 sub-populations formed in the same quantile from all of the galaxies. For example, row 'A' shows the spread of the youngest 12.5% of stellar particles within the bar region of the 191 galaxies. The distribution of $\mathcal{A}_{\rm bar}$ is also shown in the upper panel for comparison.

each violin represents the probability density distribution. Note that the overall broadness of each distribution increases and overlaps the other sub-populations as we consider younger sub-populations (i.e. moving from populations H to A), reflecting the inefficient star formation within bars. Thus the youngest populations in old bars can reach ages ~ 10 Gyr.

6.3.1 Bar Age Offset

Knowing the age of the bars in the sample allows us to measure the time delay between the formation of the bar and a stellar population. Therefore we offset the age of a sub-population, i, within a galaxy by the age of that galaxy's bar, $\mathcal{A}_{\rm bar}$, *i.e.* the time delay between their formations, as:

$$\delta\tau_i = \mathcal{A}_{\rm bar} - \mathcal{A}_{{\rm pop},i} \ , \tag{6.1}$$

where positive values of $\delta\tau$ are sub-populations formed after the bar (younger), and negative values are those formed before the bar (older). As shown in the top panel of Fig. 6.1, bars form at a wide range of times in TNG50. We present the distributions of $\delta\tau$ for all sub-populations in the bottom panel of Fig. 6.4. There is significant overlap between the sub-populations of different galaxies when we offset in this way; however, there is a sufficient difference between sub-populations much older than the bar, those born at the epoch of bar formation, and those much younger than the bar, to allow us to explore general trends in the galaxy evolution across the range of $\delta\tau$.

To explore how properties of stellar populations within the bar region vary as a function of $\delta\tau$, we consider each sub-population ignoring its order in the stellar assembly (*i.e.* ignoring its identifying label A-H) and consider $\delta\tau$ across all galaxies. We do this as we are more interested in the distribution of ages of a sub-population relative to the bar's, rather than the overall stellar assembly histories. Depending

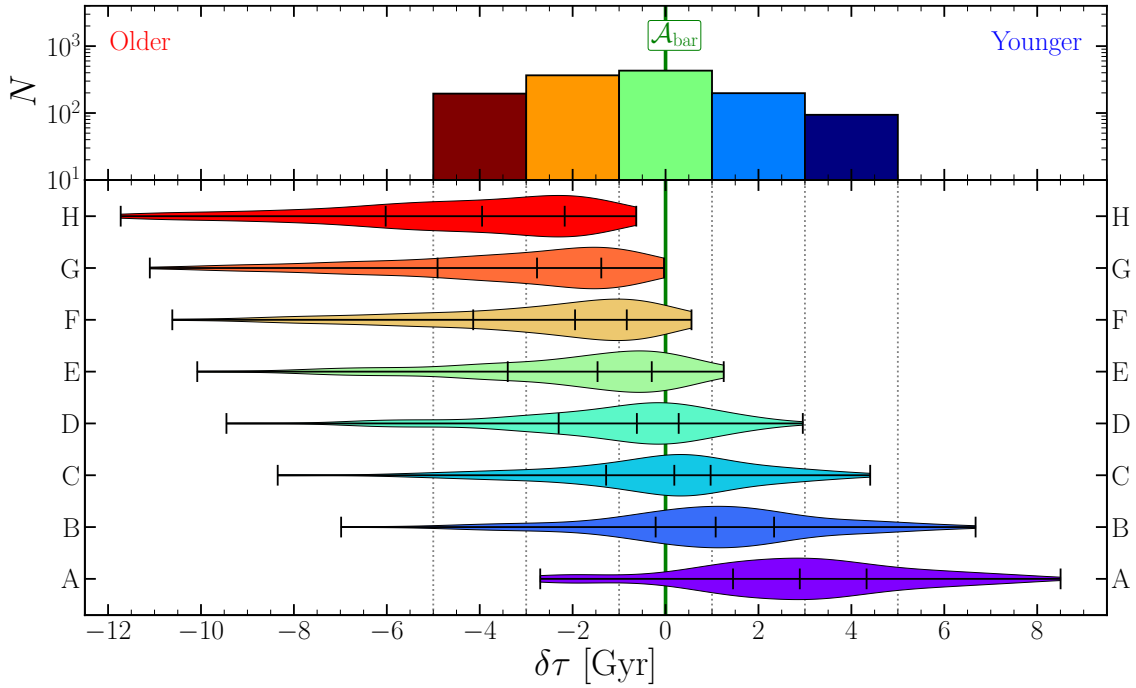

Figure 6.4: Bottom: The distribution of $\delta\tau$, the difference between the time of bar formation and its sub-populations' (A-H) ages, for all 191 barred galaxies. Top: The number of sub-populations for all barred galaxies in bins of $\delta\tau$ ignoring their ordering (summing vertically across A-H). Therefore the total area under the histogram is equal to 191 galaxies × 8 sub-populations = 1528. The vertical green line denotes $\delta\tau = 0$, or populations born at the time of bar formation and have ages $\mathcal{A}_{\rm pop} = \mathcal{A}_{\rm bar}$. Note that distributions are not symmetric about $\delta\tau = 0$, indicating that, on average, galaxies' central regions are dominated by populations older than the bar. The bins of the histogram presented in the top panel of this figure are used in the analysis presented in Fig. 6.17 only (see Section 6.5.2).

on the stellar assembly, periods of high star formation would result in multiple sub-populations within the same galaxy having very similar $\mathcal{A}_{\rm pop}$ and we would not consider them as very distinct populations from each other.

In the top panel of Fig. 6.4, we bin $\delta\tau$ for the barred sample. A bin in $\delta\tau$ contains sub-populations from many galaxies with the same age relative to their bar but may have come from different age quantiles of a galaxy (*i.e.* have a different label A-H). If we consider the bin spanning $\delta\tau = 0$, we can see many sub-populations from different quantiles (A-H) formed as the bar formed. In the youngest bins in $\delta\tau$, we find contributions from sub-populations in the youngest three quantiles (A, B and C). The oldest quantiles (G and H) all formed before the bar and therefore have $\delta\tau < 0$. Also, we note that there are more sub-populations with $\delta\tau < 0$, indicating that in TNG50, most bar/bulge regions are predominately older than the bar.

From this point onwards, we do not refer to sub-populations using their quantile label (A-H) and consider population properties as a function of $\delta\tau$ across all galaxies[1].

6.4 Kinematic Fractionation

Debattista et al. (2017) showed that the bar strength of a sub-population is a continuous function of initial radial velocity dispersion (see also Fragkoudi et al. 2017b; Athanassoula et al. 2017). As a consequence, bar strength is also a function of age, with younger populations forming stronger bars and older populations typically forming weaker bars and kinematically hotter bulges. We explore to what extent sub-populations retain a 'memory' of the evolutionary state of the galaxy when they formed by exploring their bar properties as a function of $\delta\tau$. We explore various morphological and kinematic properties of the different stellar populations.

[1]Note the binning for the analysis from this point is not restricted to the 5 bins presented in the top panel Fig. 6.4 except in Section Section 6.5.2.

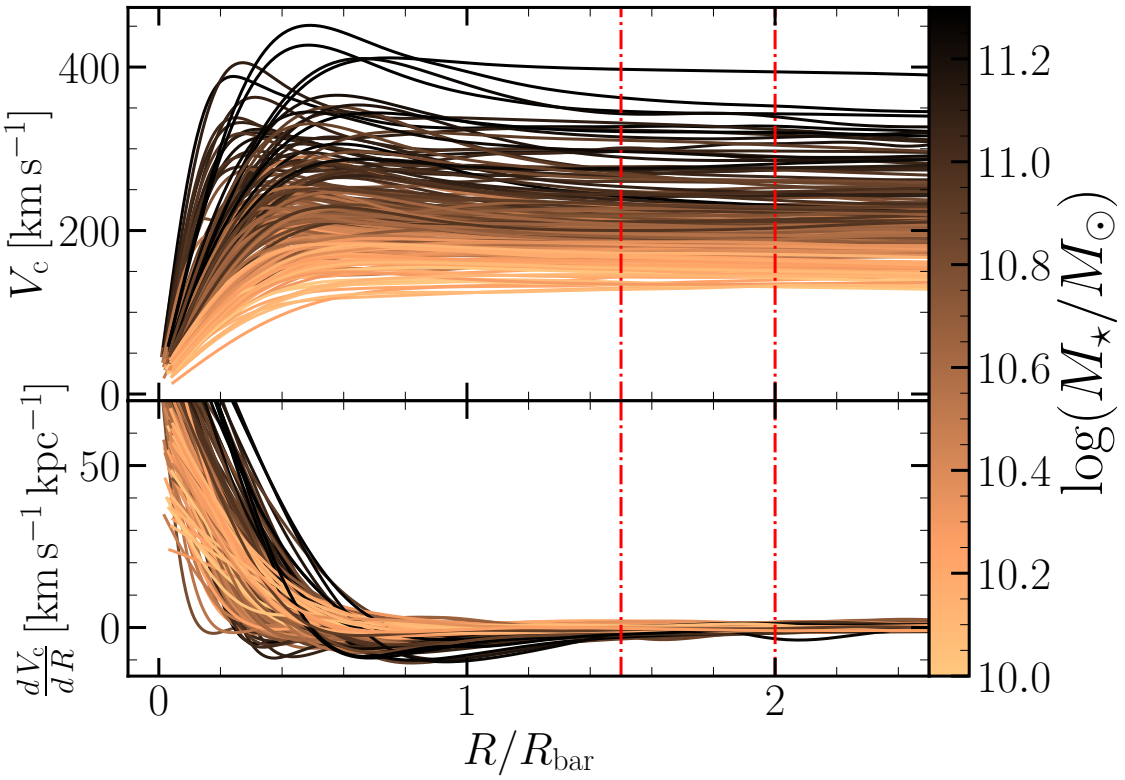

Figure 6.5: Top: the rotation curves of TNG50 barred galaxies as a function of the radius for the 191 barred galaxies. Bottom: The gradient of the rotation curves. Lines are coloured by the total stellar mass of each galaxy within $10R_{\rm eff}$. The rotation curves are largely flat between $1.5 \leq R/R_{\rm bar} \leq 2.0$ (vertical dot-dashed red lines).

To do this, we define several new quantities, normalisations and scalings of these different quantities which we summarise in Table 6.1 for the reader's convenience.

To compare kinematics between galaxies in the barred sample, we first scale the velocities by the galaxy's average mid-plane circular velocity beyond the bar radius ($1.5 \leq R/R_{\rm bar} \leq 2.0$), which we find to be a good estimate for the flat region of the rotation curve in the stellar mass range considered, as demonstrated in Fig. 6.5.

Table 6.1: Summary of quantities and notation used in this chapter.

Symbol	Description
$R_{\rm eff}$	The cylindrical radius which contains half the total stellar mass of the galaxy (the effective radius).
$R_{\rm bar}$	The bar radius defined from the $m = 2$ Fourier moment (see Section 5.3 of Chapter 5).
$V_c(R)$	The mid-plane circular velocity as a function of cylindrical radius.
$\mathcal{A}_{\rm pop}$	Average age of a sub-population of stellar particles within the bar of a galaxy.
$\mathcal{A}_{\rm bar}$	Age of the bar within a galaxy (see Section 5.4 of Chapter 5).
$\delta\tau$	The time delay between the formation of a bar and of a sub-population of stars within a galaxy.
$\overline{X_i}$	The over- and under-bars denote the quantity is scaled by the same metric measured for all bar stars (Eqn. 6.3). Subscript 'i' indicates that the quantity is presented for an individual sub-population, i.
$A_{\rm bar}$	Total $m = 2$ Fourier moment of the stellar surface density within the bar radius.
$a_{2\,\rm max}$	Peak $m = 2$ Fourier moment of the stellar surface density within the bar radius.
V^*	The asterisk denotes kinematic quantities that are scaled by the mid-plane circular velocity (V_c) between $1.5 \leq R/R_{\rm bar} \leq 2.0$ (see Section 6.4.1).
$a_2(V^*)_{\rm max}$	Peak $m = 2$ Fourier moment of the scaled spatially averaged velocity within the bar radius (Eqn. 6.3).

Continued on next page

Table 6.1 – continued from previous page

Symbol	Description
$a_2(\sigma_{V^*})_{\max}$	Peak $m = 2$ Fourier moment of the scaled spatially averaged velocity dispersion within the bar radius (Eqn. 6.3).
$\mathcal{B}$	BP strength metric defined from the 4^{th}-order Gauss-Hermite moment of the vertical velocity distribution (see Section 5.5 of Chapter 5).
R_{valley}	The location of the minima in the h_4 profile of a bar's vertical velocity distribution (see Section 6.5.1), scaled by the bar radius.
R_{BP}	The BP radius as defined by the bimodal over-density along the bar major axis (see Section 6.5.2), scaled by the bar radius.

We present an example of a random TNG50 barred galaxy in Fig. 6.6 (Subhalo ID **414917**) to demonstrate the trends of bar amplitude with relative age. In the upper panels, a transition from a strongly barred disc in the youngest sub-populations to weakly barred and then rounded, centrally-concentrated distributions is evident for decreasing $\delta\tau$. In the case of **414917**, $\mathcal{A}_{\text{bar}} = 8.69\,\text{Gyr}$, the youngest two sub-populations (A and B) formed after the bar formed and appear more strongly barred than the density distribution of all populations (upper left-hand panel). The edge-on projections are discussed later in Section 6.5.

We measure the bar amplitude ($A_{\text{bar},i}$) for each sub-population within the bar radius, R_{bar}, for all barred galaxies from the $m = 2$ Fourier component of the surface density[2]. To compare galaxies, we scale the bar amplitude of a sub-population by

[2]Although the youngest sub-populations within the bar have a highly elongated distribution, the bar amplitude of the youngest sub-population defined over the entire galaxy is low because young stars preferentially populate the stellar disc and are sparse within the bar itself (see Khoperskov et al. 2018; George et al. 2019).

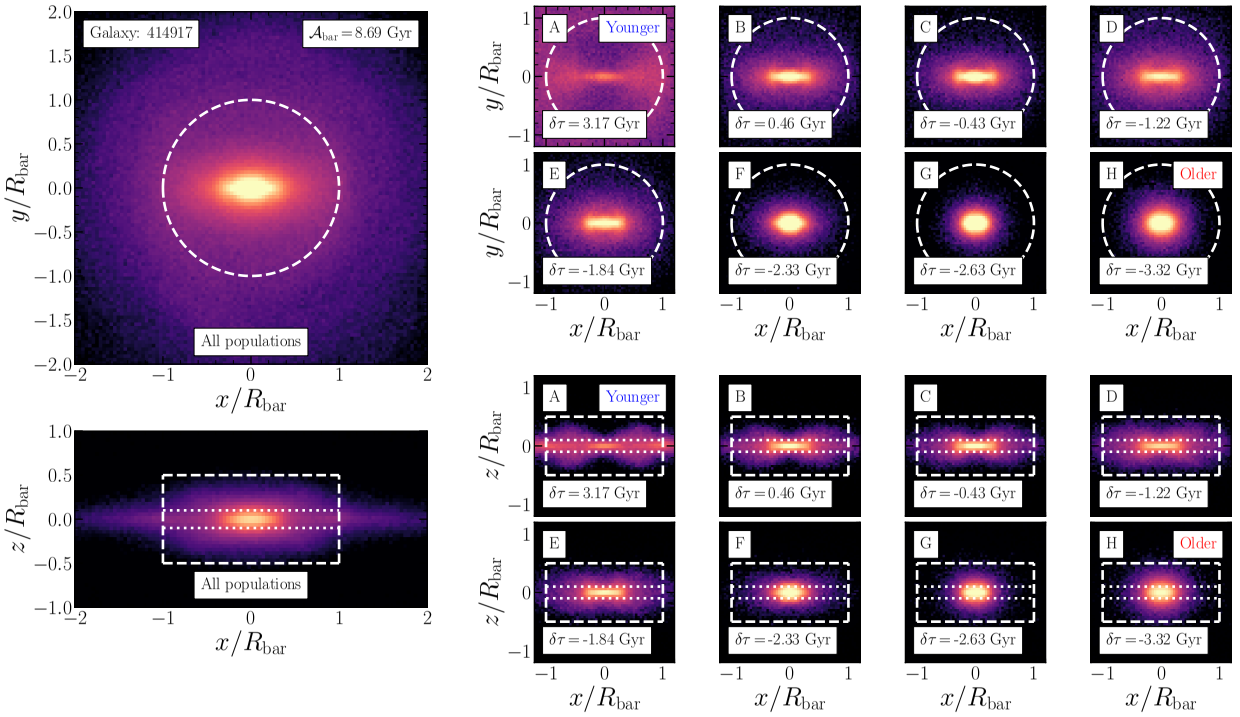

Figure 6.6: The (x, y) and (x, z) density distribution of galaxy **414917** for all star particles (top and bottom left-hand panels) and each sub-population (right-hand panels) A-H, labeled in the top left-hand corner of each panel. The relative age with respect to the bar age of each sub-population, $\delta\tau$ (Eqn. 6.1), is given in the lower caption of each panel. Only stars within the bar radius, $R < R_{\rm bar}$ and $|z|/R_{\rm bar} < 0.5$ (white dashed lines), are included in the analysis of this work. Note the disc beyond $R_{\rm bar}$ in the youngest sub-population (A), justifying the measurement of bar strength within this radius. White dotted lines in the (x, z)-projections denote the lower limits of height $|z|/R_{\rm bar} > 0.1$ used when determining the BP density bimodality in section 6.5.2.

the overall bar amplitude ($A_{\mathrm{bar,\,tot}}$) for each galaxy, *i.e.* we compute:

$$\overline{A_{\mathrm{bar},i}} = \frac{A_{\mathrm{bar},i}}{A_{\mathrm{bar,\,tot}}} \ , \tag{6.2}$$

where $i \in [A, H]$[3]. Values of $\overline{A_{\mathrm{bar},i}} > 1$ indicate a sub-population having a bar strength greater than the bar strength of the bar measured across all sub-populations of a galaxy, while values of $\overline{A_{\mathrm{bar},i}} < 1$ correspond to weaker bars.

We present the resulting distributions of $A_{\mathrm{bar},i}$ and $\overline{A_{\mathrm{bar},i}}$ as a function of $\delta\tau$ in the left panels of Fig. 6.7. The trend lines drawn for the median, 25/75 and 16/84 percentiles are calculated with adaptive bins in $\delta\tau$ containing 200 sub-populations across all 191 barred galaxies.

$A_{\mathrm{bar},i}$ increases with $\delta\tau$ for sub-populations older than the bar ($\delta\tau < 0$), whereas for younger populations ($\delta\tau > 0$) it is relatively constant. The 'break' between populations younger and older than the bar is enhanced when we scale the bar amplitudes. $\overline{A_{\mathrm{bar},i}}$ also increases from the very oldest sub-populations up to $\delta\tau = 0$ Gyr. A break or 'upturn' occurs at $\delta\tau \approx -1$ Gyr, and then flattens for $\delta\tau \geq 0$.

Alternatively, we can define the bar strength using the peak $m = 2$ Fourier amplitude within the bar radius. If we quantify the bar strength of each sub-population this way, $a_{2\,\mathrm{max},i}$, we find a similar variation with $\delta\tau$, as seen in the right panels of Fig. 6.7, including when we scale $a_{2\,\mathrm{max},i}$. As with $A_{\mathrm{bar},i}$, we find a break $\overline{a_{2\,\mathrm{max},i}}$ at $\delta\tau = 0$.

In Fig. 6.8, we present the same analysis as Fig. 6.7 but with five random TNG50 barred galaxies overlaid, signifying the tracks individual galaxies trace through this space. We find the general trends when considering all galaxies capture those of individual galaxies even though there is large scatter. As seen for TNG50 Subhalo ID **492876**), the youngest populations in barred galaxies can appear to have low bar strength due to ongoing or recent star formation. Misidentifying the precise time of bar formation may also add to the horizontal blurring of the combined trends, as

[3]We clarify that the overline denotes a scaling, not an average.

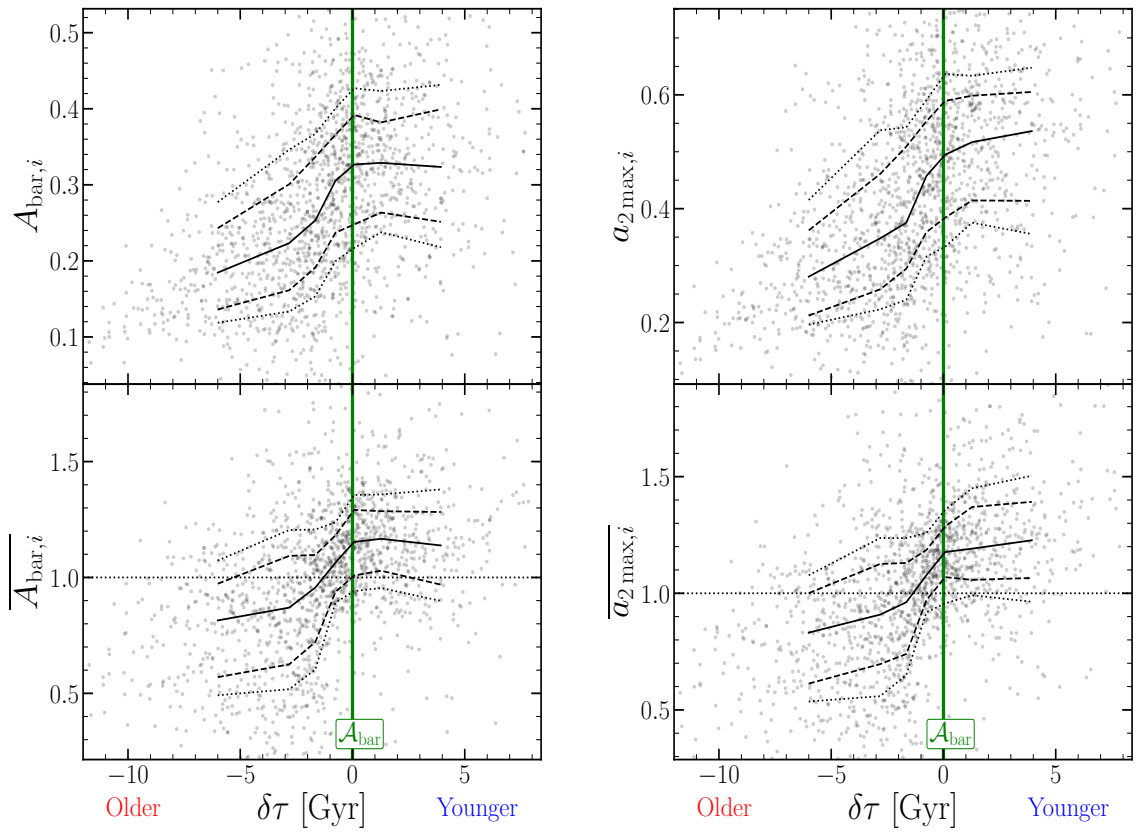

Figure 6.7: Left: The distributions of $A_{\mathrm{bar},i}$ and the scaled $\overline{A_{\mathrm{bar},i}}$ (see Eqn. 6.2) as a function of $\delta\tau$, the time delay between the time of bar formation and that of a sub-population (see Eqn. 6.1). The solid black line shows the median $A_{\mathrm{bar},i}$ where the dotted and dashed black lines represent the $25^{\mathrm{th}}/75^{\mathrm{th}}$ and $16^{\mathrm{th}}/84^{\mathrm{th}}$ percentiles, respectively. The horizontal dotted line in the lower panels donates $\overline{A_{\mathrm{bar},i}} = 1$ and $\overline{a_{2\,\mathrm{max},i}} = 1$. Right: the same as the left panels but for $a_{2\,\mathrm{max},i}$ and the scaled $\overline{a_{2\,\mathrm{max},i}}$. The vertical green line denotes $\delta\tau = 0$, or populations born at the time of bar formation and have ages $\mathcal{A}_{\mathrm{pop}} = \mathcal{A}_{\mathrm{bar}}$.

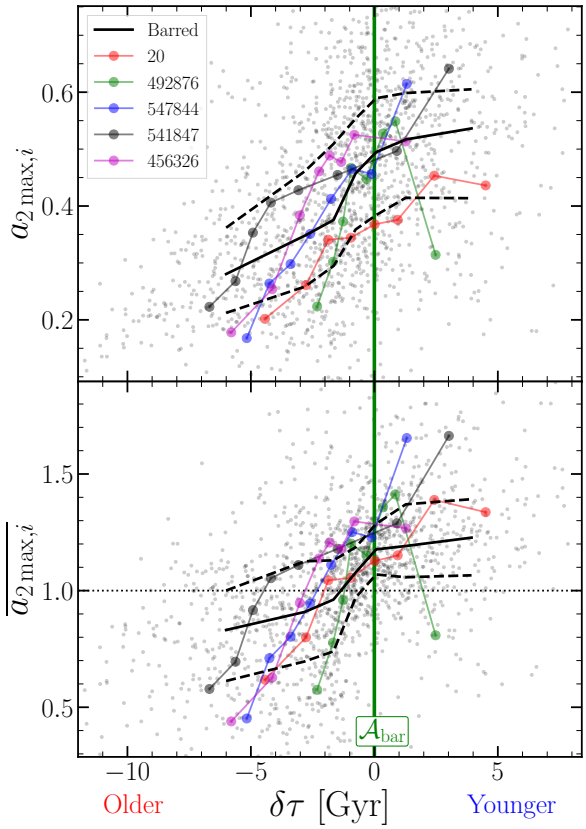

Figure 6.8: The same as the right-hand panel of Fig. 6.7 with the values of five random TNG50 barred galaxies overlaid.

may be the case with Subhalo ID **541847**).

These figures indicate that the oldest populations in a galaxy form weak bars. The bar strength increases as we approach ages closer to the bar age. Populations as old and younger than the bar have the strongest bar strengths as measured by the $m = 2$ Fourier moment of the density.

6.4.1 Kinematic Bar Strength

Gough-Kelly et al. (2022) showed that differently-aged populations within the bar region of a galaxy have distinct kinematic distributions due to forming different structures. Galactocentric cylindrical velocities, the natural frame for a rotating bar, of relatively young stars exhibit bar-aligned orbits, in contrast to the nearly axisymmetric velocity distributions of relatively old stars, which are a consequence of their respective underlying density distributions as predicted by kinematic fractionation (see Chapter 3). Using simulations, Walo-Martín et al. (2022) also showed that measures of bar strength derived from the stellar surface density correlate well with spatial measurements of stellar velocity dispersions and anisotropy.

The $m = 2$ symmetry of the bar results in quadrupolar kinematics (see Fig. 6.9). Bar supporting orbits, such as the x_1 family, are elongated along the bar major axis and produce a strong quadrupole in the galactocentric radial velocities, v_R; this quadrupole is offset from the bar major axes by $\sim 45°$ (*e.g.*, Hunt et al. 2020). Conversely, the largest values of the galactocentric tangential velocity, v_ϕ, are found on the bar minor axis on either side of the galactic centre. Towards the ends of the bar, stars on bar orbits have relatively slow tangential velocities as they reach their apocentre. The velocity dispersions of the radial and tangential velocities also peak on the major and minor axes of the bar, respectively. Therefore, stellar populations with a bar structure have average velocities (v_R and v_ϕ) and dispersions (σ_R and σ_ϕ) that exhibit quadrupole patterns in the (x, y)-plane.

6.4.1.1 Galactocentric Velocities

We define a measure of bar strength using the binned distribution of mean velocities. We bin each galaxy spatially in cylindrical radius (R) and azimuth (ϕ). Within each (R, ϕ) bin, (j, k), we calculate the average scaled velocity (scaled by the outer mid-plane circular velocity, see Fig. 6.5 and Section 6.4) for each sub-population, $\langle V^* \rangle_{(j,k)}$. We then compute the complex sum of the $m = 2$ Fourier amplitude as a function of radius:

$$a_2(V^*, R_j) = \left| \frac{\sum_k \langle V^* \rangle_{(j,k)} e^{im\phi_k}}{N_\phi} \right|, \tag{6.3}$$

where V^* is a scaled velocity component (v_R^*, v_ϕ^* or v_z^*), ϕ_k is the azimuthal angle of the bin centre, and N_ϕ is the number of azimuthal bins. As with the density metric, $a_{2,\max}$, we can define the kinematic bar strength as the maximum $m = 2$ amplitude from Eqn. 6.3 within the bar radius which we denote as $a_2(V^*)_{\max}$. Note that by binning and computing the average kinematic quantities within each bin, we are factoring out the density, so the kinematic Fourier moments are purely kinematic.

We present an example of this analysis in Fig. 6.9 for two sub-populations of the same example galaxy from Fig. 6.6 (**414917**). Each radial (j) and azimuthal (k) bin is used to calculate the Fourier amplitude following Eqn. 6.3. By presenting a relatively young sub-population (B), we can clearly see the bar in the face-on density and the corresponding $m = 2$ Fourier amplitude. For the same region, the radial and tangential velocities also exhibit quadrupolar distributions, which also produce large $m = 2$ Fourier amplitudes. In contrast, the oldest sub-population (H) has a weak bar morphology and no clear peaks in the Fourier amplitudes of the radial and tangential velocities.

In Fig. 6.10 (top left-hand panel), we present the maximum amplitude of the galactocentric radial velocities, $a_2({v_R}^*)_{\max,i}$, as a function of $\delta\tau$. The distribution is relatively flat for sub-populations older than the bar. The gradient then increases rapidly beyond $\delta\tau = 0$, though with a large scatter. When we scale by the amplitude

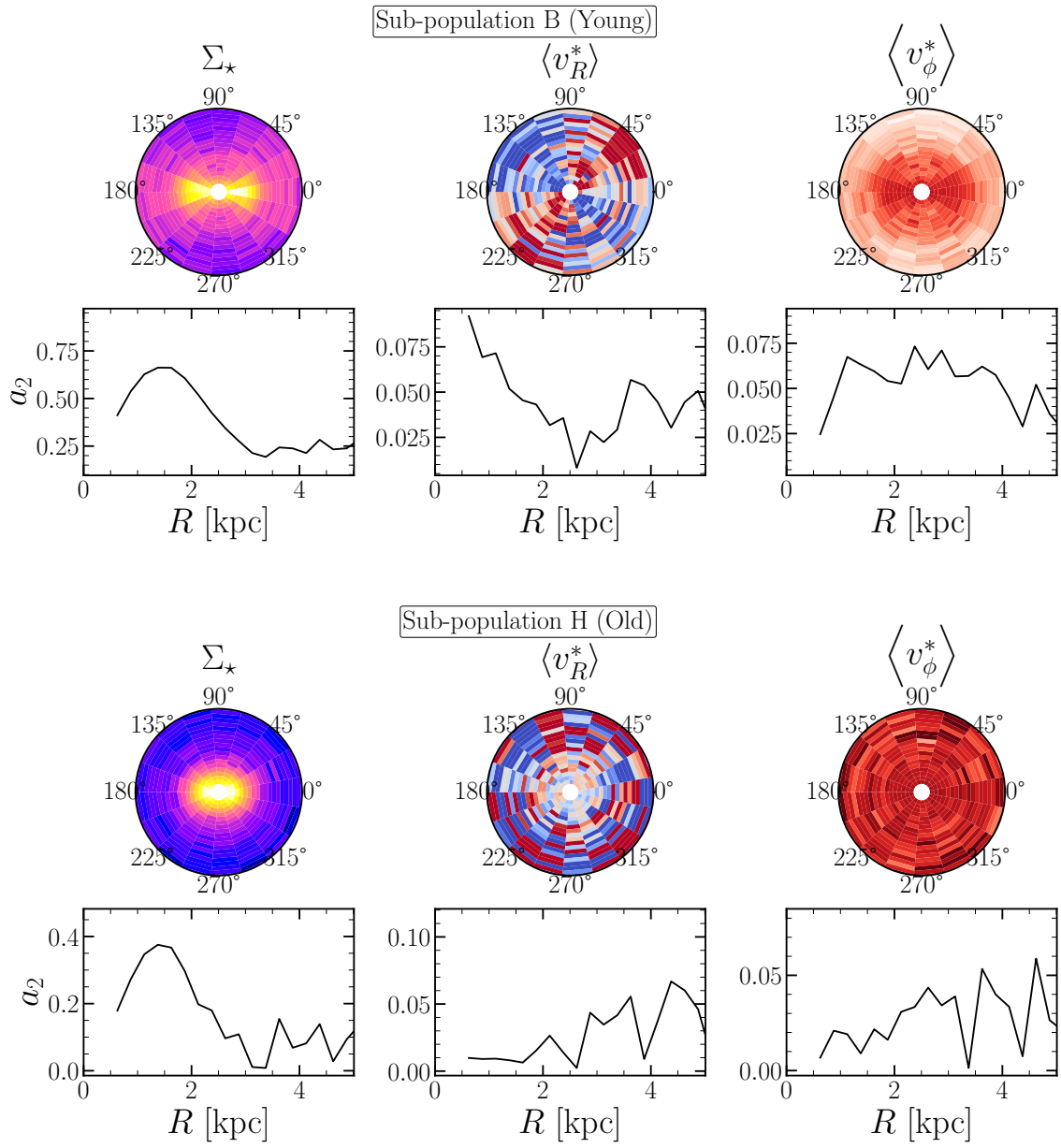

Figure 6.9: The face-on polar projection of stellar surface density (left-hand columns), average radial velocity (middle columns) and average tangential velocity (right-hand columns) for sup-populations B (top rows) and H (bottom rows) from Subhalo ID **414917**. The radial and azimuthal bins in each panel are used to calculate the $m = 2$ Fourier amplitude as described in Eqn. 6.3. The panels beneath each polar projection present the $m = 2$ Fourier amplitude for each quantity as a function of radius.

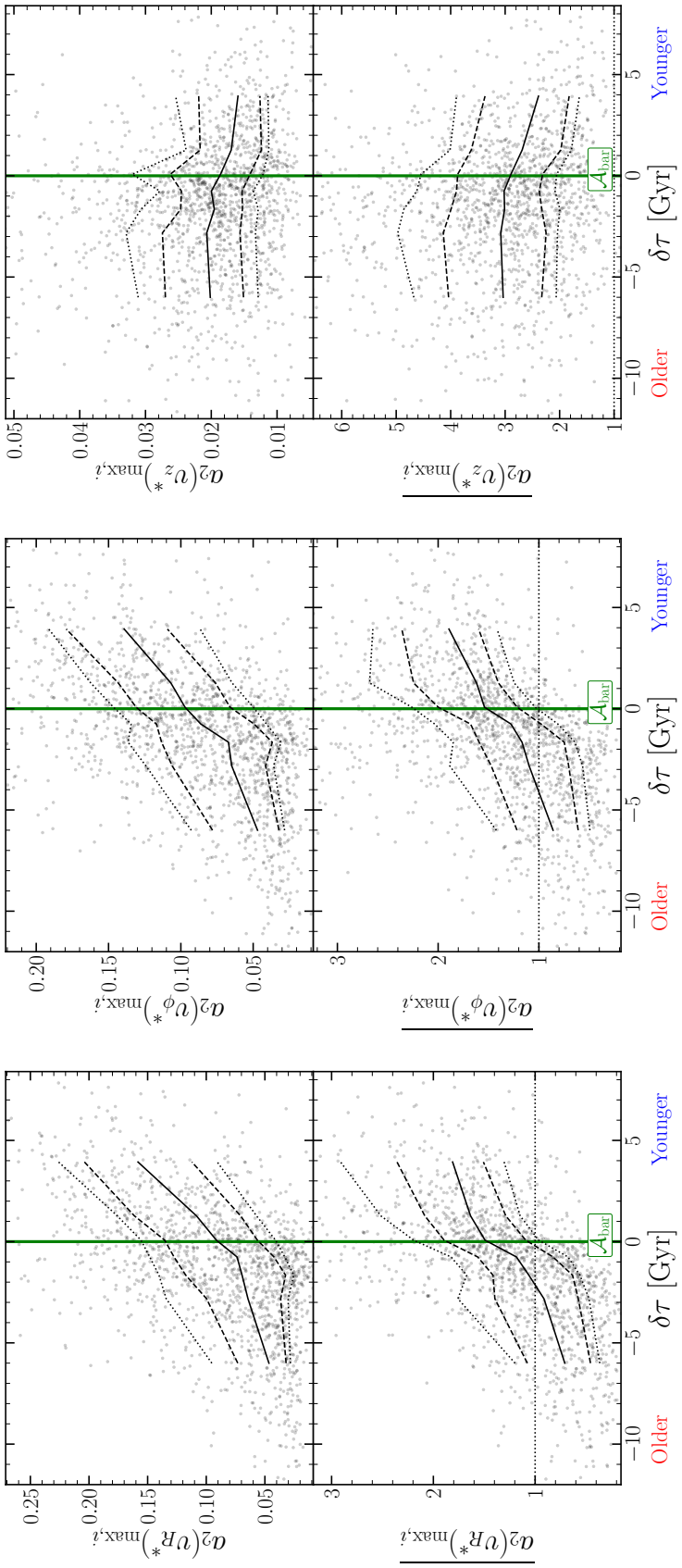

Figure 6.10: The same as Fig. 6.7 but for the distributions of $a_2(V^*)_{\max}$ (top) and $\overline{a_2(V^*)_{\max}}$ (bottom) for $V^* \in [v_R^*, v_\phi^*, v_z^*]$ (left, middle and right, respectively) as a function of $\delta\tau$.

for each bar in the same way as with the density, $\overline{a_2({v_R}^*)_{\mathrm{max},i}}$ (see Eqn. 6.2), we find a linearly increasing profile for $\delta\tau \leq 0$, followed by a rapid rise to higher $\overline{a_2({v_R}^*)_{\mathrm{max},i}}$ values (bottom left-hand panel of Fig. 6.10).

Similarly, we present the distributions of maximum $m = 2$ amplitude of the galactocentric tangential velocities, $a_2({v_\phi}^*)_{\mathrm{max},i}$ and $\overline{a_2({v_\phi}^*)_{\mathrm{max},i}}$, in the middle panels of Fig. 6.10. We find a quite similar behaviour to $a_2({v_R}^*)_{\mathrm{max},i}$.

We also examine the age dependence of the vertical kinematics. Bars drive stars to larger heights based on their initial radial velocity dispersion (Debattista et al. 2017). Yet, vertical structures in barred galaxies such as BPs are typically symmetrical about the plane except during a buckling event (*e.g.*, Sellwood & Gerhard 2020) and for some Gyr following (Cuomo et al. 2022). Since vertical velocities at the current epoch should generally average to zero regardless of whether a BP bulge structure is present[4], any signatures of non-axisymmetric distributions of vertical kinematics are expected in the velocity dispersions and not in the averaged velocities. Indeed in the right-hand panels of Fig. 6.10, we find very weak maximum $m = 2$ amplitudes of the galactocentric vertical velocities where both profiles of $a_2({v_z}^*)_{\mathrm{max},i}$ and $\overline{a_2({v_z}^*)_{\mathrm{max},i}}$ appear flat across all $\delta\tau$.

We conclude that the $m = 2$ Fourier moments of spatially averaged in-plane galactocentric velocities (v_R and v_ϕ) depend on $\delta\tau$, as was the case for the bar strength of the stellar surface density. Younger populations have asymmetric kinematics indicative of strong bars compared to older populations, where more axisymmetric velocities are measured except in the vertical component. Therefore in-plane kinematic metrics can be used as a proxy for bar strength. We quantitatively compare kinematic bar strength metrics against those measured via the stellar surface density in Section 6.4.2.

[4]Unless the galaxy is currently buckling or there is strong accretion in progress.

6.4.1.2 Velocity Dispersions

Using the same spatial binning method as for the average velocities, we also calculate the velocity dispersions in each bin and measure their maximum $m = 2$ amplitude (Eqn. 6.3) for the galactocentric velocities.

The distribution of $a_2({\sigma_R}^*)_{\max,i}$ follows qualitatively similar trends to those of $a_2({v_R}^*)_{\max,i}$ as shown in the left-hand panels of Fig. 6.11. Populations older than the bar ($\delta\tau < 0$) have a flat profile of $a_2({\sigma_R}^*)_{\max,i}$ that breaks at $\delta\tau = 0$, after which $a_2({\sigma_R}^*)_{\max,i}$ increases linearly. We also observe the same trend when we scale the values ($\overline{a_2({\sigma_R}^*)_{\max,i}}$). Similarly, $a_2({\sigma_\phi}^*)_{\max,i}$ and $\overline{a_2({\sigma_\phi}^*)_{\max,i}}$ (middle panels of Fig. 6.11) matches the trend in $a_2({v_\phi}^*)_{\max,i}$and $\overline{a_2({v_\phi}^*)_{\max,i}}$. We do note however a sharper rise in $\overline{a_2({v_\phi}^*)_{\max,i}}$ between $-1 \lesssim \delta\tau/\text{ Gyr} \lesssim 0$ and that the profile is flat for $\delta\tau > 0$.

In the right-hand panels of Fig. 6.11, we present the distributions of $a_2({\sigma_z}^*)_{\max,i}$ which, unlike $a_2({v_z}^*)_{\max,i}$, shows a mildly increasing trend with $\delta\tau$ like those of $a_2({\sigma_R}^*)_{\max,i}$ and $a_2({\sigma_\phi}^*)_{\max,i}$. Although $a_2({\sigma_z}^*)_{\max,i}$ has a weaker dependence on $\delta\tau$ and shows a weaker upturn at $\delta\tau = 0$. We also find a weak dependence in $\overline{a_2({\sigma_z}^*)_{\max,i}}$.

The velocity dispersions of the in-plane components of galactocentric velocities (σ_R and σ_ϕ) show that the $m = 2$ Fourier amplitude depends on the relative age of populations with a break observed for populations formed near the epoch of bar formation. The vertical velocity dispersion follows a similar trend with $\delta\tau$ but with a weaker break at $\delta\tau = 0$. These results indicate that velocity dispersions also trace the epoch of bar formation but have a weaker dependence than the averaged velocity. They also show that there is a stronger dependence on $\delta\tau$ in the in-plane kinematics

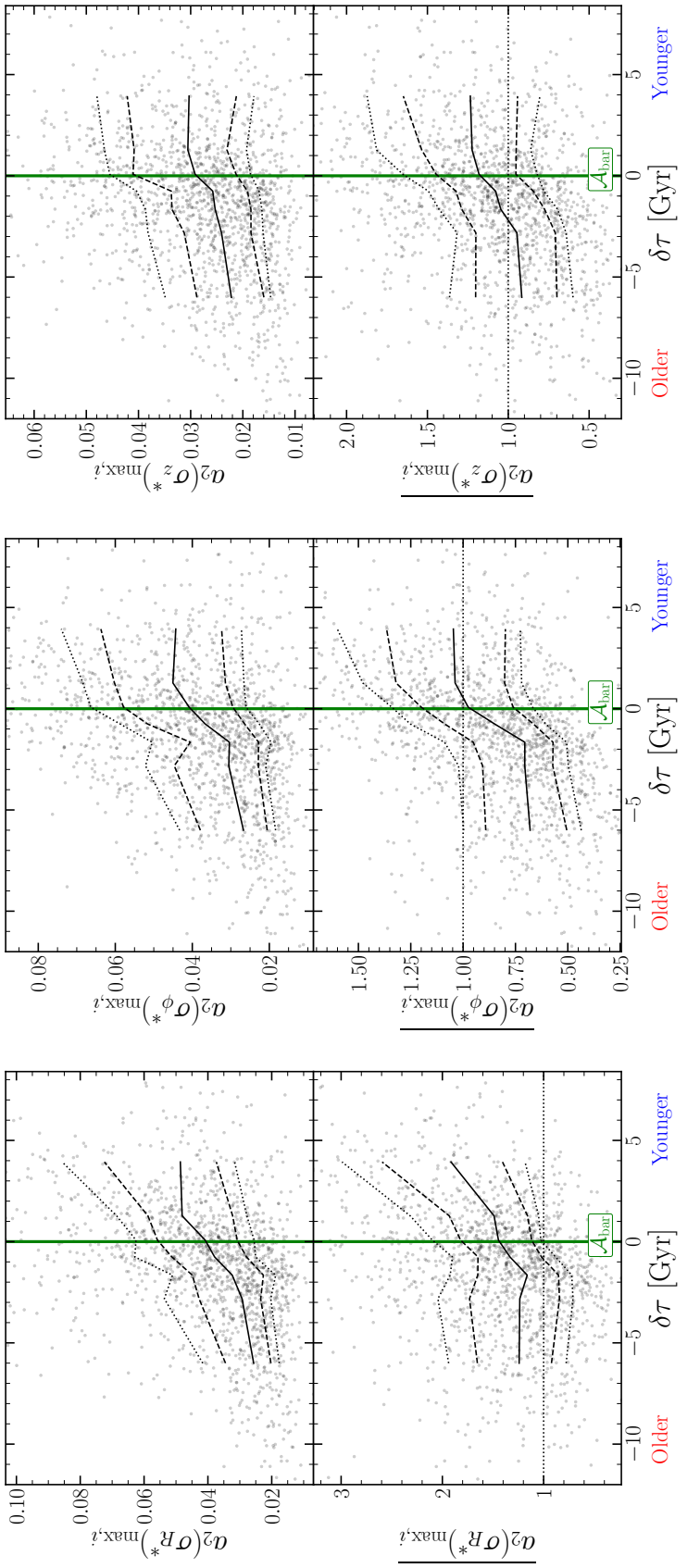

Figure 6.11: The same as Fig. 6.7 but for the distributions of $a_2(\sigma_{V^*})_{\max}$ (top) and $\overline{a_2(\sigma_{V^*})_{\max}}$ (bottom) for $\sigma_{V^*} \in [\sigma_R^*, \sigma_\phi^*, \sigma_z^*]$ (left, middle and right, respectively) as a function of $\delta\tau$.

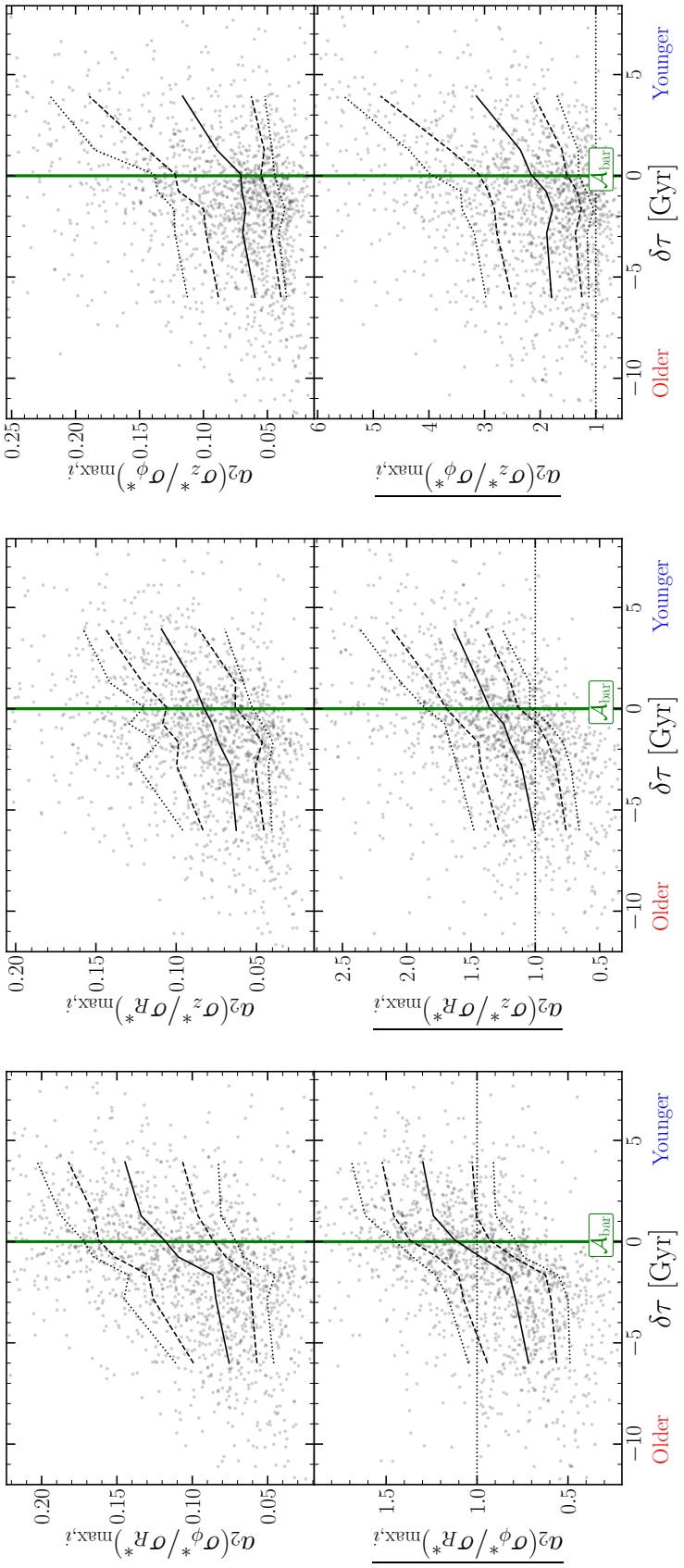

Figure 6.12: The same as Fig. 6.7 but for the distributions of $a_2(\sigma_\alpha^*/\sigma_\beta^*)_{\max}$ (top) and $\overline{a_2(\sigma_\alpha^*/\sigma_\beta^*)_{\max}}$ (bottom) for ${\sigma_\phi}^*/{\sigma_R}^*$, ${\sigma_z}^*/{\sigma_R}^*$ and ${\sigma_z}^*/{\sigma_\phi}^*$, as a function of $\delta\tau$.

6.4.1.3 Anisotropy

Walo-Martín et al. (2022) showed that the face-on distributions of velocity dispersions and of the stellar velocity ellipsoid (σ_z/σ_r and σ_ϕ/σ_r) have strong correlations with bar strength and size using the Auriga suite of simulations (Grand et al. 2017). Here we explore these non-axisymmetric distributions of the anisotropy via the $m = 2$ Fourier amplitudes of the dispersion ratios $a_2({\sigma_\phi}^*/{\sigma_R}^*)_{\mathrm{max},i}$, $a_2({\sigma_z}^*/{\sigma_R}^*)_{\mathrm{max},i}$ and $a_2({\sigma_z}^*/{\sigma_\phi}^*)_{\mathrm{max},i}$.

The profiles of $a_2({\sigma_\phi}^*/{\sigma_R}^*)_{\mathrm{max},i}$ and $\overline{a_2({\sigma_\phi}^*/{\sigma_R}^*)_{\mathrm{max},i}}$ presented in the left-hand panels of Fig. 6.12 most closely resemble the profiles of $A_{\mathrm{bar},i}$ and $a_{2\,\mathrm{max},i}$ of all the kinematic bar measurements we have explored. An increasing gradient of amplitude with $\delta\tau$ is seen in populations older than the bar ($\delta\tau < 0$) with an upturn just before the age of bar formation ($\delta\tau = -1$ Gyr) where the gradient flattens for the populations younger than the bar ($\delta\tau > 0$). The profile of $\overline{a_2({\sigma_\phi}^*/{\sigma_R}^*)_{\mathrm{max},i}}$ has a more prominent rise just before $\delta\tau = 0$ when we scale the amplitudes (Eqn. 6.2).

The profiles of $a_2({\sigma_z}^*/{\sigma_R}^*)_{\mathrm{max},i}$ and $\overline{a_2({\sigma_z}^*/{\sigma_R}^*)_{\mathrm{max},i}}$ (middle panels of Fig. 6.12) show a clear increase with $\delta\tau$, similar to the previously presented bar strength metrics. However, there is only a weak 'break' in $\delta\tau$ as seen in the amplitudes of velocity dispersions (Fig. 6.11). We find similar trends in the dependence of $a_2({\sigma_z}^*/{\sigma_\phi}^*)_{\mathrm{max},i}$ and $\overline{a_2({\sigma_z}^*/{\sigma_\phi}^*)_{\mathrm{max},i}}$, which are shown in the right-hand panels of Fig. 6.12.

These results demonstrate the non-axisymmetric anisotropy distributions in the (x, y)-planes of barred galaxies. The $m = 2$ amplitudes of the in-plane and vertical dispersion ratios depend on a sub-population's age relative to the bar, with the in-plane anisotropy having the strongest dependence on the bar formation epoch.

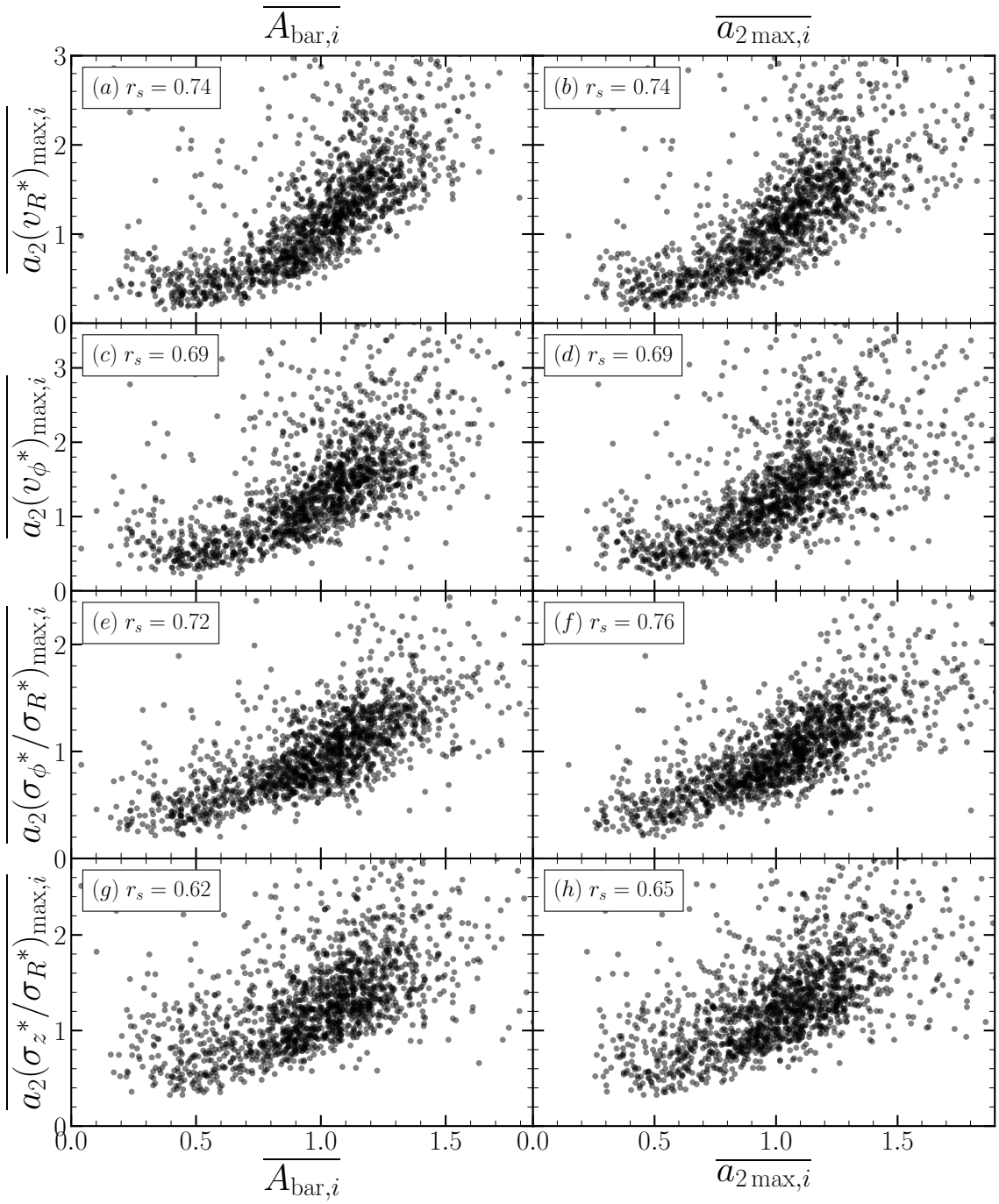

Figure 6.13: The strongest four correlations of scaled kinematic bar strengths versus scaled density bar strengths. The Spearman rank correlation coefficient (r_s) for each combination of variables is given in the upper left-hand corner of each panel. All correlations presented here have high significance ($p < 0.01$).

6.4.2 Correlations

We compare the correlations between the different kinematic bar strengths and the density bar strengths to demonstrate the utility of the kinematic metrics. We do this by considering every sub-population from every galaxy with their respective scaled Fourier amplitudes (Eqn. 6.2), calculating the Spearman rank correlation coefficient, r_s between each metric. We present the four comparisons which exhibit the strongest correlations between the kinematic metrics and density metrics in Fig. 6.13[5].

We start by comparing the kinematic bar strength measurements from the spatially averaged radial and tangential velocities, $\overline{a_2({v_R}^*)_{\mathrm{max},i}}$ and $\overline{a_2({v_\phi}^*)_{\mathrm{max},i}}$ (section 6.4.1.1). For the radial velocities, $\overline{a_2({v_R}^*)_{\mathrm{max},i}}$ correlates well with both $\overline{A_{\mathrm{bar},i}}$ and $\overline{a_{2\,\mathrm{max},i}}$, with $r_s = 0.74$ for each, respectively (panels a and b). The tangential component has slightly weaker correlations, with values of $r_s = 0.69$ in both comparisons (panels c and d).

The Fourier amplitudes of the velocity dispersion ratios (Section 6.4.1.3) also correlate strongly with density amplitudes, with the in-plane anisotropy, $\overline{a_2({\sigma_\phi}^*/{\sigma_R}^*)_{\mathrm{max},i}}$ having correlation strengths $r_s = 0.72$ and $r_s = 0.76$ (panels e and f). Correlations of $r_s = 0.62$ and $r_s = 0.65$ are found for the vertical anisotropy $\overline{a_2({\sigma_z}^*/{\sigma_R}^*)_{\mathrm{max},i}}$ (panels g and h).

These results show that the $m = 2$ Fourier amplitudes of the average velocity (v_R and v_ϕ) are better tracers of the density bar strength than the amplitudes of velocity dispersion components separately (σ_R and σ_ϕ). We find stronger correlations of dispersion ratios (anisotropy) with bar strength than the individual dispersions, as did Walo-Martín et al. (2022). A complete comparison of the correlations between all measures of kinematic bar strength (scaled and unscaled) is included in the Appendix. These correlations also suggest that bar amplitude metrics from both

[5]Each presented correlation has $p < 0.01$ therefore, we reject the null hypothesis that there is no monotonic relation.

density and kinematics are tracing similar dependencies of the stellar populations' age relative to the bar and help constrain the epoch of bar formation. We find the best tracer of bar strength is the spatial distribution of the in-plane anisotropy (σ_ϕ/σ_R).

6.5 BP Bulges

A23 identified the 106 barred galaxies in the TNG50 sample with box/peanut (BP) bulges at $z = 0$ through a combination of visual inspection and quantitative measurement of the BP 'prominence' using the fourth-order Gauss-Hermite moment of the vertical velocity distribution (h_4). Full details of the BP selection are provided in Chapter 5 (Appendix A4 of A23). In addition, A23 quantified the BP strength, denoted as $\mathcal{B}$, using the difference between the peak and the valley of the h_4 profile along the bar major axis. This also leaves us with a sample of barred galaxies that do not have a BP bulge at $z = 0$ (85, the non-BP sample).

We were able to determine the formation mechanism for the BP bulges by exploring the change of $\mathcal{B}$ through a galaxy's evolution. A rapid increase in $\mathcal{B}$ indicates a buckling event, which usually coincides with asymmetric bending of the bar in the (x, z)-plane, which A23 confirmed by visual inspection. Gradual increases of $\mathcal{B}$ without asymmetric bending instead are attributed to weak buckling or resonant trapping (Quillen 2002) though both mechanisms may have their origins in resonant excitation (Li et al. 2023). This allowed A23 to define a buckling sample of 52 galaxies and 54 weak/non-buckling galaxies (denoted BCK and WNB, respectively). A23 also defined a control sample of barred, non-BP galaxies which matched the stellar mass distribution of the BP sample (Section 5.6 of Chapter 5). A23 found that these control galaxies have, on average, shorter and weaker bars, which are key factors of why they do not form BP bulges. Here we use the same definitions of the BCK, WNB and control samples to study the properties of BPs.

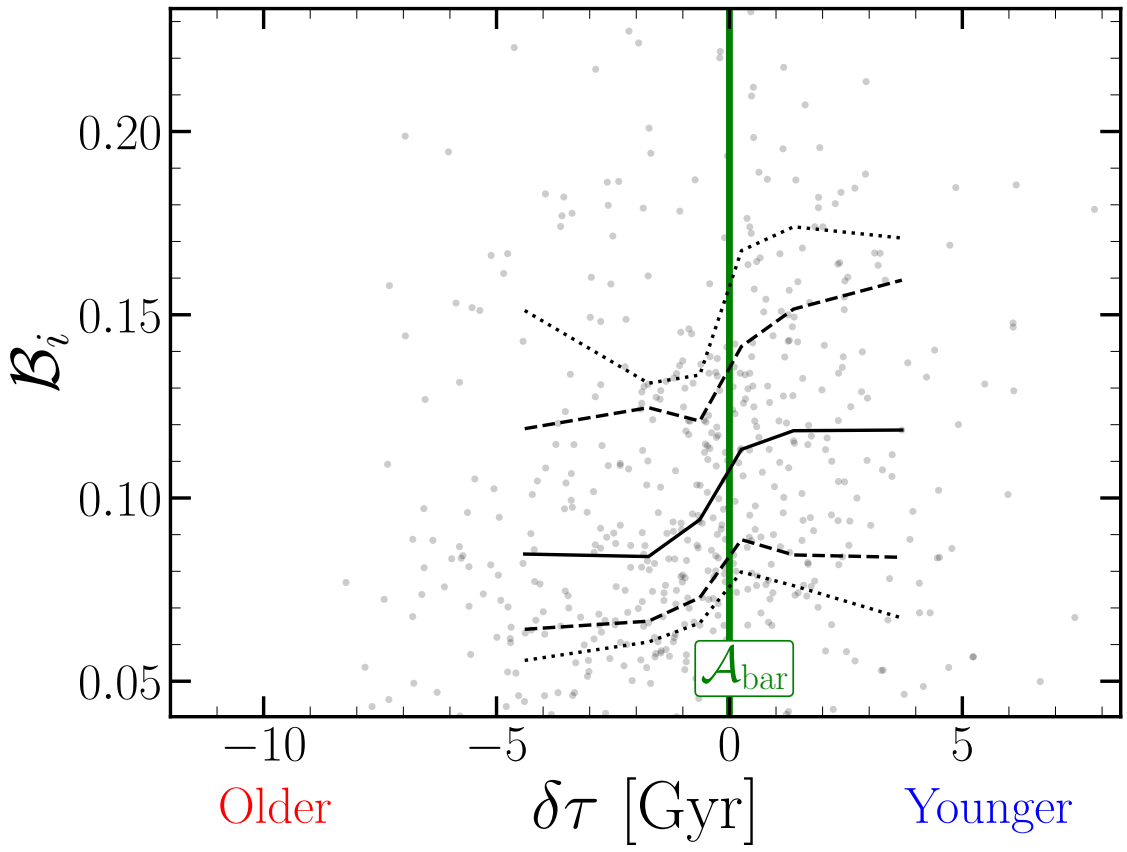

Figure 6.14: The distributions of $\mathcal{B}_i$ as a function of $\delta\tau$, the difference between the time of bar formation of a galaxy and a sub-population's average age (see Eqn. 6.1) for the 106 BP galaxies (A23).

The lower panels of Fig. 6.6 present the side-on view of TNG50 galaxy **414917**, showing the variation of bulge morphology with relative age. The bulge appears as a well-defined peanut shape in the youngest sub-populations, which weakens to become boxy and then rounded for decreasing $\delta\tau$ (older populations). The density distribution of all populations in the bulge appears box-shaped.

6.5.1 BP Strength

We now explore how the BP strength, $\mathcal{B}$, varies as a function of the relative age of a sub-population for the BP sample of barred galaxies in TNG50. We use the same methodology described in Section 5.5 of Chapter 5 (A23 Appendix A4) but measure the h_4 profiles for each sub-population at $z = 0$ separately, to compute their BP strength, $\mathcal{B}_i$.

Fig. 6.14 presents the BP strength measurements as a function of $\delta\tau$. $\mathcal{B}_i$ increases with increasing $\delta\tau$ for the BP galaxies, with the strongest BP amplitudes in populations with ages close to the bar's age, $\delta\tau \approx 0$, albeit with a large scatter. However, the gradient of the trend lines may be underestimated owing to the difficulty of measuring this quantity for the weaker BP signals in older populations. Since this technique relies on identifying two minima in the h_4 profile, we can only capture populations in which the algorithm detects two significant minima. Thus in the oldest populations, the metric may capture only the strongest cases or possibly spurious signals (see Section 5.7 of Chapter 5).

Along with the BP strength, we also track the location along the bar's major axis of the minima (valleys) in the h_4 profile (see Debattista et al. 2005; Méndez-Abreu et al. 2008; Anderson et al. 2023). We explore whether this location, normalised by the bar radius, $R_{\mathrm{valley},i}$, depends on $\delta\tau$. We find that the distributions of $R_{\mathrm{valley},i}$ and $\overline{R_{\mathrm{valley},i}}$ are flat across $\delta\tau$ (left-hand panels of Fig. 6.15).

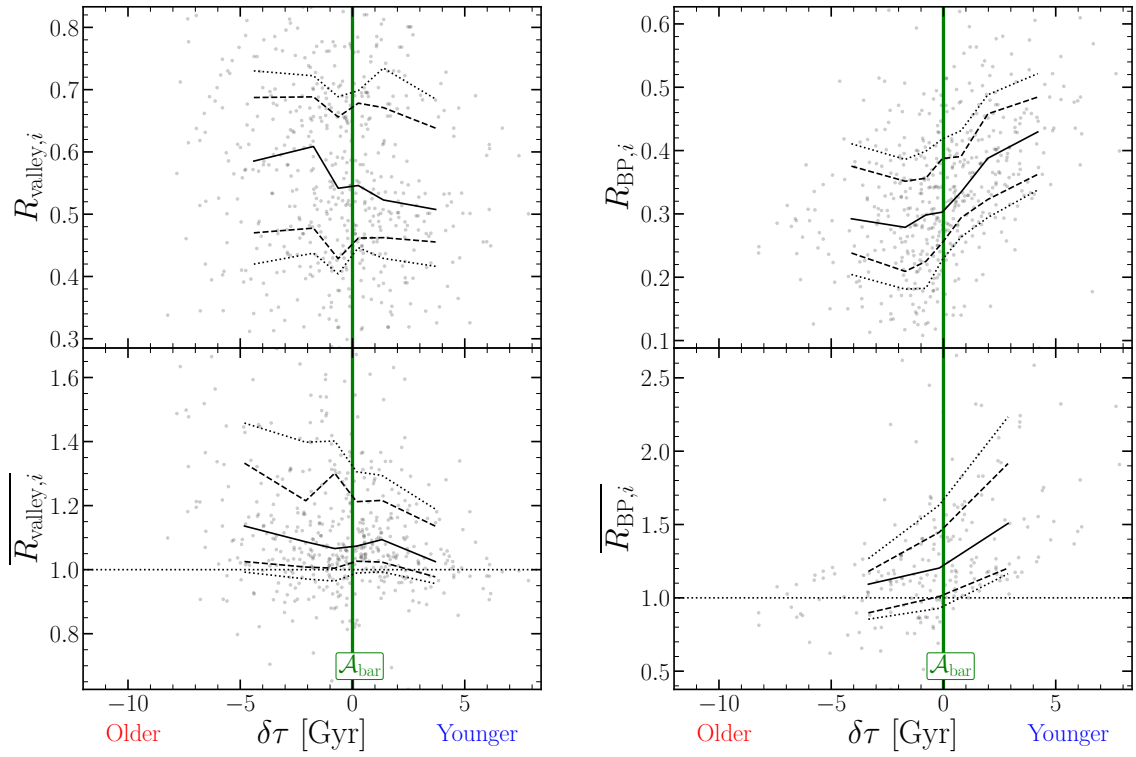

Figure 6.15: The same as Fig. 6.14 but for the distribution of $R_{\mathrm{valley},i}$, and $\overline{R_{\mathrm{valley},i}}$ (left) and for $R_{\mathrm{BP},i}$, and $\overline{R_{\mathrm{BP},i}}$ (right) and as a function of $\delta\tau$. The horizontal dotted black line denotes $\overline{R_{\mathrm{valley},i}} = 1$ and $\overline{R_{\mathrm{BP},i}} = 1$, where the BP radius of a sub-population is the same as the radius when measuring all the populations in a galaxy's bar together.

Across all populations, we find an average $R_{\mathrm{valley},i} = 0.55^{+0.16}_{-0.13}$ ($16^{\mathrm{th}}/84^{\mathrm{th}}$ percentiles), with a large scatter. When we scale these radii by measuring the h_4 valley location for all bar populations, we find that most values lie close to $\overline{R_{\mathrm{valley},i}} = 1$, as can be seen in the lower left-hand panel of Fig. 6.15. The small deviation towards values of $\overline{R_{\mathrm{valley},i}} > 1$ in the older populations is likely due to the larger uncertainties in identifying the minima associated with a weaker BP bulge (Fig. 6.14). Overall these results indicate that a BP radius defined kinematically is sensitive to the overall potential and so results in a common radius for all populations ($\overline{R_{\mathrm{valley},i}} \approx 1$).

6.5.2 Separation of Bimodal Density Distribution

In addition to identifying the BP radius kinematically, we can quantify it through the location of over-dense regions along the bar major axis. A BP bulge produces a bimodal density distribution above the plane along the bar's major axis, as seen in the lower panels of Fig. 6.6. Given this geometry, the separation between the peaks increases as a function of vertical height. Observational studies have shown that the separation between the peaks is a function of age and associated stellar parameters, such as metallicity (*e.g.* Ness et al. 2012; Uttenthaler et al. 2012; Rojas-Arriagada et al. 2014; Semczuk et al. 2022) and has been shown in simulations (*e.g.*, Athanassoula et al. 2017; Debattista et al. 2017, 2019; Fragkoudi et al. 2017b, 2020; Buck et al. 2018; Gough-Kelly et al. 2022). To explore the spatial separation of over-densities produced by the BP bulge, we define a slit along the bar's major axis, normalising the spatial dimensions by the galaxy's bar length to compare between galaxies in the BP sample. We set the width of the slit to be $0.6R_{\mathrm{bar}}$, (*i.e.*, $|y|/R_{\mathrm{bar}} < 0.3$) and restrict the vertical height out of the plane along this slit to between $0.1 \leq |z|/R_{\mathrm{bar}} \leq 0.5$. Then, we measure the density along the slit for each sub-population and, using a peak-finding algorithm[6], measure the separation

[6]Using `scipy.signal.find_peaks`.

between the two peaks (disregarding any central peak close to $x/R_{\rm bar} = 0$). We denote the BP radius computed using this method as $R_{{\rm BP},i}$.

In the right-hand panels of Fig. 6.15, we present the distribution of $R_{{\rm BP},i}$ and $\overline{R_{{\rm BP},i}}$ as a function of $\delta\tau$ for the BP galaxies. We find that populations older than the bar ($\delta\tau < 0$) have a relatively flat profile. At $\delta\tau = 0$, there is a sharp upturn, and for populations younger than the bar, $R_{{\rm BP},i}$ increases with increasing $\delta\tau$. We find a much smaller range of BP radius measurements in the density ($0.2 \lesssim R_{{\rm BP},i} \lesssim 0.5$) than in the locations of the h_4 minima, $R_{{\rm valley},i}$. This compares favourably to measurements for local galaxies, which find a range of $R_{\rm BP}/R_{\rm bar} = 0.26 - 0.58$ (mean values of 0.38 ± 0.08 Erwin & Debattista 2013).

In Fig. 6.16 we present the h_4 and density profiles for Subhalo ID: **117259**, a galaxy that forms a BP through buckling. In the youngest sub-populations (A and B), we can identify clear signals of a BP from the deep minima in h_4 and the bimodal density distribution. This demonstrates that the profiles of individual sub-populations can also be used to characterise the BP in each, even with the reduced statistics. The deep minima compared to the central peak in h_4 also suggest high BP strength (Anderson et al. 2023). As we move to older sub-populations, the h_4 profiles flatten, and the density distribution becomes singularly peaked. At intermediately aged sub-populations, peaks and valleys become challenging to identify, adding scatter to the combined distributions.

In the top panel of Fig. 6.16, we present the profiles of all stellar populations with the bar for the same galaxy. The h_4 valleys are clearly visible whereas the BP is difficult to distinguish, only appearing as 'shoulders' on the density distribution. This demonstrates that we were unable to identify the bimodality when considering the density distribution of all bar populations in aggregate for all galaxies. As noted by A23, BPs in TNG50 appear weaker than in observations. However, for 27 out of 106 (25%) BP galaxies, we can measure BPs in their overall distribution

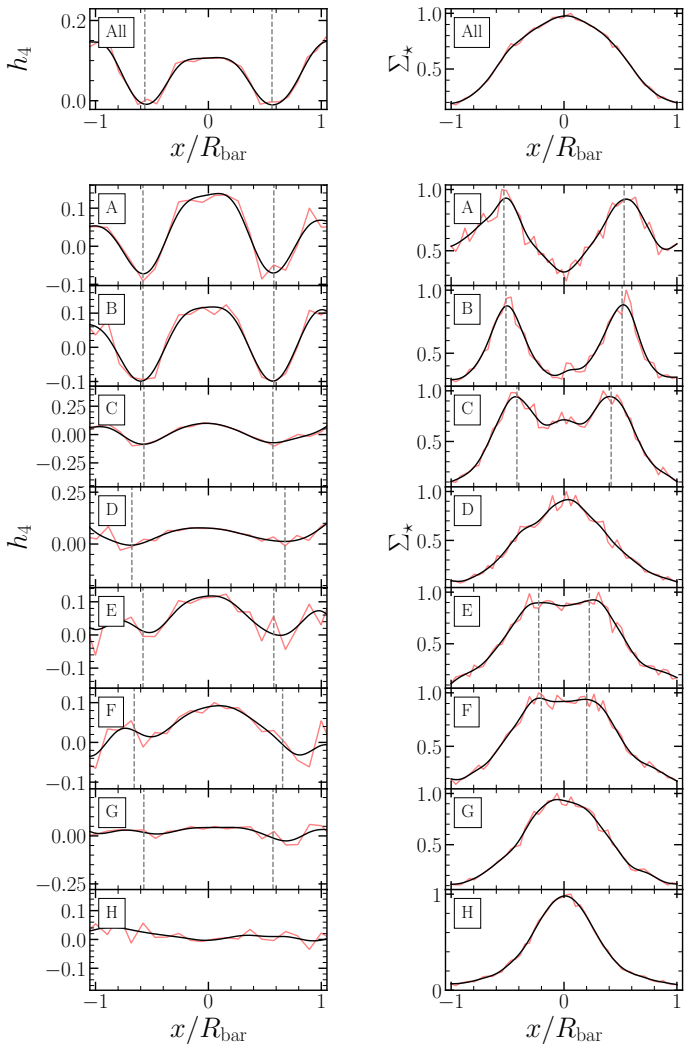

Figure 6.16: Left-hand column: average profiles of the h_4 moment of the vertical velocity distribution along the bar major axis of the sub-populations from Subhalo ID: **117259**. Right-hand column: average profiles of normalised density between $0.1 < |z|/R_{\rm bar} < 0.5$ along the bar major axis of the sub-populations from the same galaxy. Each row represents a sub-population A-H, with the top row presenting all populations within the bar radius. The vertical grey dashed lines denote the $R_{{\rm valley},i}$ and $R_{{\rm BP},i}$ for the left and right columns, respectively. The red line shows the profiles whereas the black line shows the profiles after smoothing with a Butterworth low-pass filter (Butterworth 1930).

and can scale their radii. When we scale the BP radius, $\overline{R_{\mathrm{BP},i}}$, we find an overall increasing profile of BP radius with $\delta\tau$[7]. The oldest populations have $\overline{R_{\mathrm{BP},i}} \approx 1$, while populations younger than the bar typically have larger values of $\overline{R_{\mathrm{BP},i}}$.

In the oldest populations, we only detect the bimodal density signature when they have large over-densities; the weakest bimodalities may not be detected. Nonetheless, we still identify density bimodalities in populations much older than the bar, even 5 Gyr or more before the bar formed.

We rebin the BP galaxies' sub-populations in $\delta\tau$ (see top panel of Fig. 6.4) and construct average profiles of stellar density and h_4 in the range $-5 \leq \delta\tau/\,\mathrm{Gyr} \leq 5$. Fig. 6.17 shows that the oldest bin ($\delta\tau = -4 \pm 1$ Gyr) has a relatively flat h_4 profile, with a small central peak and very shallow minima located at $|x|/R_{\mathrm{bar}} \sim 0.55$ (top left-hand panel). The density profile in the top right-hand panel for the same bin has a strong central peak with a slight broadening at small radius ($|x|/R_{\mathrm{bar}} \sim 0.2$). Moving towards $\delta\tau = 0$, the profiles of h_4 develop a larger central peak, and their valleys deepen. However, the location of the h_4 minima remains at $|x|/R_{\mathrm{bar}} \sim 0.5$. Instead, the density distributions separate, losing their central peak and producing first a flat top, before becoming two distinct peaks with a central valley. In younger sub-populations, these peaks separate further towards $|x|/R_{\mathrm{bar}} \sim 0.5$. The profiles of the youngest bins are substantially different from those of the oldest. The profile of h_4 commonly associated with a BP (central peak and two deep minima) at $|x|/R_{\mathrm{bar}} \sim 0.5$ is most evident in the youngest two bins. Similarly, the density profiles of the same bins are clearly bimodal with a central valley, with peaks at $|x|/R_{\mathrm{bar}} \sim 0.5$.

The position of the h_4 minima is sensitive to the overall potential along the bar, so its location does not change as a function of stellar age but moves outwards with the growth of the bar (Anderson et al. 2023). In contrast, sub-populations form their over-densities as their host bar grows; therefore, the BP appears to increase in

[7]Note that there are fewer data points in the lower right-hand panel of Fig. 6.15.

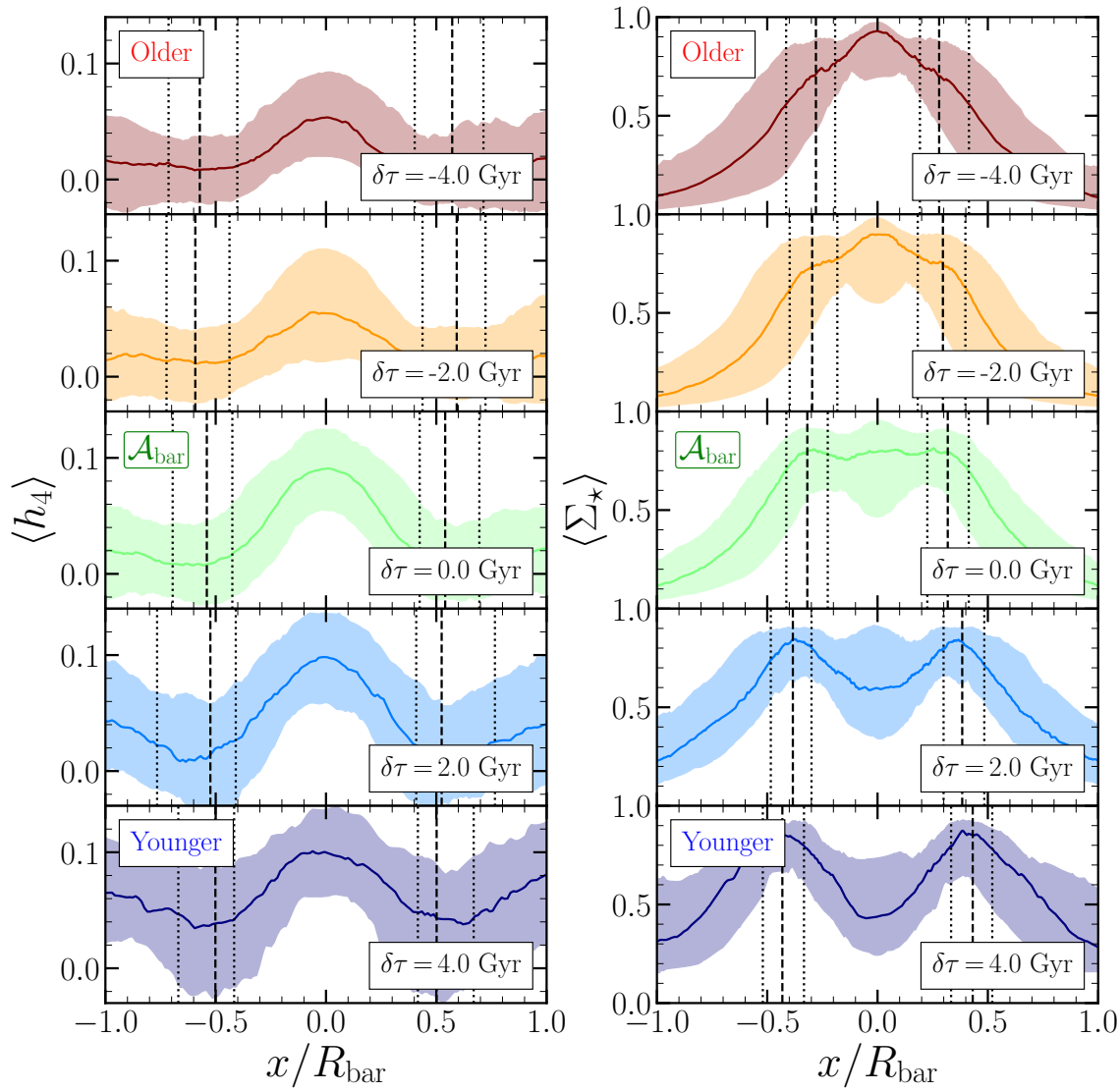

Figure 6.17: Left-hand column: average profiles of the h_4 moment of the vertical velocity distribution along the bar major axis of the sub-populations from BP galaxies. Right-hand column: average profiles of normalised density between $0.1 < |z|/R_{\rm bar} < 0.5$ along the bar major axis of the sub-populations from BP galaxies. The shaded regions outline the $16^{\rm th}$ and $84^{\rm th}$ percentiles of the profiles. Each row represents a bin in $\delta\tau$ for values of $\delta\tau = \{-4, -2, 0, 2, 4\}$ Gyr with a bin width of 2 Gyr (see top panel of Fig. 6.4). Vertical black dashed lines denote the median $R_{{\rm valley},i}$ and $R_{{\rm BP},i}$ for the left and right columns, respectively. The vertical black dotted lines denote the $16^{\rm th}$ and $84^{\rm th}$ percentiles of $R_{{\rm valley},i}$ and $R_{{\rm BP},i}$.

physical radius (as measured by the surface density) as a function of age. This would indicate that the h_4 minima are likely tied to resonant orbits which heat vertically, such as the vertical Inner Lindblad Resonance (vILR, see Beraldo e Silva et al. 2023). The pattern speed of bars decreases as they grow in length and strength, and the vILR sweeps outwards in radius. Therefore what we measure in the h_4 profile at the current epoch is due to the current potential of the bar and its vertical resonances. However, sub-populations forming their BPs earlier formed when the bar was smaller in physical size (a fraction of its size at $z = 0$). We note, however, that the orbits which built the early BP can scatter and change with the change of the potential. A detailed exploration of the orbit evolution in BP bulges is beyond the scope of this work. Yet, if the BP of a given sub-population does not itself change its physical size as the bar ages, but younger populations form their BPs at a larger radius as the bar grows, this could explain the observed trends.

We consider the variation of $R_{\mathrm{BP},i}$ with $\delta\tau$ across each BP galaxy. Approximating each galaxy's variation as linear, we fit a linear regression line in each case. Examples are shown in the top panel of Fig. 6.18. The distributions of the fit gradients and intercepts are presented in the middle panels of Fig. 6.18. Finally, the fits are shown in the lower panel of Fig. 6.18 with the median relation highlighted in yellow.

We find a clear peak in the distributions of both the gradient and intercept of the linear fits, though there is a considerable spread[8]. The median $R_{\mathrm{BP},i}$ with $\delta\tau$ relation is found to be:

$$R_{\mathrm{BP},i} = 0.042^{+0.034}_{-0.022} \times \delta\tau + 0.336^{+0.123}_{-0.100}, \tag{6.4}$$

with uncertainties given as the 16^{th} and 84^{th} percentiles. This relation indicates that sub-populations born near the time of bar formation have BPs with a measured radius between $R_{\mathrm{BP},i} \approx 0.24 - 0.46$ at $z = 0$. The gradient of this relation is likely

[8]We find no statistical difference in the distributions of these parameters when we split the BP galaxies into the two BP formation mechanisms (WNB and BCK).

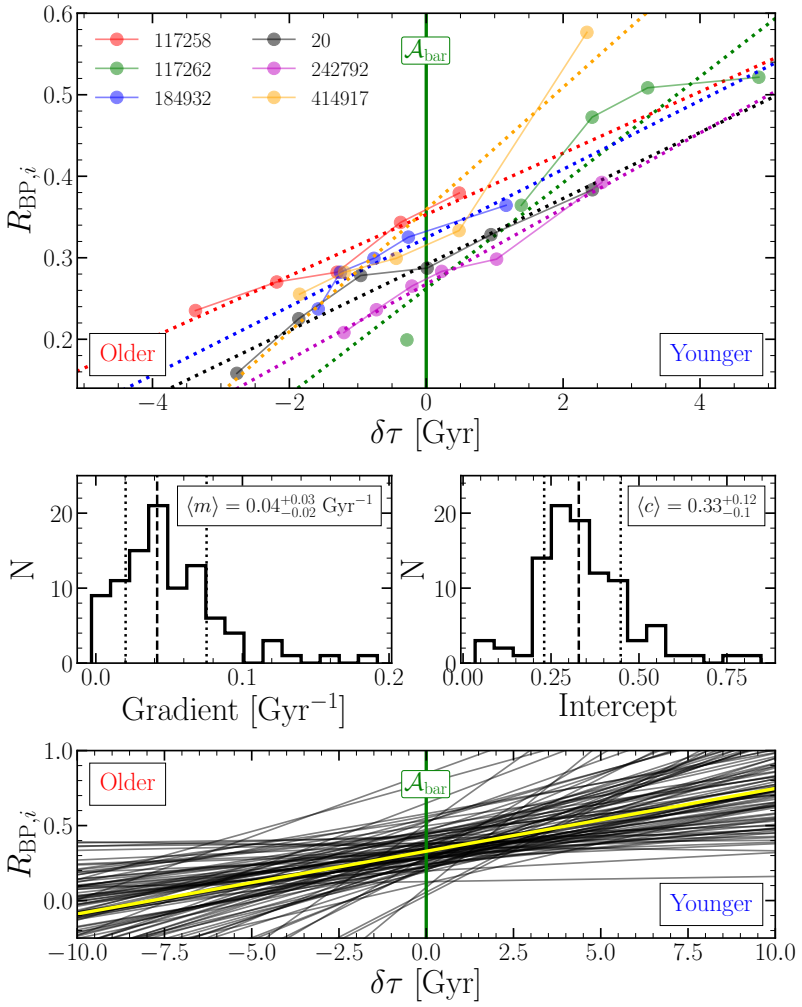

Figure 6.18: Top: the variation of $R_{{\rm BP},i}$ with $\delta\tau$ for sixe randomly chosen BP galaxies in TNG50 labeled by their IDs (note $R_{{\rm BP},i}$ is scaled by the bar radius). The corresponding coloured dashed lines are individual linear regression fits to each galaxy. Middle left-hand panel: The distribution of gradients from the linear fits. We only perform a linear fit to a galaxy if we measure three or more bimodal density distributions ($R_{{\rm BP},i}$) from the sub-populations (95 out of the 106 BP galaxies, 90%). Middle right-hand panel: the distribution of intercepts from the same linear fits. In the middle panels, the vertical dashed line indicates the location of the median. The vertical dotted lines indicate the location of the 25$^{\rm th}$ and 75$^{\rm th}$ percentiles of the distributions. Bottom panel: the yellow line shows the median fit to the $R_{{\rm BP},i}$ vs. $\delta\tau$ relation of the BP galaxies. Each black line represents the linear fit of each BP galaxy.

tied to the growth rate of bars in TNG50.

6.5.3 Population Distributions in BP Bulges

While external galaxies cannot be deconstructed by stellar ages, the separation of different age populations in the presence of a bar results in age gradients when the bar is seen side-on. Debattista et al. (2017) predicted that the average age (and consequently metallicity) distribution would be more pinched than the density distribution in a BP galaxy. This was demonstrated observationally in the metallicity distribution of NGC 4710 by Gonzalez et al. (2017). We produce maps of average stellar parameters for all stars in each galaxy in a slice of the (x, z)-projection (with the bar viewed side-on and $|y|/R_{\rm bar} \leq 0.25$) scaled by the bar radius for each galaxy. We then median-stack each map for the three subsamples of galaxies: WNB, BCK and controls with no weighting procedure (*i.e.* each galaxy gets equal weighting). Fig. 6.19 shows the distributions of the median stacked normalised log density ($\log \langle \Sigma_\star \rangle$) and age ($\langle \mathcal{A}_\star \rangle$) for each subsample[9].

The average side-on density distribution of the Control (without BP) galaxies within the bar radius is rounded, thick at the centre, and thin at the ends of the bar (upper left-hand panel of Fig. 6.19). The distribution of the WNB galaxies has a clear boxy-shaped bulge where the vertical thickness appears constant within $|x|/R_{\rm bar} < 0.5$ and outside traces a weak peanut shape. For the BCK galaxies, a similar boxy distribution is seen, with some evidence of pinching close to the galactic centre. The pinching in the BCK and WNB galaxies is visible in an unsharp mask map of the average density distributions shown in the second row of Fig. 6.19. We use the contours from the unsharp masks on the lower panels to draw attention to the BP regions.

[9]Note here we are *not* splitting the galaxies by sub-populations, rather we generate maps using all the stellar populations within the spatial selection of the bar.

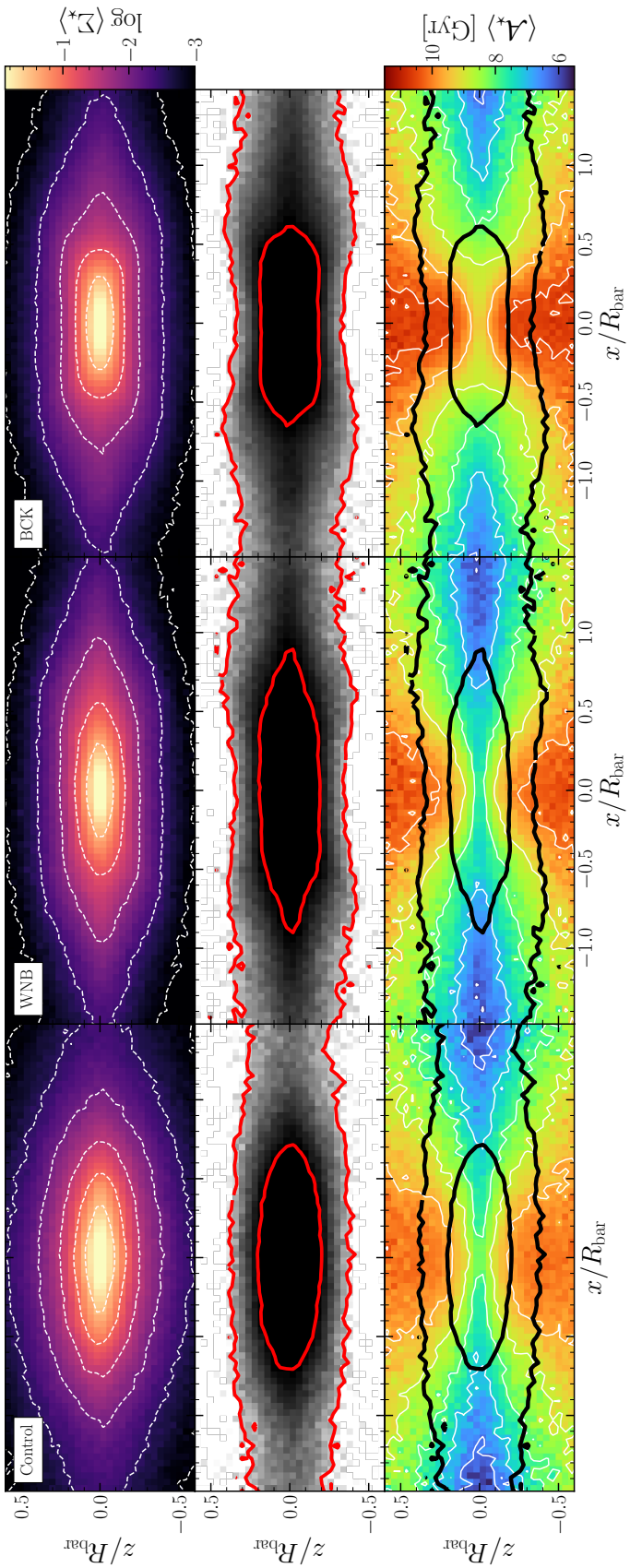

Figure 6.19: The median-stacked slices ($|y|/R_{\rm bar} \leq 0.25$) of the (x, z)-projections for the stellar parameters of normalised log surface density ($\log \langle \Sigma_\star \rangle$, top row), unsharp-masked density (middle row) and age ($\langle \mathcal{A}_\star \rangle$, bottom row) for the Control (left-hand column), WNB (middle column) and BCK (right-hand column) samples of galaxies in TNG50 scaled by the bar radius. Contours from the (x, z) unsharp-masked density are overlaid on the top four rows.

The average age distributions of all three samples of galaxies (third row of Fig. 6.19) are more pinched than the density distributions. In all cases, we find the oldest stars on the minor axis out of the plane. Towards the ends of the bar, stars are, on average younger in the plane and become older at larger heights. Therefore the age gradient with height is shallower at the ends of the bar than on the minor axis. The fact that we find such pinching in control galaxies (which have no BP) shows that populations are still heated and separated without forming the over-densities characteristic of a BP. A23 found 7 galaxies which had formed a BP which was not detectable by $z = 0$ and therefore ended up classified as a Control galaxy. This may introduce some pinching, but such galaxies represent only 8% of the Control sample.

A noticeable ordering in the amount of pinching of the age distributions increasing from the Control, WNB to BCK samples is most likely due to the same ordering of increasing bar strength identified in A23 (their figure 10). There is also likely some contribution from the interplay between stellar discs of different scale heights and ages (*e.g.* see Di Matteo et al. 2014; Fragkoudi et al. 2018).

Most strikingly, the BCK galaxies contain very old stars on the minor axis, possibly indicating that bars in BCK galaxies formed earlier than the other samples. Also, the pinching of the age distribution in BCK galaxies is quite clear. However, we must also consider the stellar assembly history of these different subsamples of galaxies. A23 found that BCK galaxies assembled their stellar mass earlier than the WNB and Control galaxies, which had half stellar-mass formation times ~ 1 Gyr later (see their figure 9). Bars also form on average ~ 2 Gyr earlier in BCK galaxies than in WNB and Control galaxies (also figure 9 of A23). This would produce systematic offsets in the age distributions.

Only in the side-on projection (x, z) do the BP galaxies demonstrate the characteristic signature of strongly pinched age contours superimposed on boxy isophotes

of density. Therefore greater pinching in stellar parameters such as age is not exclusively evidence for a BP bulge. Nevertheless, the X-shape produced by the BP in the WNB and BCK galaxies is evident in the middle and right-hand panels of Fig. 6.19 (fourth row), where stars in this region are younger than in the end-on projection (fifth row). The young vertical extensions of a bar reduce the vertical age gradient in the BP region but create a steeper 'drop' to older populations beyond the extent of the BP.

6.6 Discussion

Stellar populations with larger in-plane random motions (corresponding to older ages) respond weakly to the presence of a bar, with the opposite behaviour for cooler (younger) populations. This distinction in kinematics as a function of age causes the populations to separate (they are kinematically fractionated) as shown in isolated models (Debattista et al. 2017, 2020) and in a cosmological zoom model (Debattista et al. 2019). Here we reconfirm these results with the largest such study to date, in a fully cosmological context.

We measure the bar strength from the $m = 2$ Fourier amplitude of the stellar surface density for the sub-populations within 191 barred galaxies in TNG50 at $z = 0$. By studying these amplitudes as a function of the delay between the time of formation of a sub-population and of the bar (age relative to the bar, Eqn. 6.1) we have found an upturn in amplitude for populations born during the bar formation epoch. Sub-populations older than the bar observed at the current epoch have bar strengths weaker relative to the total strength of the galaxy. The youngest sub-populations form stronger bars than their host bar by the current epoch. The transition in bar strength happens for populations as old as the bar.

We have defined kinematic metrics of bar strength using the $m = 2$ Fourier amplitudes of spatially averaged velocities, velocity dispersions and dispersion ratios

in galactocentric coordinates. These metrics generally correlate well with the usual metrics derived from stellar surface density ($r_s \sim 0.6 - 0.7$). We find the strongest correlations between density bar strength and kinematic bar strength traced by in-plane galactocentric velocities $a_2({v_R}^*)_{\mathrm{max},i}$, $a_2({v_\phi}^*)_{\mathrm{max},i}$ and in-plane anisotropy $a_2({\sigma_\phi}^*/{\sigma_R}^*)_{\mathrm{max},i}$ ($r_s = 0.74$, 0.69 and 0.76 respectively for correlation with $a_{2\,\mathrm{max},i}$). The vertical anisotropy, $a_2({\sigma_z}^*/{\sigma_R}^*)_{\mathrm{max},i}$, also traces the density bar strength with a weaker correlation of 0.65 with $a_{2\,\mathrm{max},i}$. In agreement with Walo-Martín et al. (2022), we find metrics based on anisotropy correlate with the usual bar strength better than individual components of velocity dispersion, and we find that the spatial distribution of the in-plane anisotropy best captures the measured bar strength. The 'break' or 'upturn' of the bar amplitude profiles signifies that within the $z = 0$ stellar populations is the 'memory' of the bar formation epoch in their structure.

We find that measures of the BP strength and radius depend on a population's age relative to the bar age. The BP strength, derived from the 4^{th}-order Gauss-Hermite moment of the vertical velocity distribution (h_4) along the bar major axis, is larger for younger populations. The location of the h_4 minima associated with the BP structure (Debattista et al. 2005) as a fraction of the bar radius is invariant with stellar age because it is dependent on the total bar potential. However, since bars grow and slow during their evolution, the location of vertical resonances move out with time (Beraldo e Silva et al. 2023, and references therin). Therefore the over-densities produced by the BP structure move outwards for younger populations. From this effect, we have derived a relation using the age variation of the separation of the two arms of the BP bulge (Eqn. 6.4). The intercept of this relationship shows that populations older than the bar can have observed bimodalities and can be used to estimate the time of bar formation if the ages of populations and the BP radii are known.

The vertical gradients of stellar age within the final bulge region of BP galaxies

are shallower than barred galaxies that do not form BPs. While there is a clear decreasing gradient of age in all barred galaxies (owing to the heating of stellar discs as they age), bars in BP galaxies reduce the gradient within the bulge region by heating younger populations out of the plane to greater heights along a bar's major axis, as seen in Fig. 6.19.

6.6.1 The Milky Way

In the Milky Way, we can resolve individual stars in the bulge. This makes it possible to implement the measurements presented in this work. Previous studies have attempted to measure the bar length, strength and orientation of stellar populations within the bulge, such as RR Lyrae and RC stars with different metallicities (Dwek et al. 1995; Binney et al. 1997; Stanek et al. 1997; Fux 1999; Bissantz & Gerhard 2002; Rattenbury et al. 2007; Cao et al. 2013; Wegg & Gerhard 2013; Wegg et al. 2015; Simion et al. 2017; Dékány et al. 2019; Du et al. 2020b; Grady et al. 2020a).

We have presented methods for determining the strength of the bar from the spatial distribution of average kinematics. This is independent of the underlying density distribution, which would require large spatial coverage, high completeness or detailed knowledge of the selection function to measure correctly. Previous studies have shown distinct kinematic distributions for different populations within the Milky Way bulge (Queiroz et al. 2021), with theoretical models showing the dependence of kinematics and their bar strength with age (Debattista et al. 2017; Buck et al. 2018; Gough-Kelly et al. 2022). Therefore, within the Milky Way, we can use the kinematics of stellar populations to determine the strength of the bar without a spatially complete sample. These measured kinematic bar strengths also contain insights into the time of bar formation as, like the density metrics, they also do not follow linear functions with age but have a distinct break at stellar ages as old as the bar.

The Milky Way's BP varies in size and strength depending on the age (or metallicity) of the tracer population (*e.g.*, Ness et al. 2012; Uttenthaler et al. 2012; Rojas-Arriagada et al. 2014; Lim et al. 2021; Semczuk et al. 2022). Measuring tracer populations of varying ages within the Milky Way bulge will allow us to constrain the age of the bar following the methods presented here. For different age stellar populations in the Milky Way bulge, Semczuk et al. (2022) measured the ratio of BP radii from the distance between over-densities along the bar major axis. Standard candles such as RR Lyrae (ages > 11 Gyr, Walker 1989) and red clump (RC) giants (ages $\lesssim 10$ Gyr, Wan et al. 2017), have BP diameters estimated to be 0.7 kpc and 3.3 kpc, respectively. Scaling these values using the Milky Way bar radius of 5 kpc (Wegg et al. 2015) gives a BP radius of ~ 0.07 and ~ 0.35 for the RR Lyrae and RC populations, respectively. Using the derived relation in Section 6.5.2 (Eqn. 6.4), the Milky Way population of RR Lyrae would likely be older than the bar by at least $\gtrsim 2$ Gyr. The BP radius measured in the RC population covers a range of $\delta\tau$, which includes ages as old as the bar. The BP radius would have to be measured in exclusively young tracer populations to constrain this relation in the Milky Way and determine the bar and BP age.

6.6.2 Summary

Studying a large sample of barred galaxies from the TNG50 simulation at $z = 0$, we have shown, for the first time, a generalised view of bar-driven secular evolution of stellar populations in a fully cosmological context and demonstrated that stellar populations are fractionated. Furthermore, we have shown that stellar populations within the bulge region of barred galaxies retain a dynamical 'memory' of the bar formation epoch in their current ($z = 0$) spatial and kinematic distributions. Therefore, by studying stellar populations within the bulge of a barred galaxy at the current epoch, we can constrain the age of the bar.

Our main results are:

1. We have shown that sub-populations within the bulges of TNG50 barred galaxies are kinematically fractionated, with their bar and BP strengths increasing for younger populations.

2. Measurements of the bar strength through measuring the $m = 2$ Fourier moments of spatially averaged galactocentric velocity, velocity dispersion, and anisotropy correlate strongly with canonical metrics of the stellar surface density.

3. We demonstrate that the bar strength of sub-populations in the bulge retains the 'memory' of when the bar formed as there is a clear upturn in bar strength for sub-populations as old as the bar. Sub-populations older than the bar form weak bars, and younger sub-populations form strong bars.

4. The strength of a BP bulge as measured by h_4 (the 4^{th} order Gauss-Hermite moment of the vertical velocity distribution) increases for decreasing age. However, the location of the h_4 minima associated with the BP bulge is invariant with age and, therefore, only traces the total potential of the galaxy.

5. The BP size traced by peaks in the out-of-plane density along the bar major axis increases for decreasing age. This dependence of the relative age of sup-populations on BP radius allows for the possibility of deriving the age of a bar in galaxies hosting a BP bulge.

6. The growth of the BP embeds vertical gradients of age in the side-on projections of BP galaxies and indeed produces highly pinched distributions of age, which are more pinched than the density distribution.

6.7 Appendix A: Bar Strength Correlation Summary

We summarize in Fig. 6.20 the correlations between sub-population ages ($\mathcal{A}_{\rm pop}$), ages relative to the bar's ($\delta\tau$), and bar strength metrics defined by the stellar surface density and $m = 2$ Fourier moments of spatially averaged kinematics for the sample of TNG50 barred galaxies. Measured values are scaled following Eqn. 6.2. Also included in this figure are $m = 2$ amplitudes summed within the bar radius, denoted as $a_2(V^*)_{\rm bar}$, distinct from the maximum values used throughout the main text. These produce similar values and strong correlations with their 'max' counterparts.

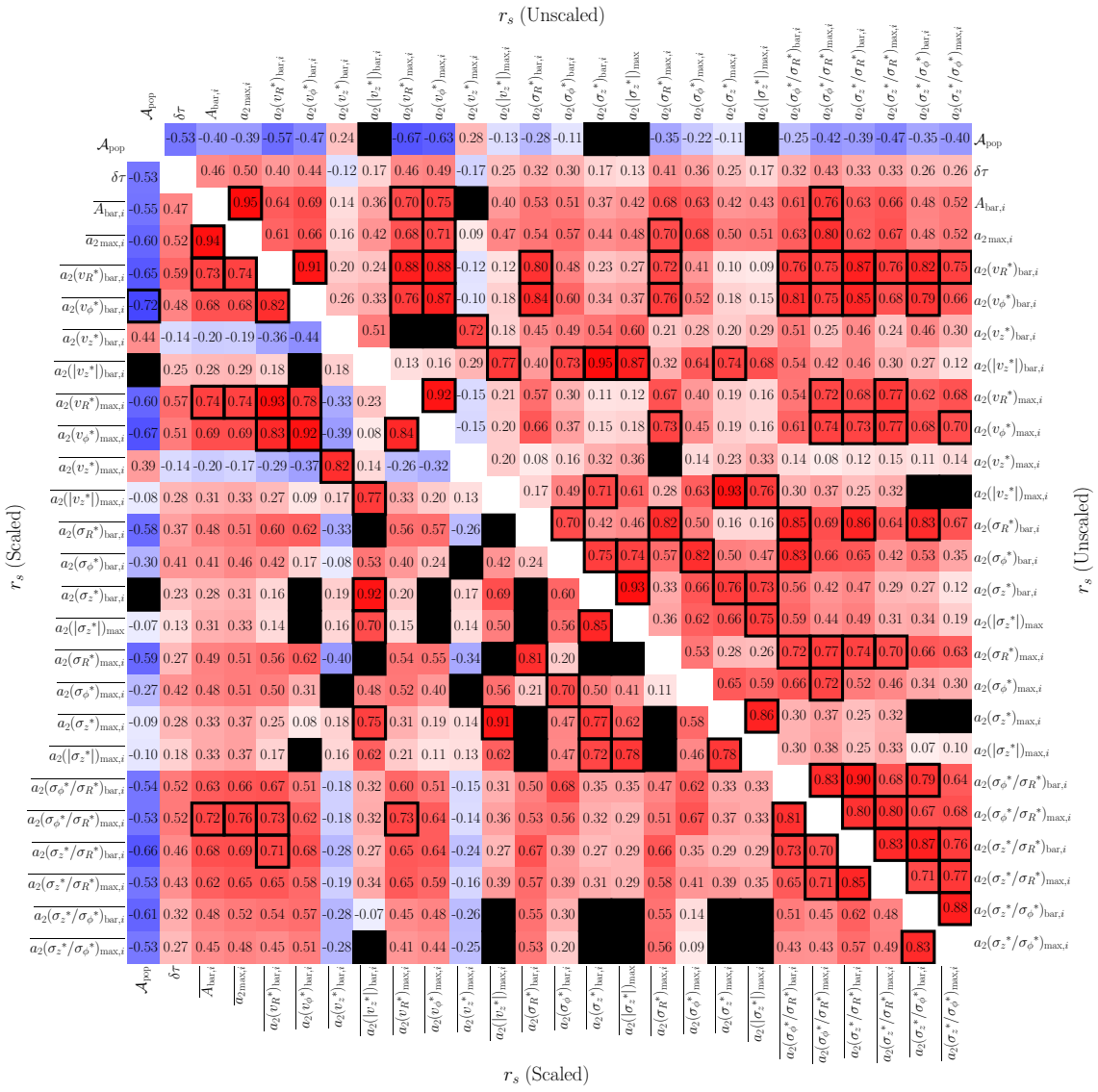

Figure 6.20: Top and right-hand axes: The Spearman rank correlation coefficients between different $\mathcal{A}_{\rm pop}$, $\delta\tau$, density measurements of bar strength ($A_{{\rm bar},i}$ and $a_{2\,{\rm max},i}$) and kinematic measurements of bar strength, ($a_2({v_R}^*)_{{\rm max},i}$, $a_2({v_\phi}^*)_{{\rm max},i}$ etc.). Strong correlations ($r_s > 0.7$) are highlighted with a black border. Statistically insignificant correlations ($p > 0.01$) are masked out as black squares. The bottom and left-hand axes show the same metrics but for the scaled quantities (Eqn. 6.2).

Chapter 7

Conclusions and Future Work

Through the work presented in this thesis, we have studied the central regions of barred galaxies using isolated simulations, cosmological simulations and observations of the Milky Way bulge in an effort to understand the evolution of stellar populations in the presence of a bar. More specifically, we have focused on how differently aged populations within the bulge respond to the bar, *i.e.* kinematic fractionation, by studying their final morphology and kinematics.

7.1 Key Results and Conclusions

7.1.1 Bulge Proper Motions

Studying the stellar on-sky motions (proper motions from the heliocentric perspective) in the bulge of a star-forming simulation, we determined that the differences in rotation curves of differently aged populations were due to them tracing different structures (Chapter 3). We demonstrated that the rotation curve separations can be explained by the distinct kinematics of populations separated by an evolving bar, as predicted by kinematic fractionation, without needing an accreted component.

Galactocentric cylindrical velocities of young stars in the model are consistent

with bar-aligned orbits. Old stars follow axisymmetric velocity distributions, with both populations reflecting their underlying density distributions. We demonstrated how these intrinsic velocities project onto longitudinal proper motions. Large galactocentric radial velocity contributions (in the young populations) produce rotation curves with forbidden velocities[1]. Differences in longitudinal proper motion rotation curves on the minor axis could also be present in an axisymmetric structure. Therefore, we must observe longitudes away from the minor axis to probe the variation of the bar's strength with age using tangential motions.

We compared the results of this analysis to *Hubble Space Telescope* observations of the Milky Way bulge, where we were able to reproduce observations of main sequence stars on the minor axis. We also made predictions for further analysis of archival data from the *Hubble Space Telescope* and future astrometric surveys of the Milky Way bulge.

7.1.2 Mira Variables

The observational data in Chapter 3 used metallicities derived from photometry to separate observed stellar populations in the Milky Way bulge. Mira variables have been shown to follow period-age relationships and can be useful probes of the dynamics of the Milky Way bulge. We have extracted Milky Way Mira variables from the latest data release of the *Gaia* satellite (*Gaia* DR3) using a novel approach.

In Chapter 4, we used a sample of long-period variables in the Large Magellanic Cloud to define methods for extracting Mira candidates using data-motivated cuts on their relative frequency error and variability amplitude, maximising their separation from SRVs.

[1]Negative longitudinal proper motion at positive longitudes, and positive longitudinal proper motion at negative longitudes.

We applied these methods to the *Gaia* DR3 long-period variable sample to generate a catalogue of 45 075 Milky Way Mira variables with dust corrections and 5D coordinates (full 6D for 3 231 sources). The spatial and kinematic distributions of these Mira candidates were found to be a function of their period and follow the expected distributions of the differently aged populations within the Milky Way. We reconfirm that Mira variables are good tracers for Galactic dynamics. However, larger samples are needed towards the central regions to be able to constrain the bar and bulge of the Milky Way.

We were also able to characterise the effects of the large variability amplitude of Miras on astrometric and photometric solutions within *Gaia*. Large variability amplitude means standard methods of weighted mean photometry can underestimate the mean flux or overestimate the mean magnitude. The same effect of weighting procedures also adds uncertainty to the astrometric solution in stars with large variability amplitude. The reason we are able to define Miras using the error on oscillation frequency is due to *Gaia* fitting only one period to the light curves. We would advocate for multi-period fitting of variable sources.

7.1.3 TNG50 Box/Peanut Bulges

In Chapter 5, we identified 608 high-mass ($\log(M/\,\mathrm{M}_\odot) \geq 10.0$) disc galaxies in the high-resolution run of the IllustrisTNG project, TNG50. From those disc galaxies, we found that 191 had bars with radius $R_{\mathrm{bar}} \geq 2.6\,\mathrm{kpc}$. We studied their density and kinematic profiles at $z = 0$ and found that 106 (55%) barred galaxies had box/-peanut bulges. To measure the box/peanut prominence quantitatively, we developed a metric using the fourth-order Gauss-Hermite moments of the vertical velocity distributions along their bars' major axis. Of these box/peanut galaxies, 52 (49%) buckled strongly at some stage in their evolution, and 54 (51%) did not, forming their BPs via resonant trapping, weak buckling or a combination of both. Studying

the full evolutionary history of this sample, we are able to determine the epoch of bar and BP formation as well as a buckling event if one occurred.

Using the box/peanut sample, we found that TNG50 matched the fraction of box/peanut bulges in barred galaxies as a function of stellar mass as observed in the local Universe. TNG50 reproduces the overall shape of the distribution when compared with observations with the same characteristic upturn at the transition mass of $\log(M/\,\mathrm{M}_\odot) \sim 10.1$; however, it does not reproduce the observed fraction, with TNG50 underproducing BPs at high mass. Observations would predict that all high-mass barred galaxies contain box/peanut bulges, yet TNG50 saturates at $\approx 60\%$ above $\log(M/\,\mathrm{M}_\odot) \sim 10.5$.

7.1.4 Kinematic Fractionation in TNG50

Studying the same sample from TNG50 at $z = 0$, we showed in Chapter 6 a generalised view of bar-driven secular evolution of stellar populations in a fully cosmological context. Stellar populations within the bulge region of barred galaxies retained the dynamical 'memory' of the bar formation epoch in their current ($z = 0$) spatial and kinematic distributions. Therefore, by studying stellar populations within the bulge of a barred galaxy, we can constrain the age of the bar.

We demonstrate that the bar strength has a clear break or upturn considering populations as old as the bar. Populations older than the bar form weak bars, and younger populations form strong bars. The strength of a box/peanut bulge increases for younger populations. However, the location of the h_4 minima associated with the BP bulge is invariant with age at $z = 0$ and, therefore, only traces the current total potential of the galaxy.

The BP size traced by peaks in the out-of-plane density along the bar major axis increases with decreasing age. This dependence of the relative age of populations on BP radius allows for the possibility of deriving the age of a bar in galaxies hosting

a BP bulge.

7.2 Further Work

7.2.1 The Next Generation of Surveys and Observatories

All-sky multi-epoch surveys provide astrometric solutions for large quantities of stars in the Milky Way. While we have studied the results of *Gaia* DR3, subsequent data releases (DR4 ∼2026 and DR5 ∼2031) will provide even larger samples of stars and offer better constraints on stars already in the catalogue. The more extended baseline of the observations by DR4 will also help characterise long-period variables. As shown in this thesis, further work can be done to improve the handling of large-amplitude variable sources when calculating photometric and astrometric solutions (Eyer & Gough-Kelly *in progress*).

The soon-to-be-completed Vera C. Rubin Observatory is conducting a ten-year survey of the Southern sky called the Legacy Survey of Space and Time (LSST), which will cover the entire observable sky every 3-4 nights. Such a long baseline and high cadence makes this survey ideal for studying the motions and variability of large samples of stars. The survey telescope is expected to be commissioned by 2025. Rubin's survey strategy is still in the process of being refined (The Rubin Observatory Survey Cadence Optimization Committee 2023). Nonetheless, it is expected to include long-term monitoring of the Milky Way bulge and therefore offers an opportunity to study its dynamical history.

Combining astrometric surveys with upcoming wide-field spectroscopic surveys such as APOGEE-2 and MOONS will allow for chemical abundance and radial velocity measurements of millions of objects. Complementing the 5D solutions of astrometric surveys with these new parameters will enable the study of the full dynamics of Milky Way bulge stars. The chemical abundances will allow us to

separate such samples of stars by metallicities with greater precision.

The *Hubble Space Telescope (HST)* can still provide insights into the motions of stellar populations of the Milky Way bulge. Indeed the predictions presented in Chapter 3 of individual *HST* fields can already be tested using archive data (Clarkson et al. *in progress*).

However, the extensive extinction in the central regions limits optical observations of the Galactic bulge. Infrared observations allow for a deeper view of the Milky Way centre. An All-Sky near-IR astrometric space mission such as *Gaia*NIR (Hobbs et al. 2021) would provide homogeneous astrometric solutions in regions close to the Galactic plane. In addition, the *Nancy Grace Roman Space Telescope* (*RST*) promises to provide high-precision astrometry with deep multi-epoch observations of the Galactic bulge and Galactic pole, providing insights into the far side of the bar, Galactic Centre and stellar halo.

Synergies between major observatories and survey efforts can be achieved by coordinating their observational scheduling, data analysis and metrics to maximise their science return (see Appendix A).

7.2.2 Further Predictions From Simulations

Models of Milky Way-like galaxies from isolated and cosmological simulations can be used to inform mock observations and catalogues of observatories. Examples of such methods have been used for survey telescopes such as *Gaia* (Hunt et al. 2015; Lowing et al. 2015; Grand et al. 2018) and have the potential to inform synergies between observatories, as mentioned above.

From this work, we have defined a large self-consistent sample of barred and box/peanut galaxies in a fully cosmological context for further study. Large numbers of bucking and weak/non-buckling galaxies can facilitate an in-depth study of the two mechanisms to find differences in their signatures, giving insights into the

frequency of buckling in the Universe.

In Anderson et al. (2023), we showed that barred galaxies, which form their box/peanut through strong buckling, appear in galaxies with strong bars that form early, which subsequently has secondary correlations with galactic properties such as total stellar mass and disc thickness. While the work presented in Chapters 5 and 6 do not directly demonstrate how the formation of a box/peanut through either buckling or resonant capture (Sellwood & Gerhard 2020), further work using our sample of galaxies will attempt to disentangle these mechanisms. Recent work by Li et al. (2022) has shown that buckling and resonant capture may also be interlinked and would require detailed orbital analysis of the stars within the bar to uncover the different 'channels' of box/peanut formation.

In our analysis, we found five buckling galaxies where their box/peanut did not survive all the way to the current epoch. Two other galaxies formed a box/peanut through weak/non-buckling, but these structures dissolved by $z = 0$. Finding these examples also opens the question of the fate of barred galaxies in the early Universe. What fraction are not bars or even discs by the current epoch? Exploring beyond the sample defined in our study, we can measure the frequency of discs, bars and box/peanut bulges as a function of redshift in TNG50. Answering such questions would help our understanding of emerging results from the *James Webb Space Telescope*.

Milky Way analogues in fully cosmological simulations can give us further insights into the dynamical history of our Galaxy. In our TNG50 sample, we find six Milky Way-like galaxies that match in their stellar mass ($\log(M_\star/\,\mathrm{M}_\odot) \approx 10.8$, Licquia & Newman 2015) and bar size ($R_{\mathrm{bar}} \approx 5\,\mathrm{kpc}$, Wegg et al. 2015)[2]. Half of these analogues formed a box/peanut bulge through buckling, while the other half formed through weak/non-buckling.

[2]We find 33 galaxies in the Milky Way's mass range of which 11 galaxies have $R_{\mathrm{bar}} > 5.5\,\mathrm{kpc}$ and 16 with $R_{\mathrm{bar}} < 4.5\,\mathrm{kpc}$.

Having the complete histories of these Milky Way analogues allows us to trace the exsitu populations and merger activity to understand their role in the bulge's formation history. Studies of Milky Way and Andromeda (M31) like galaxies in TNG50 have shown that they typically have low levels of accretion and can be used to trace accreted populations (Gargiulo et al. 2022; Sotillo-Ramos et al. 2022; Chen et al. 2023). Future work can focus on these accreted populations in the presence of a Milky Way-like bar. We can also make predictions for observations of stellar populations separated by chemistry, as TNG50 has prescriptions for chemical enrichments. This would allow for more testable constraints of kinematic fractionation in the Milky Way bulge and estimates for the epoch of the bar formation.

Bibliography

Aarseth, S. J., Gott, J. R., I., & Turner, E. L. 1979, ApJ, 228, 664

Abbott, C. G., Valluri, M., Shen, J., & Debattista, V. P. 2017, MNRAS, 470, 1526

Abraham, R. G., Tanvir, N. R., Santiago, B. X., et al. 1996, MNRAS, 279, L47

Aguerri, J. A., Méndez-Abreu, J., & Corsini, E. M. 2009, A&A, 495, 491

Aguerri, J. A. L., Muñoz-Tuñón, C., Varela, A. M., & Prieto, M. 2000, A&A, 361, 841

Algorry, D. G., Navarro, J. F., Abadi, M. G., et al. 2017, MNRAS, 469, 1054

Altmann, M., Edelmann, H., & de Boer, K. S. 2004, A&A, 414, 181

Amarante, J. A. S., Smith, M. C., & Boeche, C. 2020, MNRAS, 492, 3816

Anderson, S. R., Gough-Kelly, S., Debattista, V. P., et al. 2023, MNRAS

Appel, A. W. 1985, SIAM Journal on Scientific and Statistical Computing, 6, 85

Asplund, M., Grevesse, N., Sauval, A. J., & Scott, P. 2009, ARAA, 47, 481

Athanassoula, E. 1992, MNRAS, 259, 345

Athanassoula, E. 2002, ApJ, 569, L83

Athanassoula, E. 2003, MNRAS, 341, 1179

Athanassoula, E. 2005, MNRAS, 358, 1477

Athanassoula, E. & Misiriotis, A. 2002, MNRAS, 330, 35

Athanassoula, E., Rodionov, S. A., & Prantzos, N. 2017, MNRAS, 467, L46

Baade, W. 1944, ApJ, 100, 137

Baba, J. & Kawata, D. 2020, MNRAS, 492, 4500

Babcock, H. W. 1939, Lick Observatory Bulletin, 498, 41

Babusiaux, C. 2016, PASA, 33, e026

Babusiaux, C. & Gilmore, G. 2005, MNRAS, 358, 1309

Babusiaux, C., Gómez, A., Hill, V., et al. 2010, A&A, 519, A77

Babusiaux, C., Katz, D., Hill, V., et al. 2014, A&A, 563, A15

Bailer-Jones, C. A. L., Rybizki, J., Fouesneau, M., Demleitner, M., & Andrae, R. 2021, AJ, 161, 147

Barazza, F. D., Jogee, S., & Marinova, I. 2008, ApJ, 675, 1194

Barbuy, B., Chiappini, C., & Gerhard, O. 2018, ARAA, 56, 223

Barnes, J. & Hut, P. 1986, Nature, 324, 446

Bekki, K. & Tsujimoto, T. 2011, MNRAS, 416, L60

Bellm, E. C., Kulkarni, S. R., Graham, M. J., et al. 2019, PASP, 131, 018002

Belokurov, V., Erkal, D., Deason, A. J., et al. 2017, MNRAS, 466, 4711

Benjamin, R. A., Churchwell, E., Babler, B. L., et al. 2005, ApJ, 630, L149

Bennett, C. L., Bay, M., Halpern, M., et al. 2003, ApJ, 583, 1

Bensby, T., Adén, D., Meléndez, J., et al. 2011, A&A, 533, A134

Bensby, T., Bergemann, M., Rybizki, J., et al. 2019, The Messenger, 175, 35

Bensby, T., Feltzing, S., & Oey, M. S. 2014, A&A, 562, A71

Bensby, T., Yee, J. C., Feltzing, S., et al. 2013, A&A, 549, A147

Beraldo e Silva, L., Debattista, V. P., Anderson, S. R., et al. 2023, arXiv e-prints, arXiv:2303.04828

Beraldo e Silva, L., Debattista, V. P., Khachaturyants, T., & Nidever, D. 2020, MNRAS, 492, 4716

Berentzen, I., Heller, C. H., Shlosman, I., & Fricke, K. J. 1998, MNRAS, 300, 49

Bernard, E. J., Schultheis, M., Di Matteo, P., et al. 2018, MNRAS, 477, 3507

Bhardwaj, A., Kanbur, S., He, S., et al. 2019, ApJ, 884, 20

Binney, J., Gerhard, O., & Spergel, D. 1997, MNRAS, 288, 365

Binney, J. & Tremaine, S. 2008, Galactic Dynamics: Second Edition (Princeton University Press)

Bissantz, N. & Gerhard, O. 2002, MNRAS, 330, 591

Bland-Hawthorn, J. & Gerhard, O. 2016, ARAA, 54, 529

Blázquez-Calero, G., Florido, E., Pérez, I., et al. 2020, MNRAS, 491, 1800

Blitz, L. & Spergel, D. N. 1991, ApJ, 379, 631

Bonaca, A., Conroy, C., Wetzel, A., Hopkins, P. F., & Kereš, D. 2017, ApJ, 845, 101

Bonoli, S., Mayer, L., Kazantzidis, S., et al. 2016, MNRAS, 459, 2603

Borucki, W. J., Koch, D., Basri, G., et al. 2010, Science, 327, 977

Bournaud, F., Elmegreen, B. G., & Martig, M. 2009, ApJ, 707, L1

Bovy, J. 2015, ApJS, 216, 29

Bovy, J., Leung, H. W., Hunt, J. A. S., et al. 2019, MNRAS, 490, 4740

Bovy, J., Rix, H.-W., Green, G. M., Schlafly, E. F., & Finkbeiner, D. P. 2016, ApJ, 818, 130

Bovy, J., Rix, H.-W., Liu, C., et al. 2012, ApJ, 753, 148

Brown, T. M., Sahu, K., Anderson, J., et al. 2010, ApJ, 725, L19

Buck, T., Ness, M., Obreja, A., Macciò, A. V., & Dutton, A. A. 2019, ApJ, 874, 67

Buck, T., Ness, M. K., Macciò, A. V., Obreja, A., & Dutton, A. A. 2018, ApJ, 861, 88

Burbidge, E. M. & Burbidge, G. R. 1959, ApJ, 130, 20

Bureau, M. & Athanassoula, E. 2005, ApJ, 626, 159

Bureau, M. & Freeman, K. C. 1999, AJ, 118, 126

Burstein, D. 1979, ApJ, 234, 829

Buta, R., Crocker, D. A., & Byrd, G. G. 1992, AJ, 103, 1526

Buta, R. J., Byrd, G. G., & Freeman, T. 2003, AJ, 125, 634

Butterworth, S. 1930, Experimental Wireless and the Wireless Engineer, 7, 536

Calamida, A., Sahu, K. C., Anderson, J., et al. 2014, ApJ, 790, 164

Cao, L., Mao, S., Nataf, D., Rattenbury, N. J., & Gould, A. 2013, MNRAS, 434, 595

Cappellari, M., Emsellem, E., Bacon, R., et al. 2007, MNRAS, 379, 418

Caputo, F. 1998, The Astronomy and Astrophysics Review, 9, 33

Catchpole, R. M., Whitelock, P. A., Feast, M. W., et al. 2016, MNRAS, 455, 2216

Ceverino, D. & Klypin, A. 2007, MNRAS, 379, 1155

Chambers, K. C., Magnier, E. A., Metcalfe, N., et al. 2016, arXiv e-prints, arXiv:1612.05560

Chandrasekhar, S. 1935, MNRAS, 95, 207

Chen, L.-H., Pillepich, A., Glover, S. C. O., & Klessen, R. S. 2023, MNRAS, 519, 483

Ciambur, B. C., Fragkoudi, F., Khoperskov, S., Di Matteo, P., & Combes, F. 2021, MNRAS, 503, 2203

Ciambur, B. C. & Graham, A. W. 2016, MNRAS, 459, 1276

Clarke, A. J., Debattista, V. P., Nidever, D. L., et al. 2019, MNRAS, 484, 3476

Clarkson, W., Sahu, K., Anderson, J., et al. 2008, ApJ, 684, 1110

Clarkson, W. I., Calamida, A., Sahu, K. C., et al. 2018, ApJ, 858, 46

Clarkson, W. I., Sahu, K. C., Anderson, J., et al. 2011, ApJ, 735, 37

Cole, D. R., Debattista, V. P., Erwin, P., Earp, S. W. F., & Roškar, R. 2014, MNRAS, 445, 3352

Collier, A. 2020, MNRAS, 492, 2241

Combes, F., Debbasch, F., Friedli, D., & Pfenniger, D. 1990, A&A, 233, 82

Combes, F. & Sanders, R. H. 1981, A&A, 96, 164

Conselice, C. J., Bershady, M. A., & Jangren, A. 2000, ApJ, 529, 886

Contopoulos, G. & Grosbol, P. 1989, The Astronomy and Astrophysics Review, 1, 261

Contopoulos, G. & Papayannopoulos, T. 1980, A&A, 92, 33

Cook, K., Alcock, C., Allsman, R., et al. 1992, in American Astronomical Society Meeting Abstracts, Vol. 181, American Astronomical Society Meeting Abstracts, 38.08

Corbelli, E. & Salucci, P. 2000, MNRAS, 311, 441

Cuomo, V., Debattista, V. P., Racz, S., et al. 2022, MNRAS, 518, 2300

Cuomo, V., Lee, Y. H., Buttitta, C., et al. 2021, A&A, 649, A30

Curtis, H. D. 1988, PASP, 100, 6

Davies, R. L. & Illingworth, G. 1983, ApJ, 266, 516

Davis, M., Efstathiou, G., Frenk, C. S., & White, S. D. M. 1985, ApJ, 292, 371

de Sá-Freitas, C., Fragkoudi, F., Gadotti, D. A., et al. 2022, arXiv e-prints, arXiv:2211.07670

de Vaucouleurs, G. 1959, Handbuch der Physik, 53, 275

de Vaucouleurs, G., de Vaucouleurs, A., Corwin, Herold G., J., et al. 1991, Third Reference Catalogue of Bright Galaxies

Deason, A. J., Belokurov, V., Erkal, D., Koposov, S. E., & Mackey, D. 2017, MNRAS, 467, 2636

Debattista, V. P., Carollo, C. M., Mayer, L., & Moore, B. 2005, ApJ, 628, 678

Debattista, V. P., Earp, S. W. F., Ness, M., & Gonzalez, O. A. 2018, MNRAS, 473, 5275

Debattista, V. P., Gonzalez, O. A., Sanderson, R. E., et al. 2019, MNRAS, 485, 5073

Debattista, V. P., Liddicott, D. J., Khachaturyants, T., & Beraldo e Silva, L. 2020, MNRAS, 498, 3334

Debattista, V. P., Mayer, L., Carollo, C. M., et al. 2006, ApJ, 645, 209

Debattista, V. P., Ness, M., Earp, S. W. F., & Cole, D. R. 2015, ApJ, 812, L16

Debattista, V. P., Ness, M., Gonzalez, O. A., et al. 2017, MNRAS, 469, 1587

Debattista, V. P. & Sellwood, J. A. 1998, ApJ, 493, L5

Debattista, V. P. & Sellwood, J. A. 2000, ApJ, 543, 704

Dékány, I., Hajdu, G., Grebel, E. K., & Catelan, M. 2019, ApJ, 883, 58

Dékány, I., Minniti, D., Catelan, M., et al. 2013, ApJ, 776, L19

DESI Collaboration, Aghamousa, A., Aguilar, J., et al. 2016, arXiv e-prints, arXiv:1611.00036

Di Matteo, P. 2016, PASA, 33, e027

Di Matteo, P., Fragkoudi, F., Khoperskov, S., et al. 2019, A&A, 628, A11

Di Matteo, P., Gómez, A., Haywood, M., et al. 2015, A&A, 577, A1

Di Matteo, P., Haywood, M., Combes, F., Semelin, B., & Snaith, O. N. 2013, A&A, 553, A102

Di Matteo, P., Haywood, M., Gómez, A., et al. 2014, A&A, 567, A122

Di Matteo, P., Haywood, M., Lehnert, M. D., et al. 2019b, A&A, 632, A4

Doggett, J. B. & Branch, D. 1985, AJ, 90, 2303

Dolag, K., Borgani, S., Murante, G., & Springel, V. 2009, MNRAS, 399, 497

Drimmel, R., Cabrera-Lavers, A., & López-Corredoira, M. 2003, A&A, 409, 205

Drury, L. O. 1980, MNRAS, 193, 337

Du, H., Mao, S., Athanassoula, E., Shen, J., & Pietrukowicz, P. 2020b, MNRAS, 498, 5629

Du, M., Debattista, V. P., Shen, J., & Cappellari, M. 2016, ApJ, 828, 14

Du, M., Ho, L. C., Debattista, V. P., et al. 2020a, ApJ, 895, 139

Dubinski, J., Berentzen, I., & Shlosman, I. 2009, ApJ, 697, 293

Dwek, E., Arendt, R. G., Hauser, M. G., et al. 1995, ApJ, 445, 716

Efstathiou, G. & Jones, B. J. T. 1979, MNRAS, 186, 133

El-Badry, K., Bland-Hawthorn, J., Wetzel, A., et al. 2018, MNRAS, 480, 652

Emsellem, E., Renaud, F., Bournaud, F., et al. 2015, MNRAS, 446, 2468

Erwin, P. 2005, MNRAS, 364, 283

Erwin, P. 2018, MNRAS, 474, 5372

Erwin, P. & Debattista, V. P. 2013, MNRAS, 431, 3060

Erwin, P. & Debattista, V. P. 2016, ApJ, 825, L30

Erwin, P. & Debattista, V. P. 2017, MNRAS, 468, 2058

Erwin, P., Pohlen, M., & Beckman, J. E. 2008, AJ, 135, 20

Erwin, P., Saglia, R. P., Fabricius, M., et al. 2015, MNRAS, 446, 4039

Eskridge, P. B., Frogel, J. A., Pogge, R. W., et al. 2000, AJ, 119, 536

Eyer, L., Audard, M., Holl, B., et al. 2022, arXiv e-prints, arXiv:2206.06416

Eyer, L. & Mowlavi, N. 2008, in Journal of Physics Conference Series, Vol. 118, Journal of Physics Conference Series, 012010

Faber, S. M. & Gallagher, J. S. 1979, ARAA, 17, 135

Feast, M. & Whitelock, P. 2000, in Astrophysics and Space Science Library, Vol. 255, Astrophysics and Space Science Library, ed. F. Matteucci & F. Giovannelli, 229

Feast, M. W. 1963, MNRAS, 125, 367

Ferreira, L., Conselice, C. J., Sazonova, E., et al. 2023, ApJ, 955, 94

Ferreras, I. 2019, Fundamentals of Galaxy Dynamics, Formation and Evolution (UCL Press)

Ferreras, I., Wyse, R. F. G., & Silk, J. 2003, MNRAS, 345, 1381

Finkelstein, S. L., Bagley, M. B., Ferguson, H. C., et al. 2023, ApJ, 946, L13

Fisher, D. B. & Drory, N. 2016, Galactic Bulges, 418, 41

Fiteni, K., Caruana, J., Amarante, J. A. S., Debattista, V. P., & Beraldo e Silva, L. 2021, MNRAS, 503, 1418

Fiteni, K., Caruana, J., Amarante, J. A. S., et al. 2024

Fragkoudi, F., Athanassoula, E., & Bosma, A. 2017a, MNRAS, 466, 474

Fragkoudi, F., Di Matteo, P., Haywood, M., et al. 2017b, A&A, 606, A47

Fragkoudi, F., Di Matteo, P., Haywood, M., et al. 2017c, A&A, 607, L4

Fragkoudi, F., Di Matteo, P., Haywood, M., et al. 2018, A&A, 616, A180

Fragkoudi, F., Grand, R. J. J., Pakmor, R., et al. 2020, MNRAS, 494, 5936

Frankel, N., Pillepich, A., Rix, H.-W., et al. 2022, ApJ, 940, 61

Freedman, W. L. 2021, ApJ, 919, 16

Freeman, K., Ness, M., Wylie-de-Boer, E., et al. 2013, MNRAS, 428, 3660

Fux, R. 1997, A&A, 327, 983

Fux, R. 1999, A&A, 345, 787

Gadotti, D. A. 2009, MNRAS, 393, 1531

Gadotti, D. A., Bittner, A., Falcón-Barroso, J., et al. 2020, A&A, 643, A14

Gadotti, D. A., Sánchez-Blázquez, P., Falcón-Barroso, J., et al. 2019, MNRAS, 482, 506

Gadotti, D. A. & Sánchez-Janssen, R. 2012, MNRAS, 423, 877

Gadotti, D. A., Seidel, M. K., Sánchez-Blázquez, P., et al. 2015, A&A, 584, A90

Gaia Collaboration & et al. 2021, A&A, 649, A1

Gaia Collaboration, Helmi, A., van Leeuwen, F., et al. 2018, A&A, 616, A12

Gaia Collaboration, Luri, X., Chemin, L., et al. 2021, A&A, 649, A7

Gaia Collaboration, Prusti, T., de Bruijne, J. H. J., Brown, A. G. A., & et al. 2016, A&A, 595, A1

Gaia Collaboration, Vallenari, A., Brown, A. G. A., et al. 2022, arXiv e-prints, arXiv:2208.00211

Gardner, E., Debattista, V. P., Robin, A. C., Vásquez, S., & Zoccali, M. 2014, MNRAS, 438, 3275

Gargiulo, I. D., Monachesi, A., Gómez, F. A., et al. 2019, MNRAS, 489, 5742

Gargiulo, I. D., Monachesi, A., Gómez, F. A., et al. 2022, MNRAS, 512, 2537

Geller, M. J. & Huchra, J. P. 1989, Science, 246, 897

George, K., Subramanian, S., & Paul, K. T. 2019, A&A, 628, A24

Gerhard, O. 2002, in ASP Conf. Ser. 273: The Dynamics, Structure & History of Galaxies: A Workshop in Honour of Professor Ken Freeman, 73–+

Gerhard, O. & Martinez-Valpuesta, I. 2012, ApJ, 744, L8

Gerhard, O. E. 1993, MNRAS, 265, 213

Gilmore, G. & Reid, N. 1983, MNRAS, 202, 1025

Gingold, R. A. & Monaghan, J. J. 1977, MNRAS, 181, 375

Glass, I. S. & Evans, T. L. 1981, Nature, 291, 303

Gnedin, N. Y. 1995, ApJS, 97, 231

Goldreich, P. & Lynden-Bell, D. 1965, MNRAS, 130, 125

Gonzalez, O. A., Clarkson, W., Debattista, V. P., et al. 2018, arXiv e-prints, arXiv:1812.08670

Gonzalez, O. A., Debattista, V. P., Ness, M., Erwin, P., & Gadotti, D. A. 2017, MNRAS, 466, L93

Gonzalez, O. A., Gadotti, D. A., Debattista, V. P., et al. 2016, A&A, 591, A7

Gonzalez, O. A., Mucciarelli, A., Origlia, L., et al. 2020, The Messenger, 180, 18

Gonzalez, O. A., Rejkuba, M., Zoccali, M., et al. 2011, A&A, 530, A54

Gonzalez, O. A., Zoccali, M., Debattista, V. P., et al. 2015, A&A, 583, L5

Gough-Kelly, S., Debattista, V. P., Clarkson, W. I., et al. 2022, MNRAS, 509, 4829

Grady, J., Belokurov, V., & Evans, N. W. 2019, MNRAS, 483, 3022

Grady, J., Belokurov, V., & Evans, N. W. 2020a, MNRAS, 492, 3128

Grady, J., Belokurov, V., & Evans, N. W. 2020b, MNRAS, 492, 3128

Grand, R. J. J., Gómez, F. A., Marinacci, F., et al. 2017, MNRAS, 467, 179

Grand, R. J. J., Helly, J., Fattahi, A., et al. 2018, MNRAS, 481, 1726

Grand, R. J. J., Kawata, D., & Cropper, M. 2015, MNRAS, 447, 4018

Grand, R. J. J., van de Voort, F., Zjupa, J., et al. 2019, MNRAS, 490, 4786

Gravity Collaboration, Abuter, R., Amorim, A., et al. 2018, A&A, 615, L15

Gravity Collaboration, Abuter, R., Amorim, A., et al. 2019, A&A, 625, L10

Gravity Collaboration, Abuter, R., Amorim, A., et al. 2021, A&A, 647, A59

Green, G. M., Schlafly, E., Zucker, C., Speagle, J. S., & Finkbeiner, D. 2019, ApJ, 887, 93

Grieco, V., Matteucci, F., Pipino, A., & Cescutti, G. 2012, A&A, 548, A60

Groenewegen, M. A. T. 2004, A&A, 425, 595

Guo, Y., Ferguson, H. C., Bell, E. F., et al. 2015, ApJ, 800, 39

Guo, Y., Jogee, S., Finkelstein, S. L., et al. 2023, ApJ, 945, L10

Harris, C. R., Millman, K. J., van der Walt, S. J., et al. 2020, Nature, 585, 357

Hayden, M. R., Recio-Blanco, A., de Laverny, P., Mikolaitis, S., & Worley, C. C. 2017, A&A, 608, L1

Haywood, M., Di Matteo, P., Lehnert, M. D., Katz, D., & Gómez, A. 2013, A&A, 560, A109

Heger, A. & Woosley, S. E. 2002, ApJ, 567, 532

Hill, V., Lecureur, A., Gómez, A., et al. 2011, A&A, 534, A80

Hillebrandt, W. & Niemeyer, J. C. 2000, ARAA, 38, 191

Hobbs, D., Brown, A., Høg, E., et al. 2021, Experimental Astronomy

Hohl, F. 1971, ApJ, 168, 343

Holley-Bockelmann, K., Weinberg, M., & Katz, N. 2005, MNRAS, 363, 991

Holmberg, E. 1941, ApJ, 94, 385

Horta, D., Schiavon, R. P., Mackereth, J. T., et al. 2021, MNRAS, 500, 1385

Howard, C. D., Rich, R. M., Reitzel, D. B., et al. 2008, ApJ, 688, 1060

Hubble, E. P. 1927, The Observatory, 50, 276

Hubble, E. P. 1929, ApJ, 69, 103

Hubble, E. P. 1936, Realm of the Nebulae (New Haven, Conn.: Yale University Press)

Huertas-Company, M., Bernardi, M., Pérez-González, P. G., et al. 2016, MNRAS, 462, 4495

Hunt, J. A. S., Johnston, K. V., Pettitt, A. R., et al. 2020, MNRAS, 497, 818

Hunt, J. A. S., Kawata, D., Grand, R. J. J., et al. 2015, MNRAS, 450, 2132

Hunter, J. D. 2007, Computing in Science & Engineering, 9, 90

Iorio, G., Belokurov, V., Erkal, D., et al. 2018, MNRAS, 474, 2142

Ivezić, Ž., Kahn, S. M., & Eliason, P. 2015, arXiv e-prints, arXiv:1502.06555

Iwanek, P., Soszyński, I., & Kozłowski, S. 2021, ApJ, 919, 99

Johnson, C. I., Rich, R. M., Fulbright, J. P., Valenti, E., & McWilliam, A. 2011, ApJ, 732, 108

Johnson, C. I., Rich, R. M., Kobayashi, C., et al. 2013, ApJ, 765, 157

Johnson, H. M. 1957, AJ, 62, 19

Jones, L. & Yoachim, P. 2023, Rubin Metric Analysis Framework

Julian, W. H. & Toomre, A. 1966, ApJ, 146, 810

Jung, C. & Zotos, E. E. 2016, MNRAS, 457, 2583

Karttunen, H., Kröger, P., Oja, H., Poutanen, M., & Donner, K. J. 2017, Fundamental Astronomy (Springer)

Kepner, J. V. 1999, ApJ, 520, 59

Khoperskov, S., Haywood, M., Di Matteo, P., Lehnert, M. D., & Combes, F. 2018, A&A, 609, A60

Kim, W.-T., Seo, W.-Y., Stone, J. M., Yoon, D., & Teuben, P. J. 2012, ApJ, 747, 60

Kluyver, T., Ragan-Kelley, B., Pérez, F., et al. 2016, in Positioning and Power in Academic Publishing: Players, Agents and Agendas (IOS Press), 87–90

Klypin, A. A., Strukov, I. A., & Skulachev, D. P. 1992, MNRAS, 258, 71

Koppelman, H. H. & Helmi, A. 2021, A&A, 645, A69

Kormendy, J. 1993, in IAU Symp. 153: Galactic Bulges, ed. H. Dejonghe & H. J. Habing, 209

Kormendy, J. 2013, Secular Evolution in Disk Galaxies, ed. J. Falcón-Barroso & J. H. Knapen (Cambridge University Press), 1

Kormendy, J. & Illingworth, G. 1982, ApJ, 256, 460

Kormendy, J. & Kennicutt, R. C. 2004, ARAA, 42, 603

Kraljic, K., Bournaud, F., & Martig, M. 2012, ApJ, 757, 60

Kruk, S. J., Erwin, P., Debattista, V. P., & Lintott, C. 2019, MNRAS, 490, 4721

Kubryk, M., Prantzos, N., & Athanassoula, E. 2013, MNRAS, 436, 1479

Kuijken, K. & Merrifield, M. R. 1995, ApJ, 443, L13

Kuijken, K. & Rich, R. M. 2002, AJ, 124, 2054

Kunder, A., Koch, A., Rich, R. M., et al. 2012, AJ, 143, 57

Kunder, A., Pérez-Villegas, A., Rich, R. M., et al. 2020, AJ, 159, 270

Lacey, C. & Cole, S. 1993, MNRAS, 262, 627

Le Conte, Z. A., Gadotti, D. A., Ferreira, L., et al. 2023, arXiv e-prints, arXiv:2309.10038

Lebzelter, T., Mowlavi, N., Lecoeur-Taibi, I., et al. 2023, A&A, 674, A15

Li, X., Shlosman, I., Heller, C., & Pfenniger, D. 2022, arXiv e-prints, arXiv:2211.04484

Li, X., Shlosman, I., Pfenniger, D., & Heller, C. 2023, MNRAS, 520, 1243

Licquia, T. C. & Newman, J. A. 2015, ApJ, 806, 96

Lim, D., Koch-Hansen, A. J., Chung, C., et al. 2021, arXiv e-prints, arXiv:2101.06269

Limberg, G., Santucci, R. M., Rossi, S., et al. 2021, ApJ, 913, 11

Lin, C. C. & Bertin, G. 1985, in The Milky Way Galaxy, ed. H. Van Woerden, R. J. Allen, & W. B. Burton (Dordrecht: Springer Netherlands), 513–532

Lindegren, L., Hernández, J., Bombrun, A., et al. 2018, A&A, 616, A2

Lindegren, L., Klioner, S. A., Hernández, J., et al. 2021b, A&A, 649, A2

Loebman, S. R., Debattista, V. P., Nidever, D. L., et al. 2016, ApJ, 818, L6

Loebman, S. R., Roškar, R., Debattista, V. P., et al. 2011, ApJ, 737, 8

Łokas, E. L. 2019, A&A, 629, A52

Łokas, E. L. 2020, A&A, 634, A122

Lonappan, A. I., Kumar, S., Ruchika, Dinda, B. R., & Sen, A. A. 2018, Phys. Rev. D., 97, 043524

Lowing, B., Wang, W., Cooper, A., et al. 2015, MNRAS, 446, 2274

Lucy, L. B. 1977, AJ, 82, 1013

Lütticke, R., Dettmar, R.-J., & Pohlen, M. 2000, A&AS, 145, 405

Lynden-Bell, D. & Kalnajs, A. J. 1972, MNRAS, 157, 1

Marchetti, T., Joyce, M., Johnson, C., et al. 2023, arXiv e-prints, arXiv:2310.17542

Marchuk, A. A., Smirnov, A. A., Sotnikova, N. Y., et al. 2022, MNRAS, 512, 1371

Marinacci, F., Vogelsberger, M., Pakmor, R., et al. 2018, MNRAS, 480, 5113

Marrese, P. M., Marinoni, S., Fabrizio, M., & Altavilla, G. 2019, A&A, 621, A144

Marshall, D. J., Robin, A. C., Reylé, C., Schultheis, M., & Picaud, S. 2006, A&A, 453, 635

Martel, H. & Richard, S. 2020, MNRAS, 498, 940

Martinez-Valpuesta, I. & Shlosman, I. 2004, ApJ, 613, L29

Martinez-Valpuesta, I., Shlosman, I., & Heller, C. 2006, ApJ, 637, 214

Masters, K. L. & Galaxy Zoo Team. 2020, in Galactic Dynamics in the Era of Large Surveys, ed. M. Valluri & J. A. Sellwood, Vol. 353, 205–212

Matthews, B. W. 1975, Biochimica et Biophysica Acta (BBA) - Protein Structure, 405, 442

McWilliam, A. & Zoccali, M. 2010, ApJ, 724, 1491

Méndez-Abreu, J., Corsini, E. M., Debattista, V. P., et al. 2008, ApJ, 679, L73

Méndez-Abreu, J., Debattista, V. P., Corsini, E. M., & Aguerri, J. A. L. 2014, A&A, 572, A25

Menendez-Delmestre, K., Sheth, K., Schinnerer, E., Jarrett, T. H., & Scoville, N. Z. 2007, ApJ, 657, 790

Menon, H., Wesolowski, L., Zheng, G., et al. 2015, Computational Astrophysics and Cosmology, 2, 1

Merrill, P. W. 1923, ApJ, 58, 215

Merritt, D. & Sellwood, J. A. 1994, ApJ, 425, 551

Michel-Dansac, L. & Wozniak, H. 2006, A&A, 452, 97

Miller, G. E. & Scalo, J. M. 1979, ApJS, 41, 513

Minniti, D. 1996, ApJ, 459, 175

Mortlock, A., Conselice, C. J., Hartley, W. G., et al. 2013, MNRAS, 433, 1185

Mowlavi, N., Lecoeur-Taïbi, I., Lebzelter, T., et al. 2018, A&A, 618, A58

Naiman, J. P., Pillepich, A., Springel, V., et al. 2018, MNRAS, 477, 1206

Nataf, D. M., Udalski, A., Gould, A., Fouqué, P., & Stanek, K. Z. 2010, ApJ, 721, L28

Nelson, D., Pillepich, A., Springel, V., et al. 2019b, MNRAS, 490, 3234

Nelson, D., Pillepich, A., Springel, V., et al. 2018, MNRAS, 475, 624

Nelson, D., Springel, V., Pillepich, A., et al. 2019a, Computational Astrophysics and Cosmology, 6, 2

Nelson, E. J., van Dokkum, P. G., Brammer, G., et al. 2012, ApJ, 747, L28

Ness, M., Debattista, V. P., Bensby, T., et al. 2014, ApJ, 787, L19

Ness, M. & Freeman, K. 2016, PASA, 33, e022

Ness, M., Freeman, K., Athanassoula, E., et al. 2013a, MNRAS, 430, 836

Ness, M., Freeman, K., Athanassoula, E., et al. 2013b, MNRAS, 432, 2092

Ness, M., Freeman, K., Athanassoula, E., et al. 2012, ApJ, 756, 22

Ness, M., Hogg, D. W., Rix, H.-W., et al. 2016b, ApJ, 823, 114

Ness, M. & Lang, D. 2016, AJ, 152, 14

Ness, M., Zasowski, G., Johnson, J. A., et al. 2016a, ApJ, 819, 2

Nicholls, C. P., Wood, P. R., Cioni, M. R. L., & Soszyński, I. 2009, MNRAS, 399, 2063

Nidever, D. L., Bovy, J., Bird, J. C., et al. 2014, ApJ, 796, 38

Nikolaev, S. & Weinberg, M. D. 1997, ApJ, 487, 885

Nikzat, F., Ferreira Lopes, C. E., Catelan, M., et al. 2022, A&A, 660, A35

Nishiyama, S., Nagata, T., Baba, D., et al. 2005, ApJ, 621, L105

O'Neill, J. K. & Dubinski, J. 2003, MNRAS, 346, 251

Oppenheimer, J. R. & Volkoff, G. M. 1939, Physical Review, 55, 374

Ortolani, S., Renzini, A., Gilmozzi, R., et al. 1995, Nature, 377, 701

Patel, S. G., Fumagalli, M., Franx, M., et al. 2013, ApJ, 778, 115

Pawlak, M. 2023, A&A, 669, A60

Pérez, I., Martínez-Valpuesta, I., Ruiz-Lara, T., et al. 2017, MNRAS, 470, L122

Perryman, M. A. C. 1986, Highlights of Astronomy, 7, 673

Pfenniger, D. & Friedli, D. 1991, A&A, 252, 75

Pillepich, A., Nelson, D., Hernquist, L., et al. 2018b, MNRAS, 475, 648

Pillepich, A., Nelson, D., Springel, V., et al. 2019, MNRAS, 490, 3196

Pillepich, A., Springel, V., Nelson, D., et al. 2018a, MNRAS, 473, 4077

Planck Collaboration, Aghanim, N., Akrami, Y., et al. 2020, A&A, 641, A1

Plevne, O., Önal Taş, Ö., Bilir, S., & Seabroke, G. M. 2020, ApJ, 893, 108

Pojmanski, G. 1997, Acta Astronomica, 47, 467

Pollacco, D. L., Skillen, I., Collier Cameron, A., et al. 2006, PASP, 118, 1407

Pontzen, A., Roškar, R., Stinson, G. S., et al. 2013, pynbody: Astrophysics Simulation Analysis for Python, astrophysics Source Code Library, ascl:1305.002

Portail, M., Wegg, C., Gerhard, O., & Ness, M. 2017, MNRAS, 470, 1233

Potter, D., Stadel, J., & Teyssier, R. 2017, Computational Astrophysics and Cosmology, 4, 2

Qin, W., Nataf, D. M., Zakamska, N., Wood, P. R., & Casagrande, L. 2018, ApJ, 865, 47

Qu, Y., Di Matteo, P., Lehnert, M. D., & van Driel, W. 2011, A&A, 530, A10

Queiroz, A. B. A., Chiappini, C., Perez-Villegas, A., et al. 2021, A&A, 656, A156

Quillen, A. C. 2002, AJ, 124, 722

Quillen, A. C., Minchev, I., Sharma, S., Qin, Y.-J., & Di Matteo, P. 2014, MNRAS, 437, 1284

Raha, N., Sellwood, J. A., James, R. A., & Kahn, F. D. 1991, Nature, 352, 411

Rattenbury, N. J., Mao, S., Sumi, T., & Smith, M. C. 2007, MNRAS, 378, 1064

Reggiani, H., Schlaufman, K. C., Casey, A. R., & Ji, A. P. 2020, AJ, 160, 173

Renzini, A., Gennaro, M., Zoccali, M., et al. 2018, ApJ, 863, 16

Rich, R. M. 1990, ApJ, 362, 604

Rich, R. M., Reitzel, D. B., Howard, C. D., & Zhao, H. 2007, ApJ, 658, L29

Ricker, G. R., Winn, J. N., Vanderspek, R., et al. 2014, in Society of Photo-Optical Instrumentation Engineers (SPIE) Conference Series, Vol. 9143, Space Telescopes

and Instrumentation 2014: Optical, Infrared, and Millimeter Wave, ed. J. Oschmann, Jacobus M., M. Clampin, G. G. Fazio, & H. A. MacEwen, 914320

Rodriguez-Gomez, V., Genel, S., Vogelsberger, M., et al. 2015, MNRAS, 449, 49

Rojas-Arriagada, A., Recio-Blanco, A., Hill, V., et al. 2014, A&A, 569, A103

Rosas-Guevara, Y., Bonoli, S., Dotti, M., et al. 2022, MNRAS, 512, 5339

Roškar, R., Debattista, V. P., Stinson, G. S., et al. 2008, ApJ, 675, L65

Rubin, V. C., Ford, W. K., J., & Thonnard, N. 1980, ApJ, 238, 471

Rubin, V. C. & Ford, W. Kent, J. 1970, ApJ, 159, 379

Saha, K. & Gerhard, O. 2013, MNRAS, 430, 2039

Saha, K., Graham, A. W., & Rodríguez-Herranz, I. 2018, ApJ, 852, 133

Sahu, K. C., Casertano, S., Bond, H. E., et al. 2006, Nature, 443, 534

Saito, R. K., Hempel, M., Minniti, D., et al. 2012, A&A, 537, A107

Saito, R. K., Zoccali, M., McWilliam, A., et al. 2011, AJ, 142, 76

Sales, L. V., Navarro, J. F., Schaye, J., et al. 2010, MNRAS, 409, 1541

Sanders, J. L., Matsunaga, N., Kawata, D., et al. 2022, MNRAS, 517, 257

Sanders, J. L., Smith, L., Evans, N. W., & Lucas, P. 2019, MNRAS, 487, 5188

Scannapieco, C. & Athanassoula, E. 2012, MNRAS, 425, L10

Schawinski, K., Urry, C. M., Simmons, B. D., et al. 2014, MNRAS, 440, 889

Schlaufman, K. C., Thompson, I. B., & Casey, A. R. 2018, ApJ, 867, 98

Schmidt, M. 1957, Bulletin of the Astronomical Institutes of the Netherlands, 14, 17

Sellwood, J. A. 1981, A&A, 99, 362

Sellwood, J. A. 1985, MNRAS, 217, 127

Sellwood, J. A. 1993, in Galactic Bulges, ed. H. Dejonghe & H. J. Habing, Vol. 153, 391

Sellwood, J. A. & Debattista, V. P. 2009, MNRAS, 398, 1279

Sellwood, J. A. & Gerhard, O. 2020, MNRAS, 495, 3175

Sellwood, J. A. & Moore, E. M. 1999, ApJ, 510, 125

Sellwood, J. A. & Wilkinson, A. 1993, Reports of Progress in Physics, 56, 173

Semczuk, M., Dehnen, W., Schönrich, R., & Athanassoula, E. 2022, MNRAS, 509, 4532

Sérsic, J. L. 1968, Atlas de galaxias australes (Cordoba, Argentina: Observatorio Astronomico, 1968)

Sharples, R., Walker, A., & Cropper, M. 1990, MNRAS, 246, 54

Shen, J., Rich, R. M., Kormendy, J., et al. 2010, ApJ, 720, L72

Shen, J. & Sellwood, J. A. 2004, ApJ, 604, 614

Sheth, K., Regan, M., Hinz, J. L., et al. 2010, PASP, 122, 1397

Shvartzvald, Y., Waxman, E., Gal-Yam, A., et al. 2023, arXiv e-prints, arXiv:2304.14482

Simion, I. T., Belokurov, V., Irwin, M., et al. 2017, MNRAS, 471, 4323

Skokos, C., Patsis, P. A., & Athanassoula, E. 2002a, MNRAS, 333, 847

Skokos, C., Patsis, P. A., & Athanassoula, E. 2002b, MNRAS, 333, 861

Skrutskie, M. F., Cutri, R. M., Stiening, R., et al. 2006, AJ, 131, 1163

Smirnov, A. A. & Sotnikova, N. Y. 2019, MNRAS, 485, 1900

Smith, S. W. 1999, The Scientist and Engineer's Guide to Digital Signal Processing (California Technical Publishing), 15

Smoot, G., Bennett, C., Weber, R., et al. 1990, ApJ, 360, 685

Soderblom, D. R. 2010, ARAA, 48, 581

Sormani, M. C., Binney, J., & Magorrian, J. 2015, MNRAS, 449, 2421

Sotillo-Ramos, D., Pillepich, A., Donnari, M., et al. 2022, MNRAS, 516, 5404

Soto, M., Rich, R. M., & Kuijken, K. 2007, ApJ, 665, L31

Spano, M., Mowlavi, N., Eyer, L., Marquette, J. B., & Burki, G. 2011, in Astronomical Society of the Pacific Conference Series, Vol. 445, Why Galaxies Care about AGB Stars II: Shining Examples and Common Inhabitants, ed. F. Kerschbaum, T. Lebzelter, & R. F. Wing, 545

Springel, V. 2010, MNRAS, 401, 791

Springel, V., Frenk, C. S., & White, S. D. M. 2006, Nature, 440, 1137

Springel, V., Pakmor, R., Pillepich, A., et al. 2018, MNRAS, 475, 676

Springel, V., White, S. D. M., Tormen, G., & Kauffmann, G. 2001, MNRAS, 328, 726

Stadel, J. G. 2001, Ph.D. Thesis, University of Washington

Stanek, K. Z., Mateo, M., Udalski, A., et al. 1994, ApJ, 429, L73

Stanek, K. Z., Udalski, A., Szymanski, M., et al. 1997, ApJ, 477, 163

Steigman, G. 2007, Annual Review of Nuclear and Particle Science, 57, 463

Stinson, G., Seth, A., Katz, N., et al. 2006, MNRAS, 373, 1074

Street, R. A., Lund, M. B., Donachie, M., et al. 2018, arXiv e-prints, arXiv:1812.04445

Suberlak, K., Slater, C., & Ivezić, v. 2018, LSST Data Management Tech. Note

Taylor, M. B. 2005, in Astronomical Society of the Pacific Conference Series, Vol. 347, Astronomical Data Analysis Software and Systems XIV, ed. P. Shopbell, M. Britton, & R. Ebert, 29

The Rubin Observatory Survey Cadence Optimization Committee. 2023, Survey Cadence Optimization Committee's Phase 2 Recommendations

Toomre, A. 1964, ApJ, 139, 1217

Toomre, A. 1981, in Structure and Evolution of Normal Galaxies, ed. S. M., Fall & D. Lynden-Bell (Cambridge: Cambridge University Press), 111–136

Trabucchi, M. & Mowlavi, N. 2022, A&A, 658, L1

Trabucchi, M., Mowlavi, N., & Lebzelter, T. 2021a, A&A, 656, A66

Trabucchi, M., Wood, P. R., Mowlavi, N., et al. 2021b, MNRAS, 500, 1575

Tremaine, S. 1989, in Dynamics of Astrophysical Discs, ed. J. A. Sellwood, 231–238

Tremmel, M., Karcher, M., Governato, F., et al. 2017, MNRAS, 470, 1121

Tsikoudi, V. 1979, ApJ, 234, 842

Udalski, A., Szymanski, M., Kaluzny, J., Kubiak, M., & Mateo, M. 1992, Acta Astronomica, 42, 253

Umeda, H. & Nomoto, K. 2003, Nature, 422, 871

Uttenthaler, S., Schultheis, M., Nataf, D. M., et al. 2012, A&A, 546, A57

Valenti, E., Zoccali, M., Gonzalez, O. A., et al. 2016, A&A, 587, L6

Valenti, E., Zoccali, M., Renzini, A., et al. 2013, A&A, 559, A98

Valluri, M., Shen, J., Abbott, C., & Debattista, V. P. 2016, ApJ, 818, 141

van Albada, T. S. & Baker, N. 1973, ApJ, 185, 477

van de Hulst, H. C., Raimond, E., & van Woerden, H. 1957, Bulletin of the Astronomical Institutes of the Netherlands, 14, 1

van der Marel, R. P. & Franx, M. 1993, ApJ, 407, 525

Vásquez, S., Zoccali, M., Hill, V., et al. 2013, A&A, 555, A91

Venn, K. A., Irwin, M., Shetrone, M. D., et al. 2004, AJ, 128, 1177

Virtanen, P., Gommers, R., Oliphant, T. E., et al. 2020, Nature Methods, 17, 261

Vogelsberger, M., Marinacci, F., Torrey, P., & Puchwein, E. 2020, Nature Reviews Physics, 2, 42

Volders, L. M. J. S. 1959, Bulletin of the Astronomical Institutes of the Netherlands, 14, 323

von Hoerner, S. 1960, Zeitschrift fuer Astrophysik, 50, 184

Wadsley, J. W., Stadel, J., & Quinn, T. 2004, New Astronomy, 9, 137

Walker, A. R. 1989, PASP, 101, 570

Walo-Martín, D., Pinna, F., Grand, R. J. J., et al. 2022, MNRAS, 513, 4587

Wan, J.-C., Liu, C., & Deng, L.-C. 2017, Research in Astronomy and Astrophysics, 17, 079

Wang, L., Dutton, A. A., Stinson, G. S., et al. 2015, MNRAS, 454, 83

Wang, Y., Athanassoula, E., Patsis, P., & Mao, S. 2022, A&A, 668, A55

Wegg, C. & Gerhard, O. 2013, MNRAS, 435, 1874

Wegg, C., Gerhard, O., & Portail, M. 2015, MNRAS, 450, 4050

Wegg, C., Rojas-Arriagada, A., Schultheis, M., & Gerhard, O. 2019, A&A, 632, A121

Weinberg, M. D. 1985, MNRAS, 213, 451

Weinberger, R., Springel, V., Hernquist, L., et al. 2017, MNRAS, 465, 3291

Weiner, B. J. & Sellwood, J. A. 1999, ApJ, 524, 112

Wes McKinney. 2010, in Proceedings of the 9th Python in Science Conference, 56 – 61

WFIRST Astrometry Working Group, Sanderson, R. E., Bellini, A., et al. 2019, Journal of Astronomical Telescopes, Instruments, and Systems, 5, 044005

White, S. D. M. 1976, MNRAS, 177, 717

Whitelock, P. A., Feast, M. W., & Van Leeuwen, F. 2008, MNRAS, 386, 313

Wilson, E. B. 1927, Journal of the American Statistical Association, 22, 209

Wood, P. R., Alcock, C., Allsman, R. A., et al. 1999, in IAU Symposium Proceedings, Vol. 191, Asymptotic Giant Branch Stars, ed. T. Le Bertre, A. Lebre, & C. Waelkens, 151

APPENDIX

Woosley, S. E. & Weaver, T. A. 1995, ApJS, 101, 181

Yan, Y., Du, C., Liu, S., et al. 2019, ApJ, 880, 36

Yoshii, Y. 1982, PASJ, 34, 365

Yuan, W., Macri, L. M., He, S., et al. 2017, AJ, 154, 149

Yule, G. U. 1912, Journal of the Royal Statistical Society, 75, 579

Zasowski, G., Cohen, R. E., Chojnowski, S. D., et al. 2017, AJ, 154, 198

Zasowski, G., Johnson, J. A., Frinchaboy, P. M., et al. 2013, AJ, 146, 81

Zhang, H. & Sanders, J. L. 2023, MNRAS, 521, 1462

Zhao, D., Du, M., Ho, L. C., Debattista, V. P., & Shi, J. 2020, ApJ, 904, 170

Zoccali, M., Gonzalez, O. A., Vasquez, S., et al. 2014, A&A, 562, A66

Zoccali, M., Hill, V., Lecureur, A., et al. 2008, A&A, 486, 177

Zoccali, M., Renzini, A., Ortolani, S., et al. 2003, A&A, 399, 931

Zoccali, M., Vasquez, S., Gonzalez, O. A., et al. 2017, A&A, 599, A12

Appendix A

Roman Core Community Survey White Paper

The following extracts are contributions to a whitepaper submitted to the community-led work of defining the observational strategies for NASA's *Nancy Grace Roman Space Telescope (RST)* Core Community Surveys call and to arXiv[1], as:

Maximizing science return by coordinating the survey strategies of Roman with Rubin and other major facilities

presented by the following authors:

Submitting author: R.A. Street, Las Cumbres Observatory

Contributing authors: *S. Gough-Kelly, Jeremiah Horrocks Institute, UCLan,* C. Lam, UC Berkeley, A. Varela, M. Makler, International Center for Advanced Studies, Argentina, E. Bachelet, IPAC, J.R. Lu, N. Abrams, A. Pusack, S. Terry, UC

[1] arXiv:2306.13792

APPENDIX A

Berkeley, R. Di Stefano, CfA Harvard, Y. Tsapras, M.P.G. Hundertmark, Uni Heidelberg, R.J.J. Grand, Astrophysics Research Institute, LJMU, T. Daylan, Princeton, J. Sobeck, University of Washington

Abstract

The Nancy Grace Roman Space Telescope will be one of several flagship survey facilities operating over the next decade, starting ∼2025. The deep near-IR imaging that Roman will deliver will be highly complementary to the capabilities of other survey telescopes that will operate contemporaneously, particularly those that can provide data at different wavelengths and messengers or different time intervals. Combining data from multiple facilities can provide important astrophysical insights, provided the data acquisition is carefully scheduled and careful plans are made for appropriate joint data analyses. In this White Paper, we discuss the broad range of science that would be enabled by coordinating Roman observations of the Galactic Bulge with those of the Vera C. Rubin Observatory. Specifically, we discuss how Roman's characterisation of lensing events caused by exoplanets, stellar systems and stellar remnants can be enhanced by data from Rubin. The same data will also be highly advantageous for the determination of stellar properties and for distinguishing exoplanetary transits. It will enable more accurate period-colour-luminosity relationships to be measured for RR Lyrae throughout the Milky Way Bulge and Bar, probing Galactic structure and dynamics. But we stress that this is only a sample of the full potential and advocate for a more complete study to be made as a joint effort between these major projects. In summary, we recommend:

1. Close coordination between the groups responsible for survey strategy for the Roman Mission and Rubin Observatory to maximise the scientific return of

the combined data products.

2. Wherever possible, coordinating the timing of the Roman Bulge observation seasons with the long-baseline observations of Rubin. In particular, if Rubin undertakes rolling cadence seasons, these would be most beneficial if they occurred during the gaps in Roman Bulge seasons. We also highlight the value of acquiring contemporaneous observations in constraining the masses of free-floating planet microlensing events.

3. A broader study of the scientific potential of coordinated scheduling and data analysis from major surveys should be funded, including science by all of the Roman Core Surveys, and considering a wide range of complementary facilities and catalogues.

4. The development of metrics designed to evaluate how changes in the strategy of one survey impact the science return of another. These should be used by both surveys.

We note that we do not suggest any changes beyond the established Science Requirements for the RGBTDS in terms of survey footprint or filter selection.

A.1 Scientific Motivations

The combination of near-IR timeseries imaging from the Nancy Grace Roman Space Telescope with multi-band optical imaging from the Vera C. Rubin Observatory's Legacy Survey of Space and Time (LSST) will be highly beneficial for numerous science goals from both flagship missions. Here, we highlight the scientific benefits of the Roman Galactic Bulge Time Domain Survey (RGBTDS, see White Paper by Gaudi et al.).

A.1.1 Stellar Astrophysics and Kinematics

Multiwavelength imaging data will be important in determining stellar spectral types in the RGBTDS region, as most sources will be too faint for spectroscopy. Photometric metallicities derived from combined optical+NIR bandpasses will enable us to distinguish between metal-rich and -poor stellar populations that follow different rotation curves through the Galactic Centre (Clarkson et al. 2018) and which theory suggests support different Galactic structures (Gough-Kelly et al. 2022). Age estimates determined from isochrone fitting will be a key result, as Roman will reach the Main Sequence Turn Off at low Galactic latitude.

A.1.2 Stellar Variability

The timeseries data provided by Roman and Rubin will uncover a wealth of stellar variables, from eclipsing binaries to pulsators of all types. Multi-band timeseries photometry will reveal the varying depth of stellar-companion eclipses in different passbands, constraining the spectral type of both companions and enabling them to be distinguished from planetary transits. Time-variable colour, particularly in passbands that are widely separated in wavelength, will be a vital parameter in the accurate classification of variable stars since both Roman and Rubin will probe fainter limiting magnitudes than previous catalogues and complement Gaia Ivezić et al. (2015). Colour is also one of the essential terms in the period-colour-luminosity relationship that allows RR Lyrae to be used as standard candles. A joint analysis of Roman and Rubin data would be highly beneficial to studies of the Galactic structure in the "heart of the Milky Way". Roman GBTDS will be ideal for finding large populations of Long-Period Variables (LPVs) such as Miras and Semi-Regular Variables close to the Galactic Centre, and its high cadence timeseries is ideal for asteroseismology. It's deep limiting magnitude timeseries data will detect RR Lyrae and LPVs deep within the Galactic Bulge and Bar and even on the far side, enabling

us to map the 3D structure of the inner Milky Way, including extinction. Thanks to Roman's precise parallax measurements, these stars will be used as standard candles to underpin cosmological models and probe dust distributions in this region. But the gaps in Roman's timeseries are problematic, as LPVs commonly have periods of 100s of days. Rubin's photometry in the season gaps will constrain the morphology of the variable light curves and hence improve the measurement of their periodicities.

A.2 Synergies With Other Survey Facilities

Although we have focused on synergies with the Rubin Observatory in this White Paper, it will not be the only major survey facility with complementary capabilities, and we recommend a broader review be undertaken to evaluate the benefits of joint data analyses. For example, the Gaia source catalogue is limited to relatively bright stars within the RGBTDS field, as the crowding in this region leads to excessive demands for onboard computations. Roman photometry and astrometry will extend our view of the Bulge and Bar to regions on the far side of the Galaxy (Fig. A.2). This promises to offer a goldmine of ages and distance measurements from variable star lightcurves that will be valuable for Galactic archaeology and dynamics. It will also help us to better assess extinction and other aspects of Gaia's selection function, such as crowding.

A.3 Conclusions

The Roman GBTDS will be groundbreaking not only for exoplanetary science but for a wide range of stellar astrophysics. That the survey will be in operation at the same time as other wide-field surveys of similar limiting magnitude, sky area, and complementary time cadence and wavelength coverage offer us unique scientific opportunities. In order to maximise the science return from both Roman GBTDS

APPENDIX A

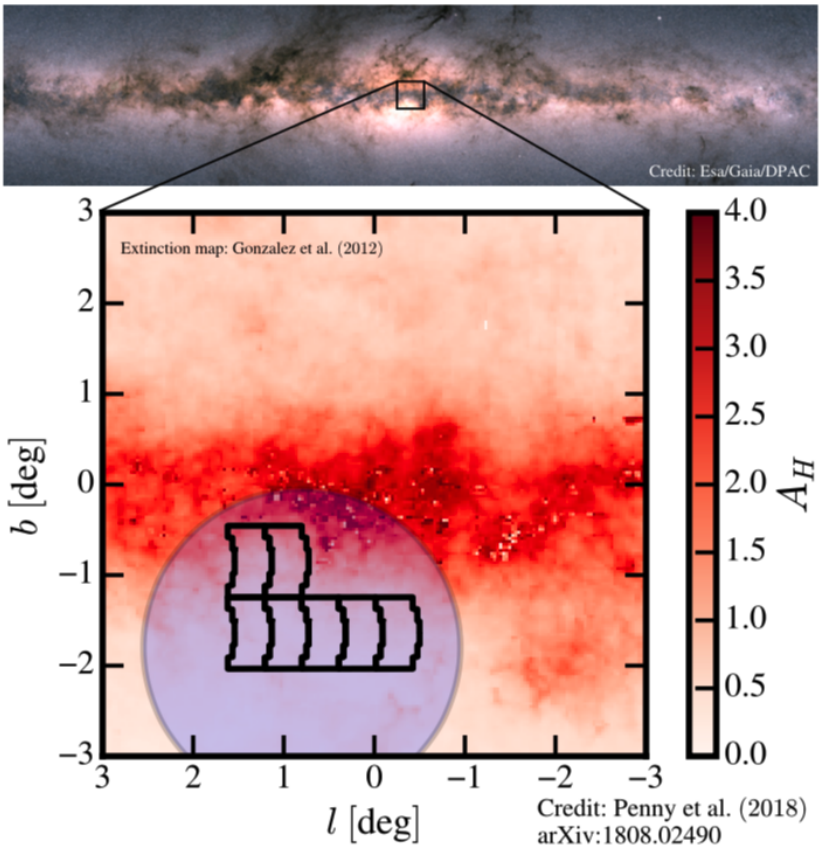

Figure A.1: (Left) Comparison of the Roman Galactic Bulge Time Domain Survey field (black mosaic outline, 1.53° × 1.5°) with the field of view of a proposed LSST Deep Drilling Field (blue circle with a 3.5° diameter, Street et al. 2018). Note that the LSST survey strategy is still being refined and could be adjusted to include a Roman field at the Galactic Centre.

and the LSST, we recommend:

1. That the RGBTDS seasons be scheduled in coordination with the Rubin Observatory's LSST, such that Rubin provides, at minimum, daily observations in at least 3 optical pass bands during the intra-season gaps. These data will provide alerts of microlensing anomalies that would otherwise be missed, as well as tighter constraints on the microlensing parallax, and hence the mass of the lensing objects, than Roman alone can achieve. The same dataset will deliver a wealth of additional astrophysics, helping us to characterise RR Lyrae in the Bulge, etc. We further recommend that opportunities for contemporaneous observations be explored. This will require close coordination between the groups responsible for the survey strategy for the Roman Mission and Rubin Observatory.

2. That a broader study of the scientific potential of coordinated scheduling and data analysis from major surveys should be funded. Due to space constraints, we have focused on science from RGBTDS, but the combination of NIR and Rubin's optical data will also be highly beneficial for the High Latitude Survey, for example, in the measurement of photometric redshifts of galaxies, characterising supernovae lightcurves and probing the edges of the Milky Way halo. Furthermore, there will be other complementary surveys operating within this timeframe, such as ULTRASAT (Shvartzvald et al. 2023), that can further extend the wavelength coverage. We advocate for close coordination of the survey observing strategies, data handling and metrics of the next generation of Great Observatories and existing catalogues such as those from Gaia.

3. That metrics be developed to evaluate how changes to one survey's strategy impact the science return from another *as a joint effort between Roman, Rubin, and other major surveys.*

APPENDIX A

We note that it would be valuable to have a common framework for writing and running survey strategy simulations and metrics rather than develop separate code bases. The Metric Analysis Framework (Jones & Yoachim 2023) is an example of a project-supported code base that has successfully integrated metric code contributed from the wider community.

We emphasise that we do not request any changes to the current design of the Roman GBTDS in terms of changing the footprint or filter selection within a specific season. Rather, we note the exciting potential benefits of simply coordinating the scheduling of the existing survey design with other facilities.

Appendix A.a: Rubin Observatory's Legacy Survey of Space and Time (LSST)

With a 9.6 sq.deg. field of view, 8.4 m aperture and spatial resolution of 0.2"/pix, Rubin Observatory can deliver optical (SDSS-u, g, r, i, z, y) imaging that is highly complementary to that of Roman in the NIR. Rubin's signature survey, LSST, is expected to begin in early 2025 and continue for 10 yrs. The details of Rubin's survey strategy are currently being refined (The Rubin Observatory Survey Cadence Optimization Committee 2023), but the most recent baseline now includes long-term monitoring of a large region of the central Bulge, fully including the RGBTDS survey footprint and operating contemporaneously (Fig. A.1). Rubin's limiting magnitude in single exposures of the crowded Bulge fields is expected to reach (u: 24.07, g: 24.90, r: 24.40, i: 23.96, z: 23.38, y: 22.49) mag. (Suberlak et al. 2018) and will probe deeper in high-latitude fields. Our simulations indicate that Rubin will be able to monitor 47% of stars detected by Roman (Fig. A.1) and that Roman will probe tens of kpc deeper than Rubin (Fig. A.2). With careful coordination between Roman and Rubin, LSST could deliver regular, long-baseline monitoring of the RGBTDS

field that would fill the Roman season gaps. This would provide more precise measurements of the microlensing parallax (both due to Earth's annual motion and the satellite parallax due to the separation of the observatories) and provide real-time alerts of anomalous features. The optical+NIR data will characterise the Spectral Energy Distribution of the microlensing source stars, a vital step in the estimation of the source star's angular radius, which allows the lens mass to be determined. It will also identify the faintest source stars for future follow-up by Adaptive Optics imaging once the lens and source stars have separated.

We note that a number of key elements of Rubin's observing strategy in the Galactic Plane remain to be decided, in particular, whether a 'rolling cadence' strategy would be beneficial. A rolling cadence divides the sky into different spatial regions. Higher cadence observations can then be performed for one region while the other(s) is observed at lower cadence. In subsequent years the regions are alternated so that the entire survey footprint eventually receives the same number of visits. Through close coordination, a Rubin rolling cadence could be applied to a small region, including the RGBTDS footprint, with the high-cadence ($\sim$1–2 visits/day) phase timed to occur during the inter-season gaps in RGBTDS. This strategy was proposed as a Rubin survey strategy White Paper in Street et al. (2018).

Appendix A.b: Predicted Depths of Roman and Rubin From a Simulation

In the top panel of Fig. A.2, we present the face-on density distribution of a Milky Way-like barred galaxy from the Auriga Project (Grand et al. 2017). The bar major axis is angled 30° from the x-axis. White contours follow lines of constant log density. The yellow circle shows the location of the approximate Solar position within the model at $X = -8.232\,\mathrm{kpc}$ (Gravity Collaboration et al. 2018, 2021). The cyan and green wedges represent the widths and approximate depths of the

Roman GBTDS footprint and a Rubin pointing, respectively (see Fig. A.1). The depth of the Rubin field is limited to a heliocentric distance of $D \lesssim 12\,\mathrm{kpc}$ from the Solar position. Assuming each stellar particle of the model represents a red clump star (RC), we assign absolute magnitudes of $M_i(\mathrm{RC}) = 0.37 \pm 0.30$ and $M_H(\mathrm{RC}) = -1.40 \pm 0.30$ (Plevne et al. 2020) convolved with a Gaussian kernel (here the H-band serves as a proxy for Roman's F146 band). Then, by converting the positions of stellar particles to heliocentric coordinates, we estimate extinction values using the `combined19` dust map of the python package `MWDUST` (Bovy et al. 2016), allowing us to calculate apparent magnitudes of these mock RC stars. In the bottom two panels of Fig. A.2, we present the apparent magnitudes in the i- and H-bands as a function of D, with the red vertical line denoting the Galactic Centre and the red vertical dashed line in the top panel showing the estimated limiting depth of the Rubin field. Rubin i-band observations are expected to be limited to $m_i \lesssim 23.5\,\mathrm{mag.}$ (horizontal dashed line) or $D \lesssim 12\,\mathrm{kpc}$, reaching just beyond the Galactic Centre. We predict that Roman's magnitude limit will allow it to probe far beyond the Galactic Centre.

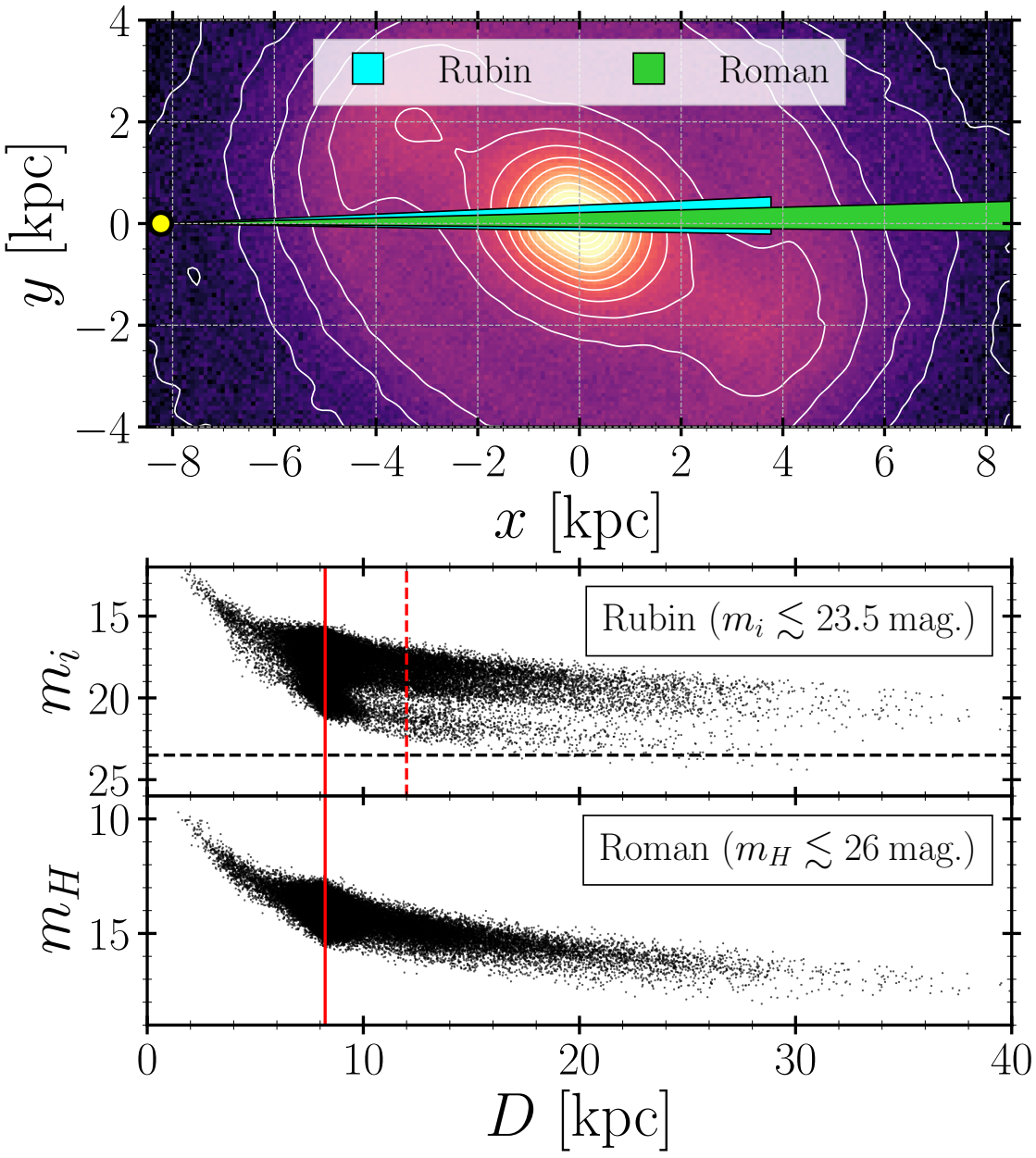

Figure A.2: (Top) The face-on density distribution of a Milky Way-like barred galaxy from the Auriga Project (Grand et al. 2017). (Bottom) The magnitude-distance distribution of synthetic red clump stars from the model. See Section A.3 for further details.